

King Khalid University



جامعة الملك خالد

Proceedings of

***13th Annual Scientific
Research Day***



**Organized by
Deanship of Scientific Research
and
College of Engineering Research Center**

Building (B) Auditorium (5)

Monday 2nd April 2018

Message from the Dean

Considering the rapid changes in the living environment, the College of Engineering here at King Khalid University is determined to nurture new talents and create engineers who can develop world class sustainable and green technologies for cleaner and sustainable environment.

Our mission is ‘To prepare a qualified engineering staff equipped with essential knowledge and skills in dealing with modern engineering technologies, in order to contribute to the development and improvement of our country’s future plans’.



The world is changing rapidly and it is facing challenges in many areas such as energy, water, food, health and environment. Challenges that creates opportunities. Engineers are best to develop process with innovative approach to tackle these challenges for a better and sustainable world. The starting point of any innovation is the laboratory apparatus and the outcome of development is the production plant. The up-to-date information about the process of development can be obtained not only from patent and published literature but also from conferences and discussed scientific meetings.

In this regard, the College of Engineering is collaborating with the Deanship of Scientific Research on an annual basis in organizing the ‘Annual Research Day’ event.

I hope this meeting will offer the most attractive platform for discussing emerging technologies that would result in multidisciplinary network, collaboration and high quality research outcomes.

Dr. Ibrahim Idris A. Falqi

Preface

The Organizing Committee extends a warm welcome to all participants with us in the 13th Annual Engineering Day hosted by the King Khalid's Deanship of Scientific Research in collaboration with the College of Engineering.

The Deanship of Scientific Research is committed to actively bring interesting and healthy research environment to King Khalid University. We want all the faculty of engineering disciplines to actively participate in research projects and to bring King Khalid University at par with other national and international educational and research institutions.

This major aim identified is to bring together academicians and research scholars of various interests on a common platform, initiating exchange of new ideas, experiences, knowledge and providing an opportunity to look for ways to find practical solutions for industrial and engineering problems.

It is a great pleasure to present the proceeding for the 13th Annual Research Day comprising of accepted research papers. The submitted papers were reviewed by the committee depending on the subject matter of the paper. Paper selected for oral presentation was on the basis of originality, significance and diversity of subjects.

Thanks to the Dr. Faleh Bin Raja Ullah Assalami, President, King Khalid University for his direct involvement and encouragement in fruitful research activities at the University and making the research funds available to the researchers.

We express our sincere thanks to all those involved in organizing this event for their support and timely help. Especial thanks for the Deanship of Scientific Research for their financial support that help directing this event.

Dr Ihab MTA Shigidi,
Organizing Committee,
13th Annual Research Day

13th Annual Research Day

Organised by the Deanship of Scientific Research in Collaboration with the College of
Engineering
Research Centre
2nd April 2018

Contents

S. No.	Title	Page No.
1	Backward-Facing Step Flow Simulation For Low And Moderate Reynolds Numbers	1
2	The Environmental Impact Of Fluoride Emissions From Aluminum Smelter At Jazan Economic City (JEC), Baish, Saudi Arabia On The Surrounding Ecosystem.	11
3	Fracture Characteristics And Size Dependent Effects Of Fibre Concrete Composites	16
4	Solar Disinfection Of Drinking Water With Nano-Titanium Dioxide	22
5	Essential Oil Of Officinal Sage Extraction And Antioxidant And Antimicrobial Activities Study	28
6	New Diagram Useful For Classification Of Water Quality	36
7	Design Of A Smart Guyed Mast To Mitigate Earthquakes	40
8	Epileptic Seizure Prediction Methods Based On EEG Signals	45
9	Development Of Corrosion Protective Coatings For Carbon Steel Using Polyaniline Modified Ferrochrome Slag Nanocomposite Materials	53
10	Evaluating The Precipitation-Topography Relationship And Precipitation Gradient Using Non-Stationary Modelling Technique In Aseer Region, Saudi Arabia	61
11	Simple And Fast Technique For Mobile Localization In 2D Environment	67
12	Universal Fuzzy Logic Controller And Application Of Genetic Algorithm For Tuning Of Scaling Factor For Real-Life Dynamic Systems	72
13	Green Siliceous Concrete Materials For Sustainability Using MCDM Approach	81
14	The Separation Of A Binary Water/Ethanol Solution Via A Continuous Feed Distillation Column As A Function Of Feed Stage Location And Reflux Ratio	90
15	Effect Of Liquid Forging Process Parameters On Properties Of Cast Metals And Alloys	95
16	Impact Of Hazardous Wastes On Human Health & Preventive Measures For A Sustainable Environment	103
17	Out Of Band Radiation Reduction In Multicarrier Cognitive Radio Systems	114
18	Integration Of The Active-Passive Architecture Techniques For Attaining Optimum Building Sustainability In The Hot-Dry Climate Regions Of Saudi Arabia	121
19	High Voltage Driver Electronics Design For DIODE Based Field Emission Display Based On Silicon Nano Electron Emitters.	127
20	Computationally Efficient Equalization Technique For High Mobility OFDMA Uplink Systems	132
21	Investigation On The Influence Of Errors On The Chatter Vibrations During Drilling Operation	144

Backward-Facing Step Flow Simulation for Low and Moderate Reynolds Numbers

C A Saleel¹ and Irfan Anjum Badruddin

Department of Mechanical Engineering, College of Engineering, King Khalid University,
PO Box 394, Abha 61411 KSA.

¹E-mail address: aveetil@kku.edu.sa

Abstract: The study of backward-facing step flows constitutes an important branch of fundamental fluid mechanics. This paper discusses the physics of flows over a backward-facing step geometry. The simulations are carried out by ANSYS 18.2 for various Reynolds numbers with an expansion ratio of 1.9423 which was adopted from the literature for the easiness of validation. The simulated Reynolds numbers are $Re=0.0001, 0.001, 0.01, 0.1, 1.0, 10, 50, 100, 200, 400$ and 800. It is understood that for the abovementioned Reynolds number range, two-dimensional predictions are enough and are carried out to provide information on the general integral properties of backward-facing step flows, on mean velocity distributions and streamlines. The stream wise velocity, transverse velocity, streamlines and vector plots are shown. The Reattachment length and other flow parameters are perfectly matching with the available literatures and hence complement information on backward-facing step flows.

Keywords: backward facing step flow, flow separation, reattachment length, recirculation eddies etc.

1. Introduction:

The study of backward-facing step flows constitutes an important branch of fundamental fluid mechanics. Flow geometry of the same is very significant for investigating separated flows. This flow is of particular interest because it facilitates the study of the reattachment process by minimizing the effect of the separation process, while for other separating and reattaching flow geometries there may be a stronger interaction between the two. The principal flow features of the backward facing step flow are illustrated in Figure 1.

The phenomenon of flow separation is a problem of great importance for fundamental and industrial reasons. For instance, it often corresponds to drastic losses in aerodynamic performances of airfoils or automotive vehicles. The backward-facing step is an extreme example

of separated flows that occur in aerodynamic devices such as high-lift airfoils at large angles of attack.

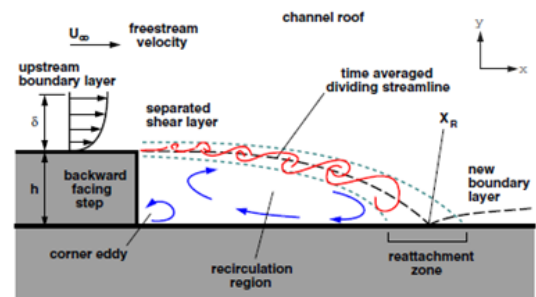


Figure 1. Detailed flow features of the backward facing step flow [1].

In these flows separation may be created by a strong adverse pressure gradient rather than a geometric perturbation, but the flow topology is similar. Also, it is important in heat exchangers

13th Annual Research Day

Organised by the Deanship of Scientific Research in Collaboration with the College of Engineering
Research Centre
2nd April 2018

and gas turbines, since the location of the reattachment zone and its flow structure also determine the local heat and mass transport properties of the flow. This geometry has been received attention for half a century. Large number of researchers have considered different aspects of this geometry from the flow pattern point of view and heat transfer. In many numerical simulations the backward facing step flow problem is used as a benchmark for validating the computational simulation algorithm.

Moffatt [2] predicted the existence of a sequence of vortices near corners under specified conditions. The flow features of flow over backward-facing step was already of curiosity even when fluid mechanical problems used to be addressed only by potential flow theory. Lee and Smith [3] shows that Potential flow theory permits the treatment of the backward-facing step flow that yields a streamline pattern which does not indicate any separation or recirculation region behind the step as shown in [2]. Taylor and Ndefo [4], Roache [5] and Durst and Pereira [6] are the few to come up initially with numerical predictions of backward-facing step flows for low Reynolds numbers. They could not get any separation at the upper corner of the step. However, a separated region was predicted at the lower corner that contained a single vortex only. The study of Ladeveze and Peyret [7] discloses that corner singularity at the step and its effect on the velocity field is not resolved in most of the numerical predictions on backward-facing step flows that have already been carried out. Experiments carried out (using Laser Doppler Anemometry) and numerical work by Armaly *et al.* [8] intensified the interest among the fluid mechanics community to revisit the backward facing step flow problem. The flow over a backward-facing step is numerically simulated by various numerical methods and accuracy by various researchers [9-26]. The numerical simulation by Biswas *et al.* [27] requires special mention as he investigated laminar backward-

facing step flow for a wide range of Reynolds numbers and expansion ratios by means of two and three-dimensional simulations. Based on a series of simulations carried out with different upstream lengths L_u , they showed that the predicted results are independent of upstream length. For a wide range of Reynolds numbers, $10^{-4} < Re_D < 1$, a corner vortex of nearly constant size is found in the concave corner behind the step. For the Reynolds number range $Re_D < 400$ the flow past the backward-facing step was predicted successfully by two dimensional computations. The three-dimensional predictions at three different Reynolds numbers ($Re_D = 397$, 648 and 800) were found to be in excellent agreement with the experimental results of Armaly *et al.* [8]. Erturk *et al.* [28] have presented a new, efficient and stable numerical method for the solution of stream function and vorticity equations. With this method they have presented steady solutions of driven cavity flow at very high Reynolds numbers (up to $Re = 21,000$) using very fine grid mesh. They have analyzed the nature of the cavity flow at high Reynolds numbers. The present simulation is carried out by ANSYS 18.2 to compare the reattachment length of corner eddies with the previously published results in the literature.

2. Geometry of Flow Domain and Boundary conditions:

Figure 2 depicts the two-dimensional channel with a backward facing step provided near the channel entrance. The finite distance in between the channel, which is small compared to its length and width makes the flow through this channel predominantly two-dimensional. In addition, an incompressible Newtonian fluid with constant fluid properties is assumed as well. Buoyant forces involved are negligible compared with viscous and pressure forces.

In order to simulate a fully developed laminar channel flow upstream of the step and to eliminate the corner effects, a standard parabolic velocity profile with a maximum velocity

$U_{max}=(3/2)U_b$ which is prescribed at the channel inlet for the present model. Cross stream velocity is equal to zero. The Neumann boundary condition can be assumed for pressure at the channel inlet. Fully developed velocity profile is assumed at the channel outlet. Pressure boundary condition need not be specified at the outlet. No slip condition ($u=0$ and $v=0$) for velocity and Neumann boundary condition for pressure are considered corresponding to wall regions.

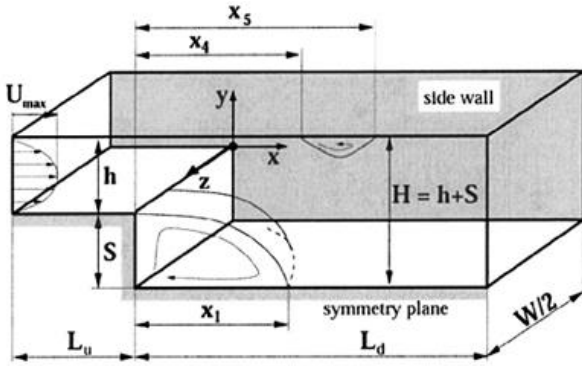


Figure 2. Sketch of the backward facing step flow configuration and definition of length scales

The following dimensions are used for the simulation: Channel upstream length, $L_u = 5$ m, Channel downstream length, $L_d = 10$ m, Channel height, $H = 1.9423$ m, Channel upstream height, $h = 1$ m and step height, $S = 0.9423$. The Reynolds number is defined with reference to channel hydraulic diameter, $D=2h$ and is given as

$$Re = Re_D = \frac{\rho U_b D}{\mu} \quad (1)$$

where ρ and μ are the density and the dynamic viscosity, respectively. As mentioned before, U_b denotes the bulk (average) velocity of the inlet flow, which corresponds in the laminar case to two-thirds of the maximum inlet velocity. Water is considered as the fluid: $\mu = 0.001$, $\rho = 1000$ kg/m³, $D = 2h = 2$ m. To ease the comparison of the results obtained by the numerical simulation using IBM, the geometry of the backward facing step flow problem was chosen in accordance to the experimental setup of Armaly *et al.* [8]. The expansion ratio is defined by

$$\frac{H}{h} = 1 + \frac{S}{h} \quad (2)$$

That is, by the ratio of the channel height H downstream of the step to the channel height h of the inflow channel, where S denotes the step height. The results are generated for an expansion ratio of 1.9423. This expansion ratio was considered in the experimental study by Armaly *et al.* [8] and the same value has been used for a set of numerical computations with the Reynolds numbers values of 0.0001, 0.001, 0.01, 0.1, 1.0, 10, 50, and 100, 200, 400, and 800 by Biswas *et al.* [27]. The results have found to be agreeing quite well.

3. Results and Discussion

In order to ensure the predicted results are grid independent, simulations are carried out with extensive grid refinement. The general features of the two-dimensional backward facing step flow field is shown for an expansion ratio of $H/h=1.9423$ at different Reynolds numbers. This expansion ratio was considered in the experimental study by Armaly *et al.* [8]. It is found from the present numerical simulations that the flow over the backward-facing step is strongly two-dimensional and non-oscillatory in the region of $Re_D < 100$. This observation was well supported and commensurate with the experiments of Armaly *et al.* [8].

Streamwise velocity contours at different Re : Figure 3 shows the stream wise velocity contours of the backward facing step flow problem in steady state flow field for an expansion ratio $H/h=1.9423$ for the Reynolds number values of 0.0001, 0.001, 0.01, 0.1, 1.0, 10, 50, and 100, 200, 400, and 800. It is being observed that the maximum velocity is at the upstream side of the channel. A vortex is also visible at the concave corner behind the step. Stream wise velocity is being fully developed far downstream of the channel. It is being noted that immediately after the concave vortex, the fluid adjacent to the walls decelerates due to the formation of the two hydrodynamic boundary layers and backward pressure.

13th Annual Research Day

Organised by the Deanship of Scientific Research in Collaboration with the College of Engineering
Research Centre
2nd April 2018

Transverse velocity contours at different Re :

Consequently, as a result of continuity principle, fluid outside these two boundary-layers accelerates. Due to this action, a transverse velocity component is engendered, which is clearly visible from the cross stream velocity contours generated for the aforesaid Reynolds numbers as shown in Figure 4, that sends the fluid away from the two plates outside the two boundary-layers and towards the centreline between the two walls. However, this action gradually decays with further increase in the axial distance downstream the backward facing step and finally vanishes when the flow becomes hydro-dynamically fully developed.

Stream lines at different Re : Figure 5 and 6 depict the streamline plots for the flow over backward facing step. The streamline plots are generated for the Reynolds number values of 0.0001, 0.001, 0.01, 0.1, 1.0, 10, 50, and 100, 200, 400, and 800. It is quite evident from the stream lines that as the Reynolds number increases there is a backward flow occurring at the step, which is result of the negative pressure developed due to separation occurring at high velocity due to high Reynolds number. The plots well agree with literature especially commensurate with the experiments of Armaly *et al.* [8] which reveals that flow over the backward-facing step is purely two dimensional and non-oscillatory in the considered region. The streamline patterns for different Re values depict that the flow follows the upper convex corner without revealing a flow separation. Furthermore, a corner vortex is found in the concave corner behind the step. In this range of very small Reynolds numbers (0.0001, 0.001, 0.01, 0.1, and 1.0), the size of this vortical structure is nearly constant varying between $x_1/h=0.3491$ (for $Re=10^{-4}$) and 0.3647 (for $Re=1$). Under these conditions, the effect of inertia forces can be assumed to be negligible compared with viscous forces often denoted as molecular transport. Hence the flow resembles that of Stokes flow. Thus the determination of the separation and

reattachment locations thus offers a severe benchmark test for any hydrodynamic model because of the highly non-linear flow kinematics in the vicinity of the step.

It has also been observed that at low Reynolds numbers the flow separates at the sharp corner and then reattaches itself to the lower boundary further downstream forming a single primary recirculating eddy. The reattachment length increases almost linearly with Reynolds number, the slight non-linear trend being attributed to viscous drag along the upper boundary. Computed non-dimensionalised reattachment lengths against inlet Reynolds number are shown in Table 1, to compare the same with the results of Biswas *et al.* [27].

Table 1. Comparison of the results for backward facing step flow

Re	Size of the corner vortex (x_1/h)	Size of the corner vortex (x_1/h)
	Present work	Biswas <i>et al.</i> [27]
0.0001	0.34	0.35
0.1	0.35	0.35
1.0	0.37	0.37
10.0	0.50	0.50
50.0	1.55	1.55
100	2.81	2.80
200	4.24	4.25
400	7.69	7.71

4. Conclusions:

Capturing of the corner eddies in backward facing step flow is numerically quite challenging and therefore, refined control volumes with the resolution in either direction of the flow domain is assumed during the flow simulation by ANSYS 18.2. For the backward-facing step flow two important parameters are evidently responsible for the corner eddies. The first is given by the geometrical configuration, which can be defined by the expansion ratio H/h . The second is the Reynolds number. The size of the corner eddy is

13th Annual Research Day

Organised by the Deanship of Scientific Research in Collaboration with the College of Engineering
Research Centre
2nd April 2018

nearly constant for all Reynolds numbers below $Re_D = 1.0$. The variation of reattachment length with respect to Reynolds numbers is shown by the length x_I of the corner eddy behind the step (recirculation region) normalized by the height above the backward facing step as a function of Re_D . However, for $Re_D > 1.0$ the corner vortex strongly increases in size. As a direct consequence, the corner vortex reaches up to the corner of the step at $Re_D = 10.0$ and covers the complete face of the step. Hence a change in the entire flow structure is observed and the notation 'corner vortex' has to be replaced by the notation 'recirculation region', for which $Re_D > 10.0$ better reflects the flow structure. With increasing Reynolds number, the size of the recirculation region steadily increases.

Acknowledgement

We acknowledge the support provided by King Khalid University, Abha, KSA for the computational facility provided for the simulation.

References

- [1] Kostas, J., Soria, J., and Chong, M., S.: A Study of a Backward Facing Step Flow at Two Reynolds Numbers, 14th Australasian Fluid Mechanics Conference, Adelaide University, Adelaide, Australia, December, 2001, pp 609-612.
- [2] Moffatt, H. K.: Viscous and resistive eddies near a sharp corner, J. Fluid Mech., Vol 18, 1964, pp. 1–18.
- [3] Lee, Y. S., and Smith, L. C.: Analysis of power-law viscous materials using complex stream, potential and stress functions, Encyclopedia of Fluid Mechanics, Flow Phenomena and Measurement, ed. N. P. Cheremisinoff, Vol 1, 1986, pp. 1105–1154.
- [4] Taylor, T. D., and Ndefo, E.: Computation of viscous flow in a channel by the method of splitting, Proc. of the Second Int. Conf. on Num. Methods in Fluid Dynamics, Lecture Notes in Physics, Vol. 8, Publisher: Springer Verlag, New York, 1971, pp. 356–364.
- [5] Roache, P. J.: Computational Fluid Dynamics, Hermosa, New Mexico, 1972, pp. 139–173.
- [6] Durst, F., and Peireira, J. C. F.: Time-dependent laminar backwardfacing step flow in a two-dimensional duct, ASME J. Fluids Eng., Vol 110, 1988, pp. 289–296.
- [7] Ladeve'ze, J., and Peyret, R.: Calcul numerique d'une solution avec singularite' des equations de Navier-Stokes: e'coulement dans un canal avec variation brusque de section, J. Mech., Vol 13, No. 3, 1974, pp. 367–396.
- [8] Armaly, B. F., Durst, F., Peireira, J. C. F., Schonung, B.: Experimental and theoretical investigation of backward-facing step flow, J. Fluid Mech., Vol 127, 1983, pp. 473–496.
- [9] Kim, J., and Moin, P.: Application of a fractional-step method to incompressible Navier-Stokes equations, J. Comput. Phys., Vol 59, 1985, pp. 308–323.
- [10] Gartling, D. K.: A test problem for outflow boundary conditions-flow over a backward-facing step, Int. J. Numer. Methods Fluids Vol 11, 1990, pp. 953–967.
- [11] Kaiktsis, L., Karniadakis, G. E., and Orszag, S. A.: Onset of three dimensionality, equilibria, and early transition in flow over a backward-facing step, J. Fluid Mech., Vol 231, 1991, pp. 501–528.
- [12] Durst, F., Peireira, J. C. F., and Tropea, C.: The plane symmetric sudden-expansion flow at low Reynolds numbers, Journal of Fluid Mechanics, Vol 248, 1993, pp 567–581.

13th Annual Research Day

Organised by the Deanship of Scientific Research in Collaboration with the College of Engineering
Research Centre
2nd April 2018

- [13] Kaiktsis, L., Karniadakis, G. E., and Orszag, S. A.: Unsteadiness and convective instabilities in a two-dimensional flow over a backward-facing step, *J. Fluid Mech.*, Vol 321, 1996, pp. 157–187.
- [14] Alleborn, N., Nandakumar, K., Raszillier, H., and Durst, F.: Further contributions on the two-dimensional flow in a sudden expansion, *J. Fluid Mech.*, Vol 330, 1997, pp. 169–188.
- [15] Brandt, A., Dendy, J. E., and Ruppel, H.: The multigrid method for semi-implicit hydrodynamic codes, *J. Comput. Phys.*, Vol 34, 1980, pp. 348–370.
- [16] Hackbusch, W.: *Multigrid Methods for Applications*, 1985, Springer, Berlin.
- [17] Lange, C. F., Schafer, M., and Durst, F.: Local block refinement with a multigrid flow solver, *Int. J. Numer. Methods Fluids* Vol 38, 2002, pp. 21–41.
- [18] Le, H., Moin, P., and Kim, J.: Direct numerical simulation of turbulent flow over a backward-facing step, *J. Fluid Mech.*, Vol 330, 1997, pp. 349–474.
- [19] Williams, P. T., and Baker, A. J.: Numerical simulations of laminar flow over a 3D backward-facing step, *Int. J. Numer. Methods Fluids* Vol 24, 1997, pp. 1159–1183.
- [20] Lee, T., and Mateescu, D., Experimental and numerical investigation of 2D backward-facing step flow, *J. Fluids Struct.*, Vol 12, 1998, pp. 703–716.
- [21] Heenan, A. F., and Morrison, J. F.: Passive control of backstep flow, *Exp. Therm. Fluid Sci.*, Vol 16, 1998, pp. 122–132.
- [22] Chiang, T. P., and Sheu, T. W. H.: A numerical revisit of backward facing step flow problem, *Phys. Fluids*, Vol 11, No 4, 1999, pp. 862–874.
- [23] Kaltenbach, H.-J., and Janke, G.: Direct numerical simulation of flow separation behind a swept rearward-facing step at $Re = 3000$, *Phys. Fluids*, Vol 12, No 9, 2000, pp. 2320–2337.
- [24] Erturk, E., Corke, T., C., and Gokcol, C.: Numerical Solutions of 2-D Steady Incompressible Driven Cavity Flow at High Reynolds Numbers, *International Journal for Numerical Methods in Fluids*, Vol 48, 2005, pp 747-774.
- [25] Barkley, D., Gomes, M. G. M., and Henderson, R. D.: Three dimensional instability in flow over a backward-facing step, *J. Fluid Mech.*, Vol 473, 2002, pp. 167–190.
- [26] Nie, J. H., and Armaly, B. F.: Three-dimensional convective flow adjacent to backward-facing step-effects of step height, *Int. J. Heat Mass Transfer*, Vol 45, 2002, pp. 2431–2438.
- [27] Biswas, G., Breuer, M., and Durst, F.: Backward-facing step flows for various expansion ratios at low and moderate ReynoldsNumbers, *J. Fluid Engg.*, Vol 126, 2004, pp 362–374.

13th Annual Research Day

**Organised by the Deanship of Scientific Research in Collaboration with the College of Engineering
Research Centre
2nd April 2018**

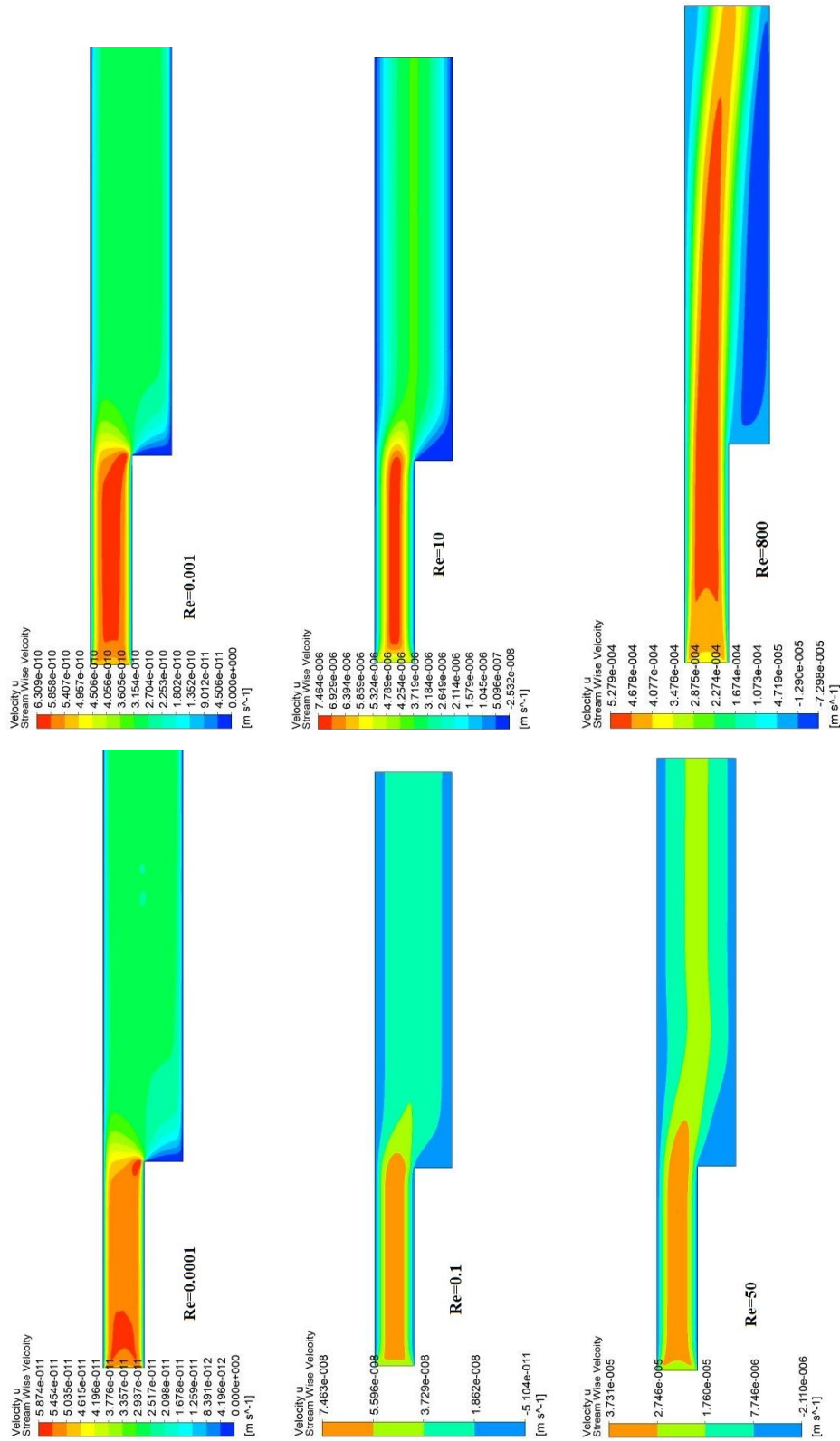


Figure 3 Stream wise velocity contours for backward facing step flow for different Reynolds numbers

13th Annual Research Day

Organised by the Deanship of Scientific Research in Collaboration with the College of Engineering
Research Centre
2nd April 2018

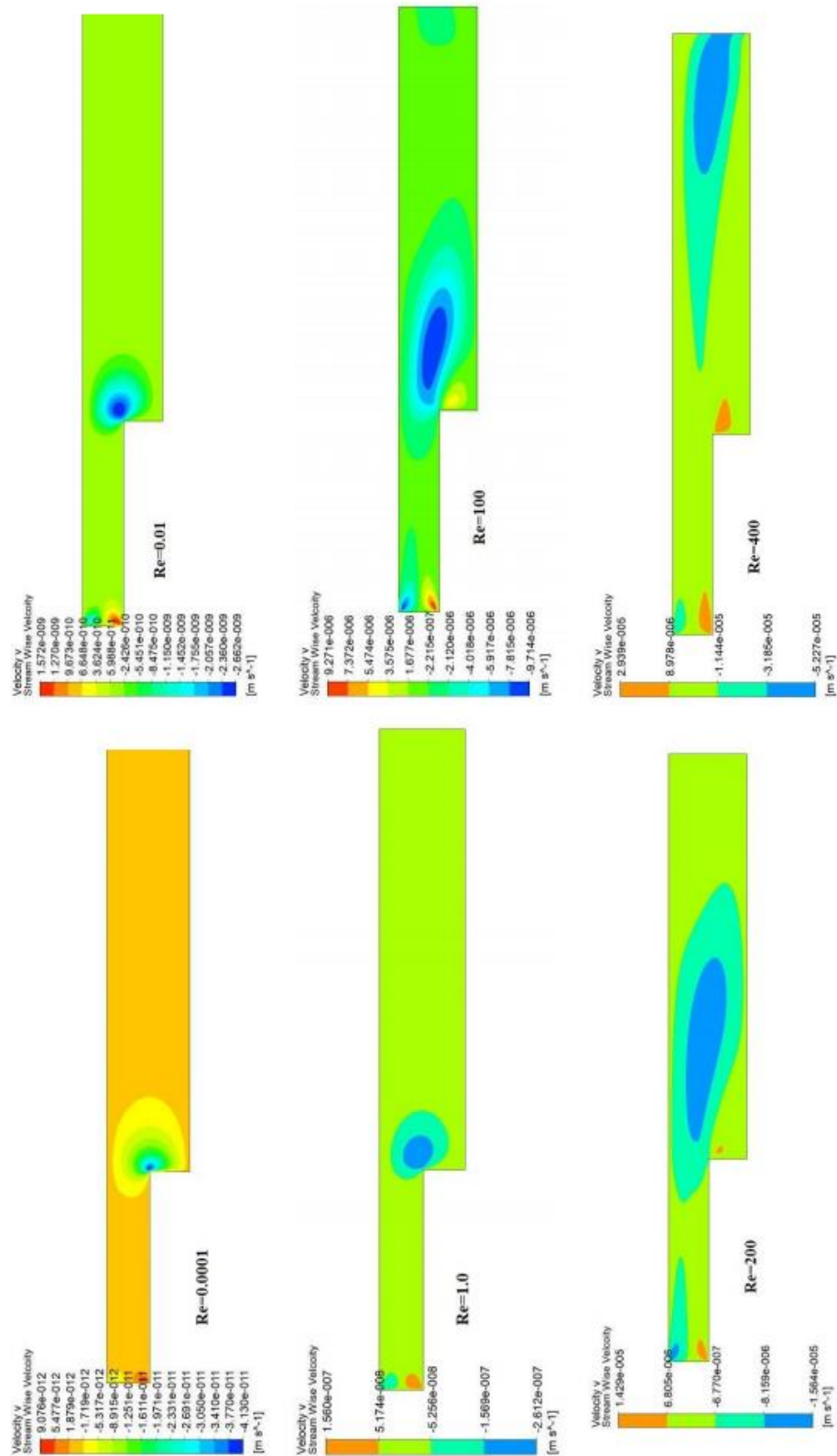


Figure 4 Transverse velocity contours for backward facing step flow for different Reynolds numbers

13th Annual Research Day

Organised by the Deanship of Scientific Research in Collaboration with the College of Engineering
Research Centre
2nd April 2018

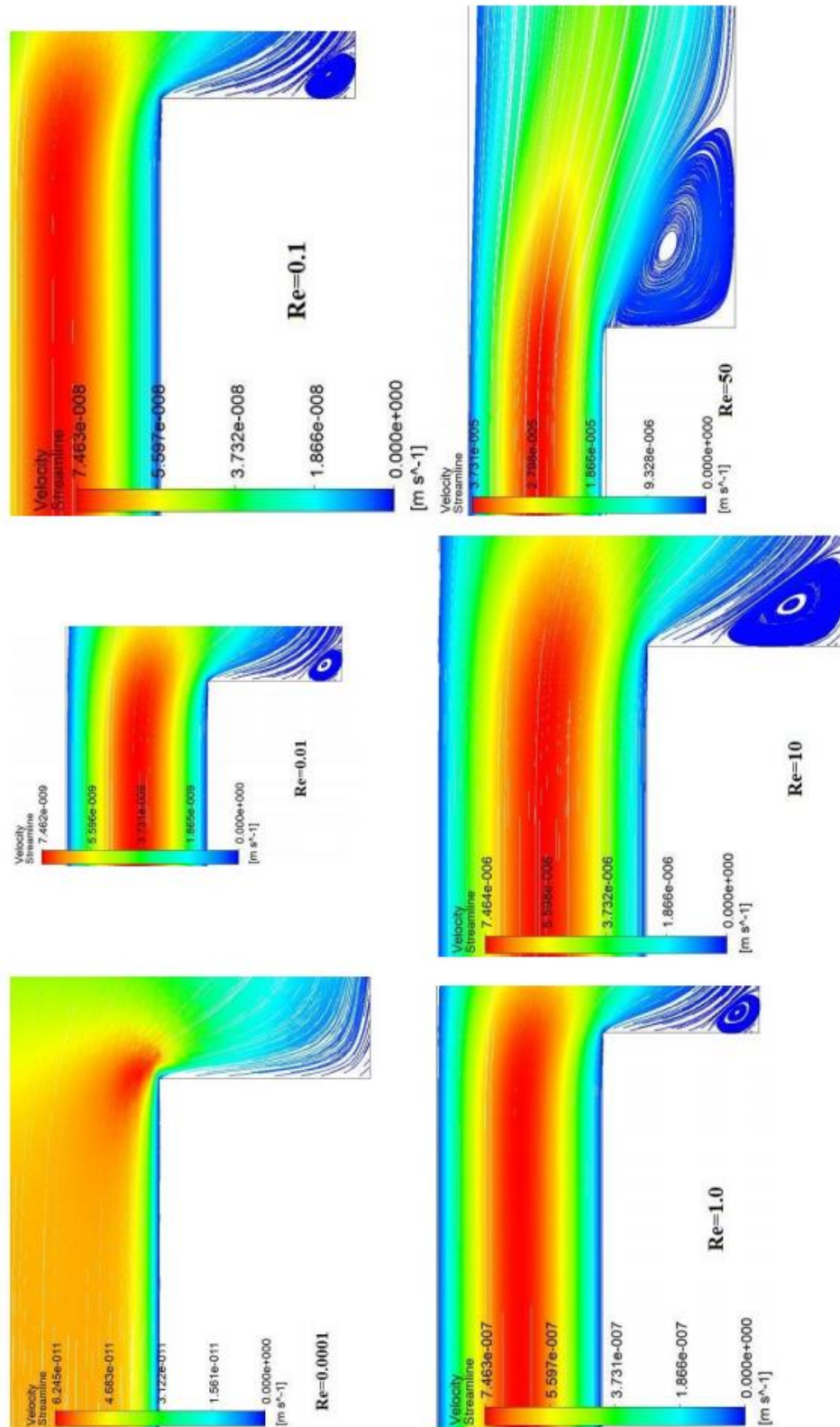


Figure 5. Streamlines in the vicinity of backward facing step for $Re=0.0001, 0.01, 0.1, 1.0, 10$ and 50

13th Annual Research Day

Organised by the Deanship of Scientific Research in Collaboration with the College of Engineering
Research Centre
2nd April 2018

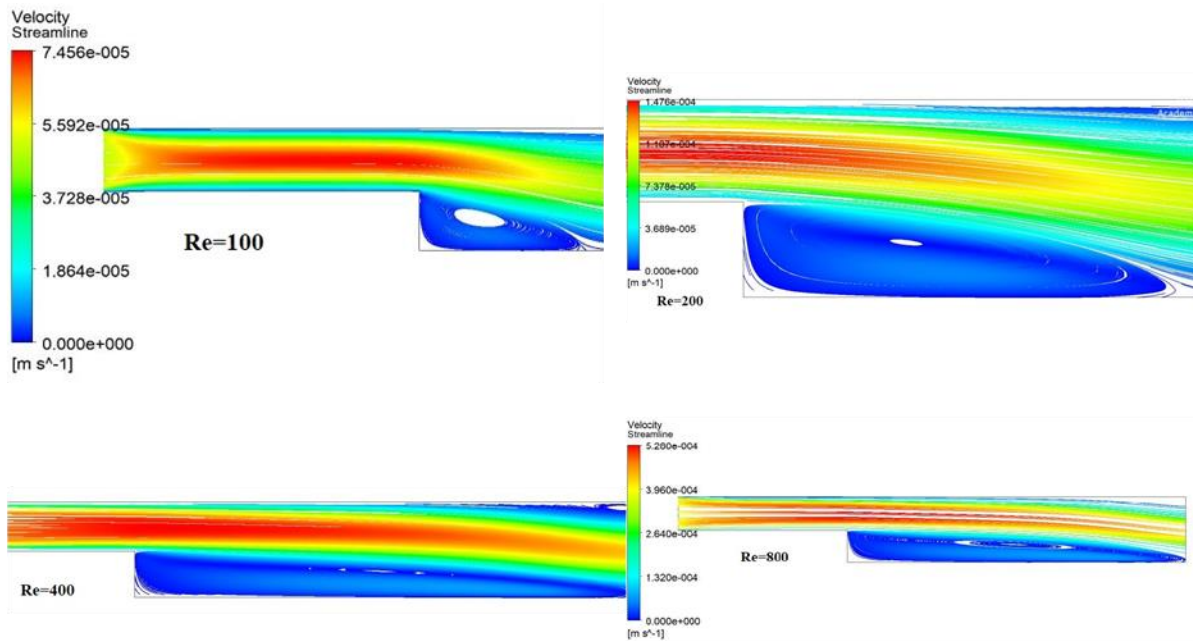


Figure 6. Streamlines in the vicinity of backward facing step for Re=100, 200, 400 and 800

13th Annual Research Day

Organised by the Deanship of Scientific Research in Collaboration with the College of Engineering
Research Centre
2nd April 2018

The Environmental Impact of Fluoride Emissions from Aluminum smelter at Jazan Economic City (JEC), Baish, Saudi Arabia on the surrounding Ecosystem.

Muhammad Arshad ^{1,*} and Ebrahim M. Eid^{2,3}

¹*Department of Chemical Engineering, College of Engineering, King Khalid University, P.O. Box 394, Abha 61411, KSA*

²*Department of Biology, College of Science, King Khalid University, P.O. Box 9004, Abha 61321, KSA*

³*Permanent address: Department of Botany, Faculty of Science, Kafr El-Sheikh University, Kafr El-Sheikh 33516, Egypt*

E-mail address: moakhan@kku.edu.sa

Abstract: The government of Saudi Arabia has inaugurated Jazan Economic City (JEC) at Baish, Jazan in 2006. Various heavy, medium and light industries are proposed for JEC with full investors ownership privileges. In the current paper, we present our findings by utilizing peer literature review, and the remote sensing techniques, the serious environmental impact of fluoride compounds emission from the future proposed Aluminum smelter at JEC on the surrounding coastal environment.

Keywords: Jazan Economic City, Coastal Wetland, arid environment, Remote Sensing, Air Pollution, Fluoride emissions, vegetation damage.

1. Introduction:

The government of Saudi Arabia have inaugurated its fourth economic city in 2006 at Baish, Jazan. An anticipated investment of \$30 to \$40 billion is expected in industrial, commercial and residential sectors and will provide 500,000 direct and indirect job opportunities mostly to the locals. The investors at JEC would have 100 percent ownership of their projects. Various heavy, medium and light industries are proposed for Jazan Economic City (JEC) such as Jazan refinery, power plant, water desalination plant, aluminum smelter, Ilmenite smelting plant, industrial port, ship building and iron ore complex besides other secondary industries.

Of the 10 recently proposed installations of Aluminum smelters for the Kingdom of Saudi Arabia, a new \$3 billion smelter is under construction at JEC with an annual production of one million metric tons. In spite of the fact that the Aluminum smelter proposed at JEC is procured on the principle of Best Available

Technology (BAT), these smelters are considered as the notorious polluter of environment [1, 2, and 3]. Primary Aluminum smelters are the main source of fluoride release in the atmosphere [1, 3 and 4]. Aluminum smelters while processing aluminum ores for the extraction of aluminum metal, releases fluoride compounds into the atmosphere. Emissions of these fluoride compounds have a serious detrimental impact when it lands on the vegetation [3, 4, and 5]. It is feared that once the aluminum plant starts its production in the near future its fluoride emissions in the hyper arid environment will totally destroy the patchy mangrove forests (Fig. 1) and other flora in the surrounding coastal regions which already under stress due to high salinity of Red Sea water [5, 6, 7 and 8].

13th Annual Research Day

Organised by the Deanship of Scientific Research in Collaboration with the College of Engineering
Research Centre
2nd April 2018



Fig. 1. Mangrove forest in the vicinity of Jazan Economic City.

Earth observation methods are available to estimate and assess the health and changes in mangrove forests by using archive and current satellite images. Increasing availability of satellite data has made the assessment of change in mangrove ecosystem feasible over a range of time period. According to Murray [8] the environmental managers, risk assessors, and ecosystem scientists can now judiciously utilize remote sensing for ecosystem risk assessments at a range of spatial scales. The research presented here is a part of our ongoing approved research project by the Deanship of scientific research at King Khalid University, Abha, Saudi Arabia aimed at focusing on assessment of the pollution impact of JEC on the surrounding coastal wetland ecosystem.

2. Materials and Methods:

2.1 Materials

The specifications of the operating system used in the research are DELL Optiplex 9020, 64-bit operating system, @ 3.6 GHz. ENVI version 5.5 (API version 3.2). ENVI image analysis software version 5.5 was used for the processing of satellite images. For the current research, GeoEye, IKONOS satellite images were provided by the King Abdul Aziz City of Science &

Technology (KACST). Landsat 5 TM and Landsat 8 data spanning over a period of 20 years and Sentinel-2 data of recent past were downloaded from United States Geological Survey (USGS) website (earthexplorer.usgs.gov). Satellite images were processed and used to determine the strategic locations for sample collection, analysis and assessment of land-use change.

2.2 Satellite image processing

The Landsat5 TM, Landsat 08 and Sentinel-2 satellite images were utilized to assess the development of Jazan Economic City (JEC) and possible environmental impacts on the surrounding ecosystem. Satellite remote sensing technique is ideal to evaluate ecosystem change at local levels and was used to locate the spatial distribution of mangrove forests close to JEC along the Red Sea coast. The satellite images were geometrically and radiometrically corrected using ENVI 5.5 software. Atmospheric correction (Dark subtraction) was performed which is required for the temporal assessment of satellite images. The satellite images were then utilized to produce land cover maps and perform change detection analysis.

3. Results and Discussion

3.1 Results

Land reclamation for industrial port at JEC is evident in Fig. 2. Existing variation in the tree population and water characteristics of polluted and non-polluted locations of mangrove forests is provided in Table. 1. Soil analysis data of mangrove forests at non-polluted sites shows significant decline in soil organic carbon (SOC) concentration from 26.0 g C kg⁻¹ at depth 0 - 5 cm to 11.7 g C kg⁻¹ at depth 45 - 50 cm, whereas, SOC concentration in the polluted site shows decline significantly with depth ranging from 23.0 g C kg⁻¹ at depth 0 - 5 cm to 9.6 g C kg⁻¹ at depth 45 - 50 cm is provided in (Table. 2).

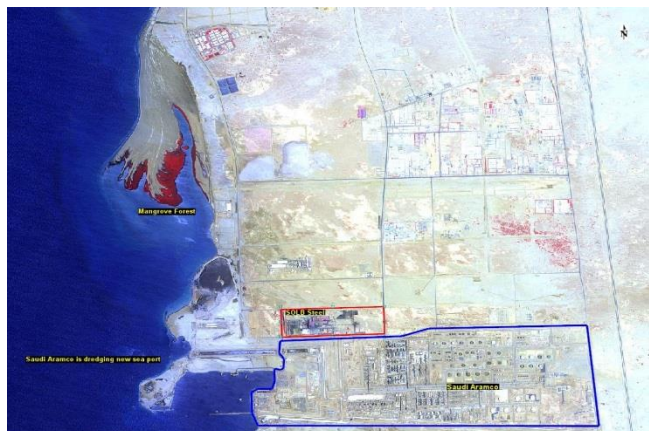


Fig. 2. Land reclamation for industrial port.

Table 1. Variation in the tree population and water characteristics (mean \pm standard error) of polluted and non-polluted locations of mangroves (*Avicennia marina*) along the southern Red Sea coast of Saudi Arabia. *t*-values represent the student's *t*-test. *: $P < 0.05$, **: $P < 0.01$, ***: $P < 0.001$, ns: not significant (after Khan et al. 2018).

Characteristic	Location		<i>t</i> -value
	Non-polluted	Polluted	
<i>Population characteristic</i>			
Tree height (cm)	78 ± 5	66 ± 4	11.1**
Tree crown diameter (cm)	120 ± 7	101 ± 6	10.5**
Tree density (individual per 100 m ²)	11 ± 1	9 ± 1	5.2**

Table 2. Mean \pm standard error of sediment bulk density (SBD), sediment organic carbon (SOC) concentration, SOC density, SOC pool and carbon sequestration rate (CSR) in polluted and non-polluted locations of mangroves (*Avicennia marina*) along the southern Red Sea coast of Saudi Arabia. *t*-values represent the student's *t*-test. *: $P < 0.05$, ***: $P < 0.001$ (after Khan et al. 2018).

Location	SBD (g cm ⁻³)	SOC concentration (g C kg ⁻¹)
Non-polluted (<i>n</i> = 200)	1.53 \pm 0.02	18.2 \pm 0.5
Polluted (<i>n</i> = 200)	1.66 \pm 0.02	14.6 \pm 0.4
Total mean (<i>n</i> = 400)	1.59 \pm 0.01	16.5 \pm 0.3
<i>t</i> -value	7.7***	7.6***

The CSR ranged between 6.6 g C m⁻² year⁻¹ in the polluted sites and 7.8 g C m⁻² year⁻¹ in the non-polluted site. It mean that the SOC stock for non-polluted site was 1.14 times higher as that of polluted sites.

3.2. Discussion

As observed above in Fig. 2, huge land is reclaimed for the construction of industrial port next to Jazan refinery for the loading/unloading activities for the transportation of raw material and finished products. The quality of sea water is disturbed by the ongoing dredging activities that will have serious detrimental impact on the mangrove forest as can be seen close to the industrial port. There is significant difference in tree heights and tree crown diameters between non-polluted and polluted sites of mangrove forests as observed in Table 2. This can be attributed to the pollution stress preventing mangrove forests at polluted sites from normal growth.

Camargo [2] stated that discharges of fluorides from anthropogenic sources including Aluminum smelters may result in a serious ecological risk for aquatic organisms. At elevated temperatures, Aluminum smelters releases fluoride compounds into the atmosphere, usually in the form of gaseous HF, silicon fluoride and particulate calcium fluoride along with various other pollutants and causes serious damage to vegetation [2]. Weinstein and Davison [5] pointed out that HF (or SiF₄) is between 1 and 3 orders of magnitude more toxic even in small releases into the atmosphere to plant life than other common pollutants (e.g., O₃, SO₂, PAN, Cl₂ or Cl⁻). According to Richer [7], larger and modern smelters limit the total fluoride emissions between 0.5 to 0.6 (kg F/t Al). Weinstein and Davison [5] pointed out that no studies have been done for arid and hyper arid regions to assess the susceptibility of native plant species to fluoride accumulation and damage. It is feared that this

13th Annual Research Day

Organised by the Deanship of Scientific Research in Collaboration with the College of Engineering
Research Centre
2nd April 2018

smelter will cause air pollution amounting to roughly 600,000 kg F/year as estimated from Richer [7]. Climatic factors, in particular rainfall, plays a major role in reducing fluoride accumulation in plants because precipitation washes away fluorides from the surface of leaves [7]. However, difference in annual rainfall between Europe and Saudi Arabia creates an entirely different scenario. For example, Sunndal Aluminum smelter at Norway receives on the average above 900 mm of rain a year [7], whereas, on the other hand, Jazan roughly receives rain not more 22 mm a year on the authority of General authority for meteorology and environmental protection (GAMEP) Kingdom of Saudi Arabia (www.pme.gov.sa). Now the point of concern is to address the issue of 600,000 kg of fluoride release per year. In literature review, fluoride is considered as the most phototoxic pollutant, causing serious injuries in susceptible species [5 and 7]. Besides fluorides, these smelters releases other pollutants such as: SO_x, NO_x, CO_x, HC, VOCs, PAHs, HCl, and gaseous chlorine [3]. Sulfur and nitrogen leads to acid rain. Studies shows air pollution from Norwegian aluminum smelters has caused extensive damage to the vegetation in the vicinity of the smelters[10]. Chlorosis is usually the first noticeable symptom in response to fluoride contact [3]. Leaf injury in the form of chlorosis and necrosis of leaf tips and margins have been observed due to fluorine emissions from aluminum smelters [3]. According to WHO, fluoride levels in atmosphere should be less than 1 µg m⁻³ to prevent effects in plants, livestock and also to protect human health [3].

Thus, in the light of above discussion, it is anticipated that the situation will be become very grave once the one million tons per annum aluminum smelter starts production if any mitigation measures were not in place.

4. Conclusions:

Concrete actions are needed to be taken by the stakeholders to make the project of JEC a success. As mentioned in the introduction, necessary steps needs to be taken to monitor and mitigate the negative impacts of air and water pollutants with particular emphasis on fluoride release from Aluminum smelters. Fluoride compounds released from Aluminum smelter will further aggravate the situation. The release of various fluoride compounds in addition to harsh climatic condition and scarcity of rain will cause extensive damage to the mangrove forests in the vicinity of the smelters and will reduce the SOC stock of mangrove forests. It is therefore, necessary to protect and restore these mangrove forests especially the polluted locations for carbon sequestration, as well as other ecosystem services that currently lack effective protection. In this regard, buffer zones should be created to prevent soil erosion and surface runoff and also impervious surface should be kept at minimum. SOC stock of soil in and around JEC should be monitored on a regular basis to assess and protect the ecosystem.

Acknowledgement

1. This study is/was sponsored by the Deanship of Scientific Research at King Khalid university under grant no. G. R. P. – 280-38.
2. The authors are thankful to United States Geological Survey (USGS) for providing access to download Landsat and Sentinel-2 satellite data for the completion of this project.
3. The authors are also thankful to the King Abdul Aziz City of Science & Technology (KACST) for providing us high resolution IKONOS and Geo-Eye satellite data for Jazan Economic City (our study area).

13th Annual Research Day

Organised by the Deanship of Scientific Research in Collaboration with the College of Engineering
Research Centre
2nd April 2018

References

- [1] Buqing Zhong, Lingqing Wang, Tao Liang, Baoshan Xing, Pollution level and inhalation exposure of ambient aerosol fluoride as affected by polymetallic rare earth mining and smelting in Baotou, north China. *J. Atmospheric Environment*. 167 (2017) 40.
- [2] Julio A. Camargo, Fluoride toxicity to aquatic organisms: a review, *J. Chemosphere*. 50 (2003) 251.
- [3] Eliza Louback, Tiago Augusto Rodrigues Pereira, Silvia Ribeiro de Souza, Juraci Alves de Oliveira, Luzimar Campos da Silva, Vegetation damage in the vicinity of an aluminum smelter in Brazil, *J. Ecological Indicators*. 67 (2016) 193.
- [4] Kate M. Brougham, Stephen R. Roberts, Alan W. Davison, Gordon R. Port, The impact of aluminium smelter shut-down on the concentration of fluoride in vegetation and soils, *J. Environmental Pollution*. 178 (2013) 89
- [5] Leonard H. Weinstein, Alan W. Davison, Native plant species suitable as bioindicators and biomonitors for airborne fluoride, *Environmental Pollution*. 125 (2003) 3.
- [6] Muhammad Nauman Ahmad, Leon J.L. van den Berg, Hamid Ullah Shah, Tariq Masood, Patrick Bükér, Lisa Emberson, Mike Ashmore, Hydrogen fluoride damage to vegetation from peri-urban brick kilns in Asia: A growing but unrecognized problem?, *J. Environmental Pollution*, 162 (2012) 319
- [7] R. A. Richer, Industrial growth and anthropogenic pollutants in arid and hyper-arid environments, *J. Arid Environments*. 112 (2015) 145.
- [8] Andreas Klumpp, Marisa Domingos, Gabriele Klumpp, Assessment of the vegetation risk by fluoride emissions from fertiliser industries at Cubatão, Brazil, *J. Science of The Total Environment*. 192 (1996) 219.
- [9] Murray, N. J., Clemens, R. S., Phinn, S. R., Possingham, H. P., & Fuller, R. A., Tracking the rapid loss of tidal wetlands in the Yellow Sea, *J. Frontiers in Ecology and the Environment*. 12 (2014) 267.
- [10] Eva Vike, Air-pollutant dispersal patterns and vegetation damage in the vicinity of three Aluminum smelters in Norway, *J. Science of The Total Environment* 236 (1999) 75

Fracture Characteristics and Size Dependent Effects of Fibre Concrete Composites

Dr. Sivakumar Anandan

Department of Civil Engineering, College of Engineering, King Khalid University,
PO Box 394, Abha 61411 KSA.
E-mail address: ksiva@kku.edu.sa

Abstract: Research studies were investigated on the fracture characteristics of different types of steel fibre reinforced high strength concrete composites. Influence of steel fibre volume fraction and its complex profile characteristics on the strength and size effect properties of various fibre reinforced concretes had been systematically studied in slender concrete beam sections. Reinforcing efficiency of concrete incorporating four types of steel fibres having the same aspect ratio with varying fibre profile - single hooked ends, crimped, double hooked ends and kinked had been experimentally analyzed in flexural bending and fracture studies. Test results showed higher flexural post peak toughness (23.48 N-m) and fracture toughness (39.62MPa√mm) for double hooked steel and crimped steel fibres substituted concretes. Steel fibre reinforced concretes containing double hooked and kinked geometry exhibited higher overall performance index. Also, high volume steel fibre substitutions (1.5% V_f) in slender concrete beams showed improved fracture toughness characteristics.

Keywords: Fibre composites, Ductility, Post crack toughness, Residual strength, Fracture toughness.

1. Introduction:

Steel fibre reinforcements in concrete is a well-known technique for transforming a brittle concrete into a ductile composite and thereby provides better mechanical properties of concrete. Fibre geometry and orientation plays a crucial role on the effective reinforcing mechanism in concrete; as fibres bridge cracks and transfer the stress effectively to matrix [1]. Research studies proved the significance of fibre addition in concrete to improve the strain hardening properties of concrete [2]. The mechanical performance of steel fibre concrete was found to be dependent on the fibre volume fraction, aspect ratio and its spatial distribution [3]. Reinforcing efficiency of fibres in concrete depends on the interfacial fibre-matrix bonding properties and frictional sliding of fibres during loading [4]. Crack bridging effect of fibres was dependent on the surface bonding of fibres and the effect of steel fibre profile on mechanical improvement of concretes was well documented

[5]. Research studies indicated that, post peak characteristics of concrete were dependent on the controlled crack widening with sufficient fibre availability. Fibre addition in concrete had consistently improved the energy absorption capacity after matrix cracking and its performance characteristics are measured by various parameters such as toughness indices, equivalent flexural strength, residual strength and fracture energy [6, 7]. The post cracking response of steel fibre concrete was systematically investigated using different sizes of notched concrete specimens and size effect due to specimen geometry [8]. The fracture properties of concrete were dependent on specimen size, fibre orientation in orthogonal direction and fibre availability at the crack front. In another study it was reported that, aligned fibre distribution provided maximum tensile stress capacity of the ultra-high performance concrete [9]. Hybrid fibre combinations at low volume fraction (0.5%) in high strength concrete exhibited higher residual strength after first cracking and a marginal

increase in compressive strength of concrete was reported [10].

2. Materials and Methods:

2.1 Concrete Materials and Proportioning

The binder used in this investigation consisted of ordinary Portland cement, locally available fine aggregate – river sand and crushed granite stone as coarse aggregates. **2.2 Steel Fibres.** Steel fibres were used as reinforcement in concrete and four types of steel fibres were used namely – single hooked ends steel, double hooked ends steel, crimped steel and kinked steel fibres (shown in **Fig.1**). High strength concrete of 45 MPa was chosen for this study and trial concrete mix proportions were arrived based on ACI 211.4R [11] mix design specifications (provided in **Fig.2**). The homogeneous dispersion of steel fibres in concrete was ensured and assessed for workability using slump cone method. Batch mixing of concrete was carried out systematically in order to produce a uniform concrete mix. Special techniques were adopted while adding fibres into the concrete mixer in order to avoid fibre balling.

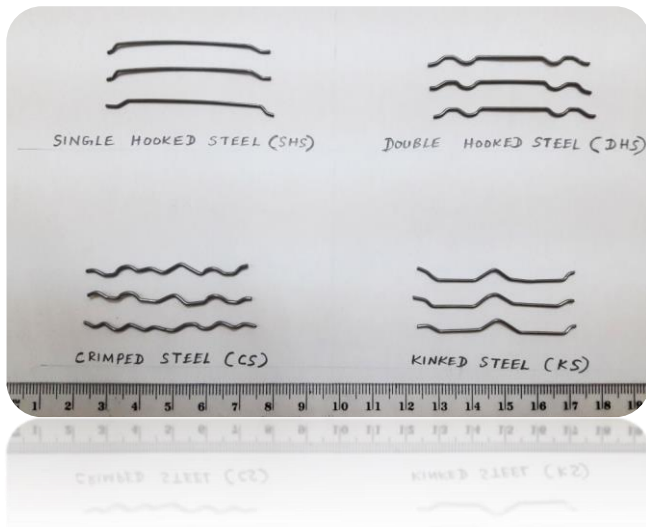


Fig.1 Various steel fibre profiles used in this study

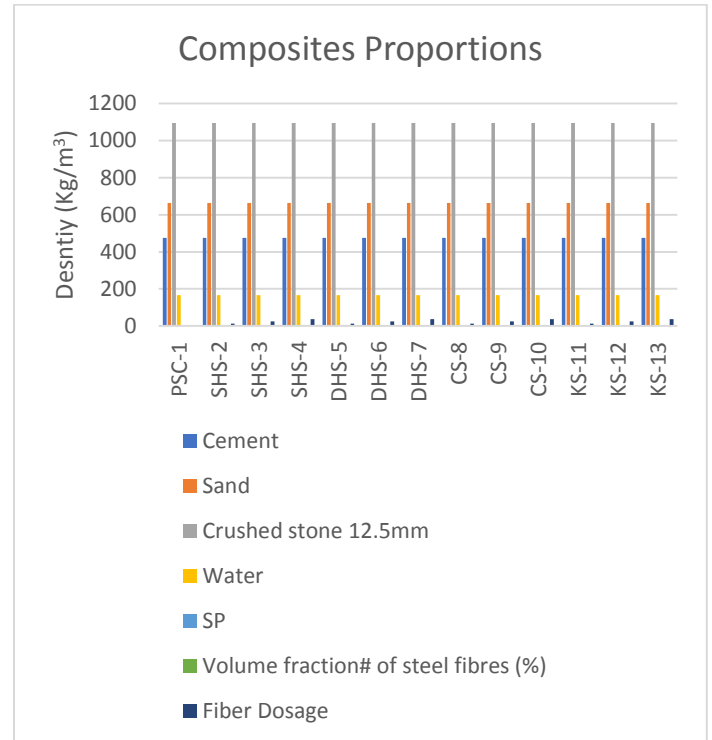


Fig.2 Various proportions of Composites Manufactured

2.2 Fracture Testing - Fracture strength/Toughness/Energy

Fracture studies were conducted as per RILEM TC – 1985 [12] recommendations using three-point bend tests in notched concrete beam specimens (shown in **Fig.3**). The test was carried out with a standard concrete beam specimen having a single central notch of 20mm depth and 4mm width. The fracture test was conducted using a servo controlled digital flexural loading machine with a pace rate of 0.2mm/min. The applied load versus crack mouth opening displacement (CMOD) was measured during the test and further used to determine the various fracture parameters of concrete specimens. The displacement was measured at the crack mouth using two mechanical dial gauges of 0.01mm accuracy attached to either sides of clip arrangement. The clip arrangement was rigidly

13th Annual Research Day

Organised by the Deanship of Scientific Research in Collaboration with the College of Engineering
Research Centre
2nd April 2018

fixed into notch opening and the readings from both dial gauges were used to measure the total crack displacement.

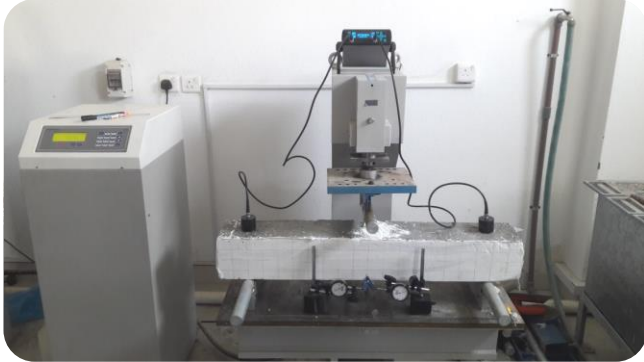


Fig.3 Fracture test setup with mechanical dial gauges – third point loading

Fracture strength (N/mm^2) was calculated from peak load at failure using strain energy principle.

Fracture toughness is defined as the resistance of the material against fracture. It was determined from a three-point bend tests on concrete specimen and calculated from the equations as given below:

a) Fracture model used in this study

$$K_{I1} = \frac{4P}{B} \sqrt{\frac{\pi}{W}} \left[1.6 \left(\frac{a}{W} \right)^{1/2} - 2.6 \left(\frac{a}{W} \right)^{3/2} + 12.3 \left(\frac{a}{W} \right)^{5/2} - 21.2 \left(\frac{a}{W} \right)^{7/2} + 21.8 \left(\frac{a}{W} \right)^{9/2} \right] \dots\dots\dots(1)$$

b) ASTM Fracture model

$$K_{I1} = \frac{6P}{BW} a^{0.5} Y$$

Where,

$$Y = \frac{1.99 - a/W (1 - a/W)(2.15 - 3.93a/W + 2.7 (a/W)^2)}{(1 + 2a/W)(1 - a/W)^{3/2}} \dots\dots\dots(2)$$

3. Results and Discussion

The experimental observations from fracture tests are provided in **Fig. 4**. Experimental

observation indicated that, the fracture in concrete specimens occurred by means of a single crack growth originated from the notch tip. Fracture strength of all fibre reinforced concrete beams was higher than plain concrete specimens (PSC-1). Similarly, the fracture strength was considerably improved for all types of fibre incorporated concrete specimens at high fibre volume fraction. Fracture strength of double hooked end steel fibre incorporated concretes (DHS-7) showed a maximum value (13.26 N/mm^2) compared to other fibre concrete specimens. Similarly, crimped steel fibre (CS-10) and kinked steel fibre (KS-13) concretes reported a similar increase in fracture strength at high volume fraction (1.5%). Test results denoted that fracture strength of fibre concrete were dependent on the effective fibre profile as in the case of double hooked steel fibre, crimped and kinked steel fibres. Since, the matrix bonding in these fibres were efficient as a result of more anchorage length (as given in Table 3). In addition, steel fibre performance was also dependent on the fibre volume fraction and preferential alignment of steel fibres normal to loading plane.

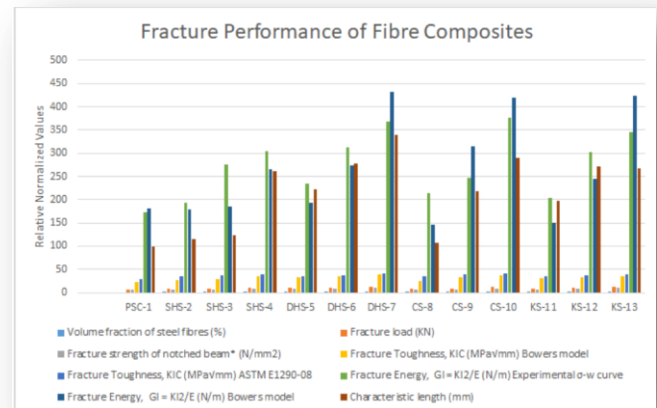


Fig. 4 Fracture Characteristics of various Fibre Composites

13th Annual Research Day

Organised by the Deanship of Scientific Research in Collaboration with the College of Engineering
Research Centre
2nd April 2018

Crack growth resistance in brittle concrete systems was effectively measured in fracture test using stress intensity factor (K_I). Energy released during work done in fracturing a material provides an indicative measure on the toughness of the composite. Comparative assessment of fracture toughness calculated from experimental observations using Bower's model and ASTM model are represented in **Fig.4**. The calculated toughness values from both the models were almost consistent and represented better interpretation. Among the various fibre concretes tested, maximum fracture toughness value of 39.62MPa√mm and 37.48 MPa√mm) was obtained for double hooked steel fibres (DHS-7) and crimped steel fibre (CS-10) respectively for concretes at high fibre volume fraction. The total energy required for growth of cracks till the energy released upon complete failure of concrete specimen provides an essential measure on the fracture energy of the composite. Test results provided in **Fig. 5** showed maximum fracture energy in the case of all fibre concretes compared to plain concrete. Among the various fibre concretes, highest fracture energy of 376 N/m and 367N/m was obtained for crimped steel (CS-10) and double hooked steel fibre (DHS-7) concretes (shown in **Fig. 6**). The corresponding performance index of various fibre composites are provided in **Fig. 7**.

Fig.5 Fracture load vs. CMOD curves for various concrete specimens tested

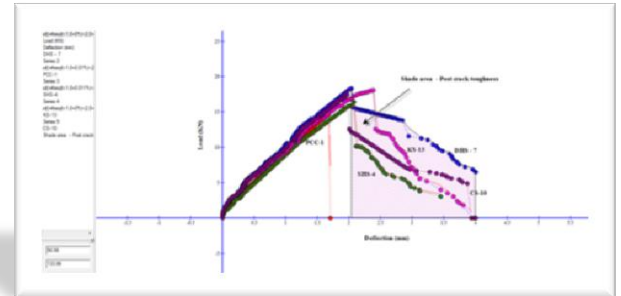


Fig. 6 Fracture toughness calculation for various Fibre Composites

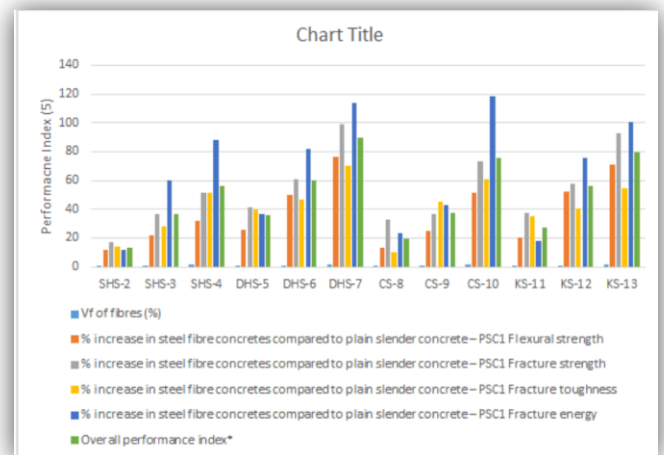
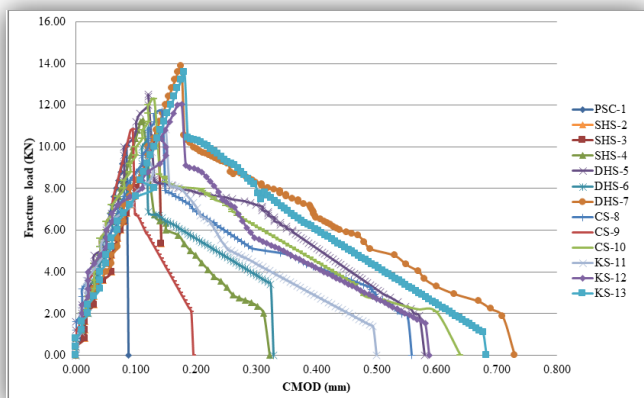


Fig. 7 Performance Index of Various Fibre Composites



The relative performance characteristics of steel fibre substituted slender concretes as compared to thick plain concrete sections were analyzed. Comparative analysis indicates that the relative strength properties of a thick plain concrete section can be obtained in slender concrete sections with sufficient steel fibre substitution. However, the reinforcing efficiency of steel fibres can be better synthesized when the fibres are aligned and having effective end

13th Annual Research Day

Organised by the Deanship of Scientific Research in Collaboration with the College of Engineering
Research Centre
2nd April 2018

anchorages. Among the various concrete specimens, the overall fibre reinforcing efficiency was maximum (363%) in the case of double hooked steel fibre concretes.

Relatively, the double hooked randomly distributed steel fibre concretes (DHR-8) at low volume fraction exhibited higher reinforcing efficiency (183.81%) as compared to aligned steel fibre concrete (SHA-6). This possibly revealed that the reinforcing efficiency of steel fibres improved with the addition of double hooked steel fibres in slender plain concrete specimens due to better end anchorages. Steel fibre addition had been realized in reduced concrete section and had shown improved fracture properties as compared to thick concrete sections (as shown in Fig. 8).

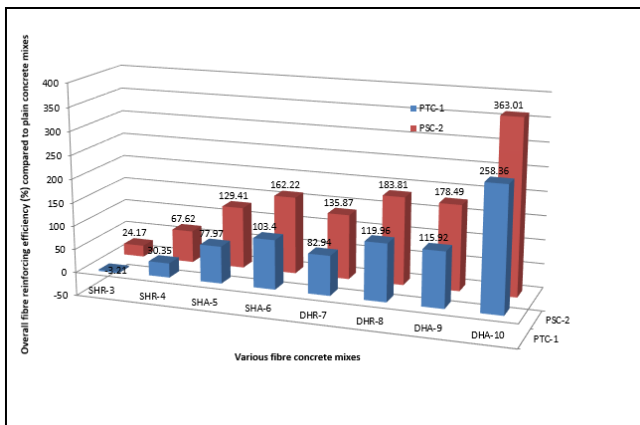


Fig.8 Comparative assessment of fibre efficiency in various concretes

Compared to thick concrete sections the increase in fracture toughness was better realized in slender concrete sections at high steel fibre substitution as well as aligned steel fibre substitution. Also, the performance levels of randomly oriented steel fibres were comparatively lower than aligned steel fibre incorporated concretes. The improvement on fracture properties was also significant in the case of complex anchorage profile of double hooked steel

fibres which provide adequate resistance for fibre pullout. The inclusion of aligned steel fibres at maximum fibre volume fraction (1%) had shown promising improvements on the fracture properties of concrete even with reduced thickness. Overall test results positively indicate that size reduction in concrete can be achieved if the required flexural resistance is compensated with the supplementary steel fibres added in concrete system. The preferred orientation of steel fibres along beam axis increased the tensile capacity of concrete specimens and hence leading to higher fracture resistance. Test results are also evident that addition of steel fibres in plain concrete can significantly use to reduce the concrete volume without compromising on the fracture properties as that obtained in the case of thick concrete sections. Also, test results indicate that aligned steel fibres at sufficient fibre volume can be useful to reduce the cross sectional size of concrete elements. It is also well documented from the test results that improved fibre matrix bonding and preferential fibre alignment were found to be an important factor for size reduction of concrete.

4. Conclusions from the study

- Based on the test results obtained from this study, some of the specific conclusions that can be drawn from this study are summarized below:
- Mechanical performance of different steel fibres in high strength slender concrete sections had been systematically investigated with different steel fibre profile – single hooked, double hooked, crimped and kinked steel fibres.
- Even though the four different types of steel fibres tested in this study had same aspect ratio, the relative improved performance of fibres in the concrete

13th Annual Research Day

Organised by the Deanship of Scientific Research in Collaboration with the College of Engineering
Research Centre
2nd April 2018

matrix was dependent on its complex profile.

- The increase in fracture strength among various fibre concretes was realized at high fibre volume fraction upto 1.5%. Among the different steel fibres, the double hooked steel fibres (DHS-7) and kinked steel fibre (KS-13) incorporated concretes exhibited highest fracture strength of 10.59 and 10.27 N/mm² respectively than other fibre concrete types.
- Fracture toughness properties of all fibre concretes were comparatively higher than plain concrete. Maximum fracture toughness of 39.62 MPa√mm was obtained for double hooked steel fibre concretes (DHS-7) followed by crimped hooked steel fibre (CS-10) of 37.48 MPa√mm.
- Fracture energy of double hooked steel and crimped steel fibre concretes recorded maximum value of 376N/m and 367N/m which indicates the consistent performance of fibres in the concrete matrix.
- Overall performance index of fibre concretes indicated that double hooked steel fibres achieved maximum reinforcing efficiency (89.76%) in high strength concrete followed by kinked steel fibre (79.83%) and crimped steel fibres (76.02%). Also, the performance characteristics of fibres in concrete were purely dependent on the post crack – bridging efficiency as a result of effective steel fibre profile.

Acknowledgement

The author gratefully acknowledges the research funding for this project No.300, provided by Deanship of Scientific Research, King Khalid University, ABHA, KSA.

References

- [1]. P. Balaguru, R. Narahari, M. Patel, Flexural toughness of steel fiber reinforced concrete, *ACI Mater. J.* 89 (6) (1992) 41–546.
- [2]. P.S. Song, S. Hwang, Mechanical properties of high-strength steel fiber reinforced concrete, *Constr. Build. Mater.* 18 (9) (2004) 669–673
- [3]. L. Soufeiani, SN. Raman, MZB. Jumaat, UJ. Alengaram, G. Ghadyani, P. Mendis. Influences of the volume fraction and shape of steel fibers on fiber-reinforced concrete subjected to dynamic loading – a review. *EngStruct* 2016;124 (1):405–17.
- [4]. N. Banthia, and J.F. Trottier, “Concrete reinforced with deformed steel fibers, Part I: Bond-slip mechanisms.” *ACI Materials Journal* Vol. 91, No. 5, September 1994, pp. 435-446.
- [5]. Jong-Han Lee, Baiksoon Cho, Eunsoo Choi. Flexural capacity of fiber reinforced concrete with a consideration of concrete strength and fiber content. *Construction and Building Materials* 138 (2017) 222–231.
- [6]. J.A.O. Barros and J.A. Figueiras, Flexural behavior of steel fiber reinforced concrete, testing and modeling, *Journal of materials in civil engineering*, 3, (1999), 277-290.
- [7]. Barros, J.A.O and Figueiras, J.A. post cracking behavior of steel fibre reinforced concrete’, *RILEM materials and structures journal*, 38(275); (2005), 47-56
- [8]. A.G. Kooiman, C van der Veen and J.C Walraven. Modelling the post-cracking behavior of steel fibre reinforced concrete for structural design purposes, *HERON*, 2000. Vol. 45, No.4.
- [9]. Luis Felipe Maya Duque and Benjamin Graybeal, Fiber orientation distribution and tensile mechanical response in UHPFRC, *Materials and Structures* (2017) 50:55, pp.1-17.
- [10]. A. Sivakumar, Manu Santhanam. Mechanical properties of high strength concrete reinforced with metallic and non-metallic fibres. *Cement and Concrete Composites.* (2007). 29(8). Pp.603-608.
- [11]. ACI 211.4R. Guide for Selecting Proportions for High strength Concrete with

13th Annual Research Day

Organised by the Deanship of Scientific Research in Collaboration with the College of Engineering
Research Centre
2nd April 2018

Portland Cement and Flyash, Farmington
Hills. MI. (2008).

[12]. RILEM TC-1985. Determination of the
fracture energy of mortar and concrete by means

of three-point bend tests on notched beams.
Materials and Structures., 18(106), 285-290.

Solar Disinfection of Drinking Water with Nano-Titanium Dioxide

Ibrahim E. EL-Seesy

Department of Mechanical Engineering, College of Engineering, King Khalid University,
PO Box 394, Abha 61411 KSA.
E-mail address: ieelseesy@kku.edu.sa

Abstract: Water disinfection processes in the presence of titanium dioxide as a photo-catalyst material provide an interesting route to destroy contaminants, being operational in the UV-A domain with a potential use of solar radiation. In recent years, advanced oxidation processes (AOP) have been developed to meet the increasing need of an effective wastewater treatment. AOP generates powerful oxidizing agent hydroxyl radicals which completely destroy the pollutants in waste water. Solar disinfection of drinking water with polyethylene terephthalate (PET) bottles coated with photo-catalyst TiO₂ has been shown to be very effective. The study is based on comparison between three systems for treating contaminated water samples using PET bottles. First system was a PET untreated bottle, the second system was a PET bottle coated with black paint on its outer surface. Finally the third system was a PET bottle coated also with a black coat on its outer surface and its inner part was treated with citric acid solution to enable np-TiO₂ to cover the surface later on, then 0.2 g of np-TiO₂ powder (of particle size < 25 nm, Sigma-Aldrich) was added. The total bacterial accounts were determined to monitor the effect in the three systems. The experimental results have shown that disinfecting water with merely UV was less effective than combining the bottle with heat effect, and adding TiO₂ film was further more benefited. This work can be applied in rural areas, with no technical support or need for expensive/dangerous chemicals for drinking safe water even if is stored for two days.

Keywords: *Water disinfection, Titanium dioxide, Solar Radiation.*

1. Introduction:

Over 30% of the population in developing countries is in need of access to safe drinking water, [1]. It is estimated that 1.1 billion people (17% of global population) lack to access to safe drinking water and 2.6 billion people (42% of global population) lack access to proper sanitation facilities (World Health Organization/UNICEF 2005), [2,3]. To reduce these numbers, there are some methods for water disinfection like chlorination, boiling and Pasteurization. Chlorination is practical for small communities but is difficult to implement at the point of use. Boiling and Pasteurization are effective in removing bacteria, yeasts, molds, and protozoa from drinking water. Both methods require heating to elevated temperatures- 65oC

for pasteurization and 100oC for boiling-for short periods of time. Pasteurization can be effectively done by solar cookers (Ciochetti & MetCalf, 1984, [4]). Boiling usually requires burning biomasses which is discouraged because it promotes the destruction of local forests that are used for other purposes. Neither boiling nor pasteurization eliminates the chemical contaminants- which increase the risk for cancer, liver and kidney problems, and nervous and reproductive systems problems, [2]. And also other conventional methods like slow sand filtration which needs large land area, manual cleaning of filters and water with low turbidity levels. In addition organic pollutants aren't fully removed from the water using this technique, [2]. Other conventional technologies used to disinfect

water are: ozonation, and artificial UV radiation. These technologies require sophisticated equipment, are capital intensive and require skilled operators, [5, 6, and 7].

An alternative treatment option Solar Water Disinfection (SODIS) was developed as an inexpensive alternative. SODIS reduces pathogens by exposing water-filled plastic bottles (mainly polyethylene terephthalate or PET) to sunlight. SODIS is primarily used to disinfect small volumes of water (< 2 liters/bottle) and depends only on sunlight for disinfection, making it ideal for rural areas. Individuals expose clear plastic PET bottles filled with contaminated water to full sunlight for 8 hours. The UV radiation in the solar spectrum disinfects water by inactivating bacteria DNA [2, 8, 9]. Fig.1 represents the SODIS process.

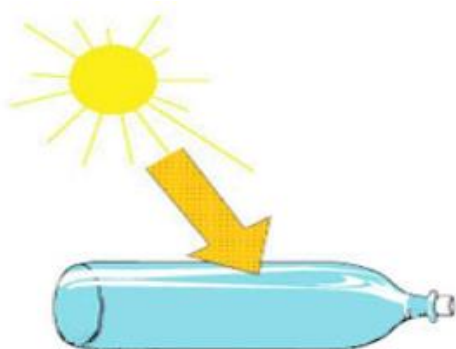


Figure 1: Depiction of SODIS [2].

However, bacteria have a self-defense mechanism, the ability to perform enzymatic DNA repair, which can result in bacterial reactivation. Therefore, while bacteria count directly after disinfection may reveal very low bacteria concentration, the bacteria with time may return in large numbers, [8]. Also it does nothing to mitigate inorganic or organic chemical waste that may be present in water. In addition, several variables including water turbidity (a measure of water clarity), total solar radiation, and ambient air temperature affect the disinfection process. It has been also suggested that the efficacy of SODIS is related to the amount of dissolved oxygen in the water at the

time of treatment [2, 10]. Paper mill wastewater is treated by solar photocatalytic oxidation with synthesized nano TiO_2 . The results showed that TiO_2 in the presence of solar light can be employed as an effective photocatalyst for the removal of chemical oxygen demand from the wastewater but in optimized conditions. A reduction of 80% of total suspended solids from the wastewater was also obtained at the same operating conditions. The experimental results had also shown that the non-biodegradable substances can be very effectively degraded by the solar photocatalytic treatment [11].

In order to increase the efficiency of the SODIS process, solar photocatalytic disinfection (AOP) was developed using titanium dioxide (TiO_2) as a photocatalyst. This method promises to increase the rate of disinfection of microorganisms while eliminating organic pollutants, such as fertilizers herbicides and pesticides. Titanium dioxide works much like SODIS in that it, too, generates hydroxyl radicals, peroxides and super-oxides. Figure 2 shows the mechanism of work of TiO_2 .

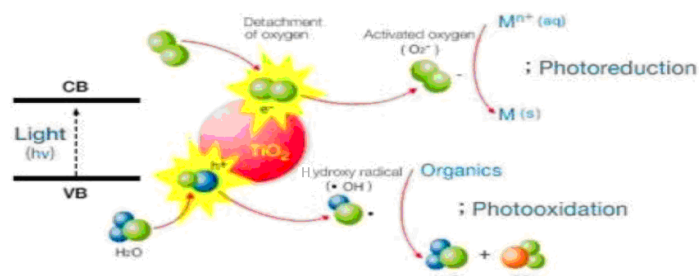
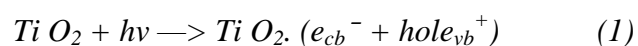


Figure 2: Photo -reduction and Photo-oxidation with Titanium Dioxide [2].

2. Theoretical Analysis:

If a photon promotes an electron from the valence band to the conduction band a "hole" with a positive charge is left in the valence band:



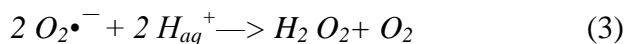
The superoxide radical is formed by the addition of a single electron:

13th Annual Research Day

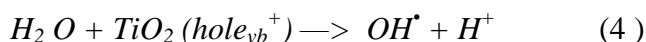
Organised by the Deanship of Scientific Research in Collaboration with the College of Engineering
Research Centre
2nd April 2018



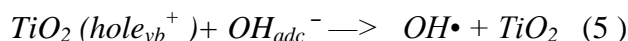
Hydrogen peroxide is formed during the reaction:



The OH radical is formed from either the reaction of water with an electron hole:



Or through the reaction of a hydroxide ion with a hole:



From equations (1-5), due to the presence of highly reactive oxidizing species, water can be disinfected from pollutants and chemicals and organisms as well effectively, [2].

However, the photo-oxidation and photo-reduction capabilities of AOP are superior to those of SODIS for the destruction of E. coli bacteria, and organic chemical effluents, [2, 8, 11, 12, 13]. The evolution of structure and microstructure as well as charge separation for a series of highly reactive nano crystalline TiO₂ photo-catalysts is certified by the degradation-mineralization of various model pollutants under UV light [14].

This work aims to make a study on SODIS-AOP technique and making it simple to be applied in rural regions and to study the storage of the disinfected water to determine the safety period of using the disinfected water with this technique water. Such remote communities typically suffer from fecal contamination of transient water sources, rather than chemical or radiological contaminants. To address this problem a low-cost continuous-feed water treatment facility has been designed and developed. The facility utilizes solar (UVA) radiation to treat pathogens. Additionally, the facility is designed such that it can be manufactured in-situ from limited or improvised resources at low capital and maintenance costs. The system is modular so that multiple systems

can be used to increase water treatment capacity as required. Testing indicates that 3 modules of the design can treat 34 L of water in 4 hours producing a 4-log reduction in E. Coli (from 8 × 10⁵ CFU/ml) with a residence time of less than 30 minutes [15].

3. Experimental Procedure

The study is based on three systems for treating contaminated water sample using PET bottles. First system was a PET untreated bottle, the second system was a PET bottle coated with black paint on its outer surface. Finally, the third system was a PET bottle coated also with a black coat on its outer surface and its inner part was treated with citric acid solution to enable np-TiO₂ to cover the surface later on, then 0.2 g of np-TiO₂ powder (of particle size <25 nm, Sigma-Aldrich) was added and the bottle was shaken manually and carefully to make a thin film on a half of the bottle. Then the bottle was washed twice with distilled water, so the extra loose powder is removed, [2].

The three bottles were exposed to the sun light for half an hour before usage to guarantee their sterilization before conducting the experiment, and then they were filled with water sample contaminated with bacteria.

4. Results and Discussion

The bacteriological examination was conducted on water samples to examine three different parameters UV, heat, and photocatalytic oxidation with np-TiO₂. These parameters include the total bacterial counts/ml. the sample was free from Aerobic and Anaerobic bacteria. The parameters expect of total bacteria counts didn't disappear at 33°C, 51°C in case of using untreated PET bottles with a thin film of np-TiO₂.

To evaluate the effectiveness of the three systems of treating the infected water, table (1) shows the data if the bacteriological analysis and

13th Annual Research Day

Organised by the Deanship of Scientific Research in Collaboration with the College of Engineering
Research Centre
2nd April 2018

the effect if the solar energy (UV and heat) and the effect of photocatalytic oxidation by np-TiO₂ thin film removing bacteria. To achieve this aim, total bacterial counts were determined to monitor the effect of UV in case of untreated PET bottle, the effect of heat (and UV) in case of the half black PET bottle, and finally the effect of the photocatalytic oxidation in case of the half black PET bottle treated with thin film of np-TiO₂.

Table (1): The effect of the solar energy and the photocatalytic oxidation by np-TiO₂ thin film on the total bacterial counts (CFU/ml), at 37 °C of the atmosphere:

Sample	(A) Untreated bottle (CFU/ml)	(B) Half black bottle (CFU/ml)	(C) Half black-TiO ₂ thin film treated bottle(CFU/ml)	Sample Temperature (°C)
Exposure time	Total bacterial count/ml			
0 hr	44	44	44	25
After 1 hr	37	18	16	37
After 2 hrs	13	12	2	45*
After 3 hrs	12	1	0	51*
Efficiency of bacterial Removal (%)	72.7	97.7	100	

* In case of the untreated bottle temperature of the sample was steady at 33 °C.

In table (1), the sample at room temperature 25°C, was 44 CFU/ml as starting the experiment, while the bacterial counts for the untreated bottle after exposure to the sun, at 33°C (for water, but for the atmosphere was 37°C) were, 37, 13, and 12 CFU/ml, although in case of using the half black bottle, the bacterial counts were 18 at 37°C, 12 at 45°C, and 1 at 51°C. However, the bacterial counts for the half black bottle treated with np-TiO₂ thin film were 16 at 37°C, 2 at 45°C, and 1 at 51°C.

By increasing time of exposure to UV light, for all the systems, the bacterial counts were dropping gradually, but in the second system it dropped faster due to the heat caused by the half black side of the bottle, and dropped faster in the third system due to the effective photocatalytic oxidation by np-TiO₂ thin film.

From table (1) it is obvious that the treatment of np-TiO₂ to the PET bottle was superior to the other systems in this study, due to the effectiveness of the photocatalytic oxidation process occurred by the TiO₂ nano particles exposed to UV light, fig.3 shows the total bacterial counts for the three times against time.

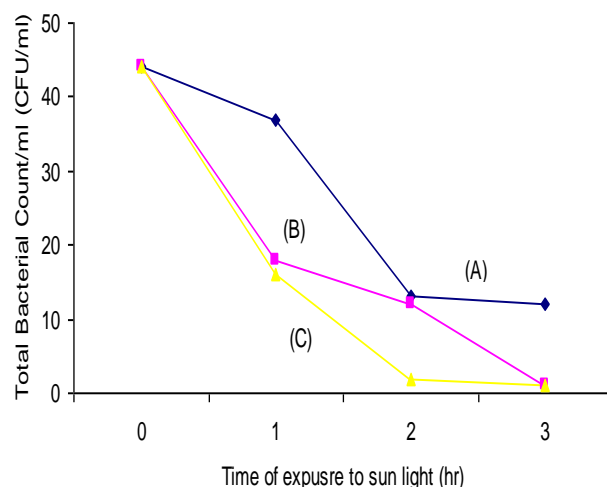


Figure 3: Total bacterial counts/ml against time, A: untreated bottle, B: half black bottle, C: half black and half TiO₂ film bottle.

After storing these samples for 48 hours and again conducting them for determining the total bacterial counts, the results discovered the following data in table (2). From table (2) another criterion was added to this study, revealing that the np-TiO₂ treated PET bottle system was still superior to the other systems, and so it adds to the benefits of using np-TiO₂ thin films in water treatments as its sterilizing effect lasted to a longer period of time.

13th Annual Research Day

Organised by the Deanship of Scientific Research in Collaboration with the College of Engineering
Research Centre
2nd April 2018

Table (2): The effect of the storage of water samples after treatment for 48 hrs on the total bacterial counts (CFU/ml) for the samples, at 25 °C:

Sample	Untreated bottle (CFU/ml)	Half black bottle (CFU/ml)	Half black-TiO ₂ thin film treated bottle (CFU/ml)
	the total bacterial count/ml		
After 24	0	0	0
After 48 hrs	1800	32	1

5. Conclusions:

As a final result of this study, the experimental results show acceptable agreement with previous studies [have reference] one can conclude that the UV for three hours is not enough in killing all bacteria, but by photocatalytic reaction that was guaranteed in two hours. This work can be applied in rural areas, with no technical support or need for expensive/dangerous chemicals for drinking safe water even if is stored for two days.

Acknowledgement

The author acknowledges M. Kamel, Water Pollution Department, National Research Center, Cairo, Egypt.

References

- [1] Christine Rojko; MS Thesis, "Solar disinfection of drinking water", Worcester Polytechnic Institute, USA, 2003.
- [2] Eric Richard Morgan; MS Thesis, "Solar water purification with PET bottles coated with TiO₂ using improved binding agents", University of Massachusetts Lowell, USA, 2008.
- [3] World Health Organization/UNICEF; "Water for Life, Making it Happen", ISBN 92 4 1562935.
- [4] David A. Ciochettit and ROBERT H. METCALF; " Pasteurization of Naturally Contaminated Water with Solar Energy", Applied and Environmental Microbiology, 45: 223-228, 1984.
- [5] Acher A., E. Fischer, R. Turnheim, and Y. Manor; "Ecologically friendly wastewater disinfection techniques", Water Research, 31:1398-1404, 1997.
- [6] Pelizzetti E.; "Solar water detoxification.Current status and Perspectives", Journal of physical chemistry, 212:207-218, 1999.
- [7] U.S.Environmental Protection Agency,"Ultraviolet light disinfection technology in drinking water application: an over view", EPA 811-R-96-002.U.S.Environmental Protection Agency, Washington D.C., 1996.
- [8] Robert Williams and John Duffy; "Solar water purification: storage test for the determination of bacteria regrowth and taste test in TiO₂ coated PE Tbottles"
<http://energy.caeds.eng.uml.edu/peru>.
- [9] Heredia, Manuel; "Photocatalytic Destruction of Water Pollutants Using a TiO₂ Film in PET Bottles.", MS thesis, Energy Engineering Program. Lowell, University of Massachusetts Lowell, USA, 2006.
- [10] Reed R. H.; "Solar inactivation of fecal bacteria in water: the critical role of oxygen", Letters in Applied Microbiology, 24:1–5, 1997.
- [11] Montaser Y. Ghaly, Tarek S. Jamil, , Ibrahim E. El-Seesy, Eglal R. Souaya, and Rabab A. Nasr; " Treatment of highly polluted paper mill wastewater by solar photocatalytic oxidation with synthesized nanoTiO₂ ", Chemical Engineering Journal, 168(2011): 446-454.
- [12] Peter Dubro, and John Duffy; "Dye Indicator for the Effectiveness of TiO₂ Water Purification." Proceedings Annual Meeting American Solar

13th Annual Research Day

Organised by the Deanship of Scientific Research in Collaboration with the College of Engineering
Research Centre
2nd April 2018

Energy Society. Boulder, CO: American Solar Energy Society, 2007.

[13] Tarek S. Jamil, Montaser Y. Ghaly, Ibrahim E. El-Seesy, Eglal R. Souaya, and Rabab A. Nasr; " A comparative study among different photochemical oxidation processes to enhance the biodegradability of paper mill wastewater ", Journal of Hazardous Materials 185 (2011), 353-358.

[14] Likodimos V., A. Chrysi, M. Calamiotou, C. Fernandez-Rodriguez, J.M. Doña-Rodrez, D.D.

Dionysiou, and P. Falaras ; " Microstructure and charge trapping assessment in highly reactive mixed phase TiO₂ photocatalysts ", Applied Catalysis B: Environmental 192 (2016) 242–252.

[15] Kalt, P., Birzer, C., Evans, H., Liew, A., Padovan, M. and Watchman, M. ; " A solar disinfection water treatment system for remote communities", Procedia Engineering, Vol. 78,(2014), 250-258.

Essential Oil Of Officinal Sage Extraction And Antioxidant And Antimicrobial Activities Study

Atef El Jery

Department of Chemical Engineering, College of Engineering, King Khalid University,
PO Box 394, Abha 61411 KSA.
E-mail address: ajery@kku.edu.sa

Abstract: This study aims to evaluate the composition, the antioxidant and antimicrobial activity of the essential oil of Sage officinale, the extraction was carried out by hydro-distillation. The yield of EO is 3.23%. Analysis of Sage officinale essential oil by CPG-MS identified 26 compounds. Among the majority identified compounds of the essential oil of sage are: trans-decalone (20.33%), 1,8-cineole (15.0%), α -thujone (14.89%), viridiflorol (9.91%), trans- β -caryophyllene (9.27%), carvone (6.19%) and β -thujone (5.68%). The study of antioxidant power by the DPPH method showed the existence of an antioxidant activity of the essential oil of dry sage leaves. The evaluation of antibacterial activity revealed the inhibition of bacterial growth for most tested strains that are of different kinds.

Keywords: Essential oil ; *Salvia officinalis* L. ; Antimicrobial - Antioxidant activities.

1. Introduction:

In order to contribute to the development of the essential oils of the plants growing in southern of Tunisia, we are interested in our work with the medicinal plant of *Salvia officinalis* L. The medicinal plants are as many rich sources of pharmacologically active substances. These herbs have been used in a wide range of purposes, including medicine, nutrition, flavors, beverages, dyeing, repellents, perfumes, cosmetics, charms, smoking and industrial uses. Sage is present in different areas. The leaves are well known for their antioxidant properties, especially in the food industry. It is appreciable on human health through biological activities, such as antibacterial, fungistatic, virostatic, astringent, eupeptic and antihydrotic effects. It is known in the pharmaceutical and medicinal fields, such as the management of Alzheimer's disease [1], by hypoglycemic and antimutagenic activities [2]. It is included as an active ingredient in combination plant preparations for the treatment of acute and chronic bronchitis [3]. It has strong antitumorigenic [4], antisudoral, anti-anesthetic,

antidiarrheal, resolutive and vulnerable activities. In addition, it is involved in various cytotoxic treatments, nerve, digestion [5].

Several recent studies have studied the chemical composition of the essential oil of *Salvia officinalis* in different regions on both sides of the Mediterranean basin [6, 7 and 8], etc.

In order to exploit the plants growing in Tunisia and known for their medicinal properties, we have studied the physico-chemical properties of essential oils extracted by hydrodistillation of *salvia officinalis*, picked from the south of Tunisia. The identification of the chemical compounds of the extracted essential oil was carried out by means of gas chromatography coupled to mass spectrometry (GC/MS), followed by the study of antioxidant activity by the free radical scavenging method (DPPH), and the study of antibacterial activity by the well method.

2. Materials and Methods:

2.1. Sampling and preparations

The freshly harvested plant components from the south of Tunisia, in spring – winter,

13th Annual Research Day

Organised by the Deanship of Scientific Research in Collaboration with the College of Engineering
Research Centre
2nd April 2018

2016. Soon after collection, *Salvia officinalis* plant samples were carried from field to the laboratory in aluminum foil, and then washed with tap and distilled water respectively, in order to remove the foreign particle from the plants. The seeds were then air dried for 2 weeks at ambient temperature without exposing to sunlight before use. The leaves detached from the stems, and then was decorticated using the decortivating disc mill machine.

2.2. Determination of Moisture Content

A fraction of the leaves dried is carried out also in an isothermal oven at 60 ± 2 °C for 3 hours and 30 minutes in order to measure the moisture content. Six cleaned samples of 30 g of leaves were weighed in a crucible and dried in an oven and weighed after every 30 min. The procedure was repeated to achieve the constant weight of sample. The equation (1) is used to calculate the percentage moisture content in the seeds.

$$\text{Moisture (\%)} = \left(\frac{m_1 - m_2}{m_1} \right) \times 100 \quad (1)$$

m_1 : sample weight before drying;
 m_2 : sample weight after drying.

2.3. Oil Separated and percentage yield

Dried aerial leaves of *Salvia officinalis* (200 g + 1 liter of distilled water) were separately crushed and put into Clevenger-type hydro-distillation for 4 hours. The collected liquid results in distillates, with thin layers of oil at the surface, will thereafter be separated, after standing liquids. The extracted essential oil, then stored at 4 °C for further investigation. After, it is carried out in separating ampoules in which the preceding mixtures separate into two immiscible phases. An aqueous phase, generally denser, is located in the lower part and an organic phase, of lower density and containing the essential oils and the petroleum ether as a solvent, is located above. Separation by rotary evaporator apparatus makes it possible to rapidly eliminate a volatile solvent by evaporation and then transferred to

measuring cylinder. The oil volume was recorded and the yield expressed as oil content (%) by the following equation:

$$\text{Yield (\%)} = \left(\frac{w_1}{w_2} \right) \times 100 \quad (2)$$

Where:

w_1 : weight of the extract before distillation;
 w_2 : weight of separated oil.

2.4. Determination of pH value

The value of pH of *Salvia officinalis* leaves was measured using pH meter (Metrohm AG 913). The pH electrode immersed into the oils samples and the pH value can be read and recorded.

2.5. Chemical analysis of essential oils

Essential oil obtained from the hydrodistillation, were analyzed by GC-FID to identify chemical composition and quantified by gas chromatogram type Hewlett Packard 5890, equipped with an FID detector, equipped with a DB-5 column (0.25 mm film thickness silicone capillary of dimension 25 m \times 0.25 mm). The furnace temperature was maintained at 50 °C for one minute and then increased by ramping up to 280 °C at rate 9 °C/min and hold for 5 minutes. The injection temperature was set at 240 °C, while the temperature of the detector was maintained at 250 °C. At the rate 1.2 ml/min, carrier gas flowed into the system, and 0.2 μ l volumes of feed were injected in Split mode. The concentration of the injected oil is 1% in hexane. The percentage by mass of the various chemical constituents of the *Salvia officinalis* oil is given on the relative surface area of the peaks (GC-FID). The essential oil components were identified and determined by the GC/MS, HP 5890 gas chromatogram coupled to an HP 5972 mass spectrum under the same CG analysis conditions, but with a one DB-5 column (0.25 mm thickness of film, 30 m \times 0.25 mm, dimension). The energy of ionization is 70 eV. The mass order is 40-300 m/z. The oil

13th Annual Research Day

Organised by the Deanship of Scientific Research in Collaboration with the College of Engineering
Research Centre
2nd April 2018

composition is distinguished on the basis of their mass spectrum with those reference compounds defined in the HP Chemstation, Wiley 275 Library, and comparing retention times published in the literature [9].

2.6. Strains

The oil from leaves part of the plant *Salvia officinalis* were tested on microorganisms. Ten bacteria make part of six Gram-positive (*Enterococcus faecalis* (Causes infections and inflammations in the lungs), *Micrococcus luteus* (Responsible for nosocomial diseases in immunocompromised patients), *Salmonella enterica* (causes fever and food poisoning), *Bacillus subtilis* (pathogenic and found in food), *Bacillus subtilis*, and *Staphylococcus aureus* (pathogen and food poisoning)), with four Gram-negative bacteria (*Escherchia coli* (pathogen and part of the intestinal flora), *Klebseilla pneumoniae* (implicate in cases of nosocomial pneumonia), *Shigella* (pathogen for humans is may cause intestinal infections) and *Agrobacteruim* (Cause of vomiting, pain abdominal and diarrhea)) were used. All those strains were obtained from Medical Faculty of Sfax (Tunisia). The used strains were isolated from Tunisia, especially from soil litter, the isolation method followed as reported in Travers et al. [10].

2.7. Assays for antimicrobial activity

Prescribed methods of research group Perez et al. [11] were used for the agar-well diffusion. Trypticase soy agar was autoclaved at the temperature 45 °C and cooled to room temperature in a water bath facilitate with the temperature controlling system. A total volume 25 ml of concentration 1 % (v/v) culture of the bacterial strain poured over every sterile petri dish. The culture then stored at very low temperature around 4 °C. A test solution volume of 80 ml were dispensed into a well of dug into the set agar. All cultures, then kept in the refrigerator (4 °C) for 1 to 2 hours before

incubation, then after incubating at 37 °C for at least 18 to 24 hours. The average inhibition zone diameter was noted after each experiment.

2.8. Determination of total polyphenol content

GC-FID technique were used to indentified for chemical composition of essential oil and quantified by gas chromatogram. For the essential oil of *Salvia officinalis* leaves, the amount of total phenolic was quantified by the regent of Folin and Ciocalteau using the procedure of Yan et al. [12] and Kumar et al. [13]. Samples of *Salvia officinalis* part (10 µl) were mixed to 750 µl of an aqueous solution of Follin-Ciocalteau reagent at 10 %. After 2 min of incubation at room temperature, 250 µl of Na₂CO₃ (20 %) in water was added. The reaction tube was further incubated for one hour at ambient temperature in the absence of any light. The absorbance was measured at 765 nm. Gallic acid was the standard used to determine the total phenol content in the all extracts and expressed according to the following equation:

$$\text{Polyphenaks (\%)} = \left(\frac{\frac{\text{OD}_{\text{sample}} \times 0.2}{\text{OD}_{\text{standard}}}}{\text{Sample concentration}} \right) \times 100 \quad (3)$$

2.9. Determination of total flavonoid content

Total flavonoid content was determined by the colorimetric assay of aluminum chloride [14]. A solution of the essential oil diluted 10 times with ethanol is prepared. Then poured into a glass tube 250 µl of this essential oil and 75 µl of NaOH at 5%, this mixture will be incubated at rest for 6 min at room temperature. Then, 150 µl (7%) of aluminum chloride (AlCl₃) will be added to the mixture for another incubation for 5 min. Then 500 µl of sodium hydroxide (NaOH) is also added to the mixture. The optical density is measured by the spectrophotometer at 510 nm. The total flavonoid assay was measured three times for each part of the extract according to the following equation:

$$\text{Flavonoids (\%)} = \left(\frac{\frac{\text{OD}_{\text{sample}} \times 0.05}{\text{OD}_{\text{standard}}}}{\text{Sample concentration}} \right) \times 100 \quad (4)$$

2.10. Determination of DPPH free radical-scavenging activity

The free radical scavenging capacity extract methanol for each sample of *Salvia officinalis* was evaluated with the methodology described by Blois [15] as elaborated by El mastas et al. [16]. After preparation of 2,2-diphenyl-1-picrylhydrazyl (DPPH) solution and 1 ml of DPPH solution was added to 1 ml of the methanol extract solution at various concentrations ranging from 200 to 1000 µg/ml with an interval of 200 µg/ml, absorption was measured at 517 nm up to one hour. Following equation was used to calculate scavenging capacity of DPPH radical.

$$\text{Inhibition (\%)} = \left(\frac{\text{OD}_{\text{control}} - \text{OD}_{\text{sample}}}{\text{OD}_{\text{control}}} \right) \times 100 \quad (5)$$

Where:

OD_{control}: Absorbance of the control reaction;

OD_{sample}: Absorbance in presence of all extract samples.

All tests were effectuated in triplicates. The concentrations of extract giving 50 % inhibition: IC₅₀ (µg/ml) were deduced from the graphs of scavenging effect percentage against extracts concentrations [17].

3. Results and Discussion

3.1. Influence of drying on the vegetable matter mass

The experimental results of the drying operation of sage leaves in an oven have been exploited. *Figure 1* represents the evolution of the mass of plant matter as a function of time. The mass of the material of the initial sage leaves is 20 g. it was brought to a stable temperature of 60 °C along the drying time.

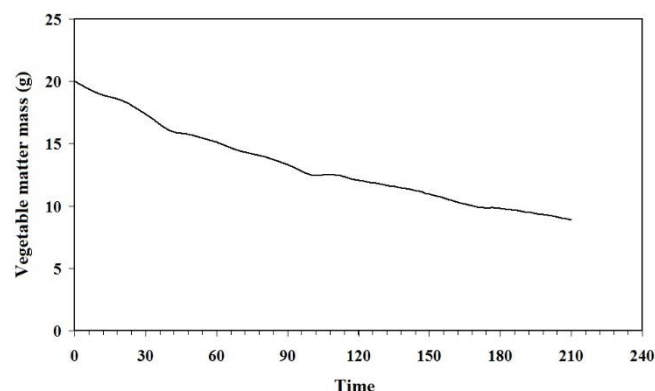


Figure (1) Evolution of vegetal mass over time.

It has been noticed that the amount of vegetable matter decreases rapidly during drying. The drying rate was faster in the first two hours and then slowed down during the remaining drying period. Indeed, they lose their half-weight after 2 hours and 15 minutes. It goes from 20 g at t = 0 to 7.84 g after 3 hours 30 minutes. This concludes that sage leaves are rich in water that weighs more than half.

3.2. Essential oil extraction

From 200 g of officinal sage leaves mass in one liter of distilled water, a volume of 9 ml of essential oil was extracted with yellowish colour and a spicy odour has a note of rosemary. This essential oil is characterized by a density of $\rho_{\text{sage}} = 719.8 \text{ kg/m}^3$. The extraction yield was determined $\eta = 3.235 \%$.

3.3. Physicochemical analysis of sage essential oil

The pH of the sage extract is 2.4; this proves that the medium is a strong acidic. Practically this value is similar to those given by Fellah et al. [19], from Marsa and Jebel Oust regions sage oil.

3.4. Antioxidant activity test

After dosing and incubation at one hour, the optical density of standard and the solution containing sage extract, the samples were measured. Polyphenols = $134.33 \pm 17.61 \text{ µg/ml}$, flavonoids = $119.50 \pm 18.75 \text{ mg/ml}$ and the

13th Annual Research Day

Organised by the Deanship of Scientific Research in Collaboration with the College of Engineering
Research Centre
2nd April 2018

percentage inhibition of the DPPH radical, $IC_{50} = 970 \pm 5.5 \mu\text{g/ml}$. These values show that the sage essential oil sample is richer in polyphenols than in flavonoids and is an antioxidant.

3.5. Antimicrobial test

Our extract oil is tested on 10 bacterial strains of six Gram-positive: *Enterococcus faecalis*, *Micrococcus luteus*, *Salmonella enterica*, *Bacillus subtilis*, *micrococcus luteus* and *Staphylococcus aureus*, and four Gram-negative bacteria: *Escherichia coli*, *Klebsiella pneumoniae*, *Shigella* and *Agrobacterium*. It has been noticed that the essential oil of *Salvia officinalis* exhibits antimicrobial activity against all strains tested, except the case of *Pseudomonas*

Aeruginosa. The degree of intensity of the antibacterial activity differs from one strain to another depending on the sensitivity towards our samples. It has been noted that the activity is better for the cases of *Escherichia Coli*, *Enterococcus Faecalis*, *Bacillus Aureus*, *Bacillus Subtilis* and *Agrobacterium* following the presence of a large clear halo (figure 2). A moderate activity for the case of *Salmonella*, *Shigella*, *Klebsiella Pneumoniae*. A small halo on the petri dish shows that the activity is weak for the case of *Staphylococcus Aureus* and *Micrococcus luteus*. It was concluded that sage essential oil has an important inhibitory effect against the microorganisms studied.

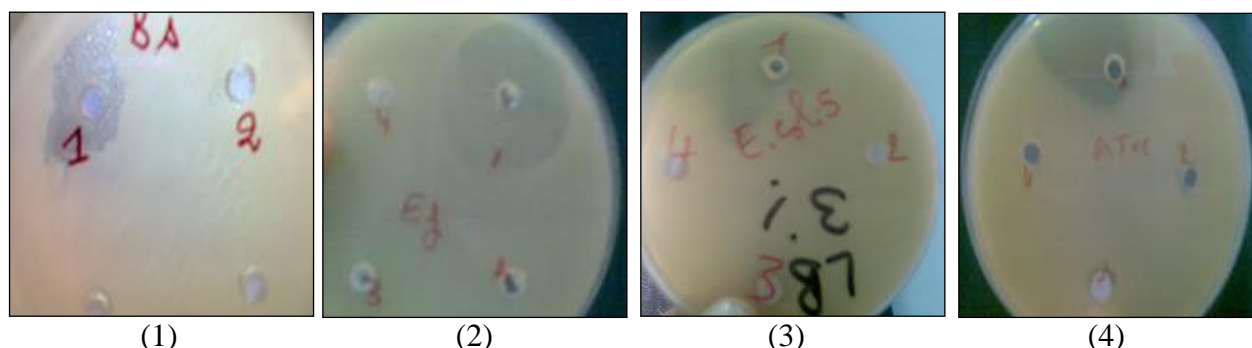


Figure (2) Antimicrobial test results with a large bright halo: Strains: (1) *Bacillus Suptilus*, (2) *Enterococcus Fecalis*, (3) *Escherichia Coli*, (4) *Agrobacterium*.

3.6. Chemical composition of the officinal sage essential oil

The essential oils extracted from dried leaves, of *Salvia officinalis* by steam distillation process. Sage oil is aromatic in odor and somewhat bitter in taste. The results obtained further analyzed qualitatively and quantitatively by GC/MS, to identifying the components. These compounds are detected by peaks presented in the spectrum of figure 3. All the compounds acquired are listed in the order of their elution in table 1, indicating the chemical compounds and their percentages. Chromatographic analyzes determined the chemical composition of essential oils constituents, 100% with 26 compounds greater than 0.3% on percentage.

The prevalent leaves constituents were monoterpenes oxygenated (8 compounds) representing 65.75% of the total leaf oil. The major components were camphor (20.30%), 1,8-cineole (15.10%), α -thujone (14.89%), carvone (6.19%) β -thujone (5.68%) and. Significant amounts of sesquiterpenes hydrocarbons and oxygenated representing respectively (11.26% - 6 compounds) and (11.58% - 2 compounds) were mainly dominated by viridiflorol (9.91%), trans- β -caryophyllene (4.00%), germacrene-B (2.52%) and germacrene-D (2.13%). A monoterpenes hydrocarbons were representing 8.49%, with moderate amounts such as camphene (2.58%) and β -pinene (2.06%). Ester and hydrocarbons were presented by very low contents.

13th Annual Research Day

Organised by the Deanship of Scientific Research in Collaboration with the College of Engineering
Research Centre
2nd April 2018

Four compounds that occur in the leaves oil of *Salvia officinalis* plant which are: camphor, 1,8 cineole, α -thujone and viridiflorol with significant percentages. In total, essential oil compositions of *Salvia officinalis* was considered as a rich source of monoterpenes oxygenated. Many essential oils have antimicrobial properties, these properties are due to the availability of active components, mostly isoprenes such as monoterpenes, sesquiterpenes.

Significant chemical properties differences are found in the essential oil of *Salvia officinalis* originating in Tunisia and in Algeria or Libya. All such differences could be due to many reasons like plantation field geography, the effects of climate, season of harvesting, soil type, age of plant parts, the used plant material condition, the plant part used, sample collection time, etc. Other major compound classes in *Salvia officinalis* plant parts were the alkanes comprised only C₁₀ to C₁₅ chain lengths at different amounts. The main structures of constituents of different parts of *Salvia officinalis* essential oils are presented in figure 4.

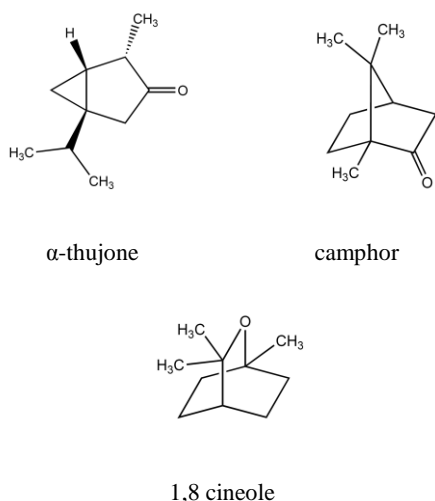


Figure (4) Structures of the most abundant compounds identified in *Salvia officinalis* essential oils.

By a comparative study with the essential oil of *Salvia officinalis* collected from Marsa and Djebel Ouest [20] whose constituents identified

are 92.23%. There was a relatively large difference in composition. More components were present in our extract but absent in that of Marsa. such as: α -terpinene (0.32%), γ -terpinene (0.59%), *trans*-decalone (20.30%), cheptanone (0.38%), terpineol (2.16%), borneol (1.15%), carvone (6.19%), bornyl-acetate (1.60%), β -bourbonene (0.89%), β -elemene (0.82%), α -humulene (2.13%), germacrene-B (0.90%), globulol (1.67%) and naphthalene (0.86%). Others are not present in our extract such as: *U-phallandrene* (0.34%), limonene (6.56%), terpinolene (0.36%), linalool (2.02%) and *E-sesquilavandulol* (5.04%). The common compounds are in various percentages and for those raised in our sample are listed in Table 2.

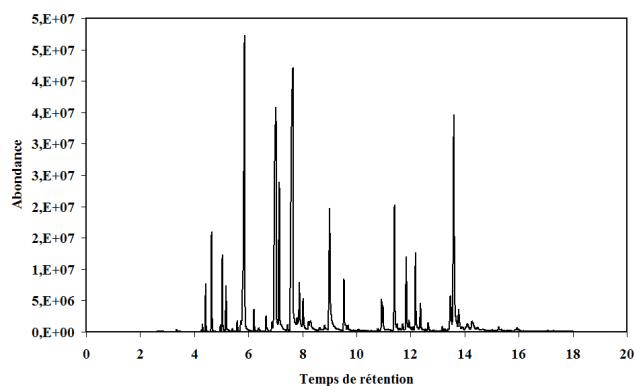


Figure (3) Chromatography of the extract.

Table 1: Chemical Analysis Results of Sage Oil Using GC-MS for Compounds Percentage greater than 0.3%.

components	Retention time (min)	% compounds
α -Pinene	4.42	1.15
Camphene	4.64	2.58
β -Pinene	5.04	2.06
Myrcene	5.18	1.26
α -Terpinene	5.59	0.32
Benzene	5.73	0.36
1,8-Cineole	5.86	15.0
γ -Terpinene	6.21	0.59
α -Terpinolene	6.66	0.53
α -Thujone	7.02	14.89

13th Annual Research Day

Organised by the Deanship of Scientific Research in Collaboration with the College of Engineering
Research Centre
2nd April 2018

<i>β-Thujone</i>	7.15	5.68
<i>Camphor</i>	7.64	20.30
<i>2-Norpinanone, 3,6,6-trimethyl-</i>	7.80	0.38
<i>Borneol</i>	7.89	2.16
<i>Terpineol</i>	8.03	1.15
<i>Carvone</i>	9.01	6.19
<i>Bornyl-Acetate</i>	9.54	1.60
<i>β-Bourbonene</i>	10.93	0.89
<i>β-Elemene</i>	10.98	0.82
<i>Trans-β-Caryophyllene</i>	11.41	4.00
<i>α-Humulene</i>	11.85	2.13
<i>Germacrene-D</i>	12.18	2.52
<i>Germacrene-B</i>	12.37	0.90
<i>Globulol</i>	13.48	1.67
<i>Viridiflorol</i>	13.61	9.91
<i>12-Oxabicyclo[9.1.0]dodeca-3,7-diene, 1,5,5,8-tetramethyl-, [1R-(1R@,3E,7E,11R@)]</i>	13.78	0.86
<i>Total (%)</i>		100
<i>hydrocarbons</i>		0.36
<i>Monoterpenes hydrocarbons</i>		8.49
<i>Monoterpenes oxygenated</i>		65.85
<i>Sesquiterpenes hydrocarbons</i>		11.26
<i>Sesquiterpenes oxygenated</i>		11.58
<i>Sesquiterpenoids oxygenated</i>		0.86
<i>Ester</i>		1.6

Table 2: Comparative study of extracted compounds percentages.

components	% Marsa	% Djebel Ouest	% Present study
<i>Camphor</i>	2.10	3.38	20.30
<i>α -Pinene</i>	0.83	0.69	1.15
<i>Camphene</i>	0.68	0.81	2.58
<i>Myrcene</i>	0.65	1.40	1.26
<i>1,8-Cineole</i>	8.58	16.96	15.00
<i>Germacrene-D</i>	0.22	0.27	2.52

<i>β-Pinene</i>	2.19	5.19	2.06
<i>α-Thujone</i>	25.02	26.49	14.89
<i>Trans-β-Caryophyllene</i>	5.20	9.04	4.00
<i>Viridiflorol</i>	18.96	13.04	9.91

The compounds percentages of this study as *α-pinene*, *camphene*, *myrcene*, *1,8-cineole* and *germacrene-D* are more higher, whereas for *β-pinene*, *α-thujone*, *trans-β-caryophyllene* and *viridiflorol* are lower than those of Marsa. These show the effect of the origin of the plant on the nature and the percentage of each compound that constitutes the extract in the essential oil.

4. Conclusion

In this work, twenty-six compounds have been identified in the essential oil of sage, picked from the Tataouine region (Tunisia) during its vegetative stage. The extraction of this oil is carried out by hydrodistillation, enabling a high essential oil yield to be obtained 3.23%. A study of the antioxidant activity was carried out. Concentrations of polyphenols, in flavonoids and median inhibitory concentration (IC₅₀) were determined. These results confirm the powerful antioxidant potential of the essential oil of this species. More, the antimicrobial test has been demonstrated a great inhibitory power of the essential oil of *Salvia officinalis* with regard to 10 very pathogenic bacteria and known by the high frequencies to contaminate foodstuffs, and the adverse effects on human health. The chemical composition of our sample was performed by means of gas chromatography coupled with mass spectrometry, which allowed us to identify 26 constituents. Qualitatively, the different oils obtained have different chemical compositions. However, the essential oil of the Tunisian sage is characterized by a variation of the compositions and remains to reveal a perfect agreement with the international standards.

This oil can be used in different fields such as the phytosanitary industry, cosmetic and pharmaceutical.

13th Annual Research Day

Organised by the Deanship of Scientific Research in Collaboration with the College of Engineering
Research Centre
2nd April 2018

References

- [1] M.C. Cuvelier. C. Berset. H. Richard (1994). Antioxidant constituents in sage (*Salvia officinalis*). Journal of Agricultural and Food Chemistry 42. 665–669.
- [2] D. Baricevic a.. S. Sosa b. R. Della Loggia b. A. Tubaro b. B. Simonovska c. A. Krasna c. A. Zupancic. (2001) Topical anti-inflammatory activity of *Salvia officinalis* L. leaves: the relevance of ursolic acid. Journal of Ethnopharmacology 75. 125–132.
- [3] S. Akhondzadeh. M. Noroozian. M. Mohammadi. S. Ohadinia. AH. Jamshidi. M. Khani (2003) *Salvia officinalis* extract in the treatment of patients with mild to moderate Alzheimer's disease: a double blind. randomized and placebo-controlled trial. J. Clin. Pharm. Ther. 28. 53–59.
- [4] C.T. Ho. M.F. Wang. G.J. Wei. T.C. Huang. M.T. Huang (2000) Chemistry and antioxidative factors in rosemary and sage. Biofactors 13. 161–166.
- [5] K. Laghrifl. A. Lemrhari. R. Zouhair. M. El Idrissi (2013) Chemical composition of essential oil of sage officinale. ScienceLib Editions Mersenne 5.
- [6] E. Putievsky. U. Ravid. D. Sanderovich (1992) Morphological observation and essential oils of sage (*salvia officinalis* L.) under cultivation. J. Essent. Oil Res.. 4. 291–293.
- [7] E. Tsankova. A .N. Konkchiev. E M. Genova (1994) Constituents of essential oils from three *Salvia* species J. Essent. Oil. Res. 6. 375.
- [8] R. Piccaglia. M. Marotti (1993) Characterization of several aromatic plants grown in northern Italy. Flavour Fragrance Journal. 8. 112–115.
- [9] Adams RP. (1995). Identification of essential oil components by gas chromatography/mass spectroscopy. Allured Publishing Corporation. Carol Stream. IL. USA pp:312–452.
- [10] Travers, R.S., Martin, P.A.W. and Reichelderfer, C.F. (1990). Selective process for efficient isolation of soil *Bacillus* species. Applied and Environmental Microbiology. 53:1263–1266.
- [11] Perez, C., Paul, M. , Bazerque, P. (1990). Antibiotic assay by agar-well diffusion method. Acta Biol. Med. Exp. 15:113–115.
- [12] Yuan V.Y., Bone D.E., Carrington F. (2005). Antioxidant activity of dulse (*Plmaria palmata*) extract evaluated in vitro. Food Chem. 91:485–494.
- [13] Kumar A., Chattopadhyay S. (2006). DNA damage protecting activity and antioxidant potential of pudina extract. Food chem. 100:1377–1384.
- [14] Jia Z., Tang M., Wu J. (1999). The determination of flavonoid contents in mulberry and their scavenging effects on superoxide radicals. Food Chem. 64:555–559.
- [15] Blois MS. (1958). Antioxidant Determination by the Use of a Stable Free Radical. Nature. 181, 1199–1200.
- [16] Elmastas M., Isildak O., Turkekul I., Temur N. (2007). Determination of antioxidant activity and antioxidant compounds in wild edible mushrooms. J. Food Compos. Anal. 20:337–345.
- [17] Shimada K., Fujikawa K., Yahara K., Nakamura T. (1992). Antioxidative properties of xanthone on the auto oxidation of soybean in cyclodextrin emulsion. J. Agr. Food Chem. 40:945–948.
- [18] Brantner A., Males Z., Pepeljnjak S., Antolic A. (1996). Antimicrobial activity of *Paliurus spina-christi* Mill, J. Ethnopharmacol. 52:119–122.
- [19] Fellah S., Romdhane M., Abderraba M. (2006). Extraction et étude des huiles essentielles de la *salvia officinalis*.l cueillie dans deux régions différentes de la Tunisie, Journal of the Algerian Chemical Society. 16. 2:193–202.

New Diagram Useful For Classification Of water Quality

Elhag, A. B¹

¹Department of Civil Engineering, College of Engineering, King Khalid University,
PO Box 394, Abha 61411 KSA.
E-mail address: abalhaj@kku.edu.sa

Abstract: Due to human and human activities the groundwater is polluted. This is the serious problem now a century. Thus the analysis of the water quality is very important to preserve and prefect the natural eco system. The primary objective of this paper is to study the groundwater quality parameters. The mechanism of chemical reactions leading to the change in the composition of groundwater and source of the dissolved ions in the groundwater can be understood by Banaga's diagram. The Banaga method is not only shows graphically the nature of a given water sample and dictates the relationship to other samples but there are a number of different methods and schemes used to classify natural water quality, source, origin and determine their suitability for different purposes depending on the concentrations of the basic components. The new diagram is useful for better understanding the evolution of hydrochemical parameters of groundwater that can be by plotting the concentration of major cations and anions in % meq/l, and it is divides the water quality into five types. The results of this analysis were compared with the water quality standards of Piper diagram.

Keywords: *Hydrochemical facies, new Banaga diagram, water quality.*

1. Introduction:

The movement of percolating water through larger pores is much more rapid than through the finer pores. The overall effect of all these factors is that the composition of groundwater varies from time to time and from place to place. Groundwater often consists of seven major chemical elements Ca^{+2} , Mg^{+2} , Na^+ , K^+ , HCO_3^- , SO_4^{-2} and Cl^- , all groundwater contains salts in solution that are derived from the location and past movement of the water through the different rock formations. It can also act as a strong weathering agent apart from general solution effect. Consequently, the chemical composition of groundwater will vary depending upon several factors like frequency of precipitation, which will leach out the salts, time of stay of rain water in the root-zone and intermediate zone, presence of organic matter etc. In this paper was innovate and create new graphs, which are more useful for bringing out the chemical relationships amongst

groundwater samples and display a brief description of the water quality data. The graphs can aid in comparing analysis and for emphasizing similarities and differences between the other standard possible plotting methods as Banaga diagrams and Piper (Figs. 1 and 2) respectively.

To understanding the quality of groundwater is as important as it's quantity because it is the main factor determining the suitability for domestic, drinking, agricultural and industrial purposes. (Etu-Efeotor, 1998) announced that the Groundwater is never really chemically pure as water invariably dissolves some of the minerals it comes in contact with, at any given time. Hydrochemical processes such as dissolution, precipitation, ion exchange processes and the residence time along the flow path control the chemical composition of groundwater, and hydrochemical characterization of water body presents the condition of water with respect to its quality measuring parameters considered under

13th Annual Research Day

Organised by the Deanship of Scientific Research in Collaboration with the College of Engineering
Research Centre
2nd April 2018

the study. On the other hand, the dissolved constituents in groundwater are primarily controlled by the original chemical characters and temperature of the water entering the zone of saturation; the distribution, solubility and exchange capacity of minerals in the rock; the porosity and permeability of the aquifer and the flow path ways of the water (Back and Hanshaw, 1965; Freeze and Cherry, 1979; Appelo and Postma, 1996; Mazor, 1997).

The mineral substances dissolved in water are divided into macro-component (Na^+ , K^+ , Ca^{2+} , Mg^{2+} and SO_4^{2-} , Cl^- , HCO_3^- , CO_3^{2-}) and micro-component (ions of lithium, rubidium, caesium and anions – bromine, iodine, fluorine, boron and ions of heavy metals) (Aderibigbe, T. A et al, 2015) Certain combination of anions and cations in water distinguishes the hydrochemical water types (Hartman, 2005).

2. Materials and Methods:

2.1 Materials

Different graphical and statistical techniques have been developed to describe the concentrations or relative abundances of major constituents and the pattern of variability in the different water samples. Banaga diagram is made of combination of four different fields that has been recently used to classify the water into different water types based upon the cations and anions concentrations in the form of major ions percentage in triangle and rectangular fields. Percentages are calculated in terms of equivalent in millions of main ions.

2.2 Experimental Procedure

The new diagram is the planning division of arithmetic to distinguish the various groundwater groups in terms of the main chemical components and the most important characteristic of this scheme is the speed and ease of dropping points it is composed of positive and negative ions together, and construct relative abundance of chief cations with the percent meq/l of Ca^{2+} ,

Mg^{2+} Na^+ and K^+ are plotted on diamond-shaped, while relative abundance concentration of anions with the percent meq/l of $\text{HCO}_3^- + \text{CO}_3^{2-}$, Cl^- and SO_4^{2-} are plotted on diamond-shaped.

3. Results and Discussion

Snow crystal growth by vapor deposition generally occurs along one of two planes: the basal plane along one of three a-axes or the perpendicular plane or c- axis (Fig. 1). The chemical parameters of groundwater play a significant role in classifying and assessing water quality. In this paper a number of techniques and methods have been developed to interpret the chemical data. Banaga has summarized the various modes of data representation and has discussed their possible uses. In this paper, a description is given, using a table (1) and a number of figures (1), of the different water types, after dropping a column from the middle of each rib passes the point 50%.

Banaga Diagrams are a combination anion and cation triangle and rectangle shape (Fig. 1), which can be used to interpretation as to the origin of the water represented by the analysis and to characterize different water types. Banaga divided waters into four basic types. Water that plots at zone (2) classified as $\text{Ca}^{2+} + \text{Mg}^{2+}$ and $\text{Cl}^- + \text{SO}_4^{2-}$, which the results in an area is permanent hardness water. The water that plots within the zone (3) shows that the $\text{Ca}^{2+} + \text{Mg}^{2+}$ and HCO_3^- and the region of water increase more than 50% and this kind of water have a temporary hardness, and hydrogeologically formation described as shallow and fresh water (recharge area). Water plotted at the lower corner of the diamond is primarily composed of alkali carbonates ($\text{Na}^+ + \text{K}^+$ and $\text{HCO}_3^- + \text{CO}_3^{2-}$). Water lying nears the right-hand side of the diamond may be considered the older brackish and saltwater saline ($\text{Na}^+ + \text{K}^+$ and $\text{Cl}^- + \text{SO}_4^{2-}$). while zone (4), describe the water is composed of ($\text{Na}^+ + \text{K}^+$ and $\text{Cl}^- + \text{SO}_4^{2-}$) may be considered the older brackish and saltwater saline and ancient marine (discharge area), and it is danger for irrigation

operations because they contain a high concentration of sodium ion. Water is described in the zone (3) as ($\text{Na}^+ + \text{K}^+$ and $\text{HCO}_3^- + \text{CO}_3^{2-}$) Table (1).

Table 1: It divides the quality of water to five different types.

Type of water	Zone No.
Alkaline bicarbonate	1
Alkaline sulphate chloride	2
Alkali sulphate chloride	3
Alkali bicarbonate	4

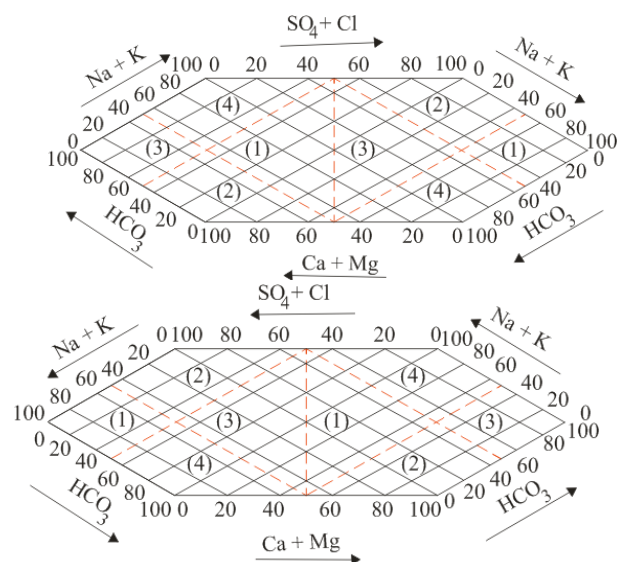


Figure (1) Showing Banaga diagrams.

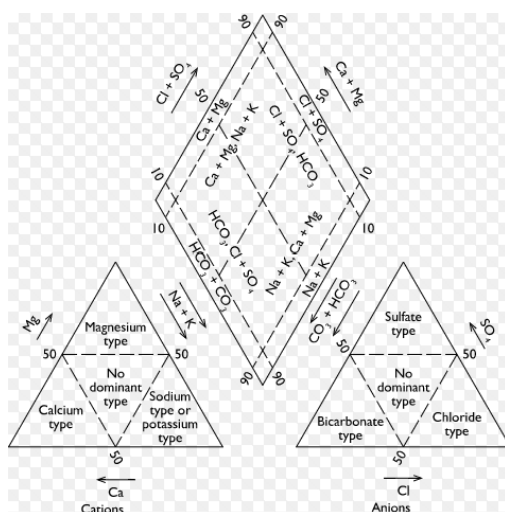


Figure (2) Showing Piper diagram.

4. Conclusions:

The Banaga diagram is made of combination of different fields that has been recently used to classify the water into different water types based upon the cations and anions concentrations in the form of major ions percentage, which including four types of water table (1).

The interpretation of hydrochemical analysis reveals that the major ions data were plotted on Banaga's diagram indicated that four hydrogeochemical type facies.

Acknowledgement

The author would like to thank King Khalid University, Department of Civil Engineering for supporting this work.

References

- [1] T.A. Aderibigbe, A. AzeezJimoh, C. Olisah, Hydrochemical Studies of Surface Water and Groundwater in Lagos State, Southwest Nigeria. IOSR Journal of Environmental Science, Toxicology and Food Technology (IOSR-JESTFT) e-ISSN: 2319-2402, p- ISSN: 2319-2399. Volume 9, Issue 12 Ver. III (2015) pp. 43-52 www.iosrjournals.org.
- [2] C.A.J. Appelo, and D. Postma, Geochemistry, groundwater and pollution" Balkema, Rotterdam, Netherlands, (1996) pp. 536.
- [3] W. Back, B.B. Hanshaw, Chemical geohydrology. In: Advances in Hydrosience, (Chow VT, ed). Academic Press, New York, USA, (1965).
- [4] J.O. Etu-Efeotor, Hydrochemical Analysis Surface and Groundwater of Gwagwalada Area of Central Nigeria, Global Journal of Pure and Applied Sciences, Vol. 4, No. 2, (1998) pp. 153-162.
- [5] R.A. Freeze, and J.A. Cherry, Groundwater, Prentice Hall, Englewood Cliffs, New Jersey, USA, (1979).
- [6] J. Hartman, Z. Berna, D. Stuben, N. and Henze, A statistical procedure for the analysis of seismotectonically induced

13th Annual Research Day

Organised by the Deanship of Scientific Research in Collaboration with the College of Engineering
Research Centre
2nd April 2018

- hydrochemical signals: a case study from the eastern Carpathians. Romania Tectonophysics, 405: (2005) 77-98.
- [7] R.E. Mazar, Chemical and Isotopic Groundwater Hydrology – The Applied Approach” Marcel Dekker, New York, USA. (1997).
- [8] A.M. Piper, A graphic procedure in geochemical interpretation of water analyses Am. Geophys. Union Transactions. 25: (1944) 914-923.
- H.R. Milward, B.J. Belhouse, G.Walker, Screw thread flow promoters: an experimental study of ultrafiltration and microfiltration, J. Membr. Sci.106 (1995) 269.
- [2] Z.F.Cui, K.I.T.Wright, Flux enhancement with gas sparging in downwards crossflow ultrafiltration: performance and mechanism, J. Membr. Sci.117(1996) 109.

Design of a Smart Guyed Mast to mitigate Earthquakes

Mohamed Hechmi ELOUNI¹ and Nabil BEN KAHLA¹

¹Department of Civil Engineering, College of Engineering, King Khalid University,
PO Box 394, Abha 61411 KSA.
E-mail address: melouni@kku.edu.sa

Abstract: Guyed masts are tall thin vertical space truss structures supported laterally by high strength guy wires. They are flexible structures and are very sensitive to vibrations induced by Wind or earthquakes. The main objective of this paper is to design a smart guyed tower with a total height of 292.8 meters to mitigate earthquakes. A non-linear model of the guyed mast is presented. The Finite Element model of the tall mast is coupled with a nonlinear cable taking into account the quadratic and cubic nonlinear couplings between in-plane and out-of-plane motions. Pairs of force actuator- displacement sensor are collocated at the bottom stage of guy wires in order to implement active tendons. A robust control strategy based on decentralized parallel PPF-DVF (Positive Position Feedback - Direct Velocity Feedback) had been employed. The responses with and without control are studied. The results obtained indicate that the active control strategy presented in this paper is adequate for vibration attenuation of tall guyed masts.

Keywords: *Smart structure,; earthquake ; guyed mast ; vibration; active control ; nonlinear cables.*

1. Introduction:

Guyed masts are tall thin vertical space truss structure supported laterally by high strength guy wires. In general, they are designed to support antennas for telecommunications and broadcasting applications. Warsaw Radio Mast (646.4 m) was the tallest guyed mast in the world before it collapsed in 1991 during guy wire exchange. The tallest existing mast is now KVLV-TV mast (USA) with 628.8 m. These structures are slender, light and flexible which makes them sensitive to vibrations induced by wind, rain or even earthquakes. Vibrations may be reduced using passive, semi-active or active methods. Active control [1] uses a set of actuators and sensors connected by feedback or feed forward loops. Over the past three decades, studies on the guyed masts have focused on the dynamic analysis under wind and seismic excitations. Only a few papers have investigated the vibration control of these flexible structures. Preumont and coworkers [2] proposed an active

tendon control method using pairs of displacement actuators and force sensors collocated at the lower end of strings and an Integral Force Feedback control law. They validated their strategy numerically and experimentally on a small scale mock-up model. Later, Błachowski [3] proposed an algorithm for optimal predictive control of a 100-meter- high mast supported by 6 active cables under wind excitations. Chakhari et al [4] investigated the vibration control of a tall guyed mast using parallel PPF-DVF but they presented a linear model of the structure.

In this paper, the previous model is extended to be nonlinear. The Finite Element model of the tall mast is coupled with a nonlinear cable taking into account the quadratic and cubic nonlinear couplings between in-plane and out-of-plane motions. It investigates the active vibration control of a 292-meter-high guyed mast supported by 18 active cables using pairs of force actuator- displacement sensor collocated at the bottom stage of guy wires and a robust control

strategy based on decentralized parallel PPF-DVF.

2. Modeling of the smart guyed mast

2.1 Nonlinear modelling of an inclined small sag cable

The inclined small sag cable is modelled accounting for general support movement and the quadratic as well as cubic nonlinear couplings between the in-plane and out-of-plane motions. The cable model is written in a local coordinate system as shown in Fig. 9; the local x axis is taken along the chord line and y axis in the horizontal plane, while the z axis is in the gravity plane and perpendicular to the chord line. The cable displacements are separated into three parts: the static, the quasi-static and the dynamic contributions. Assuming a constant stress along the cable span and a small sag, the static profile of an inclined cable can be approximated by a parabola. The dynamic motion on the cable subjected to the excitation of its supports formulated in a discrete manner is obtained using the Ritz method which is based on approaching the solution of variational problem by a finite sum of shape functions. The “separation of variables” method is employed to write the shape functions with two well separated factors (geometric and temporal). After writing the expressions of the kinetic and potential energy, the Lagrange equations are used to derive the equations of motion of the cable (for more details see reference [28]).

2.2 Out-of-plane cable motion

The equation of motion of the transverse out-of-plane displacements of the cable governing the generalized coordinates y_n of the n th out-of-plane mode of vibration can be written as follows:

$$\frac{1}{2}ml \left\{ \ddot{y}_n + 2\xi_{y_n}\omega_{y_n}\dot{y}_n + \frac{n^2\pi^2}{ml^2}(T_0 + T_q + T_d)y_n \right\} =$$

$$F_{y_n} - \frac{ml}{n\pi}(\ddot{v}_a + (-1)^{n+1}\ddot{v}_b)$$

(1)

Where:

m and l are respectively the mass per unit length and the chord length of the cable.

ξ_{y_n} , ω_{y_n} and F_{y_n} are respectively the modal damping, the frequency and the modal component of the external forces applied to the cable, associated to the generalized coordinates y_n of the cable mode n .

T_0 is the static tension in the cable at its equilibrium.

T_q is the tension increment induced by the support movement.

T_d is the tension increment induced by the dynamic motion of the cable; it is responsible for the quadratic and cubic nonlinear couplings between in-plane and out-of-plane motions.

\ddot{v}_a and \ddot{v}_b are respectively the transverse acceleration of the anchorage points a and b according to the axis y .

2.3 In-plane cable motion

The equation of motion describing the in-plane displacements of the cable (perpendicular to its chord line) governing the generalized coordinates z_n of the n th in-plane mode of vibration and accounting for the effect of gravity (

$\gamma = \rho g \cos \theta$), is expressed as follows:

$$\begin{aligned} & \frac{1}{2}ml \left\{ \ddot{z}_n + 2\xi_{z_n} \omega_{z_n} \dot{z}_n + \frac{n^2 \pi^2}{ml^2} (T_0 + T_q + T_d) z_n \right\} = \\ & F_{z_n} - \frac{ml}{n\pi} (\ddot{w}_a + (-1)^{n+1} \ddot{w}_b) \\ & + \frac{ml^2 E_q \gamma}{(\sigma^s)^2} \frac{(1 + (-1)^{n+1})}{(n\pi)^3} (\ddot{u}_b - \ddot{u}_a) - \frac{\gamma A l}{T_0} \frac{(1 + (-1)^{n+1})}{n\pi} T_d \end{aligned} \quad (2)$$

Where E_q is the effective modulus of elasticity (see Appendix), γ is the component of distributed weight along the cable, ρ is the cable density, g is the gravity, θ is the angle of the chord line with respect to the horizontal, A is the cross section of the cable and σ^s is the static stress,.

ξ_{z_n} , ω_{z_n} and F_{z_n} are respectively the modal damping, the frequency and the modal component of the external forces applied to the cable, associated to the generalized coordinates z_n of the cable mode n .

\ddot{w}_a and \ddot{w}_b are respectively the in-plane acceleration of the anchorage points a and b according to the axis z .

\ddot{u}_a and \ddot{u}_b are respectively the longitudinal acceleration of the anchorage points a and b according to the axis y .

2.4 Coupling between the nonlinear cables and the FE model of the guyed mast

As an alternative to a general nonlinear Finite Element approach which would be extremely time consuming, we had developed, using SDTools and Matlab/Simulink, a software which combines a Finite Element model of the linear structure with a nonlinear analytical model of the cables accounting for general support movement and cubic and quadratic couplings between in-plane and out-of-plane motions of the cable. The principle of coupling is that the structure motion imposes displacements to the cables supports and the reactions of the cables supports act like external forces to the structure.

The global equation of motion of the guyed mast including the nonlinear dynamics of the n_c cables and active damping can be written in modal coordinates as follows:

$$\begin{aligned} & \mu_i \{ \ddot{e}_i + 2\xi_i \omega_i \dot{e}_i + \omega_i^2 e_i \} = F_i + \phi_i^T B {}^n F_{cont} \\ & - \phi_i^T \sum_k^n \left[(L_a^{kT}, L_b^{kT}) (F_{u_a}^k, F_{v_a}^k, F_{w_a}^k, F_{u_b}^k, F_{v_b}^k, F_{w_b}^k)^T \right] \end{aligned} \quad (3)$$

Where μ_i , ξ_i , ω_i and F_i are respectively the modal mass, the modal damping, the frequency and the modal component of the external forces applied to the mast without cables, associated to the generalized coordinates e_i of the mast mode i .

ϕ_i represents the mode shapes of the mast without cables. L_a^{kT} and L_b^{kT} are the transformation matrices allowing the passage from the global coordinates of the mast to the local coordinates of the cable k . $F_{u_a}^k, F_{v_a}^k, F_{w_a}^k, F_{u_b}^k, F_{v_b}^k$ and $F_{w_b}^k$ are the reaction forces on the anchorage points (a and b) written in the local coordinates of the cable k . B is the influence matrix relating the local coordinate systems of the active tendons to the global coordinates. ${}^n F_{cont}$ are the control forces of the n active cables:

$${}^n F_{cont} = {}^n H_3(s) ({}^n x_i - {}^n x_j) = [-{}^n g_1 s + \frac{{}^n g_2}{1 + \tau s}] ({}^n x_i - {}^n x_j) \quad (4)$$

Where $({}^n x_i - {}^n x_j)$ are the relative displacements of the extremities (i and j) of the cables projected on the chord lines, s is Laplace variable τ is a design parameter; ${}^n H_3(s)$ is the feedback controller law of the proposed concept and the controller gains ${}^n g_1$ and ${}^n g_2$ can be tuned to get optimal damping on the target modes. The block diagram of the proposed control system is given in Figure 1.

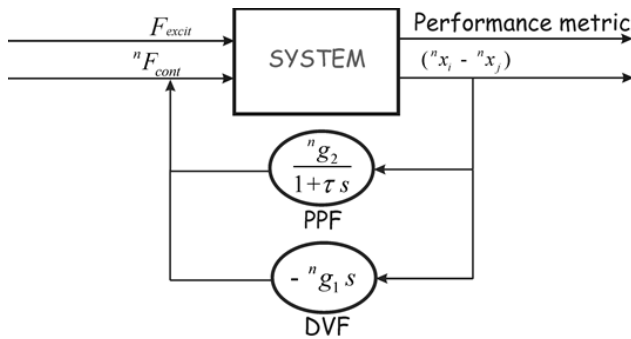


Figure (1) Block diagram of the proposed control system.

3. Numerical example:

The tall guyed mast shown in Figure 2 has a height of 292.8 m and is made up of 297 nodes, 900 bars and 18 cables. It's a three legged pinned base mast, laterally supported at six levels by a set of three pre-stressed cables. The mast has a triangular cross-section (see Figure 3c) and it is made up of fifty identical panels, each having a width and length of 3.05 m. A typical panel consisting of nine pinned end members is shown in Figure 3d. The bars are steel solid rounds. The diameters of the struts, diagonals and chords are respectively 5.1 cm , 7.7 and 10.2 cm solid rounds. The mast is laterally supported at six levels by a set of three 2.54 cm diameter cables which have a breaking tension of 54268 daN. The pretension of the cables is equal to 12% of the breaking tension. The natural damping of the structure is equal to 2% for all modes [6] and aerodynamic damping is not considered because earthquake loads are assumed to occur under still air conditions and mast members are bolted, For more details about the mast please see [7].

4. Results and Discussion

The active damping Active damping is added to the cable structure by using pairs of collocated displacement actuator and force sensor located on all cables and decentralized Integral force feed

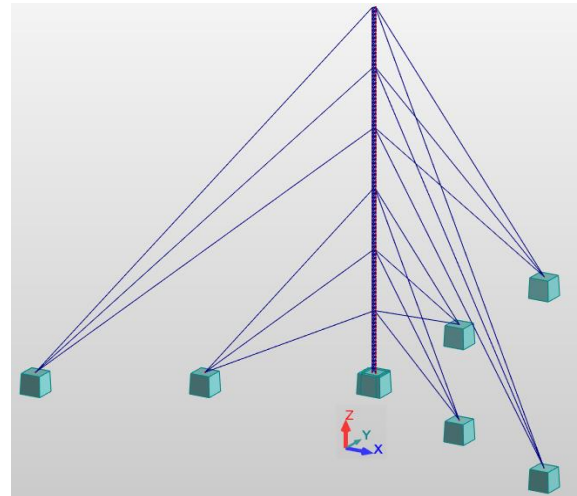


Figure (2) The 3D FE model of the guyed mast.

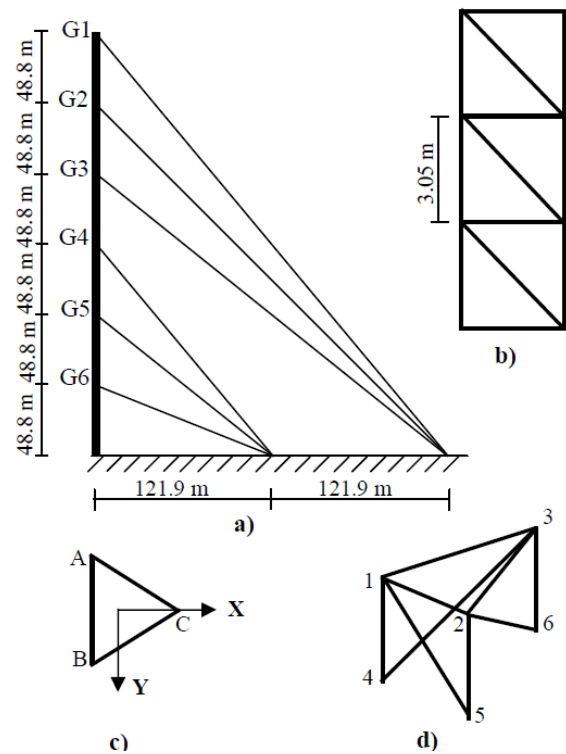


Figure (2) The guyed mast [5]: a) profile; b) elevation; c) cross-section; d) typical mast panel.

back control law. The optimal gain of the compensator is determined using root locus technique. The bridge is excited horizontally by tow different earthquakes records:

-EL CENTRO: the N-S component recorded at

the Imperial Valley Irrigation District substation in El Centro, California, during the earthquake of May 18th, 1940;

-MEXICO: the N-S component recorded at Mexico city in 1985.

Figure 4 shows the evolution in time of the horizontal displacement x of the top node for the cases with and without control. The top horizontal displacement X is attractively damped for ELCENTRO and MEXICO earthquakes. All cables are kept away from the plasticity zone and bars are prevented from buckling. Results revealed that the proposed active control strategy is adequate for vibration attenuation of tall guyed masts. All the cables are used as active tendons which lead to a high cost of the active control strategy. That's why the number of active tendons must be optimized.

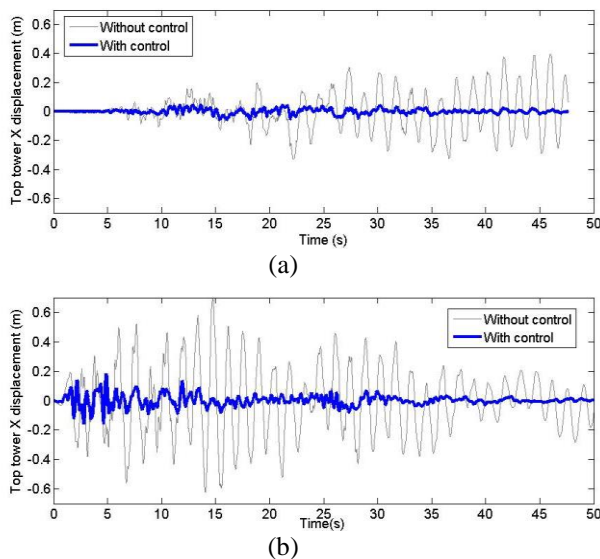


Figure (4) Evolution in time of the horizontal displacement of the top node(G1) under seismic excitations: a) MEXICO b) ELCENTRO.

5 Conclusions and future works

The dynamic analysis of a smart guyed mast with and without active damping has been investigated. A non-linear model of the guyed mast is presented. The Finite Element model of the tall mast is coupled with a nonlinear cable

taking into account the quadratic and cubic nonlinear couplings between in-plane and out-of-plane motions. The active damping is provided through the use of pairs of force actuators and displacement sensors located on each active cable. A robust control strategy based on decentralized parallel PPF-DVF is employed. The horizontal displacements are attractively damped, all cables are kept away from the plasticity zone and bars are prevented from buckling. In this study the control cost will be high because all active tendons were used for the control. An optimization procedure should be implemented to reduce the number of active cables in order to reduce the high cost of energy needed for active control. Also Semi-active control using Magneto-Rheological dampers could be used to reduce the high cost of the active control.

References

- [1] S. Korkmaz, A review of active structural control: challenges for engineering informatics, *Comp. & Struct.*, 89, (2011), 2113–2132.
- [2] A. Preumont, F. Bossens, Active tendon control of vibration of truss structures: Theory and experiments, *Journal of Intelligent Materials Systems and Structures*, 2-11, (2000), 91-99.
- [3] B. Blachowski, Model based predictive control of guyed mast vibration, *Journal of theoretical and applied mechanics*, 45 (2007), 405-423.
- [4] M. H. El Ouni, N. Ben Kahla, Numerical study of the active tendon control of a cable-Stayed bridge in a construction Phase. *Shock and Vibration* (2014), Article ID 937541.
- [5] M. Chakhari, M. H. El Ouni, N. Belhaj Ali, N. Ben Kahla, Active vibration control of a tall guyed mast under seismic excitation. *The 6th International Congress Design and Modeling of Mechanical Systems CMSM'2015*, 25-27 March, Tunisia.

13th Annual Research Day

Organised by the Deanship of Scientific Research in Collaboration with the College of Engineering
Research Centre
2nd April 2018

[6] T.H. Kewaisy Nonlinear Dynamic Interaction
between Cables and
Mast of Guyed Tower. Systems
Subjected To Wind-Induced Forces. PhD,
Faculty of Texas Tech University, USA.
(2001)

[7] N. Ben Kahla, M.H. El Ouni, Response of tall
guyed masts to earthquake motion.
International Conference on Applied
Mechanics and Modeling, 2006, Hamamet,
Tunisia.

Epileptic Seizure Prediction Methods Based on EEG Signals

Mohammed Sayeeduddin Habeeb¹ Mohammed Abdul Muqeet¹ Zeeshan Ahmad¹

¹Department of Electrical Engineering, College of Engineering, King Khalid University,
PO Box 394, Abha 61411, KSA.

E-mail address: mabdulmuqeet@kku.edu.sa

Abstract: According to a study in 2010, epilepsy is a major neurological disorder affecting more than fifty million persons throughout the world. The incidence of epilepsy is over 6.54 for every thousand individuals in the Kingdom of Saudi Arabia. Epileptic seizures are fatal and may even lead to death. Thus, effective methods for seizure detection play a prominent role in epilepsy management. Various patient-specific seizure detection methods have been developed since the second half of the 1990s. The false detection probability of such methods is found to be very low. An increased number of false detections will considerably reduce the utility of seizure detection systems. A major disadvantage of patient-specific methods is that they have low cross-patient utility. Another major challenge is to develop systems that can detect seizures as early as possible with acceptable rates of false detection. Novel signal processing and estimation/detection techniques can be used to extract significant features and parameters from electroencephalogram (EEG) signals. The extracted information could be used to develop seizure detection and monitoring systems with very low false alarm rates and early detection capability. In this research, we undertake a survey of some of the recent important methods proposed for seizure detection.

Keywords: *Electroencephalography (EEG), Epilepsy, Epileptic seizures, seizure detection, false detection, monitoring systems, false alarm.*

1. Introduction:

Epileptic seizures are caused due to transient and unexpected electrical disturbance of the brain. According to a report by the International League Against Epilepsy (ILAE) commission, epilepsy affects more than 65 million people throughout the world [1]. Electroencephalogram (EEG) signals contain rich information on the electrical activity generated by the nerve cells in the cerebral cortex. These signals are widely utilized for clinically assessing the brain activities. The detection of signal discharges in the EEG is an important component in the diagnosis of epilepsy. To improve the quality of life of epileptic patients, it is very important to develop automated techniques for detecting seizure. An effective seizure prediction approach would improve the quality of life of the patients. A warning system to detect seizures of patients is very important to avoid injury or death, which may happen due to the involuntary physiological responses occurring during seizure.

There are different methods for seizure detection investigation such as electroencephalogram (EEG) [2], electrocardiography (ECG) [3], accelerometer [4-5] or a combination of these methods. However, EEG is considered the most common and reliable modality for epilepsy diagnosis and analysis. Large number of brain information which is valuable for seizure detection is provided by EEG [2]. The main steps carried out for EEG-based seizure detection are: (1) pre-processing, (2) feature extraction and (3) classification. For automatic analysis of EEG signals, machine learning techniques and signal processing also play an important role.

EEG is classified in two types i.e., intracranial EEG (iEEG) and scalp EEG (sEEG). In the iEEG, electrodes are placed directly on the exposed surface of the brain to record the electrical signal, where as in sEEG, electrodes are placed on the scalp area based upon certain placement specifications, to record electrical signals from brain. Seizure prediction is based on

the hypothesis that there exists a transition state (preictal) between the interictal (normal state) and the ictal state (seizure) [6].

A seizure detection algorithm is proposed using recurrent neural network in both time and frequency domain in [7]. EEG signals are segmented and the selected segments are analyzed using time-frequency methods. Several features representing the energy distribution in the time-frequency plane are extracted. These features were classified using artificial neural networks [8]. In [9], seizure prediction performance of techniques like L1-regularized logistic regression, convolution networks, and support vector machines are compared. Hamid Vavadi et al. separated EEG signals as alpha, beta, theta, gamma and delta sub-bands by using wavelet transform in [10]. They calculated approximate entropies for EEG and sub-bands and classified these features using T-test.

A patient-specific algorithm for seizure prediction is proposed in [11]. This method extracted spectral power in 9 bands from each of 6 electrodes. They achieved sensitivity of 77.8% (35 of 45 seizures) using Cost-Sensitive Support Vector Machines. Back propagation neural networks are implemented for classification in [12]. A detection accuracy of 94.69% is achieved using multilayer perceptrons for classification and wavelet functions and wavelet threshold for feature extraction [12].

In the work outlined in [13], a comprehensive study on state-of-the-art methods for seizure detection is presented and a reliable and practical epilepsy detection method that can balance computational complexity and detection accuracy is proposed. The combination of complexity analysis and spectrum analysis on an EEG that can perform robust evaluations on the collected data is presented. Details about the versatile signal processing and analysis framework for Electroencephalogram (EEG) signals is presented in [14]. In this framework the signals were decomposed into the frequency sub-bands using

Discrete Wavelet Transform (DWT) and a set of statistical features were extracted from the sub-bands to represent the distribution of wavelet coefficients. Principal components analysis (PCA), independent components analysis (ICA) and linear discriminant analysis (LDA) are used to reduce the dimension of data. Then these features were used as an input to a support vector machine (SVM) with two discrete outputs: epileptic seizure or not. A machine learning approach to constructing patient-specific classifiers that can detect the onset of an epileptic seizure through analysis of the scalp EEG is proposed in [15].

A patient-specific classification algorithm is proposed to distinguish between preictal and interictal features extracted from EEG recordings in [16]. It demonstrates that the classifier based on a Cost-Sensitive Support Vector Machine (CSVM) can distinguish preictal from interictal with a high degree of sensitivity and specificity, when applied to linear features of power spectrum in 9 different frequency bands [16]. An automated system of epileptic seizure prediction based upon Hilbert Huang transform and Bayesian classifiers was developed in [17]. This system predicts seizure with a sensitivity of 96.5%.

2. A Comparative Study on the EEG Signal Feature Extraction and Epileptic Seizure Classification:

In this section we compare relevant techniques for extracting various features from EEG signal which are useful for effectively detecting/classifying the epileptic seizures. In the upcoming section, we first outline some feature extraction models that are used in the recent literature.

2.1 Feature Extraction Models

Since the EEG signals possess inherent random nature, recent techniques that are available in the literature are making use of different feature extraction techniques for

improving the classification/detection accuracy. The features will help to reduce the computational complexity as well as the false alarm probabilities of the techniques, thereby improving the reliability. The feature vector extracted from the scalp EEG windows is a global spatial average across EEG channels. Recent techniques use various features in transform domain as well as the information theory perspective. In this paper we list a few techniques that are common in many literatures.

2.1.1 Global Cross Frequency Coupling (GCFC) Index

Cross frequency coupling index is a feature which is extracted from the wavelet coefficient. It has a close relationship with the average cross information content in between the higher and lower frequency content of the signal. The first procedure to obtain the GCFC is to obtain the continuous wavelet transform (CWT). The CWT can capture both the spectral and temporal characteristics of a signal effectively. Time-frequency spectrograms are obtained by applying a CWT. It is a well-known fact that Morlet Wavelet acts as a better choice wavelet decomposition due to its Gaussian nature. A complex Morlet wavelet, on the EEG time-series recordings $x(t)$, can be applied as

$$W(s, t) = \int x(t) \phi_{s,t}^*(t) dt \quad (1)$$

Where $\phi_{s,t}^*(t)$ is the Morlet Wavelet. In [18], a Morlet CWT with bandwidth of 6Hz is used to obtain spectrograms over 2 frequency ranges for each 2s epoch: a low frequency range denoted $f_L \in (1;1.1;1.2;.....1.10)Hz$ and a high frequency range denoted $f_H \in (20;21;22;....150)Hz$. The low frequency range was selected to cover the delta and theta ranges while the high frequency range was cut off at 150 Hz to encompass the maximal extent of the 3 dB below-maximum of the average CFC values, whose computation is discussed in [18,19]. The CWTs were computed with a buffer on either side of the epoch to mitigate the end effects introduced by the CWT

filtering operation at the low frequency scales. Note that the Gaussian nature of the Morlet wavelet provides a smooth windowing which will reduce the adverse effects due to windowing. AGCFC measure can now be computed from the complex wavelet coefficients of f_ϕ and f_A for each seizure detection which was found to be of high index value for false alarms [18].

2.1.2 Empirical mode decomposition (EMD)

Another well-known technique is the Empirical mode decomposition (EMD) which is a data-dependent approach suitable for decomposition of a nonlinear and non-stationary signal into symmetric, amplitude and frequency modulated (AM-FM) components known as intrinsic mode functions (IMFs). The IMFs are obtained from the EMD method to satisfy two conditions as explained in [20]. Namely:

- (i) Number of maxima and number of minima should have difference of at most one.
- (ii) The mean value of two envelopes, one formed by connecting local maxima and another formed by connecting local minima of the signal should be zero.

IMFs can be derived from a signal $s(t)$ using iterative process known as sifting process which is expressed as [20].

$$s(t) = \sum_{i=1}^M IMF_i(t) + R(t) \quad (2)$$

Where M is number of extracted IMFs and $R(t)$ is the residual. Once the IMF is obtained, it is defined as $IMF_1(t) = d(t)$. Now a residual signal is obtained as $g(t) = s(t) - IMF_1(t)$, which serves as the new signal to extract the next IMF by applying sifting process. The sifting process is repeated until the residual obtained becomes monotonic function from which, further no more IMF can be extracted. This decomposition method is adaptive, and therefore, highly efficient. Since the decomposition is based on the local characteristic time scale of the data, it is applicable to nonlinear and non-stationary

processes [20]. The procedure is detailed in section 2.2 of [20].

2.1.3 Independent Component Analysis (ICA) for Dimensionality Reduction and Feature Extraction

ICA is a feature extraction method that transform multivariate random signal into a signal having components that are mutually independent. The ICA is also used for dimensionality reduction of the signal. Independent components can be extracted from the mixed signals by using this method. In this manner, the information carried by one component cannot be inferred from the others. Statistically this means that joint probability of independent quantities is obtained as the product of the probability of each of them. With an assumption of absence of noise, the multivariate density function can be written as [21]

$$p(x(t)) = \prod_{i=1}^C p(x_i(t)) \quad (3)$$

Let the observed signal be the combination of different components, the source signals can be separated by using the suitable decomposition technique because of the independent property of the observed signal as mentioned in section 2.1.1, 2.1.2, 2.1.3. In EEG feature extraction the samples of EEG were recorded at sampling frequency f_s . The independent components were identified and the remaining components being correlated with the other ones. In [22], ICA has been used for seizure classification/detection. The Alarms detected were found to be of low index value due to absence of noise figure.

2.2 Classification Methods

A great number of classification methods are used to detect normal, ictal and preictal stages. In this paper we compare the performance of two classification/detection techniques. The first technique used was multi-layer perceptron neural network (MLPNN) for classification.

However, the second one is a patient-specific detection algorithm (PSDA) [28].

2.2.1 Classification Technique using the Multi-Layer Perceptron Neural Network (MLPNN):

MLPNN is a neural network with multiple layers. Except the input layer, each layer consist of a user non-linear activation function. In [23-25], the MLPNN with three layers: input, hidden and output layer, each layer contains at least one neuron. There is a non-linear mapping between input space and output space in MLPNN that determines the output and compares it with the desired output. Then it propagates error signal and adjust the connection weights correspondingly [23-25]. The architecture of MLPNN with hidden layer is shown in **Figure 1**.

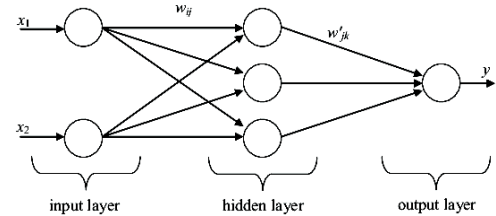


Figure 1. Architecture of MLPNN with one hidden layer [25]

In the MLPNN, each neuron j in the hidden layer sums its input signals x_i after multiplying them by the strengths of the respective connection weights w_{ji} and computes its output y_j as a function of the sum

$$y = f\left(\sum w_{ji}x_i\right) \quad (4)$$

Where f is the activation function essential to transform the weighted sum of all signals impinging onto a neuron. The input to the neural network can be any feature mentioned in the section 2.1.1, 2.1.2 and 2.1.3. The statistical measures used to evaluate the performance were:

- True positives (TP): the number of seizures identified by the automated system and by the EEG experts.
- False positives (FP): the events identified as seizures by the automated system but not by the EEG experts.

- False negatives (FN): the events identified as seizures by the experts but missed by the automated system.

The sensitivity value (true positive, same positive result as the diagnosis of expert neurologists) was calculated by dividing the total of diagnosis numbers to total diagnosis numbers that are stated by the expert neurologists. Sensitivity, also called the true positive ratio, is calculated by the equation [26].

$$\text{Sensitivity} = \text{TPR} = \frac{TP}{TP + FN} * 100\% \quad (5)$$

Specificity value is calculated by dividing the total of diagnosis numbers to total diagnosis numbers that are stated by the expert neurologists. Specificity, also called the true negative ratio, is calculated by the equation [26].

$$\text{Specificity} = \text{TNR} = \frac{TN}{TN + FP} * 100\% \quad (6)$$

2.2.2 Patient-Specific Detection Algorithm (PSDA):

PSDA is one of the efficient techniques mentioned in [28]. In the processing stages of the patient-specific detector, the detector passes L -second epochs from each of N EEG channels through the filter bank. In turn, the filter bank computes for each channel M features that correspond to the energies within M frequency bands. The M features extracted from each of the N channels are then concatenated to form a MN element vector X_T that automatically captures the spectral and spatial relations between channels. Next, the W feature vectors X_T , X_{T-L} , and $X_{T-(W-1)L}$ are concatenated to form the feature vector X_T . This vector, which contains $W \times M \times N$ elements, automatically captures the time evolution of spectral and spatial relations among the input EEG channels.

Finally, the feature vector X_T is assigned to the seizure or non-seizure class using a two-class support-vector machine classifier with cost factor J , radial basis kernel with parameter γ , and trade-off between classification margin and error C . The detector declares a seizure after one

feature vector X_T is assigned to the seizure class based on specificity (TNR) and sensitivity (TPR) [28]. A major disadvantage of patient-specific methods is that they have low cross-patient utility. Another major challenge is to develop systems that can detect seizures as early as possible with acceptable rates of false detection [27].

3. Results and Discussion

In this study, we consider a scenario with a set 15 patients including two subsets, epileptic seizure and seizure free. The sampling rate of EEG signal is 173.61Hz. The subsets include the EEG signals recorded using surface EEG recordings from patients employing standard international 10–20 electrode placement scheme.

In Figure 2, we provide a comparative study of the false detection rate with different feature extraction techniques for epileptic seizures. It can be seen that ICA is having lower false alarm probability when compared to other feature extraction methods. The patient-specific detector shows good specificity when compared to other technique. It does not declare the bursts occurring nature in the EEG signals as false detections because it has learnt, through training that these are features of the patient's baseline activity. On the other hand, the MLPNN detector declare many of these burst as seizure events even though they have spatial and spectral characteristics that differ significantly from those of the actual seizure.

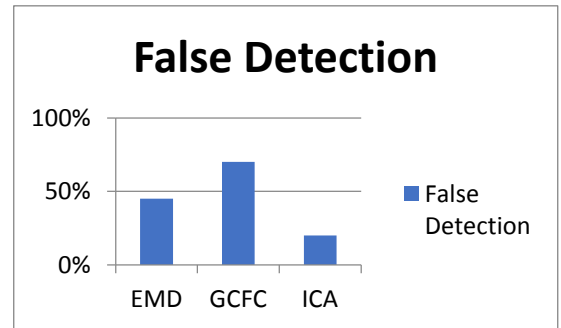


Figure 2. False Alarm detection [29]

From Figure 3 it is found that, the MLPNN algorithm failed to detect many of the test seizures. A possible explanation for MLPNN poor sensitivity is the overlap of eye-blinks on the frontal channels with seizure discharges on the temporal channels. Patient specific algorithms are generally designed to classify EEG seizures containing rapid eye-blinks as corrupt and unlikely to contain a seizure with a better sensitivity.

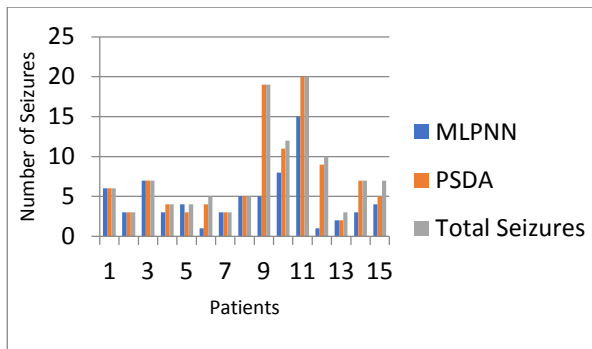


Figure 3. Comparison of Sensitivity [29]

In Figure 4, we compare the specificity of MLPNN and patient-specific algorithms. It is found that both techniques were successful in detecting the onset of seizures. However, the MLPNN algorithm exhibited poor specificity because it declared false detections whenever the rhythmic activity is commonly observed within the recorded EEG of the patient [29].

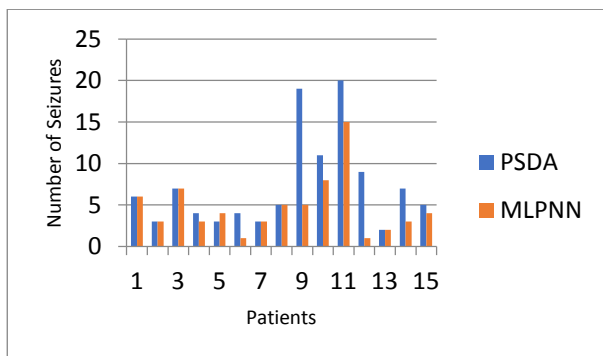


Figure 4. Comparison of Specificity [29]

4. Conclusions:

Epilepsy is a major neurological disorder affecting more than fifty million persons throughout the world. Recent studies reveal that the incidence of epilepsy is over 6.54 for every thousand individuals in the Kingdom of Saudi Arabia. Epileptic seizures are fatal and may even lead to death. Hence effective techniques for seizure detection play a prominent role in epilepsy management. Various techniques have been proposed in the literature to address this issue. In this paper, we have compared the performance of two techniques. One is the PSDA and the other is the technique which makes use of the MLPNN for the classification/detection.

The false detection probability of PSDA is found to be very low. A major disadvantage of patient-specific methods is that they have low cross-patient utility. Another major challenge is to develop systems that can detect seizures as early as possible with acceptable rates of false detection. It is found that both techniques were successful in detecting the onset of seizures. However, the MLPNN algorithm exhibited poor specificity and sensitivity. The study reveals that there is great demand of novel low complexity real time signal processing techniques for epileptic seizure detection.

Acknowledgement

We are thankful to King Khalid University for encouraging in presenting our contribution.

References

- [1]. D.J. Thurman et al; ILAE Commission on, Epidemiology, "Standards for epidemiologic studies and surveillance of epilepsy," *Epilepsia*, Vol. 52, supplement 7, pp. 2–26, 2011.
- [2]. L. Orosco, A.G. Correa, E. Laciari, "Review: A Survey of performance and techniques for automatic epilepsy detection," *J. Med. Biol. Eng.*, Vol. 33, No. 6, pp. 526-537, 2013.

13th Annual Research Day

Organised by the Deanship of Scientific Research in Collaboration with the College of Engineering
Research Centre
2nd April 2018

- [3]. M.B. Malarvili, Mesbah M., "Newborn seizure detection based on heart rate variability," *IEEE Trans Biomed Eng*, Vol. 56, pp. 2594–603, 2009.
- [4]. A. Dalton, Patel S, Chowdhury AR, Welsh M, Pang T, Schachter S, et al., "Development of a body sensor network to detect motor patterns of epileptic seizures," *IEEE Trans Biomed Eng*, Vol. 59, pp. 3204–11, 2012.
- [5]. S. Beniczky, Polster T, Kjaer TW, Hjalgrim H, "Detection of generalized tonic-clonic seizures by a wireless wrist accelerometer: a prospective, multicenter study," *Epilepsia*, Vol. 54, No. 4, pp. e58–61, 2013.
- [6]. Turkey N, Alotaiby, Saleh A, Alshebeili, Faisal M, Alotaibi and Saud R, Alrshoud, "Epileptic Seizure Prediction Using CSP and LDA for Scalp EEG Signals", Volume 2017 (2017), Article ID 1240323, 11 pages.
- [7]. Srinivasan V, Eswaran C, Sriraam N. Artificial neural network based epileptic detection using time-domain and frequency-domain features. *J Med Sys* 2005; 29: 647-660.
- [8]. Tzalles A Z, Tsipouras M G, Fotiadis D I. Automatic seizure detection based on time-frequency Analysis and artificial neural networks. *Comput Intel Neurosci* 2007; 2007: 1-13.
- [9]. Mirowski PW, LeCun Y, Madhavan D, Kuzniecky R. Comparing SVM and convolutional networks for epileptic seizure prediction from intracranial EEG. *Iee Mach L Sig Proc* 2008; 244-249.
- [10]. Vavadi H, Ayatollahi A, Mirzaei A. A wavelet-approximate entropy method for epileptic activity detection from EEG and its sub-bands. *J. Biomed Sci Eng* 2010; 3:1182-1189.
- [11]. Netoff T, Park Y, Parhi K. Seizure prediction using cost-sensitive support vector machine. *2009 Annual International Conf Eng Med Biol Soc* 2009; 3322-3325.
- [12]. Abibullaev B, Seo HD, Kim MS. Epileptic spike detection using continuous wavelet transforms and artificial neural networks. *World Sci Publ Comp* 2010; 8: 33-48.
- [13]. Liang SF, Wang HC, Chang WL. Combination of EEG complexity and spectral analysis for epilepsy diagnosis and seizure detection. *Eurasip J Adv Sig Proc* 2010; 2010: 1-15.
- [14]. Subasi AH, Gursoy ML. EEG signal classification using PCA, ICA, LDA and support vector machines *Exp Sys Appl* 2010; 37: 8659-8666
- [15]. Shoeb A, Gutttag J. Application of machine learning to epileptic seizure detection. *Int Conf Mach Learn* 2010; 975-982.
- [16]. Park Y, Luo L, Parhi KK, Netoff T. Seizure prediction with spectral power of EEG using cost-sensitive support vector machines. *Epilepsia* 2011; 52: 1761-1770.
- [17]. Ozdemir N, Yildirim E. Patient specific seizure prediction system using hilbert spectrum and bayesian networks classifiers. *Hindawi Publ Corp* 2014; 2014:1-10.
- [18]. E. M. Gerber et al, "Non-Sinusoidal Activity Can Produce Cross-Frequency Coupling in Cortical Signals in the Absence of Functional Interaction between Neural Sources", *PLoS One*, vol. 11, no. 12, Dec 2016.
- [19]. J. Aru et al, "Untangling cross-frequency coupling in neuroscience," *Curr. Op. in Neurobiology*, vol. 31, pp. 51-61, 2015.
- [20]. Huang, N. E., Shen, Z., Long, S. R., Wu, M. C., Shih, H. H., Zheng, Q., et al. (1998). The empirical mode decomposition and the Hilbert spectrum for nonlinear and nonstationary time series analysis. *Proceedings of the Royal Society of London. Series A: Mathematical, Physical and Engineering Sciences*, 454, 903–995.

13th Annual Research Day

Organised by the Deanship of Scientific Research in Collaboration with the College of Engineering
Research Centre
2nd April 2018

- [21]. Cao, L. J., Chua, K. S., Chong, W. K., Lee, H. P., &Gu, Q. M. (2003). A comparison of PCA, KPCA and ICA for dimensionality reduction in support vector machine. *Neurocomputing*, 55, 321-336.
- [22]. M. Ungureanu, C. Bigan, R. Strungaru, V. Lazarescu. "Independent Component Analysis Applied in Biomedical Signal Processing". *MEASUREMENT SCIENCE REVIEW*, Volume 4, Section 2, 2004
- [23]. Meyer-Baese A. Pattern recognition for medical imaging. California Elsevier AcadPres 2004.
- [24]. Haykin S. Neural networks: A comprehensive foundation. New Jersey Pren H 1999.
- [25]. Zurada JM. Introduction to artificial neural systems. St Paul West Publ Comp 1992
- [26]. AbdulhamitSubasi."EEG signal classification using wavelet feature extraction and a mixture of expert model".Volume 32, Issue 4, May 2007, Pages 1084-1093
- [27]. El-Naqa I, Yang Y, Wernick MN, Galatsanos NP, Nishikawa RM. A support vector machine approach for detection of microcalcifications. *IeeeTrans Med Imag* 2002; 21: 1552-1563.
- [28]. Abe S. patient specific detection algorithm for Pattern Classification. New York Sprin 2005.
- [29]. International Database www.physionet.org

Development of Corrosion Protective Coatings for Carbon Steel Using Polyaniline Modified Ferrochrome Slag Nanocomposite materials

Mohammad Ilyas Khan and Abubakr Mustafa

Department of Chemical Engineering, College of Engineering, King Khalid University,
PO Box 394, Abha 61411 KSA.
E-mail address: mkaan@kku.edu.sa

Abstract: The corrosion protection ability of waste slag material from a ferrochrome industry was investigated. As a nanomaterial, this compound was used as received as well as a composite with polyaniline. The nanocomposites were prepared by in-situ polymerization technique. The prepared materials were characterized by FTIR, XRD and SEM. The anticorrosion performance of waste slag nanomaterial, polyaniline and a nanocomposite of this material with polyaniline was evaluated by incorporating these pigments in a commercial epoxy paint system. The prepared coatings were investigated for their anticorrosion ability by exposure to corrosive media in salt spray chamber as well as the electrochemical potentiodynamic polarization (PDP) and electrochemical impedance spectroscopy (EIS) methods. The results show that the nanocomposite pigments performed better, followed by the ferrochrome nanomaterial and polyaniline respectively. Modification of the nanomaterial (raw material) with polyaniline has significantly improved the anticorrosion properties of the paint system used.

Keywords: carbon steel, corrosion inhibition, ferrochrome slag, electrochemical, polyaniline

1. Introduction:

Corrosion is a natural phenomenon and has a significant impact on the socio-economic aspects of life. Carbon steel is commonly used as a construction material in various applications such as in construction, transportation, pipeline etc. However, the life span of carbon steel like many other materials is limited primarily due to corrosion. To overcome this issue, the use of various types of commercially available anticorrosion paints and inhibitors are being introduced into the market. However, researchers and scientists are always on the outlook for more efficient, cheaper and environmental friendly coatings and inhibitors. Among the conductive polymers, polyaniline is probably the one of the oldest synthetic conductive polymer [Prokeš et. al 2001]. It is the green protonated emeraldine base that exhibits the conductive form of polyaniline [Stejskal et. al 1996]. The exact mechanism of protection offered by conductive polymers is still not clear but one of the most commonly accepted

mechanism is the surface ennobling and anodic passivation of the steel surface induced by the inherent redox capability of conductive polymers. Another recently proposed mechanism of protection is the so called self-healing mechanism in which doping the conductive polymers with suitable anionic inhibitors can act as a reservoir of corrosion inhibitors [Niratiwongkorn 2016].

Protective coatings are commonly used to protect steel structures against corrosion. The use of organic-inorganic composites or hybrid materials have proven to be effective because it combines the various attractive properties such as flexibility, ductility and dielectric of organic as well as the desirable properties such as thermal stability, strength and hardness etc. of the inorganic constituent [Sulaiman 2015]. The use of conductive polymers modified inorganic nanoparticles are also known to improve the physical properties of materials [Kalendova 2017]. These types of modified pigments are

capable of providing the highest level of protection against corrosion. The use of polyaniline modified anticorrosive pigments include; polyaniline-SiO₂ composite [Al-Dulaimi et. al, 2011 and Ruhi et.al, 2014], polyaniline-Fe₂O₃ composite coatings [Sathiyarayanan et.al, 2007], polyaniline-ZnO-epoxy composite coatings [Mustafaei 2014], polyaniline-TiO₂ composite containing coatings [Sathiyarayanan, 2007], polyaniline glass flake composite coatings [Sathiyarayanan, 2008] and various other inorganic pigments as corrosion inhibitors [Kalendova 2008]. The current research is focusing on investigating the use of waste slag material from ferrochrome industry as corrosion inhibitor for carbon steel. The surface of these pigments will be modified by treatment with polyaniline. The anti-corrosion efficiency will be evaluated both for the untreated pigments and for the pigments modified with polyaniline. The use of this material as a corrosion inhibitor is scarce in literature and therefore, is the focus of the current research.

2. Materials and Methods:

2.1 Materials

The ferrochrome slag waste material was taken from a steel manufacturing facility in Oman. Hydrochloride and ammonium peroxy disulphate (APS) was purchased from Sigma Aldrich and used without any modifications.

2.2 Preparation of PANI-ferrochrome slag nanomaterial

Aniline hydrochloride (2.59g) was dissolved in distilled water in a 50 ml volumetric flask. Also, ammonium peroxy disulphate (5.71g) was dissolved in a 50 ml volumetric flask. Both solutions were kept in an ice-cold bath for 1 hour. Pre-cooled APS solution was added dropwise to the aniline hydrochloride solution while

constantly stirred using a magnetic stirrer. The composite material with polyaniline was prepared in similar manner except that the nanoferrochrome material was added during mixing and polymerization. After the APS solution completely added, the stirring was continued for another two hours to allow complete polymerization. The mixture was then filtered, and filtrate was washed several times with distilled water to try neutralizing the pH of the filtrate. Following filtration, the solid filtrate was dried in the oven at 60⁰ C for 24 hours. The dried medium was then grounded in mortar and sieved to size of less than 126 µm.

2.3 Preparation of the coating formulations

Epoxy zinc rich phosphate primer was used. The nanomaterials incorporated into the primer was 1% by weight. Three nanomaterials namely polyaniline (sample A), untreated slag material (sample B), polyaniline-slag material composite (C) were tested. These materials were blended into the primer using commercial blender in a paint manufacturing facility. The blended coatings were applied on carbon steel coupons using spray coating technique. The coated samples were allowed to cure for 7 days and then subjected to salt spray testing.

2.4 Characterization of the nanomaterials

The structure of the synthesized polymer and composites was characterized by means of an IR spectrometry (TA instrument with universal ATR attachment, range 400–4000 cm⁻¹).. As for the X-ray Diffractometer (Rigaku, Japan) using Cu K α radiation ($\lambda = 0.15406 \text{ \AA}$) with operating voltage of 40 kV and current of 30 mA was employed to examine the phase and crystal structure identification in a 2 θ range from 10 to 80°. Surface morphologies of synthesized polymer and composite samples were analyzed using Scanning electron microscopy (JSM-6360,

13th Annual Research Day

Organised by the Deanship of Scientific Research in Collaboration with the College of Engineering
Research Centre
2nd April 2018

JEOL) at an acceleration voltage of 20 kV and irradiation current of 10 μ A.

2.5 Characterization of the coated steel panels

2.5.1 Dry film thickness measurements

Dry film thickness measurements were carried out according to ISO 19840 using commercial coating thickness meter. Thickness measurements were conducted at five different points and the average values are used in the final evaluation. The results are presented in Table 1.

	A (PANI)	B (NANOMATERIAL)	C (NANOCOMPOSITE)
1	38	39	48
2	44	43	55
3	28	37	39
4	31	41	48
5	41	35	34
AVERAGE	36	39	45

Table 1: Dry film thickness of the coated steel panels

2.6 Exposure in Salt Spray Chamber

Test specimens were subjected to salt spray testing conditions in accordance with ASTM B117. Additional specimens were tested for corrosion by direct immersion in 3.5% sodium chloride solution in accordance with ASTM B895. Salt spray testing method provides a controlled corrosive environment that has been utilized to produce relative corrosion resistance information for the test samples exposed in the test chamber.

2.7 Electrochemical testing

Electrochemical corrosion tests were conducted using the Gamry Potentiostat Reference 600 together with Echem analyst software to analyze the experimental data. Conventional three electrode assembly was used to perform the electrochemical experiments in which MS specimen with exposure area of 1cm² acts as working electrode, silver/silver chloride

(Ag/AgCl) electrode and graphite rod act as reference and counter electrode respectively. MS specimens were immersed for about 1 h to check the steady-state prior to each measurement. Potentiodynamic polarization tests were performed at the potential of ± 250 mV from open circuit potential (OCP) at a scan rate of 1 mVs⁻¹. Electrochemical impedance spectroscopic tests were monitored over the frequency range of 10⁴ to 10 mHz, with acquirement of 10 points per decade and a signal amplitude of 10 mV at OCP. All measurements were repeated at least three times and good reproducibility of the results was observed.

3. Results and Discussion

3.1 FTIR Analysis

The synthesized nanomaterials were characterized by FTIR as presented in Figure 1. The nanocomposite spectra show the typical PANI spectra with some features of nanomaterial confirming the formation of the nanocomposite material. The spectral bands at around 1242 and 1296 is that of C-N bond, C=N at around 1561, C=C is at around 1474 and C-H is at around 1110 cm⁻¹.

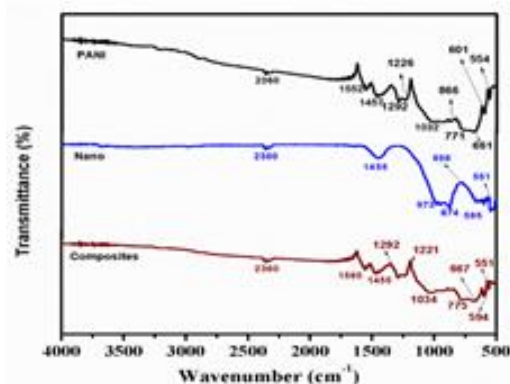


Figure 1: IR spectra of synthesized PANI and its nanocomposite

3.2 XRD Analysis

The XRD data for all the three samples is presented in Figure 2. The XRD pattern obtained for PANI is similar to the one reported by [Sathayanaranan 2007 and Mustafai et. al 2014]. The two main Bragg diffraction peaks of PANI appeared at angles of $2\theta = 19.3$ and $2\theta = 25.7$ in the spectrum as reported by [9]. The presence of the rigid aromatic backbone of PANI makes it a semi-crystalline polymer [L. Shi et. Al. 2009]. The peaks of the nanomaterial (raw material) has become smaller by the addition of PANI as shown by the spectra of the nanocomposite that confirms the formation of the organic-inorganic nanocomposites.

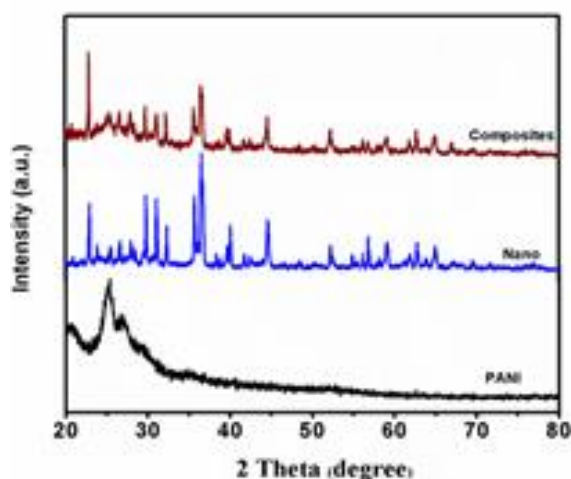


Figure 2: XRD pattern of synthesized PANI and its nanocomposite

3.3 SEM Analysis

Agglomerated structure of PANI is clearly visible in the case of PANI while the nanomaterial seems to exhibit a more quartz or crystal-like structure. As for the nanocomposite material, the coverage of the nanostructures by PANI can be clearly seen as shown in Figure 3.

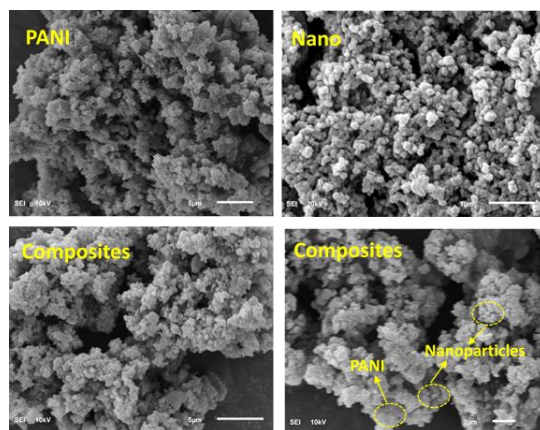


Figure 3: SEM images of synthesized PANI, nanomaterial and its nanocomposites

3.4 Salt Spray Exposure Test

As shown in Figure 4, the results of the salt spray test reveal that the sample coated with the paint containing PANI (sample A) has experienced the most corrosion. The paint system containing the nanomaterial (sample B) exhibits less corrosion than the PANI system followed by the coating system containing the nanocomposite of PANI and Nanomaterial (sample C). In other words, the coating system containing the nanocomposite pigment exhibited the least corrosion as anticipated.



Figure 4: Salt spray exposure results

3.5 Electrochemical corrosion studies

As for the electrochemical results, the typical potentiodynamic polarization results for PANI, nano and nanocomposite coated MS specimens in 3.5% NaCl solution at 25 °C after 24 h immersion are presented in Figure 5.

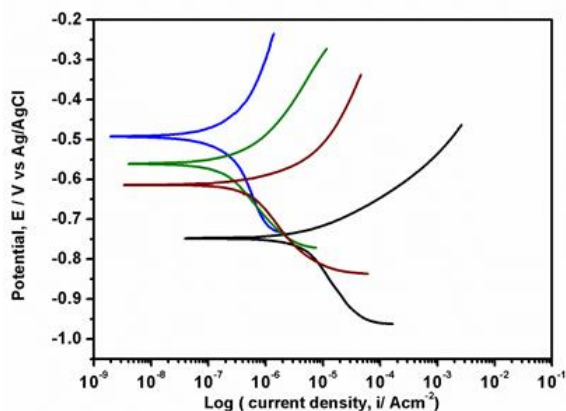


Figure 5: Polarization curves of uncoated and coated MS specimens in 3.5 % NaCl solution

The electrochemical parameters extracted from the Tafel plot analysis are presented in Table 2. The MS specimens with coatings exhibited more positive E_{corr} values compared to that of the bare specimen, indicating that the polymer coatings become a physical barrier for diffusion of aggressive species from solution and improve the corrosion resistance of the MS specimens [Kumar 2015]. In particular, a larger shift of E_{corr} towards nobler direction was observed with an inclusion of PANI nanocomposites into the coatings.

Samples	E_{corr} (mV Vs Ag/AgCl)	I_{corr} $\mu\text{A}/\text{cm}^2$	β_a (mV/dec.)	β_c (mV/dec)	CR (mm/yr)
Bare	-748	3.510	158	62	40.69
PANI	-614	0.668	127	73	7.74
NANO	-561	0.865	187	98	10.14
PANI/NANO	-493	0.171	165	75	1.98

Table 2: Polarization parameters for uncoated and coated MS samples in 3.5% NaCl at 25 °C after 24h immersion

Moreover, a significant shift towards lower current densities (i_{corr}) was observed, and particularly, i_{corr} was reduced by about two orders of magnitude. The corrosion rate (CR) was calculated using the i_{corr} values and Eq. (1).

$$\text{CR} = 3268 \times i_{\text{corr}} \times \text{EW}/D - (1)$$

where i_{corr} denotes the corrosion current density (mA cm^{-2}), EW and D is the equivalent weight and density (g cm^{-3}) of the specimen, respectively. Generally, the high corrosion potential along with the low corrosion current density of the coatings specifies a lower corrosion rate with a higher corrosion protection performance [Attarzadeh et. al 2008]. From the obtained results, it is revealed that the presence of PANI into the coatings act as a barrier which restrict the permeation of the electrolyte and also reducing the corrosion rate by participating in the electrochemical reactions. Furthermore, the inclusion of PANI nanocomposite into the coating matrix could hinder the corrosion process of the MS specimens due to the existence of nanomaterial within the PANI matrix which might function as a reinforcement network and make a coating which is more compact and corrosion resistant [Kumar and Rajendran 2013].

In order to further gain an insight into the corrosion protection behavior of PANI and its nanocomposite coated MS specimens, EIS tests were conducted and the results obtained are presented in Figure 6 and 7 in Nyquist and Bode formats respectively.

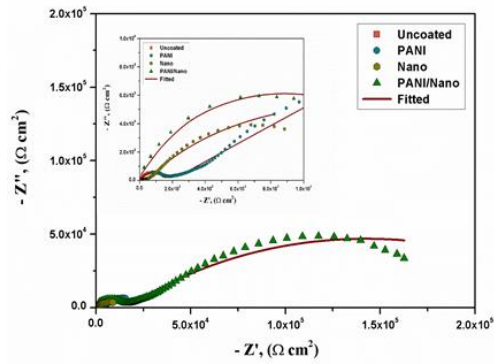


Figure 6: Nyquist plots of uncoated and coated CS specimens in 3.5 % NaCl solution

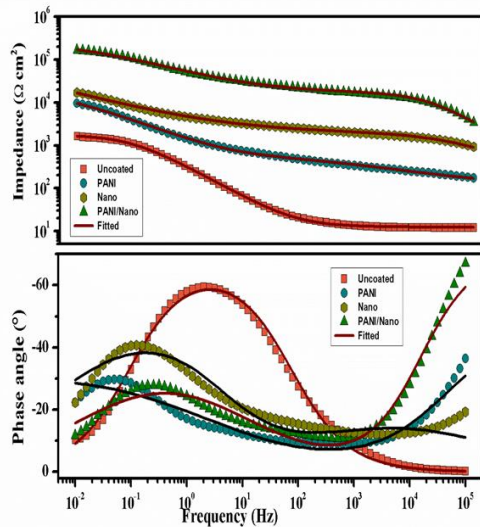


Figure 7: Bode plots of uncoated and coated MS specimens in 3.5 % NaCl solution

Nyquist diagram of the coated MS specimens exhibited two time constants at low and high frequency regions (Fig. 6), whereas the former is attributed to the responses of electrolyte/coating interface, the latter is associated with the corrosion processes occurring at the electrolyte/metal interface [Imaz et. al 2014]. Generally, the length of the semicircle arc is related with the polarization resistance (R_p) and therefore the corrosion rate; the lengthier the semicircle arc, the lesser the corrosion rate [Maocheng et. al 2013]. Comparing the Nyquist plots of the bare and coated specimens, the

coated specimens exhibited the highest R_p . Specifically, the diameter of the capacitive arc for the PANI nanocomposite coatings is observed to be larger in comparison to others, signifying that the nanocomposite coatings conferred the highest corrosion protection performance on the MS specimens in 3.5% NaCl solution.

Bode plots of the bare and coated MS specimens are presented in Figure 7. The impedance parameters of interest was generated by fitting the experimental data into equivalent circuit models, and the achieved fitting values displayed proper reliability with the experimental results. The equivalent circuit models are represented as (Fig. 8a) $R_s(R_{ct}Q_{dl})$ for the bare and (Fig. 8b) $R_s(R_fQ_f)(R_{ct}Q_{dl})$ for the coated specimens, where R_s , R_{ct} , R_f means the solution, charge transfer, and film resistances, respectively, and Q_{dl} and Q_f are the double layer and coating capacitances, respectively [Kumar and Gasem 2015]. Constant phase elements (CPE/Q) were used to get the accurate fitting by replacing the capacitive elements in the circuits. The impedance of a CPE can be represented as:

$$Z_{CPE} = [Y_0 (j \omega)^n]^{-1}, \quad (2)$$

where Y_0 and n are frequency independent parameters and ω is the angular frequency [Hattori et. al 2010]. The obtained experimental results were well fitted to the theoretical data and the estimated impedance values are listed in Table 3.

Samples	R_s ($\Omega \text{ cm}^2$)	R_{ct} ($k\Omega \text{ cm}^2$)	R_f ($k\Omega \text{ cm}^2$)	CPE_{dl} ($\mu F \text{ cm}^{-2}$)	n_{dl}	CPE_f ($\mu F \text{ cm}^{-2}$)	n_f	$\chi^2 \times 10$
Bare	28.2	1.76	-----	838.60	0.80	-----	-----	2.25
PANI	173.3	9.45	2.23	231.65	0.96	99.00	0.94	3.30
NANO	152.0	16.54	2.15	180.00	0.94	3.84	0.92	2.47
PANI/NANO	121.0	166.80	46.96	10.54	0.97	0.74	0.96	3.21

Table 3: EIS parameters for uncoated and coated MS samples in 3.5% NaCl at 25 °C after 24 h immersion

Generally, the impedance values at the lower frequency region (10 mHz) hold an important part in relating the electrochemical behavior and integral features of the coating at the interface [Pawar et. al 2017]. All of the coatings exhibited a higher impedance value at a lower frequency region compared to that of the bare MS specimen. From the Table 3, the R_{ct} value of the coated MS specimens increased from 1.76 k Ω cm² for bare to 9.45, 16.54 and 166.8 k Ω cm² for the PANI, nano and PANI nanocomposites coated specimens, respectively, representing improved corrosion protection behavior for the coatings. Generally, R_f values could be influenced by the number of pores/passageway networks in the metallic surface, through which the permeation of corrosive species occurs [Pawar et. al 2017]. The highest R_f value was observed for the specimens coated with PANI nanocomposites, demonstrating that the micro cracks and pores are closed by the reinforcement of nanocomposites. Hence, the inclusion of PANI nanocomposites seems to significantly decrease the porosity of the coatings by filling the probable micro cracks/cavities inside the coating [Kumar et. al 2012]. Moreover, this performance proficiently hinders and extends the diffuse pathway of aggressive elements, such as Cl^- and H_2O [Jafari et. al 2016]. From the obtained results, it can be concluded that the MS specimens coated with PANI nanocomposite display enhanced corrosion protection behavior in 3.5% NaCl solution. Maintain two columns of text throughout the writing of your paper, except for the title and abstract section.

4. Conclusions:

In this paper, the anticorrosion performance of three different pigments namely; waste slag nanomaterial, polyaniline and a nanocomposite of these two materials was evaluated by incorporating these pigments in a commercial epoxy zinc rich phosphate primer. As highlighted in both salt spray and electrochemical tests, the coating formulation that contain the

nanocomposite demonstrate superior corrosion protection properties. The results show that the nanocomposite pigments performed better, followed by the nanomaterial and polyaniline respectively. As expected, modification of the nanomaterial (raw material) with polyaniline has significantly improved the anticorrosion properties of the paint system used.

Acknowledgement

The author gratefully acknowledges the research funding for this project No.455, provided by Deanship of Scientific Research, King Khalid University, ABHA, KSA. Also, the author would like to acknowledge the technical support of Engineer Mohamed Al-Zaher (Manager of R & D) of Aljazeera Paints Company in Khamis Mushayt.

References

1. J. Prokeš, J. Stejskal, M. Omastová, Chemické listy, 95 (2001) 484.
2. J. Stejskal, P. Kratochvíl, A. D. Jenkins, Polymer, 37 (1996) 367.
3. T. Niratiwongkorn, G. E. Luckachan, V. Mittal, RSC Adv., (2016) 43237.
4. R. Suleiman, H. Dafalla, B.El Ali, RSC Adv., (2015) 39155.
5. A. Kalendova, E. Halecka, K. Nechvilova, M. Kohl, Koroze a ochrana materiálu, 61 (2017) 39.
6. A. A. Al-Dulaimi, S. Hashim & M.I. Khan, Sains Malaysiana, 40 (2011) 757.
7. G. Ruhi, H. Bhandari, S. K. Dhawan, Prog. Org. Coat., 77 (2014) 1484.
8. S. Sathiyarayanan, S. Syed Azim, G. Venkatachari, Synth. Met. 157 (2007) 751.
9. A. Mostafaei, F. Nasirpouri, Prog. Org. Coat., 77 (2014) 146.
10. S. Sathiyarayanan, S.Syed Azim, G. Venkatachari, Prog. Org. Coat., 59 (2007) 291.

13th Annual Research Day

Organised by the Deanship of Scientific Research in Collaboration with the College of Engineering
Research Centre
2nd April 2018

11. S. Sathiyarayanan, S. Syed Azim, G. Venkatachari, *Electrochimica Acta*, 53 (2008) 2087.
12. A. Kalendova, D. Vesely, J. Stejskal, *Prog. Org. Coat.* 62 (2008) 105.
13. L. Shi, X. Wang, L. Lu, X. Yang, X. Wu, *Synth. Met.* 159 (2009) 2525.
14. A. M. Kumar, B. Suresh, S. Ramakrishna and Kye-Seong Kim, *RSC Adv.* 5 (2015) 99866.
15. N. Attarzadeh, K. Raeissi, M.A. Golozar, *Prog. Org. Coat.* 63 (2008) 167.
16. A. M. Kumar, N. Rajendran, *Ceram. Int.* 39 (2013) 5639.
17. N. Imaz, M. Ostra, M. Vidal, J.A. Díez, M. Sarret, E. García-Lecin, *Corros. Sci.* 78 (2014) 251.
18. Y. Maocheng, A. C. Vetter, J. V. Gelling, *Corros. Sci.* 70 (2013) 37.
19. A. M. Kumar, Z. M. Gasem, *Surf. Coat. Technol.*, 276 (2015) 416.
20. M. Hattori, A. Nishikata, T. Tsuru, *Corros. Sci.* 52 (2010) 2080.
21. P. G. Pawar, R. Xing, R. C. Kambale, A. M. Kumar, S. Liu, S. S. Latthe, *Prog. Org. Coat.* 105 (2017) 235.
22. A. M. Kumar, S. Nagarajan, N. Rajendran, T. Nishimura, J. Solid State Electrochem. 16 (2012) 2085.
23. Y. Jafari, S.M. Ghoreishi, M. S. Nooshabadi, *Synth. Met.* 217 (2016) 220.

13th Annual Research Day

Organised by the Deanship of Scientific Research in Collaboration with the College of Engineering
Research Centre
2nd April 2018

Evaluating the Precipitation-Topography Relationship and Precipitation Gradient Using Non-Stationary Modelling Technique in Aseer Region, Saudi Arabia

Dr Javed Mallick and Dr. Nabil Ben Kahla¹

¹Department of Civil Engineering, College of Engineering, King Khalid University,
PO Box 394, Abha 61411 KSA.
E-mail address: jmallick@kku.edu.sa

Abstract: The mountainous of Aseer region, corresponds to the Afromontane phytogeographic region, is an eco-sensitive zone and has complex relationship between topography and rainfall. The region is located inland of the red sea escarpment edge in the west. Therefore, rainfall can occur during any month of the year in the mountain of the high Aseer region when moist air forces up the escarpment from the red sea. Monitoring the rainfall data and its topographical elevation variable in Aseer region is an essential requirement for feasible and accurate rainfall-based data for different applications, such as hydrological and ecological resources management in rugged terrain and remote areas. The relationship of elevation and rainfall are spatially non-stationary, non-linear, scale dependent and often modelled by conventional regression models. Therefore, a local modelling technique, geographically weighted regression (GWR), applied to deal with non-stationary, non-linear, scale dependent problems. The GWR using topo-climatic data (elevation and rainfall) to analyze the cumulative rainfall data for rainy months (March to June) of the four years estimated from CHIRPS product for Aseer region. The bandwidth (scale-size) of the Aseer region rainfall-elevation relationship has stabilized at round off 12 km. By selecting the suitable bandwidth, the spatial pattern of the rainfall-elevation relationship was significantly enhanced by using the GWR than the traditional Ordinary Least Squares (OLS) regression model. GWR local modelling techniques estimated well in terms of accuracy, predictive power, and decreased residual autocorrelation. Therefore, the GWR, local modelling approach managed to produce more accurate estimates by taking into account local characteristics.

Keywords: Ordinary Least Squares (OLS) regression; Geographically weighted regression; Non-stationarity; CHIRPS product; Aseer region.

1. Introduction:

Spatial modelling of rainfall is important for evaluating, and predicting spatial patterns and amounts of rainfall for various hydrological studies and water resource management (1, 2). The rainfall is complex geographical phenomena and the topography of a region plays an important role in controlling the amount and the spatial distribution of the rainfall (3). Many researchers have evaluated the relationship between the spatio-temporal rainfall distributions and topographic variables such as elevation (4), Geo-location (5, 6), slope and aspect (7), wind information (8) and, proximity to the sea or large water bodies (9). These topographical variables

has been used to explore the relationships between topography and the spatial distribution of annual (10), seasonal (11), and monthly (12) rainfall using bivariat and multiple regression models and geostatistical methods (13). Monitoring the rainfall data is important for flood and drought-prone regions. Therefore, accurate rainfall data for different applications are required for management of, hydrological, natural and ecological resources management in rugged terrain. In Aseer region, Saudi Arabia, conventional rain gauges are the primary source of rainfall data (14). However, the distribution of rain-gauge network are inadequate to provide reliable rainfall assessment due to their non-

13th Annual Research Day

Organised by the Deanship of Scientific Research in Collaboration with the College of Engineering
Research Centre
2nd April 2018

uniform spatial coverage (i.e., raingauges distribution), and missing data within a very large area (13). Remote sensing-based (onboard satellite) rainfall measurements may assist ample data with high spatio-temporal resolution over the large extents where conventional rain-gauge data are unavailable or scarce (15).

Climate Hazards Group InfraRed Precipitation with Stations (CHIRPS) based on multiple data sources is relatively new rainfall data product with high spatio-temporal resolution. The product was developed by the USGS (United States Geological Survey), EROS (Earth Resources Observation and Science) center with the collaboration of Santa Barbara Climate Hazards Group, University of California (15).

Rainfall is a non-stationary phenomenon, occurs in the region and local landscape conditions (such as land use, vegetation and topography), causes a non-homogenous rainfall distribution that varies over space and time (16). Many studies have investigated the non-homogenous rainfall distribution using Non-Stationary Modelling Technique i.e. Ordinary Least Square (OLS) and Geographically Weighted Regression (GWR) which are extensively implemented regression techniques for modelling the rainfall-elevation relationship (13). OLS regression method the variable estimates are applied in a single model to all data and uniformly distributed over the whole geographic area of interest. The OLS regression model hypothesized the relationship is geographically constant, and its coefficients are also constant. Whereas GWR, the variable estimates are performed using a method in which the contribution of a sample to analysis is weighted based on its spatial proximity to the geographic space of interest under consideration. Hence, the weighing of observation is not constant in the calibration but differ with different locations. The present study, aims to examine the rainfall-topography relationship using non-stationary modelling technique in Aseer region, Saudi Arabia.

Study area: The Aseer region located in the southwestern part of Saudi Arabia having an area of 84240 km² that shares a short border with Yemen. The boundary of the Aseer region lies between the latitude of 17°21'56.506"N and 21°2'11.176"N and longitude of 41°17'54.353"E and 44°31'22.668"E. It consists of mountains, plain, and valleys of the Arabian highlands. The elevation varies from 0 to 2990m with a mean and std. dev. of 1313m and 544.3 respectively. The climate of the region differs considerably depending on topography, slope, aspect and season. The highlands of this region collect variable rainfall caused by the southwestern monsoon, which carries wet oceanic winds (14). This region has the highest average rainfall in Saudi Arabia distributed over 2-4 months during the spring and summer growing seasons (March-June) while rainfall that occurs during the rest of the year is negligible (17).

2. Materials and Methods:

2.1 Data and Material used

The topography obtained from SRTM data (The Shuttle Radar Topography Mission) by USGS with a spatial resolution of 90 meters. The CHIRPS v.2.0 provides rainfall datasets at a 3km spatial resolution. These data is created coupled with geostationary infrared satellite rainfall estimates in conjugation with rain gauge observations that are interpolated to create gridded precipitation datasets. Monthly grids (March, April, May and June) over 1988, 1998, 2000 and 2016 study period were downloaded from CHIRPS website. The margins of this time period was selected because of the significant difference in cumulative rainfall (March, April, May and June) occurred in the region during the years 1988, and 2000 which were low rainfall years, and 1998 and 2016 were high rainfall years.

2.2 Methodology

Generation Topographical Variable from DEM:
The highlands of Aseer mountainous region

13th Annual Research Day

Organised by the Deanship of Scientific Research in Collaboration with the College of Engineering
Research Centre
2nd April 2018

collect variable rainfall caused by the southwestern orographic rainfall, which carries wet oceanic winds (14). The geographic phenomenon of orographic rainfall produced when moist air lifted as it moves over a mountain range. The elevation has considerably stronger correlation with rainfall data as compared to other variables derived from DEM/topography. GTOPO30 with a spatial resolution of 90 m has been used to derive elevation as topographical variable. The topographical elements extracted at the scale of 1–10 km are strongly correlated with the rainfall as compared to other spatial resolutions (11). Hence, in this study the ideal spatial resolution 1 km has been considered for derivation of elevation.

Modelling Methods: The spatial evaluation has been performed to compare the rainfall data and elevation using Ordinary least squares (OLS) and Geographically Weighted Regression (GWR) models. These two models have been applied to the complete dataset and also each sub-region (lowland and upland) using ArcGIS software.

Ordinary Least Squares (OLS) Model: The Ordinary least squares is a method for estimating the unknown variables in a linear regression model. The stationary characteristics of the OLS regression method show that a single model is applied to entire region and is uniformly distributed over the entire geographic area. The OLS regression model hypothesized the relationship is geographically constant, and its coefficients are also constant. GWR model is an extension of the normal regression method and deals with the spatial non-stationarity of empirical relationships. It is a local regression technique appropriate for spatial data with some degree of spatial dependence (18). The technique disseminates information that is locally linked and allows regression model variables to vary in spatial domain. GWR infers the problem of spatial non-stationarity by examining the relationship between elevation and rainfall data

as explanatory variables at every observed point (19).

3. Results and Discussion

Analysis of Rainfall Data: Aseer region has the highest average rainfall in Saudi Arabia distributed over four months (March, April, May and June). The distribution of complete dataset of low rainfall years accounted of mean 75.5mm and 73.4 mm of 1988 and 2000 respectively, whereas the distribution of complete dataset of high rainfall years accounted with a mean value of 111.4 mm and 147.7 mm in 1998 and 2016 respectively.

Bandwidth Scale-Dependency: The relationship between topography and rainfall in the Aseer region, Saudi Arabia during the four years is scale-dependent. The Stationarity Index (SI) for the year of 1988, 1998, 2000 and 2016 and justifies the scale-dependency of non-stationarity which was evident by changing the scale of investigation. All the years, the SI was higher for small bandwidths, while broadened the bandwidth the SI index got flattened (stabilized). Also, the index values were not stationary in any of the investigated spatial scales, which show having a high non-stationary data. The SI decreased abruptly with an increase in bandwidth that stabilized around 12 km; this suggests that this is the appropriate scale of the rainfall-elevation relationship, viz. the lowering geographical area with which a reliable relationship can establish for the whole study area.

The GWR and OLS Model Assessment Model assessment were carried out between GWR and OLS models for 1988, 1998, 2000 and 2016 outputs. The coefficient of determination (R^2) for GWR was much higher than OLS model for all four years. The GWR models deviate less while OLS models are uneven in their estimations. In GWR model, the coefficient of determination (R^2) ranges between 0.86 to 0.94 and the coefficient of determination (R^2) ranges from 0.22 to 0.35 for the OLS models.

Geographical pattern of the Rainfall-Elevation relationship:

In the present study, elevation was computed based on the optimal pixel size (1km) of DEM taken from the correlation study (11). There is spatiotemporal variability found in the rainfall-topography correlation throughout the Aseer region. GWR models produced the maps of slope parameters (β coefficients), local R^2 , and standardized residuals (StdResid) to identify the geographical variability relationships between effective bandwidth and related factors. The coefficient of determination (Local R^2) ranges from 0 to 1, which demonstrates the local regression model fit with the observed values and the local models with high values being preferable whereas the low values perform poorly. The objective of mapping the local R^2 values to verify if GWR predicts better and prediction becomes poor, it may give indications about significant variables that may be missing from the regression model. Residuals are the variation between the observed and predicted y values respectively. Standardized residuals have a mean of 0 and a standard deviation of 1. In the low rainfall years (1988 and 2000) it shows (fig1) that the local fits are high ($R^2 > 0.4$) in the north-western (Al Namas, Sabat Alalayyah and Bisha) the western and north-eastern (Tathleeth and Morighan) and south-west (Abha, Alsooda, Muhayil) part of Aseer region. It signifies that rainfall is a very useful determinant in these areas, whereas the local fits (R^2) are lower in the north and north-central parts of Aseer region that signifies that the land use and other ecological factors have strong influences in these areas. The figure 1 shows the high rainfall years (1998 and 2016) that the local fits are high in north-western and north-eastern part of Aseer region whereas in north and north-central part of Aseer region depicted lower local fits.

The local fits perform better in the rainfall year of 2016 than the relatively low rainfall in 1988, although the general or somehow the clustering

variability is similar in all the four years (figure 1-2). The vast majority of the rainfall coefficients are positive, inferring that an increase in elevation relates to an increase in rainfall. However, the rate of variations increases significantly throughout some part of north and north-central part of Aseer region (Fig. 1-2).

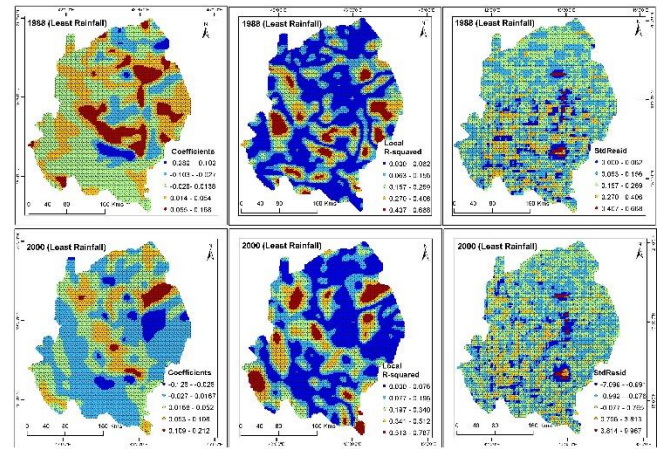


Figure 1: Spatial variation of regression outputs of low rainy months (1988-2000) from the GWR model for effective bandwidth (a) Slope Parameter (β coefficient); (b) Local R-squared (R^2); (c) Standardized residuals.

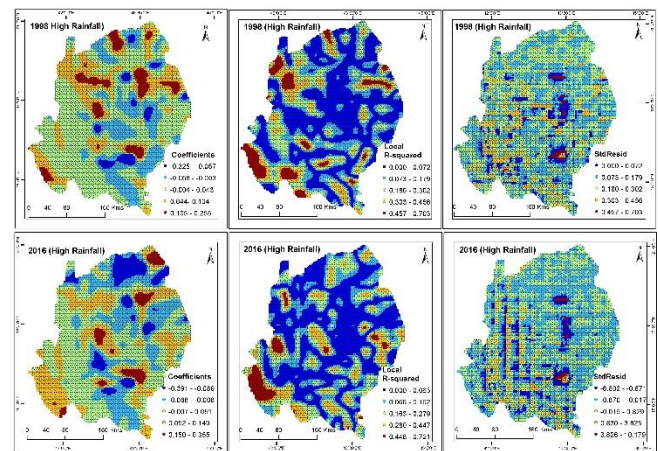


Figure 2: Spatial variation of regression outputs of high rainy months (1998-2016) from the GWR model for effective bandwidth (a) Slope Parameter (β coefficient); (b) Local R-squared (R^2); (c) Standardized residuals.

The strength of the associations is higher in the year of 1988 and 2000 than that of 1998 and 2016. Although rainfall coefficients were lower in most of the high rainfall year of 1998 and 2016 than of low rainfall year 1988 and 2000, an

13th Annual Research Day

Organised by the Deanship of Scientific Research in Collaboration with the College of Engineering
Research Centre
2nd April 2018

apparently high cluster extending over central and western part had remarkably high values that exceeded all the coefficient values of 1988 and 2000. The findings suggest that elevation was sensitive to rainfall in Aseer region in all the rainfall years.

The results demonstrated that the elevation-rainfall relationship is not stationary over Aseer semi-arid region during the rainy months (March-June) in the years of 1988-2000 and 1998-2016. The study findings recommend that elevation is a significantly powerful predictor of rainfall if spatial non-stationarity can be integrated into the regression model. In the study region, the coefficient relationship was positive across most of the region. However, very weak or negative relationships found in some patches. Moreover, the importance of association also varied across the study area. GWR is a function to detect the continuous variation in respect to spatial relationships by incorporating the local information with considerably efficient performance as compared with the global OLS models.

4. Conclusions:

The main objective of the study is to examine the spatial variation in rainfall-topography relationship using non-stationary modelling technique in semi-arid Aseer region, Saudi Arabia. The GWR using topo-climatic data (elevation and rainfall) to analyze the cumulative rainfall data for rainy months (March to June) of the four years estimated from CHIRPS product. In the GWR, the variable use a method in which the contribution of a sample to analysis the weighted which based on its spatial proximity to the specific geographic space of interest under consideration. Hence, the weighting of observation is not constant in the calibration but differ with different locations. GWR models produced the maps of slope parameters (β coefficients), local R^2 , and standardized residuals (StdResid) to identify the geographical variability relationships between effective bandwidth and

related factors. The coefficient of determination (R^2) for GWR was much higher than OLS model for all four years. The results validated the hypothesis that GWR local modelling is a viable alternative to OLS global modelling in heterogeneous areas that are sensitive to ecological changes. The GWR approach produced better predictions, lower autocorrelation in the residuals and highlighted interesting local variations. As such, GWR is strongly suggested as both an explanatory and exploratory method in spatiotemporal analysis and water resource modelling where spatial constancy in relations between variables is part of further research. The GWR, local modelling approach managed to produce more accurate estimates by taking into account local characteristics.

Acknowledgement

The authors acknowledge the Deanship of Scientific Research for proving administrative and financial supports. Funding for this work has been provided by the Deanship of Scientific Research; King Khalid University, Ministry of Education, Kingdom of Saudi Arabia under award numbers R.G.P.1/28/38 (1439).

References

1. Abdullah MA, and Al-Mazroui MA. 1998. Climatological study of the southwestern region of Saudi Arabia—I. Rainfall analysis. *Climate Research*, vol. 9, no. 3, pp. 213–223.
2. Gouvas M, Sakellariou, N, Xystrakis F. 2009. The relationship between altitude of meteorological stations and average monthly and annual precipitation,” *Studia Geophysica et Geodaetica*, vol. 53, no. 4, pp. 557–570, 2009.
3. Richardson CW. 1981. Stochastic simulation of daily precipitation, temperature, and solar radiation. *Water Resour. Res.* 17(1): 182–190.
4. Mair A, Fares A. 2011. Comparison of rainfall interpolation methods in a mountainous region of a Tropical Island. *J Hydrol Eng* 16:371–383. doi:10.1061/(ASCE)HE.1943-5584.0000330

13th Annual Research Day

Organised by the Deanship of Scientific Research in Collaboration with the College of Engineering
Research Centre
2nd April 2018

5. Oettli P, Camberlin P. 2005. Influence of topography on monthly rainfall distribution over East Africa. *Climate Research* 283: 199–212.
6. Buytaert W, Celleri R, Willems P, De Bièvre B, Wyseure G. 2006. Spatial and temporal rainfall variability in mountainous areas: a case study from the south Ecuadorian Andes. *Journal of Hydrology* 329(3–4): 413–421
7. Konrad CE. 1996. Relationships between precipitation event types and topography in the southern blue ridge mountains of the southeastern USA,” *International Journal of Climatology*, vol. 16, no. 1, pp. 49–62, 1996.
8. Johansson B, Chen D. 2003. The influence of wind and topography on precipitation distribution in Sweden: statistical analysis and modelling. *Int. J. Climatol.* 23(12): 1523–1535, doi: 10.1002/joc.951
9. Buytaert W, Celleri R, Willems P, De Bièvre B, Wyseure G. 2006. Spatial and temporal rainfall variability in mountainous areas: a case study from the south Ecuadorian Andes. *Journal of Hydrology* 329(3–4): 413–421
10. Razmi R, Balyani S, Daneshvar MR. 2017. Geo-statistical modeling of mean annual rainfall over the Iran using ECMWF database. *Spat. Inf. Res.* 25: 219. <https://doi.org/10.1007/s41324-017-0097-3>
11. Kumari M, Singh CK, Basistha A, Dorji S, Tamang TB. 2017. Non-stationary modelling framework for rainfall interpolation in complex terrain. *Int. J. Climatol.* 37: 4171–4185. doi:10.1002/joc.5057
12. Johnson GL, Hanson CL. 1995. Topographic and atmospheric influences on precipitation variability over a mountainous watershed. *J Appl Meteorol* 34:68–87. doi:10.1175/1520-0450-34.1.68
13. Al-Ahmadi K, Al-Ahmadi S. 2013. Spatiotemporal variations in rainfall–topographic relationships in southwestern Saudi Arabia. *Arab. J. Geosci.* 7(8): 3309–3324, doi: 10.1007/s12517-013-1009-z.
14. Vincent P. 2008. Saudi Arabia: An Environmental Overview. Taylor and Francis, London.
15. Funk C, Peterson P, Landsfeld M, Pedreros D, Verdin J, Shukla S, Husak G, Rowland J, Harrison L, Hoell A. 2015. The climate hazards infrared precipitation with stationsda new environmental record for monitoring extremes. *Sci. data* 2.
16. Sierra JP, Arias PA, Vieira SC. 2015. Precipitation over northern South America and its seasonal variability as simulated by the CMIP5 models. *Adv Meteorol.* 2015:634720. doi: 10.1155/2015/634720
17. Wheeler HS, Larentis P, Hamilton GS. 1989. Design rainfall characteristics for south-west of Saudi Arabia, *Proc. Instn. Civ. Engrs.*, Part 2, pp. 517–538.
18. Kalogirou S. 2003. The Statistical Analysis and Modelling of Internal Migration Flows within England and Wales.
19. Brunsdon C, Fotheringham AS, Charlton ME. 1996. Geographically weighted regression: a method for exploring spatial nonstationarity. *Geogr. Anal.* 28(4): 281–298, doi: 10.1111/j.1538-4632.1996.tb00936.x.

Simple and fast technique for mobile localization in 2D Environment

Monji Zaidi¹, Mohammed Usman¹

¹Department of electrical Engineering, College of Engineering, King Khalid University,
PO Box 394, Abha 61411 KSA.
E-mail address: amzaydi@kku.edu.sa

Abstract: In this paper, a new efficient geometric approach with a reduced number of iterations makes it possible to estimate, with a minimal error, the position of a Terminal Mobile (TM) moving in a wireless environment. The position of the TM is obtained based on the variations of the received signal and the geometric disposition of the TM and three Access Point (APs) rigorously chosen. This technique can be used in Indoor or Outdoor environments. Our approaches is based on simple instructions (Addition multiplication and shift), they will then be easily implemented on a hardware target. The use of these approaches will therefore study the gains obtained by adding geo-location information in Handoff management.

Keywords: mobility, 2D localization, Terminal mobile, Access Point, fast convergence.

1. Overview of basic geo-localization techniques:

Different position estimation techniques have been proposed [1] to calculate the position of the TM. This is why different types of information (the air signal travel time, the received signal angle, and the signal level) are involved to facilitate the design of position estimation algorithms. The main objective in most geolocation algorithms is to obtain higher estimation accuracy.

Given the coordinates of the BS_j, (j = 1, 2, 3), (x_j, y_j), and D_j the distances between the TM and BS_j. The details on the TOA (Time of Arrival) technique (Figure 1 (a)) are given in [2] and [3] and the TM (x, y) coordinates with respect to BS₁ can be calculated as follows:

$$\begin{bmatrix} x \\ y \end{bmatrix} = \frac{1}{2} \begin{bmatrix} X_2 & Y_2 \\ X_3 & Y_3 \end{bmatrix}^{-1} + \begin{bmatrix} X_2^2 + Y_2^2 + d_1^2 - d_2^2 \\ X_3^2 + Y_3^2 + d_1^2 - d_3^2 \end{bmatrix}$$

The TDOA technique (Figure 1 (b)) is clearly presented in [4]. There are therefore two estimated time differences d_(j, 1) between BS₁ and the jth base station (j = 2, 3). TM coordinates.

(x, y) with respect to BS1 can be calculated in terms of D₁ as follows:

$$\begin{bmatrix} x \\ y \end{bmatrix} = - \begin{bmatrix} X_2 & Y_2 \\ X_3 & Y_3 \end{bmatrix}^{-1} * \left\{ \begin{bmatrix} d_{2,1} \\ d_{3,1} \end{bmatrix} d_1 + \frac{1}{2} \begin{bmatrix} d_{2,1}^2 - K_2 + K_1 \\ d_{3,1}^2 - K_3 + K_1 \end{bmatrix} \right\}$$

Where

$$K_1 = X_1^2 + Y_1^2$$

$$K_2 = X_2^2 + Y_2^2$$

$$K_3 = X_3^2 + Y_3^2$$

The arrival angle technique determines the position of TM (x, y) based on triangulation, as shown (Figure 1 (c)). The intersection of two lines of direction θ_1 and θ_2 respectively, defines a single position. The AOA technique is presented in [5], and the position of the TM (x, y) is given as follows:

$$x = \frac{Y_2 - Y_1 + X_1 \tan(\theta_1) - X_2 \tan(\theta_2)}{\tan(\theta_1) - \tan(\pi - \theta_2)}$$

$$y = Y_1 + (x - X_1) \tan(\theta_2)$$

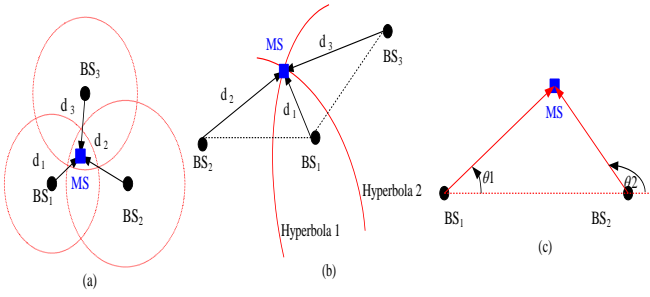


Figure (1) Fundamental techniques of geolocation: (a) TOA; (b) TDOA; (c) AOA

2. A new geo-location approach based on three APs.

A TM is necessarily located in the overlapping region (delimited by the points A, B and C) as shown in the figure. 2. Thus, it is necessarily in the region formed by points BS₁, BS₂ and BS₃. But, it is noted that the intersection of the three circles may not be guaranteed to the extent of the actual signals. Therefore, with the above hypothesis, we are led to judge whether the three circles intersect or not in our localization algorithm.

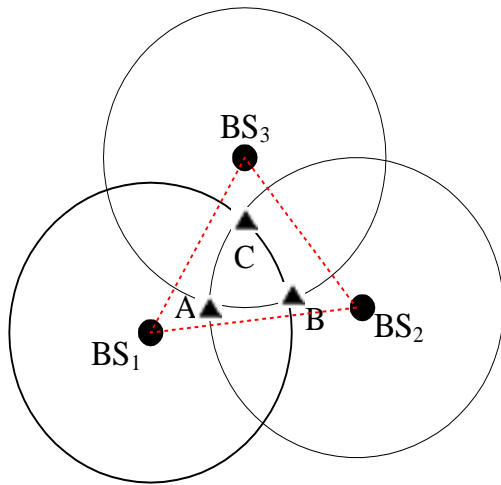


Figure (2) Three neighboring BSs and associated area of overlap

If the circles intersect, as shown in Figure 2, three triangles can be drawn: BS₁MSBS₂, BS₂MSBS₃ and BS₃MSBS₁

Assumptions

- The different APs are placed (two to two) at equal distance.
- The coordinates of the three APs are known by the TM.
- The TM can inquire only about the power received from each AP.
- D: the distance between two APs (The BSs are placed at equal distance).
- $d_1 + d_2 > D$; $d_2 + d_3 > D$ and $d_3 + d_1 > D$

We note by:

A₀, B₀ and C₀ the orthogonal projections of TM on segments (BS₁ BS₂), (BS₂, BS₃) and (BS₃ BS₁) respectively

d₁, d₂ and d₃: The distances between the MS and BS₁, BS₂ and BS₃ respectively.

θ₁₂ is the geometric angle between the (MS-BS₁) and (BS₁BS₂). (θ₁₃ and θ₂₃ are defined in the same way). We first look at the triangle BS₁MSBS₂. Based on the above assumptions and the following figure, we can then write:

$$r_1 = d_1 \cos \theta_{12}$$

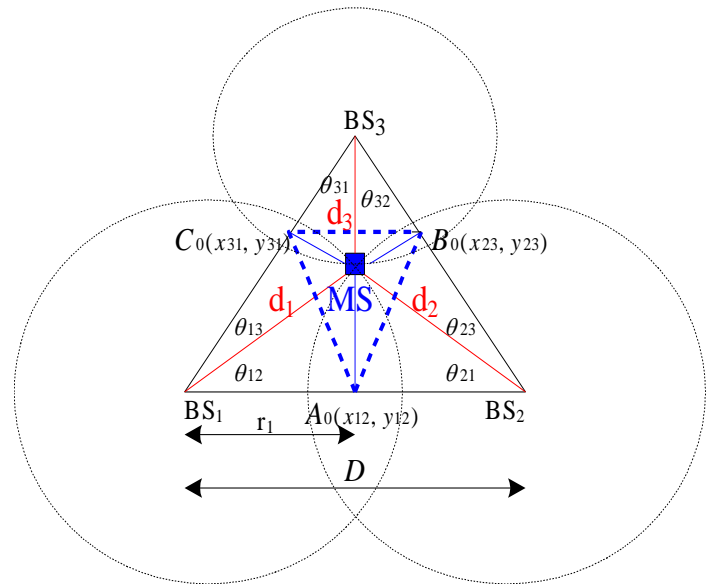


Figure (3) Associated triangles of the intersection of three starting circles

13th Annual Research Day

Organised by the Deanship of Scientific Research in Collaboration with the College of Engineering
Research Centre
2nd April 2018

We can also write:

$$d_2^2 = (D - r_1)^2 + (d_1^2 - r_1^2) \Rightarrow$$

$$d_2^2 = (D - d_1 \cos \theta_{12})^2 + (d_1^2 - d_1^2 \cos^2 \theta_{12}) \Rightarrow$$

$$d_2^2 = D^2 + d_1^2 - 2Dd_1 \cos \theta_{12} = D^2 + d_1^2 - 2Dr_1 \Rightarrow$$

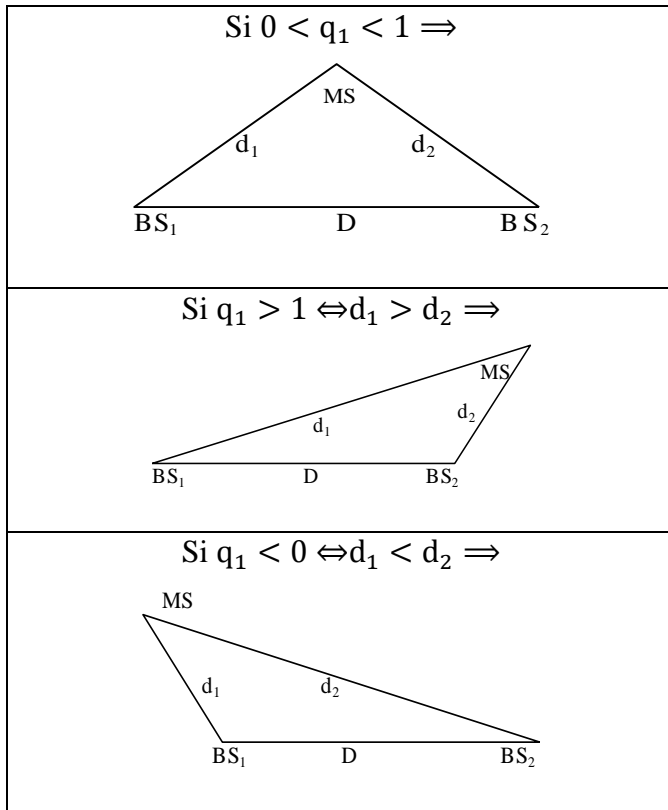
$$r_1 = \frac{D^2 + d_1^2 - d_2^2}{2D}$$

$$q_1 = \frac{r_1}{D} = \frac{D^2 + d_1^2 - d_2^2}{2D^2}$$

Here we define the first factor q_1 by:

$$q_1 = \frac{r_1}{D} = \frac{D^2 + d_1^2 - d_2^2}{2D^2}$$

The value of parameter q_1 allows us to learn about the shape of the triangle BS_1MSBS_2 for example.



The coordinates (x_{12}, y_{12}) of point A_0 are given in [6] by:

$$x_{12} = q_1 X_2 + (1 - q_1) X_1$$

$$y_{12} = q_1 Y_2 + (1 - q_1) Y_1$$

Where:

(X_1, Y_1) and (X_2, Y_2) are the coordinates of BS_1 and BS_2 , respectively.

Let r_2 be the distance between BS_1 and B_0 and r_3 the distance between BS_3 and C_0 . As previously described, we can obtain the coordinates of the points B_0 and C_0 as:

$$x_{23} = q_2 X_3 + (1 - q_2) X_2$$

$$y_{23} = q_2 Y_3 + (1 - q_2) Y_2$$

$$x_{31} = q_3 X_1 + (1 - q_3) X_3$$

$$y_{31} = q_3 Y_1 + (1 - q_3) Y_3$$

Where:

$$q_2 = \frac{r_2}{D} = \frac{D^2 + d_2^2 - d_3^2}{2D^2}$$

$$q_3 = \frac{r_3}{D} = \frac{D^2 + d_3^2 - d_1^2}{2D^2}$$

The TM is then located in a new region $A_0B_0C_0$, which is smaller in surface area relative to the $BS_1BS_2BS_3$ starting surface. In other words we have just created three new virtual BSs placed at A_0 , B_0 and C_0 respectively.

It is very easy to calculate the distances between the SM and the new points A_0 , B_0 and C_0 using the Pythagoras formula. So.

$$d(MS, A_0) = \sqrt{d_1^2 - r_1^2},$$

$$d(MS, B_0) = \sqrt{d_2^2 - r_2^2},$$

$$d(MS, C_0) = \sqrt{d_3^2 - r_3^2}$$

Now, with the three new virtual BSs, MS can redo the same calculations, as shown above. During this second iteration, the orthogonal

projections of the SM on (A_0B_0) , (B_0C_0) and (C_0A_0) will be made to obtain the new points A_1 , B_1 and C_1 that their coordinates can determine as previously. The area of $A_1B_1C_1$ is smaller than that of $A_0B_0C_0$.

At the i^{th} iteration, the SM will be located in a triangle $A_iB_iC_i$ which is smaller in area than

$A_{i-1}B_{i-1}C_{i-1}$. The triangle $A_iB_iC_i$ allows designing the next triangle $A_{i+1}B_{i+1}C_{i+1}$ and so on.

After a small number of iterations (no more than 10), the coordinates of the three vertices of the triangle (A, B and C) converge to the actual coordinates of the SM. At the limit, the triangle $A_{\text{conv}}B_{\text{conv}}C_{\text{conv}}$ of vertices A_{conv} , B_{conv} and C_{conv} will be considered as a point. So, it is possible to write:

$$X_{A\text{conv}} \approx X_{B\text{conv}} \approx X_{C\text{conv}}$$

$$Y_{A\text{conv}} \approx Y_{B\text{conv}} \approx Y_{C\text{conv}}$$

And we can at this stage determine the coordinates of the SM as follows:

$$X_{\text{MS}} = \frac{X_{A\text{conv}} + X_{B\text{conv}} + X_{C\text{conv}}}{3}$$

$$Y_{\text{MS}} = \frac{Y_{A\text{conv}} + Y_{B\text{conv}} + Y_{C\text{conv}}}{3}$$

The division by 3 implies that at the convergence the SM is equivalent to the center of gravity of the triangle $A_{\text{conv}}B_{\text{conv}}C_{\text{conv}}$. The following figures (section 3) show the evolution and the convergence of the coordinates of the three vertices of for different values of d_i (d_1 , d_2 and d_3),

3. Simulation results for a case study:

The coordinates of BS_1 in meters $(X_1, Y_1) = (0, 0)$,
The coordinates of BS_2 in meters $(X_2, Y_2) = (100, 0)$,
The coordinates of BS_3 in meters $(X_3, Y_3) = (50, 86)$.

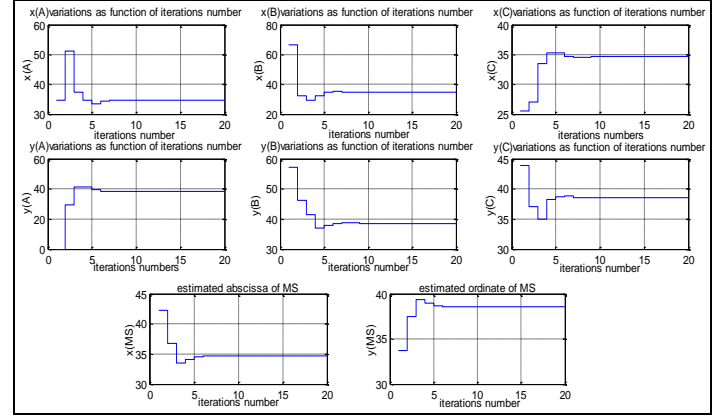


Figure (4) Scenario 1:

$d_1 = 52 \text{ m}$, $d_2 = 76 \text{ m}$ and $d_3 = 50 \text{ m}$

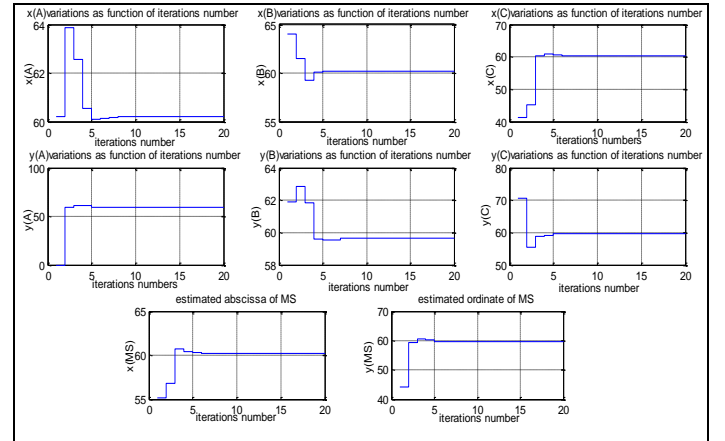


Figure (5) Scenario 2:

$d_1 = 85 \text{ m}$, $d_2 = 72 \text{ m}$ et $d_3 = 29 \text{ m}$

Figure 5 shows how coordinates (X,Y) of the triangle vertices (A,B,C) converge to the MS coordinates. It shows the number of iterations useful to determine the MS position. By running proposal technique and based on several simulations performed for random positions of the MS, around 10 iterations are useful to determine the MS coordinates. This result reflects a high responsiveness level of the algorithm especially when operating over fast hardware platform. It is an indication of the usefulness of triangular convergence localization for tracking applications where localization process should recomputed and update the MT position within a restricted time. In a noisy channel, the responsiveness is almost similar and the number of iterations is around 11 (Figure 6 and 7).

13th Annual Research Day

Organised by the Deanship of Scientific Research in Collaboration with the College of Engineering
Research Centre
2nd April 2018

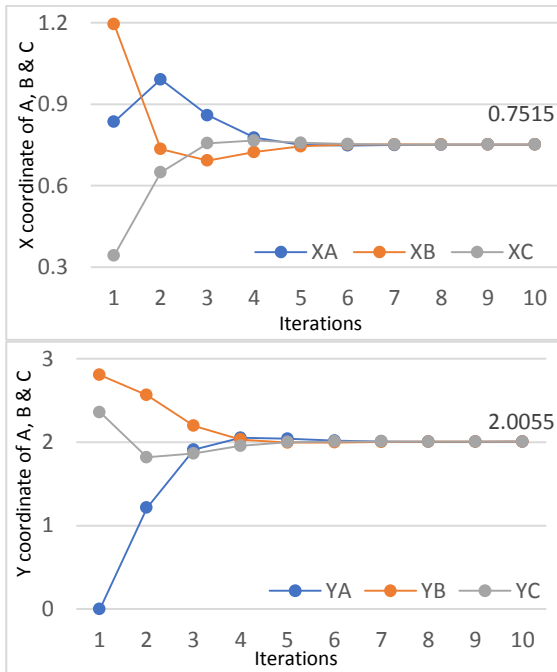


Figure (6) Number of iterations useful for locating the MS (noiseless).

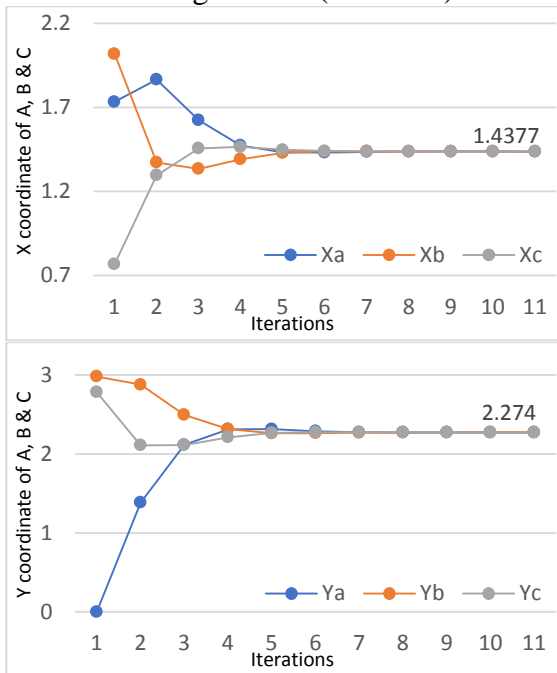


Figure (7) Number of iterations useful for locating the MS (noisy).

4. Conclusions:

This work presents new geometric technique that is based on three distances measurements to determine the position of a mobile object. We note that all needed tasks in this proposal are additions, subtractions and multiplications operation, the implementation is simplified which reduces complexity. Results show that with a few number of iterations ($k \leq 10$), the proposed algorithm converges and provides with a good accuracy the position of MS. Hence, the main advantages of the proposed algorithm are: implementation simplicity, and low computation overhead.

Acknowledgement

This study is/was sponsored by XXXXX,

References

- [1] Ridha Ouni, Monji Zaidi, "EToA: New 2D geolocation-based handover decision technique" 2 (2016) pp 28–32.
- [2] Jami M., Ali R.F. Ormondroyd, "Comparison of Methods of Locating and Tracking Cellular Mobiles, Novel Methods of Location and Tracking of Cellular Mobiles and Their System Applications," (Ref.No.1999/046), IEE Colloquium, London UK, 1/1-1/6.
- [3] Zhao Y. "Standardization of Mobile Phone Positioning for 3G Systems," IEEE Communications Magazine, No.4, Vol.40, (July 2002), pp.108-116.
- [4] Y.T. Chan, K.C. Ho, "A simple and efficient estimator for hyperbolic location," IEEE Transactions on Signal Processing, 42(8)
- [5] Alba Pages-Zamora, Josep Vidal, Dana H. Brooks, "Closed-form solution for positioning based on angle of arrival measurements," in: Proc. of the 13th Sym. on Personal, Indoor and Mobile Radio Communications, September 2002, vol. 4, pp. 1522–1526.
- [6] Chi-Kuang Hwang and Kun-Feng Cheng "Wi-Fi Indoor Location Based on RSS Hyper-Planes Method," Chung Hua Journal of Science and Engineering, Vol. 5, No. 4, pp. 37-43 (2007)

Universal Fuzzy Logic Controller and Application of Genetic Algorithm for Tuning of Scaling Factor for Real-life Dynamic Systems

Mohammad Fazle Azeem¹ and Hamid Naseem¹

¹Department of Electrical Engineering, College of Engineering, King Khalid University,
PO Box 394, Abha 61411 KSA.
E-mail address: mazeem@kku.edu.sa

Abstract: Fuzzy logic is a major paradigm in soft computing which provides a means of approximate reasoning not found in traditional crisp logic. Crisp logic is limited to deals only with linear systems, while Fuzzy Logic can be applied to highly non-linear and complex system. Most of the classical control techniques fail in controlling the complex non-linear dynamic system. Fuzzy Logic Controller has shown the potential to control complex non-linear systems. It has been discovered that the Knowledge Based Fuzzy Logic Controller has universal controlling capability with appropriate learning of scaling factors corresponding to a particular dynamic system. Genetic Algorithms have demonstrated to be a robust and powerful tool for optimization problems. For this research Genetic Algorithm has been employed for learning of scaling factor of Knowledge Based Fuzzy Controller. Two approaches namely Modified Queen Bee and Roulette Wheel for parent selection in Genetic Algorithm is compared. The applied Genetic Algorithm utilizes the weighted crossover operator. A fitness function, which guides the evolution process, is defined as inverse of Integral Time Absolute Error. The proposed method is applied, for the tuning of input and output scaling factors of Knowledge Based Fuzzy Logic Controller, on four complex non-linear systems. The simulation results are encouraging.

Keywords: *Dynamic System, Fuzzy Logic Controller, Genetic Algorithms.*

1. Introduction:

Fuzzy Logic Control (FLC) [1], contrary to classical control systems that involve rigorous mathematical analysis, is one non-analytical approach. In a Fuzzy Knowledge Base Controller (FKBC) the knowledge is expressed by means of intuitive linguistic rules that make ease to a human expert for understanding the behavior of FKBC. Designing a fuzzy system is nothing but formulating the implicit knowledge of the underlying process into a set of linguistic variables and fuzzy rules by interviewing an expert. In particular for complex control tasks, obtaining the fuzzy knowledge base from an expert is often based on a tedious and unreliable trial and error approach. To overcome these limitations many researches have been attracted by the task of combining FLC with other intelligent schemes and no doubt there were

many successful attempts also. This paper too aims to provide a suitable and efficient technique to enhance the interpretability in Genetic Algorithm (GA) based fuzzy logic controllers.

Unlike neural networks, generic fuzzy systems are unable to learn from data. However, several techniques have been proposed to extract fuzzy rules from training data gathered from observation of the control strategies [2-3]. The majority of applications in the domains of genetic-fuzzy systems are concerned with the optimization of fuzzy logic controllers [4-5]. GAs have been used by many researchers [6-8] who alter membership function in response to the changes of task environment to produce more for fuzzy logic control.

In this paper, modified queen bee evolution for weighted crossover based GA has been proposed and it is tested for tuning of scaling factor for the same Fuzzy Knowledge Base Controller (FKBC)

on four complex non-linear examples. The results are compared with roulettes wheel parent selection. Obtained results are encouraging.

This paper is organized into four sections. In section 2, Fuzzy Knowledge Base Controller (FKBC) Genetic Algorithm (GA) are briefly described. Simulation results are presented in section 3. Section 4, recapitulates the drawn conclusion.

2. Hybridization of FKBC with GA

2.1 Fuzzy Knowledge Base Controller (FKBC)

Fuzzy logic control was first introduced by Mamdani [9] and is based on Zadehs's theory of fuzzy sets [10]. Design of FKBC is introduced with two important stages: knowledge base design and FKBC tuning.

By FKBC, we mean a control law that is described by a knowledge-based system consisting of IF-THEN rules with vague predicates and fuzzy logic inference mechanism. A typical rule of FKBC is as follows:

IF e is **N** and ce is **P** THEN du is **Z**

The error $e(k)$ and its change $ce(k)$ as the input or antecedents, and change of control $du(k)$ as the outputs or consequents of rule base.

where $e(k) = \text{set-point}(k) - \text{response}(k)$;

and $ce(k) = e(k) - e(k-1)$

FKBC can be represented as:

$$du(k) = f[e(k), e(k-1)] \quad (1)$$

Where a rule base describes a nonlinear function $f(*)$. Each of the rules of FKBC is characterized with an IF part called antecedent and with a THEN part called consequent, thus FKBC is a kind of state variable controller governed by a family of rules and fuzzy inference mechanism.

Equation (1) represents PD-type FKBC. In the case of PI-type FKBC the actual value of the controller output (u) is obtained by:

$$u(k) = u(k-1) + du(k) \quad (2)$$

The block diagram of FKBC is shown in Figure 1. In this work the scaling factors K_e , K_{ce} , and K_{du} have been tuned and keeping the same knowledge base for all application examples. The knowledge base is discussed in section 2.3.

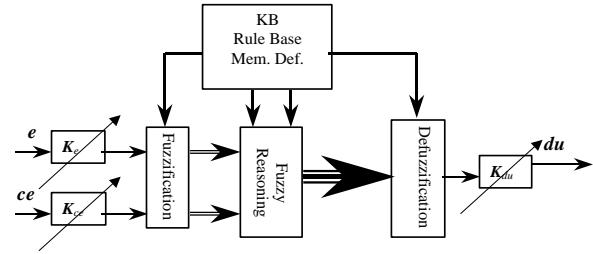


Figure (1) Block diagram of FKBC.

2.2 Genetic Algorithm (GA)

The Genetic Algorithm is a probabilistic computer driven search and optimization technique modeled after the mechanics of genetic evolution. [11-12]. Unlike many classical optimization techniques, GA's do not rely on computing local derivatives to guide the search process, rather GA's perform random search. For this, all they need is an objective function. Reciprocal of the Integral Time Absolute Error (ITAE) is used as the objective function, called as fitness, to guide the GA based search process. The ITAE and the objective function are defined by (3) and (4) respectively. GA's are also more likely to arrive at the global optima because they work on a population of points as opposed to conventional optimization techniques.

$$ITAE = \int_0^t t \cdot |e| \cdot dt \quad (3)$$

$$fitness = \frac{1}{ITAE} \quad (4)$$

In general, a GA consists of three fundamental operators: reproduction (parent selection), crossover and mutation. GA's is started with a set of solutions (represented by chromosomes) called population, generated randomly, and the evolutionary process of reproduction, crossover and mutation are used to generate an entirely new population from the existing population. The reproduction operator selects good chromosomes in the population to form the mating pool. Selection of chromosome for parenthood can range from a totally random process to one that is biased by the chromosome fitness. The modified

Queen bee evolution operators are discussed in subsection 2.2.1. Crossover operator is used to exchange genetic materials between the parents with the aim of obtaining better chromosomes. Two parent chromosomes are selected from the mating pool randomly and the crossover rate determines the probability of producing a new chromosome from the parents. A number of crossover operators are discussed in the literature [13-16]. The crossover operator relevant to the investigations in this paper is detailed in subsection 2.2.2. The mutation operator is next applied. The mutation operator takes each child chromosome and randomly change some of its genes with a given mutation probability. Flipping a bit in the binary coded GA does mutation. While in non-binary coded GA, mutation involves randomly generating a new character in a specified position.

2.2.1 Modified Queen Bee Evolution (Parent selection operator)

The queen bee algorithm is described in [17], this algorithm is limited to a single pool (honeycomb). Author has another concept that bee algorithm should not be restricted to a single pool. In nature honeycombs grow around queen bee, and if any queen bee will born in a honeycomb, she build another honeycomb by sharing the members from her parent honeycomb. The same concept is applied in proposing the modified queen bee algorithm. The schematic diagram of splitting of pools, generation by generation, with the availability of queen bee for modified bee genetic algorithm is shown in Figure 2. Since each member (solution) of the pool has to crossover with queen (most fitted solution) of the pool. After splitting the parent pool due to the birth of queen bee (next most fitted solution), above-mentioned mating process makes the specified population size of the pool. The new queen in a pool is identified if any solution has the fitness very close (say 98%) or above of the fitness of the mother queen. At the same time some of the beehives disappear due to

some accidental process, i.e., death of queen bee, attack of bear/harvester in search of honey as food, storm etc. Only the best fitted beehives survive longer. This process is also imitated in the proposed genetic algorithm by limiting the number of pools. It is shown in the last stage of Figure 2. By limiting the six pools in a generation least fitted pools, i.e., pool 1 and pool 7 are disappearing from that generation.

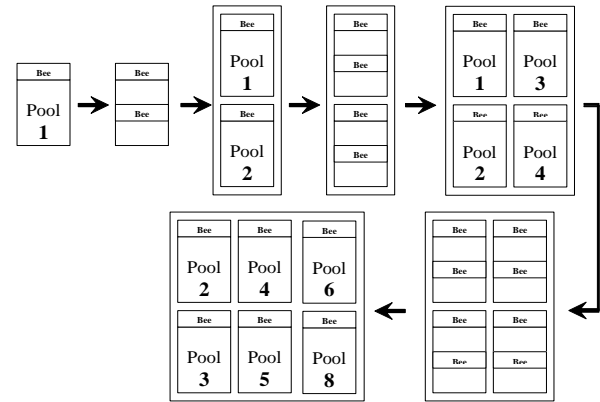


Figure (2) Schematic diagram of splitting of pools generation by generation in modified Queen bee evolution

2.2.2 Weighted Based Crossover Operator

In uniform crossover the gene selection is purely random. Each bit is crossed with some probability, typically one half. For each gene in the chromosome, one random value R is generated. If R is more than the probability, the corresponding bit in parent 1 is copied to child 2 and the corresponding bit in parent 2 is copied to child 1, otherwise the corresponding bit in parent 1 is copied to child 1 and the corresponding bit in parent 2 is copied to child 2.

In weighted based crossover operator gene selection is based on the weights assigned to the genes for crossover operation. This will guide GA to search for more new state space [14]. The Uniform crossover is a special case of weighted uniform crossover. In weighted uniform crossover, weights are assigned to each bit/gene in the chromosome according to the similarity of the test patterns in the population and weighted

uniform crossover is performed which is based on some probability that depends on the weights of the parent bits. For example, two parents P1 and P2 are selected to produce two child chromosomes C1 and C2. Each gene $G_{i,1}$ in parent P1 competes against the corresponding gene $G_{i,2}$ of parent P2. If weight $W_{i,1}$ is equal to $W_{i,2}$, the bits are crossed with a given probability as in uniform crossover. If $W_{i,1}$ and $W_{i,2}$ are different, both the child chromosomes are assigned the value of the lighter bit, i.e., bit with weight 0 as shown in Figure 3. The rules for Weight based crossover operator are shown in Table 1.

The Genetic Algorithm based on modified queen bee evolution is described in Algorithm 1.

Table 1: Rules For WCO

OPERATION	Bit/gene Weight of Parent 1	Bit/gene Weight of Parent 2
Same as uniform crossover	0	0
Assign bit of P1 to both C1&C2	0	1
Assign bit of P2 to both C1&C2	1	0
Same as uniform crossover	1	1

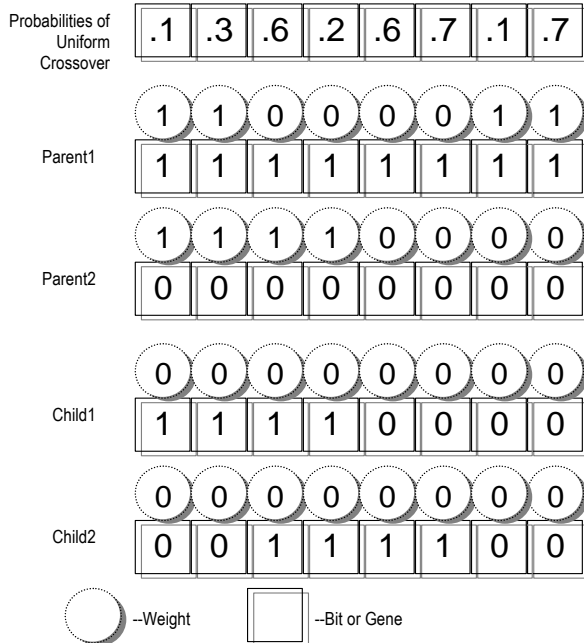


Figure (3) Schematic representation of weight base uniform crossover

Algorithm 1:

```

//t: generation//, //n: population size in a pool//,
//pl: number of pools//, //P: populations//,
//plmax: maximum number of pools//
//ξ: normal mutation rate//,
//pm: normal mutation probability//,
//pm: strong mutation probability//,
//Iq: a queen bee//, //Im: selected bee//
1  t ← 0: pl(t) ← 1; initialize P{pl(t)}; evaluate P{pl(t)}
2  while 1 (not terminate condition)
3  do
4      t ← t+1
5      while 2 [pl(t)]
6      do 2
7          select P{pl(t)} from P{pl(t-1)(*)}
8          P{pl(t)} = [ Iq{pl(t-1)}, Im{pl(t-1)} ]
9          recombine P{pl(t)}; do crossover; do mutation (*)
10         for i=1 to n
11             if i ≤ (ξ×n)
12                 do mutation with pm
13             else
14                 do mutation with pm'
15             end if
16         end for
17         evaluate P{pl(t)}; search for new_ Iq{pl(t)}
18         if ( new_ Iq{pl(t)} found )
19             split the pool and new_pl(t) ← pl(t)+1
20         else
21             new_pl(t) ← pl(t)
22         end if
23         if (new_pl(t) > plmax)
24             pl(t) ← plmax (oldest pool deleted)
25         end if
26     end while2
27 end while1
  
```

2.3 Implementation

For the design of FKBC, the domain of e , ce and du [-1, +1] are partitioned into three Fuzzy sets (N, Z, P) by Gaussian membership functions (with variance 0.4246) as shown in Figure 4. The nine rules of FKBC are listed as lookup table in Table 2. For 'and' an implication operation 'min' operator is used, while 'max' operator for 'or' and aggregation operation. Centroid method of defuzzification is applied.

The same designed FKBC is applied to four different examples. The models in Example1, Example2 and Example3 are taken from [18] with addition of delay factor while the Example4 is taken from [19]. These models are only used for simulation and appear as black box to the FKBC. A genetic algorithm, based on modified

queen bee evolution and weight base crossover, tunes the scaling factors of FKBC. Reciprocal of ITAE is used to determine the fitness of solution, which guides the whole evolution process. The results obtained are compared with the GA using roulette wheel method of parent selection. Rests of the GA operators remains the same as of the earlier one. Various parameter values for GA are listed in Table 3.

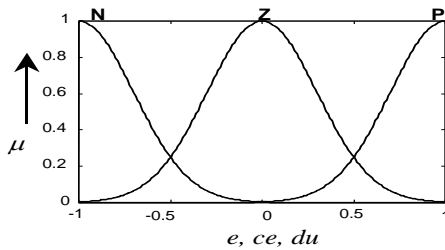


Figure (4) Partition of e , ce and du by Gaussian membership functions.

Table 2: 9 Rules of FKBC

ce	N	Z	P
e			
N	1. N	4. N	7. Z
Z	2. N	5. Z	8. P
P	3. Z	6. P	9. P

Table 3: Values of GA Parameters

Parameters	Values	
	Modified Queen bee	Roulette Wheel
Crossover Probability (p_c)	0.8	0.8
Normal Mutation Probability (p_m)	0.01	0.01
Population Size	15	100
Individual bit length	10	10
Normal Mutation Rate (ξ)	0.6	--
Normal Mutation Probability (p_m)	0.4	--
Maximum Number of Pools	9	1

Note that the population size for modified queen bee method is fifteen in a pool. As the simulation

progress and the maximum number of pool, i.e. nine, reached the number of solution is to be one hundred thirty five. However, in the beginning the number of solution, whose fitness has to be tested, is far less than the number of solution for the roulette wheel method. The simulation is carried out for small size problem; it can be applied to large size problem too.

3. Results and Discussion

3.1 Example1: Absolutely Stable System

The model transfer function is:

$$G_1(s) = 2e^{-s} / [(s+1)(s+2)] \quad (5)$$

This is an absolutely stable system because all poles lie in the left half of the s-plane on real axis (i.e., $s = -1, -2$). Since the poles lies on the real axis of s-plane, it gives an offset error in step-response. In addition to this the presence of dead time makes the system difficult to control. Therefore the use of PI-like FKBC structure as given in (2) is justifiable.

The learning patterns of scaling factors K_e , K_{ce} and K_{du} for example 1 are shown in Figure 5. The maximum fitness value of 3.4×10^{-3} with ITAE=294.5208 is achieved in ten generation with modified queen bee evolution. Figure 6, shows the responses of the system after learning using the learned values of parameters based upon above mentioned methods.

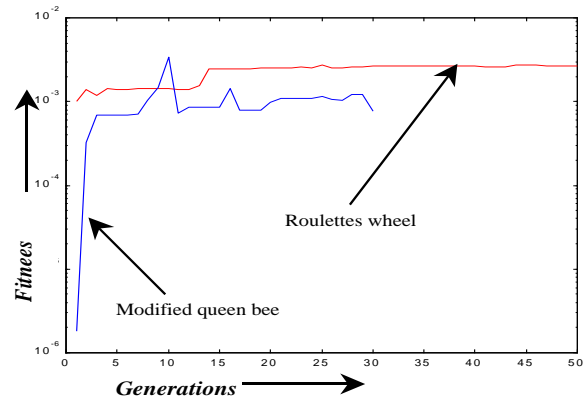


Figure (5) GA based Learning patterns for Example 1.

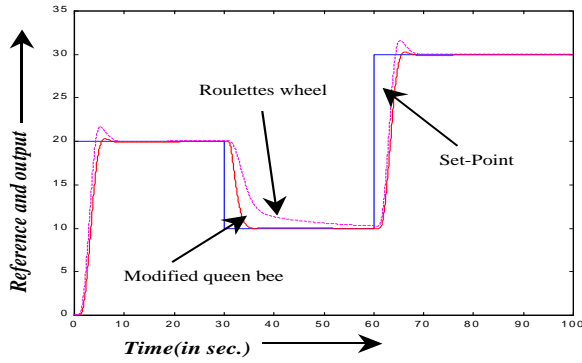


Figure (6) Responses for Example 1.

3.2 Example2: Under damped Stable System

The model transfer function is:

$$G_2(s) = 2e^{-s} / [s(s + 1.4) + 2] \quad (6)$$

System in (6) is under damped and stable, because the open poles are complex conjugate and lie in left half of the s-plane (i.e., $s = -0.7 \pm j1.229$) and produce a damped oscillatory response for a step input, besides this the presence of dead time makes the system more difficult to control. PD-like FKBC structure as given in (1) is used for improving the performance of the system.

The learning patterns of scaling factors of FKBC for system in (6) are shown in Figure 7. The maximum fitness value 1.9×10^{-3} with ITAE=520.6633 is achieved in 25 generation with modified queen bee evolution. Figure 8, shows the responses of the system after learning with the learned parameter obtained from described methods of evolution.

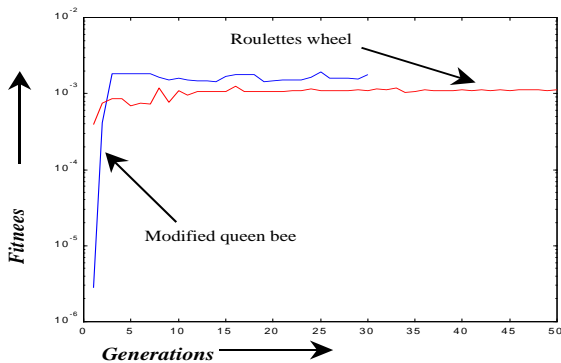


Figure (7) GA based Learning patterns for Example 2.

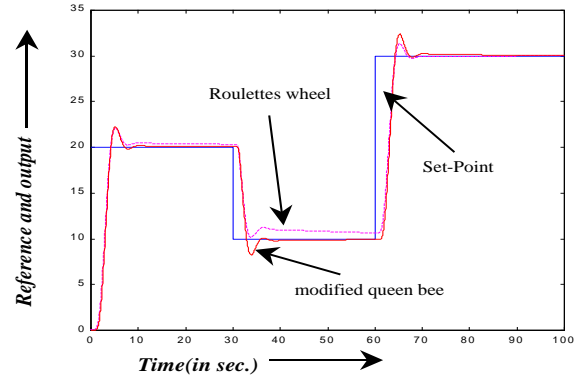


Figure (8) Responses for Example 2.

3.3 Example3: Marginally Stable System

Let us consider a marginally stable system whose transfer function is:

$$G_3(s) = 10e^{-s} / s(s + 10) \quad (7)$$

This is a marginally stable system because one of its poles is at origin of the s-plane (i.e., $s = 0$). Moreover, presence of dead time makes the system more difficult to control. For such system PD-like FKBC structure is an obvious choice.

The learning patterns of scaling factors of FKBC for system in (7) are shown in Figure 9. The highest fitness value 5.7×10^{-3} with ITAE=175.0739 is achieved in 17 generation with modified queen bee evolution. Figure 10, shows the responses of the system after learning using the learned parameters.

3.4 Example4: Nonlinear System

Consider a nonlinear system governed by:

$$\frac{d^2 y(t)}{dt^2} + \frac{dy(t)}{dt} + 0.25y^2(t) = u(t - 0.1) \quad (8)$$

System expressed by (8) is a second order nonlinear system. Its open loop response shows highly over damped characteristic. For such system PI-like FKBC structure is an obvious choice.

The learning patterns of scaling factors of FKBC for system in (8) are shown in Figure 11. The highest fitness value of 2.0×10^{-3} with

ITAE=501.4122 is achieved in 24 generation with modified queen bee evolution. Figure 12 shows the responses of the system after learning using the learned parameters. Since the learned parameters are very closed, as shown in Table 4, the reason for overlapping response is because.

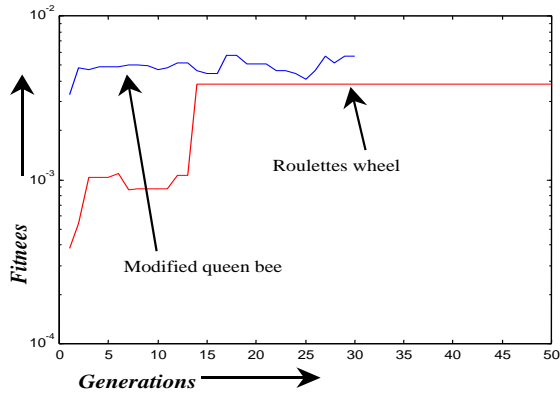


Figure (9) GA based Learning patterns for Example 3.

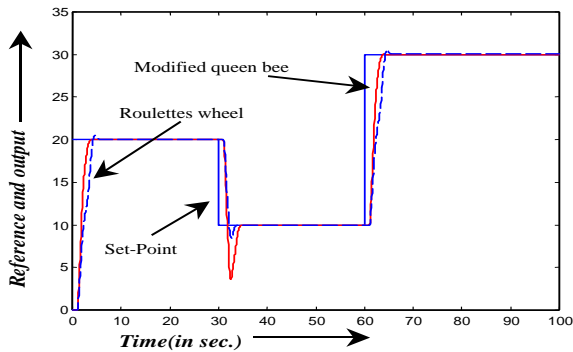


Figure (10) Responses for Example 3.

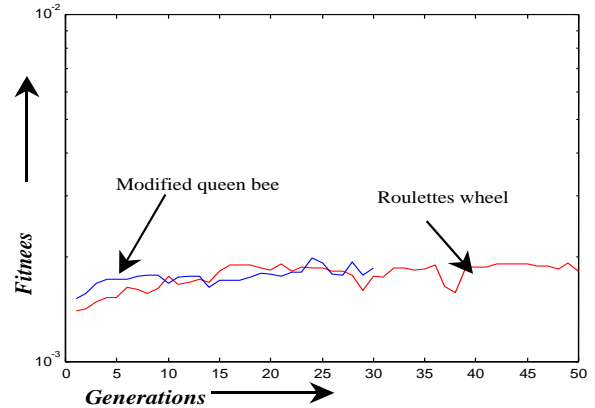


Figure (11) GA based Learning patterns for Example 4.

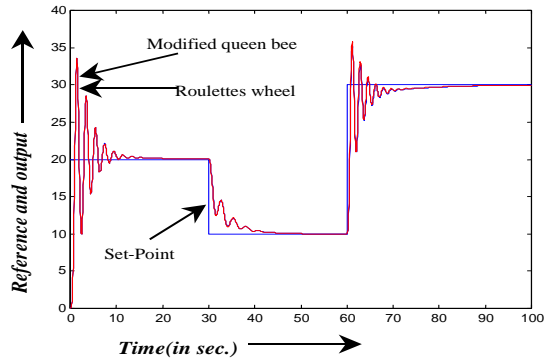


Figure (12) Responses for Example 4.

Comparison of results for all examples is given in Table 4. It is obvious from the table that the maximum fittest solution, for all the examples is obtained by modified queen-bee based GA method.

Table 4: Comparison of Results

13th Annual Research Day

Organised by the Deanship of Scientific Research in Collaboration with the College of Engineering
Research Centre
2nd April 2018

Result Parameters		Fitness	ITAE	Generation	K_c	K_e	K_{ce}
Example1	Modified Queen bee	3.4×10^{-3}	294.5028	10	0.0061	0.0101	127.0528
	Roulettes Wheel	2.7×10^{-3}	365.9086	76	0.0090	0.0148	64.8045
Example2	Modified Queen bee	1.9×10^{-3}	520.6633	25	0.0096	0.0098	54.6070
	Roulettes Wheel	1.2×10^{-3}	810.4989	16	0.0163	0.0057	10.3460
Example3	Modified Queen bee	5.7×10^{-3}	175.0739	17	0.0808	0.0355	34.4839
	Roulettes Wheel	3.9×10^{-3}	253.9126	14	0.0813	0.0519	23.4516
Example4	Modified Queen bee	2.0×10^{-3}	501.4122	24	0.0100	0.0010	993.2258
	Roulettes Wheel	1.9×10^{-3}	520.6725	49	0.0099	0.0009	997.0968

4. Conclusions:

The proposed modified queen bee evolution is implemented for the tuning of FKBC scaling factor for non-linear complex system. The result is compared with roulette wheel parent selection method. Comparison results are encouraging. Results show that faster learning is achieved by modified queen-bee based GA besides better performance (less value of ITAE) of closed loop system. Moreover, same FKBC is applied for all the four examples.

Acknowledgement

We are highly thankful to the King Khalid University and College of Engineering for providing this excellent platform of Research Day to present our research work.

References

- [1] Zadeh L. A., "Outline of a new Approach to the Analysis of complex systems and decision process", IEEE Trans. Syst. Man. Cybern., vol. 3, no. 1, pp.28-44, 1973 & vol 15, pp. 15-30, 1979
- [2] G. Caste llano, G. Attolico, and A. Distant, "Automatic generation of fuzzy rules for

reactive robot controllers", Robot. Auton. Syst., vol.22, pp. 133–149, 1997.

- [3] L. X. Wang and J. M. Mendel, "Generating fuzzy rules by learning from examples", IEEE Trans. Syst., Man, Cybern., vol. 22, pp 1414–1427, Feb. 1992.
- [4] D. Park, A. Kandel, and G. Langholz, "Genetic-based new fuzzy reasoning models with application to fuzzy control", IEEE Trans. Syst., Man, Cybern., vol. 24, pp. 39–47, Jan. 1994
- [5] F. Hoffmann and G. Pfister, "Learning of a fuzzy control rule base using messy genetic algorithms", in Genetic Algorithms and Soft Computing. Ser. Studies in Fuzziness and Soft Computing, F. Herrera and J. L. Verde gay, Eds. Heidelberg, Germany: Physica-Verlag, 1996, vol. 8, pp. 279–305.
- [6] C.L. Karr and E.J. Gentry, "Genetic algorithm for fuzzy logic controller", AI Expert Vol 2 pp. 26-33, 1991.
- [7] C.L. Karr and E.J. Gentry, "Fuzzy control of pH using GA", IEEE Trans. Fuzzy System, vol. 3, pp. 185-193, 1994.
- [8] Chokri, Djemel, Nabil, Adel, "Design of optimal FLC with GA", IEEE Intern. sym. on intelligent control. pp.98-103, 2002.
- [9] E.H. Mamdani and S Asian, "An experiment in linguistic synthesis with a fuzzy logic controller", Int. J. Man-Mach. Stud. vol.7, no.1, pp.1-13, 1975.
- [10] Zadeh L.A., "Fuzzy sets", Inf. Contr., vol 21. pp. 338-353, 1965.
- [11] Holland J.H, "Adaptation in neural and artificial systems", Univ. of Michigan press, Ann Arbor, 1975.
- [12] Davis, L, "A handbook of Genetic Algorithms", Van Nostrand Reinhold, New York 1990.
- [13] D.E. Goldberg, "Genetic Algorithm in search, optimization and Machine learning", Addison-Wesley 1989.

13th Annual Research Day

Organised by the Deanship of Scientific Research in Collaboration with the College of Engineering
Research Centre
2nd April 2018

- [14] Bhuvaneswari MC and Sivavandam SN, “Genetic Algorithm based Test Generation: An Analysis of Crossover Operators”, The Journal of The Computer Society of India, vol. 32, No.1, pp10-17.
- [15] DF. Jong KA and SpearsWM, “An Analysis of the interacting roles of population size & cross over in genetic Algorithms”, in Proc. of the first workshop on parallel problem solving from nature, Schwefel HP and Manner R (Eds), Dotmund, West Germany (Springer-verlag, Berlin, 1990), pp.39-47.
- [16] Syswerda G, “Uniform crossover in Genetic Algorithms”, in Proc of the third international conference on Genetic Algorithms, Schaffer, J (Ed); (Morgan Kauffman Publishers, Cambridge, MA, 1989), pp. 2-9.
- [17] Sung Hoon Jung, “Queen bee evolution for genetic algorithms”, Electronics letters, 20th March 2003, Vol. 36 No. 6 pp. 575-576. Online No.20030383, DOI: 10.1049/el: 20030383,IEEE 2003.
- [18] Cheong, F. and Lai, R, “On simplifying the automatic design of a fuzzy logic controller”; in Proc. NAFIPS. 2002, Annual Meeting of the North American, Fuzzy Information Processing Society, 2002, pp.481–487, 27-29 June 2002
- [19] Rajni K. Mudi and Nikhil R. Pal, “A robust self-tuning scheme for PI- and PD-type fuzzy controllers”. IEEE Trans. On Fuzzy Systems. 7(1). pp. 2—16, February 1999.

13th Annual Research Day

Organised by the Deanship of Scientific Research in Collaboration with the College of Engineering
Research Centre
2nd April 2018

Green Siliceous Concrete Materials for Sustainability using MCDM Approach

Mohd. Ahmed¹, M.N. Qureshi², Javed Mallick¹

¹Department of Civil Engineering., College of Engineering, King Khalid University,

²Department of Industrial Engineering., College of Engineering, King Khalid University,

PO Box 394, Abha 61411 KSA.

E-mail address: mall@kku.edu.sa

Abstract: There are numbers of siliceous concrete materials available now-a days ranging from industries by-products, agro-products, waste product to newly engineered materials. Due to the wide range impact of the use of different construction materials on the society, economy and environment, the selection of the siliceous materials for concrete is challenging and development of multi-criteria decision-making (MCDM) techniques may be utilized to incorporate social, economic and environmental aspect of green and sustainable material. The paper proposes a decision support framework for sustainability and green qualification of concrete siliceous material considering technical, environmental, social and economic indicators. It is concluded that among the sustainable goals to be fulfilled by the concrete siliceous materials, the environmental criteria to be taken as the priority objectives for the selection of siliceous concrete materials and social criteria have lesser impact for the selection of siliceous concrete materials. The engineered materials are found to be the most preferred siliceous concrete materials for sustainability. The present study thus offer an important contribution by developing MCDM based decision support framework to qualify the construction siliceous material as green and sustainable in order to provide much needed sustainability and an enhanced eco-friendly environment.

Keywords: Concrete Manufacturing, Fuzzy TOPSIS, Multi Criteria Decision Making(MCDM, Green Siliceous Materials, Sustainability

1. Introduction:

Concrete is a mixture of aggregate and cementitious material. The siliceous materials can be added to concrete for making concrete eco-friendly material with enhanced durability and reduced production cost. The selection of construction material to provide all-round performance is a complex process. It is the significant issue in a construction sector as the materials account for a considerable portion of the structure total cost [1]. The cement component in concrete production is the most expensive and has negative impact on environment. The cement production emits approximately 5% of global carbon dioxide and consumes about 5% of global energy [2]. Thus, it is mandatory to follow standards for most needed sustainability in construction industry to make the concrete materials, cost and resource

effective, and environment friendly. It is pointed out that Technique for Order of Preference by Similarity to Ideal Solution (TOPSIS) is the suitable MCDM technique for sustainable concept selection [3]. The environmental, social and economic impact based selection model is developed by [4] for sustainable building materials and established that environmental criteria should be given priority over the social and economic criteria for sustainable building construction. The factors that hinder the selection of sustainable building materials by construction industry stockholders are examined in [5] and identified that perception of extra cost and lack of materials information are the main obstacles to sustainable materials selection. The MCDM techniques Fuzzy Extended Analytical Hierarchy Process (FEAHP) [6], integrated AHP–TOPSIS–entropy methods approach [7] and Fuzzy

13th Annual Research Day

Organised by the Deanship of Scientific Research in Collaboration with the College of Engineering
Research Centre
2nd April 2018

Analytic Hierarchical Process [8] are applied for the sustainable ranking of the structural material. An integrated multi criteria decision making approach based on case study and respondent feedback, for sustainable material selection for construction industry in given in [9]. Choosing by Advantages (CBA) approach has been used by [10] to compare and select the building material based on sustainable criteria.

The material selection for concrete products for green or sustainable qualification are carried out using well-defined sustainable indicators related to technical, environmental, and socio-economic issues. The applications of MCDM for the selection of green construction materials especially siliceous concrete materials for construction industry are exceedingly scarce. The present study has applied MCDM techniques based on fuzzy technique for order of preference by similarity to ideal solution (FTOPSIS) approach for qualifying green materials to siliceous construction materials.

2. Selection of Sustainability Evaluation Indicators:

The sustainability indicators satisfying the technical, environmental, social and economic criteria are framed for evaluating sustainability of siliceous material. In the present research, wide spectrums of indicators have been employed. The present model adopts eight (8) technical, six (6) environmental, three (3) social and three (3) economical situations based indicators in ranking of siliceous concrete materials. The adopted technical sustainability indicator for concrete siliceous material includes relative proportion of concrete components, material availability, support of siliceous material to concrete curing system, compaction system, cohesiveness and consistency of concrete mix and effect of addition of siliceous material on strength and durability requirement of concrete. The sustainability indicators for the selection of concrete siliceous material to achieve the environmental objectives covers energy

conservation, concrete material conservation, waste material utilization, conformation to environmental standards, reduction in carbon foot print and resistance to extreme exposure conditions. The sustainability indicators for concrete siliceous material to fulfill the socio-economic goals are considered as waste material cleaning, public welfare and safety, increased employment, concrete production cost, siliceous material transportation cost and life-long maintenance cost. The twenty sustainability indicators as listed in Table 1 that are formed through comprehensive literature review and experts' opinion.

Table 1: Sustainable Criteria along with Sustainability Indicators (Sub-criteria) for Selection of siliceous Concrete Materials

Criteria	Sub-criteria (<i>Indicators</i>)
Technical	<i>Support to Concrete Curing System</i>
	<i>Support to Concrete Compaction System</i>
	<i>Support to Cohesiveness of Concrete Mix</i>
	<i>Support to Consistency of Concrete Mix</i>
	<i>Comply Strength Requirement of Concrete Mix</i>
	<i>Comply durability Requirements of Concrete Mix</i>
	<i>Relative Proportion of Concrete Components</i>
	<i>Siliceous Material Availability</i>
Environm-ental	<i>Energy Conservation</i>
	<i>Concrete Material Conservation</i>
	<i>Waste Material Utilization</i>
	<i>Conformation to environmental standards</i>
	<i>Reduction in Carbon Foot Print</i>
	<i>Resistance to Extreme Exposure conditions</i>
Social	<i>Waste Material disposing</i>
	<i>Public Welfare and Safety</i>
	<i>Increased Employment</i>
Social	<i>Concrete Production Cost</i>
	<i>Siliceous Material Transportation Cost</i>
	<i>Life Long Maintenance Cost</i>

3. Fuzzy TOPSIS methodology

The fuzzy sets theory was introduced by [11] to express the linguistic terms in decision-making process to reduce the difficulty of human judgment. The TOPSIS method, a linear weighting technique, was first proposed by [12]. The weights to the criteria can be assigned using variety of method for instance analytic hierarchy process (AHP), analytic network process (ANP), entropy analysis, mean weight (MW), standard deviation (SD), eigenvector method etc. The proposed MCDM based Fuzzy TOPSIS approach is implemented to the problem of ranking the sustainable concrete siliceous material. Based on in-depth literature review and for model framework, eleven most common siliceous concrete materials are identified. It includes Nano-Cement, Nano-Particles of Siliceous Material, Natural Pozzolana, Metakaolin, Silica Fume, Fly Ash, Rice Husk Ash, Blast Furnace Slag, Lime Stone, Waste Glass, and Recycled Aggregate etc.. The adopted Fuzzy-TOPSIS based framework for the ranking of sustainable siliceous concrete materials is shown in Figure 1.

The experts having commendable experience in concrete technology, is asked to judge and rank the selected sustainable criteria and sustainable indicators. A questionnaire (Sample Questionnaire-1 is shown in Appendix-I) based on linguistics terms and triangular fuzzy number (TFN) is offered for establishing the importance of criteria and role of siliceous concrete materials towards sustainability. Questionnaire-1 uses five linguistic terms [13], namely *very low*, *low*, *medium*, *high* and *very high*, along with corresponding triangular fuzzy numbers (TFN) of (0,0.1,0.3), (0.1,0.3,0.5), (0.3,0.5,0.7), (0.5,0.7,0.9) and (0.7,0.9,1) respectively reflecting the importance weights of each performance criteria in providing sustainability in concrete siliceous material. Later on Questionnaire-2 was administered which uses five linguistic terms [14], namely *Very poor*, *Poor*, *Fair*, *Good* and *Very good*, along with corresponding triangular fuzzy numbers (TFN) of (0,1,3), (1,3,5), (3,5,7), (5,7,9) and (7,9,10) to ascertain the role of each

concrete siliceous material to provide the much needed sustainability on the selected set of twenty criteria. In order to find the preferential sustainable concrete siliceous material, the selected criteria were further utilized to rate the performance of each preferential concrete siliceous material using notion i.e. displaced ideal separated away from the ideal solution the least [15]. According to [12], the chosen alternative should have the ideal distance (most nearest to positive and most farthest from the negative) in comparison to others i.e. the alternatives should not only have the shortest distance from the positive ideal reference point (PIRP), but also have the longest distance from the negative ideal reference point (NIRP). The standard algorithms given in literature [1] are used.

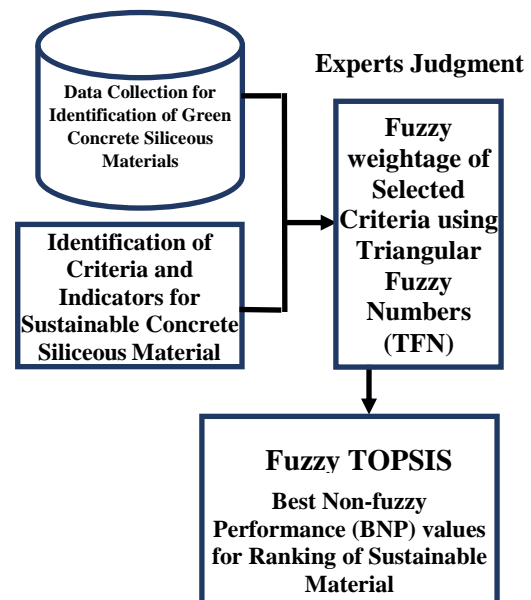


Figure 1. Fuzzy-TOPSIS Based Framework for Sustainable Ranking of Siliceous Concrete material

3.1 Construction of the fuzzy decision matrix for sustainability problem

Given m alternatives for sustainable concrete supplementary material, n selection criteria and k expert group comprising experts, a typical fuzzy multi-criteria group decision-making

sustainability problem can be expressed in matrix format as:

$$\tilde{D} = \begin{matrix} & C_1 & C_2 & \dots & C_n \\ \begin{matrix} A_1 \\ A_2 \\ \vdots \\ A_m \end{matrix} & \begin{bmatrix} a_{11} & a_{12} & \dots & a_{1n} \\ a_{21} & a_{22} & \dots & a_{2n} \\ \vdots & \vdots & \ddots & \vdots \\ a_{m1} & a_{m2} & \dots & a_{mn} \end{bmatrix} \end{matrix}, \quad i = 1, 2, \dots, m; j = 1, 2, \dots, n \quad (1)$$

where A_1, A_2, \dots, A_m are the alternatives materials to be chosen, C_1, C_2, \dots, C_n denote the sustainability evaluation criteria for concrete supplementary material, \tilde{D}_{ij} represents the rating of alternative materials A_i with respect to sustainability criterion C_j evaluated by k experts. Since the perception toward ranking the sustainable concrete supplementary material is subject to an individual's experience, intuition or knowledge, this study therefore applies the method of average value to integrate the fuzzy performance score \tilde{x}_{ij} for k experts concerning the same evaluation criteria, that is

$$\tilde{x}_{ij} = \frac{1}{k} (\tilde{x}_{ij}^1 + \tilde{x}_{ij}^2 + \dots + \tilde{x}_{ij}^k) \quad (2)$$

where \tilde{x}_{ij}^k is the rating of alternative A_i with respect to criterion C_j evaluated by the k^{th} expert and $\tilde{x}_{ij}^k = (a_{ij}^k, b_{ij}^k, c_{ij}^k)$.

3.2 Normalization of fuzzy decision matrix

The various criteria required to select the sustainable concrete supplementary material are measured in different units hence they are required to be normalized. The present case adopts linear scales to transform the normalization function in order to preserve the property that the ranges of normalized TFN to be included in [0, 1]. If \tilde{R} denotes the normalized fuzzy decision matrix, then

$$\tilde{R} = [\tilde{r}_{ij}]_{m \times n}, i = 1, 2, \dots, m; j = 1, 2, \dots, n \quad (3)$$

$$\text{where } \tilde{r}_{ij} = \left(\frac{a_{ij}}{c_j^+}, \frac{b_{ij}}{c_j^+}, \frac{c_{ij}}{c_j^+} \right)$$

$$C_j^+ = \max_i C_{ij} \quad (4)$$

3.3 Construction of weighted normalized fuzzy decision matrix for sustainability problem

Considering the different weight of each sustainability criterion, the weighted normalized decision matrix can be computed by multiplying the importance weights of evaluation criteria and the values in the normalized fuzzy decision matrix. The weighted normalized decision matrix \tilde{v} is defined as

$$\tilde{v} = [\tilde{v}_{ij}]_{m \times n}, i = 1, 2, \dots, m; j = 1, 2, \dots, n \quad (5)$$

$$\tilde{v}_{ij} = r_{ij} \otimes \tilde{w}_j \quad (6)$$

where \tilde{w}_j represents the importance weight of criterion C_j obtained through

$$\tilde{w}_j = \frac{1}{K} (\tilde{w}_j^1 + \tilde{w}_j^2 + \dots + \tilde{w}_j^k) \quad (7)$$

where k is the number of expert members in a group and \tilde{w}_j^k represents the fuzzy weight of j th criteria assessed by k th expert.

3.4 Determination of the FPIRP and FNIRP

The fuzzy positive ideal reference point (FPIRP, A^+) and fuzzy negative ideal reference point (FNIRP, A^-) in the interval [0, 1] can be represented as:

$$A^+ = (\tilde{v}_1^+, \tilde{v}_2^+, \dots, \tilde{v}_n^+) \quad (8)$$

$$A^- = (\tilde{v}_1^-, \tilde{v}_2^-, \dots, \tilde{v}_n^-) \quad (9)$$

where $\tilde{v}_j^+ = (1, 1, 1)$ and $\tilde{v}_j^- = (0, 0, 0)$, $j = 1, 2, \dots, n$

3.5 Calculation for the distances of each concrete supplementary material to FPIRP and FNIRP

The distance of each concrete supplementary material alternate from fuzzy positive ideal reference point (FPIRP) and fuzzy negative ideal

reference point (FNIRP) can be derived respectively as:

$$d_i^+ = \sum_{j=1}^n d(\tilde{v}_{ij}, \tilde{v}_j^+),$$

$$i=1, 2, \dots, m; j=1, 2, \dots, n \quad (10)$$

$$d_i^- = \sum_{j=1}^m d(\tilde{v}_{ij}, \tilde{v}_j^-),$$

$$i=1, 2, \dots, m; j=1, 2, \dots, n \quad (11)$$

where $d(\tilde{v}_{ij}, \tilde{v}_j)$, denotes the distance measurement between two fuzzy numbers, d_i^+ represents the distance of alternative L_i from FPIRP, and d_i^- is the distance of alternative L_i from FNIRP.

3.6 Process to obtain the closeness coefficient and rank the order of alternatives

Once the closeness coefficient (CC) is determined, the ranking order of all alternatives can be obtained, allowing the decision-makers to select the most feasible alternative. The closeness coefficient of each alternative is calculated as

$$cc_i = \frac{d_i^-}{d_i^+ + d_i^-}, \quad i=1, 2, 3, \dots, m \quad (12)$$

An alternative with index cc_i approaching 1 indicates that the alternative is close to the fuzzy positive ideal reference point and far from the fuzzy negative ideal reference point. A large value of closeness index indicates a good performance of the alternative A_i .

4. Assessment of Sustainable Siliceous Concrete Material

The ranking of concrete siliceous material with sustainable objectives is a multi-criteria decision-making process. After the initial problem formulation, expert advice and opinion may be sought to determine the sustainable assessment criteria and indicators. Experts may employ their vast experience and expertise while ranking concrete siliceous material according to merits for sustainability. The use of linguistic terms and corresponding TFN will help to make their decision in fuzzy based assessment. The fuzzy TOPSIS methodology is employed. The

five experts were asked to judge the role of criteria in providing the sustainability. They may also be asked to judge the role of each concrete siliceous material in providing the sustainability. The detailed methodology adopted in ranking the concrete siliceous material, as per the closeness to sustainability goals, is documented in the following section.

5. Calculation of the synthetic importance weights of evaluation criteria

The expert group expressed their opinion in linguistic terms for their preference of sustainability evaluation indicators [13], namely very low, low, medium, high and very high, corresponding to its TFN. To understand the importance order of these selection criteria, the center of area (COA) method [16] was utilized to de-fuzzify TFN into corresponding best non-fuzzy performance (BNP) values. The twenty most important sustainable indicators for assessing concrete siliceous materials for sustainability with corresponding BNP values are presented in Table 2 as C_1 (0.66), C_2 (0.72), C_3 (0.70), C_4 (0.7267), C_5 (0.76), C_6 (0.72), C_7 (0.6867), C_8 (0.42), C_9 (0.7667) and C_{10} (0.8667), C_{11} (0.80), C_{12} (0.7667), C_{13} (0.7333), C_{14} (0.7667), C_{15} (0.4133), C_{16} (0.3933), C_{17} (0.38), C_{18} (0.4267), C_{19} (0.40), and C_{20} (0.46). The maximum BNP value is obtained for sustainable indicator of 'concrete material conservation (C_{10})', while the minimum BNP value is obtained for sustainable indicator of 'increased employment (C_{17})'.

5.1 Construction of the fuzzy decision matrix

The ranking of concrete siliceous materials is an important issue for sustainable concrete objective. In order to accomplish sustainability goal, a systematic performance analysis of various sustainability criteria and their indicators are carried out. The experts gave their feedback in linguistic terms. The experts used the linguistic terms very poor, poor, fair, good and very good

13th Annual Research Day

Organised by the Deanship of Scientific Research in Collaboration with the College of Engineering
Research Centre
2nd April 2018

along with TFN as depicted in appendix-I, to express their opinions for each concrete siliceous materials based on their individual capability against each sustainability evaluation indicators. The fuzzy performance ratings of each concrete siliceous material regarding evaluation indicators are averaged to synthesize the various individual judgments. With Eq. (1), the synthetic fuzzy decision matrix can be computed. Fuzzy weights are obtained after normalizing the BNP values.

Table 2: The fuzzy importance weight, BNP and rank of each Indicator

Indicators	Fuzzy importance weight	BNP values	Rank
C ₁	(0.460,0.660,0.860)	0.66	13
C ₂	(0.540,0.740,0.880)	0.72	9
C ₃	(0.500,0.700,0.900)	0.70	11
C ₄	(0.540,0.740,0.900)	0.7267	8
C ₅	(0.580,0.780,0.920)	0.76	6
C ₆	(0.540,0.740,0.880)	0.72	9
C ₇	(0.500,0.700,0.860)	0.6867	12
C ₈	(0.220,0.420,0.620)	0.42	16
C ₉	(0.580,0.780,0.940)	0.7667	3
C ₁₀	(0.700,0.900,1.000)	0.8667	1
C ₁₁	(0.620,0.820,0.960)	0.80	2
C ₁₂	(0.580,0.780,0.940)	0.7667	5
C ₁₃	(0.540,0.740,0.920)	0.7333	7
C ₁₄	(0.580,0.780,0.940)	0.7667	3
C ₁₅	(0.220,0.420,0.600)	0.4133	17
C ₁₆	(0.240,0.380,0.560)	0.3933	19
C ₁₇	(0.220,0.420,0.500)	0.3800	20
C ₁₈	(0.240,0.420,0.620)	0.4267	15
C ₁₉	(0.240,0.400,0.560)	0.40	18
C ₂₀	(0.260,0.460,0.660)	0.46	14

5.2 Calculation of normalized fuzzy decision matrix and weighted normalized matrix

The ensure that the normalized triangular fuzzy numbers were included in the interval [0, 1], linear scale transforms function is used. The synthetic fuzzy decision matrices are normalized using the Eqs. (2) – (4). Normalization process is carried out by dividing each row by maximum of that row. The normalized fuzzy numbers are later on applied importance weights, since the

importance weights of criteria are different, Equations (6) and (7) can be employed for the fuzzy weighted normalized decision matrix.

5.3 Determination of the fuzzy positive and fuzzy negative ideal reference point

As the positive TFN are in the range of [0, 1], so the fuzzy positive ideal reference point and fuzzy negative ideal reference point can be defined as:

$$A^+ = [(1,1,1), (1,1,1), (1,1,1), (1,1,1), (1,1,1)]$$

$$A^- = [(0,0,0), (0,0,0), (0,0,0), (0,0,0), (0,0,0)]$$

5.4 Calculation for the distance of each concrete siliceous material to FPIRP and FNIRP and determining the closeness coefficient (CC) for ranking of concrete siliceous material

The distance of each concrete siliceous material to the FPIRP and FNIRP can be calculated using Eqns. (10) and (11). Once the distances of concrete siliceous material from FPIRP and FNIRP are determined, the closeness coefficient for the concrete siliceous material alternatives can be obtained with Eq. (12). Closeness coefficients are calculated based on the obtained FPIRP and FNIRP. Figure 2 depicts the graphical representation of concrete siliceous materials ranking as per the obtained Closeness Coefficients.

13th Annual Research Day

Organised by the Deanship of Scientific Research in Collaboration with the College of Engineering
Research Centre
2nd April 2018

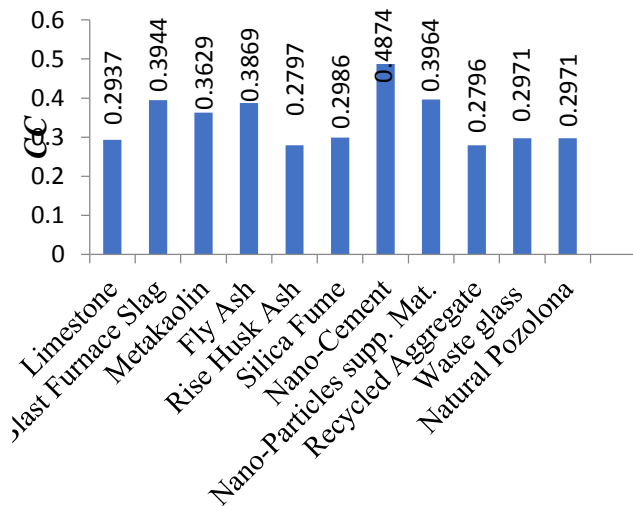


Figure 2 Ranking of each Alternative Material based on Closeness Coefficient

6. Results and Discussion

The Fuzzy- TOPSIS based approach has been implemented to rank the siliceous concrete materials for sustainable development. Various sustainable criteria viz. technical, environmental and socio-economy are considered. It has been observed that, in accomplishing the sustainable goals for siliceous concrete materials, the environmental criteria play a central role, whereas the social criteria play the minor role. It has also been observed that, the most effective sustainable indicator for the ranking of siliceous concrete materials is the 'concrete material conservation'. It indicates that concrete material conservation a major issue and use of siliceous concrete material should be mandatory in construction industry for sustainable development. The least effective sustainable indicator observed is 'the enhanced employment' and siliceous concrete materials application has no major impact on society development. Among the eleven selected siliceous concrete materials, Nano-engineered materials namely Nano-cement and Nano-particles of siliceous material topped the ranked for manufacturing the sustainable concrete. The siliceous materials come next for the sustainable concrete construction. The

recycled material to be used as siliceous concrete materials occupies a lowest rank among the sustainable concrete materials. The ranking of the material in descending order of preference to produce sustainable concrete is: Nano-cement > Nano-particles of siliceous material > Blast Furnace Slag > Fly Ash > Metakaolin > Silica Fume > Waste Glass > Natural Pozzolona > Lime Stone > Rice Husk Ash > Recycled Aggregate, where '>' represents preference over other concrete material. The corresponding closeness coefficients of the eleven siliceous concrete materials are: 0.4874>0.3965 >0.3945>0.3870 > 0.3630>0.2987>0.2971>0.2971> 0.2937> 0.2798 >0.2796 where '>' represents preference over other.

7. Conclusions

Construction industry must look for the sustainability framework to overcome global resources scarcity and environmental impact by adopting sustainable materials in concrete manufacturing processes. The much-needed sustainability may be accrued by considering factors related to technical and environment as well as the socio-economic factors. The concrete manufacturing must adapt to environmental friendly material and processes, which should not only be cost-effective but also provide economic value and safety for the society. In the present study more comprehensive criteria are selected in order to provide sustainability. Moreover, the study adopts twenty sustainability indicators for sustainable siliceous concrete materials, thus covering the sustainability aspects to a larger extent. It is found from the adopted MCDM approach that among the selected sustainable indicators, the most effective sustainable indicator for the ranking of siliceous concrete materials is the concrete material conservation. The least governing sustainable indicator is the enhanced employment. It can be concluded from the study that large scale use of siliceous concrete materials in construction industry will

13th Annual Research Day

Organised by the Deanship of Scientific Research in Collaboration with the College of Engineering
Research Centre
2nd April 2018

help in conservation of basic concrete materials and environmental protection, though it will not have direct impact on society development.

The ranking of the siliceous concrete materials resulted from the present model is based on the *CC* and materials can be classified into two groups i.e. Group I and II. Group I materials are having $CC > 0.3500$ whereas Group II materials are having $CC < 0.3500$. The selected siliceous concrete materials namely, Nano-cement and Nano-particles of siliceous siliceous material, Blast Furnace Slag, Fly Ash and Metakaoline exhibit larger *CC* value hence classified as Group I materials, thus possess higher potential of providing sustainability. The siliceous concrete materials namely, Silica Fume, Waste Glass, Natural Pozolona, Lime Stone and Rice Husk Ash exhibit lower values of *CC*, hence may be regarded to lower capability towards achieving the sustainability in comparison to the Group II. The nano-engineered material, though costly, will prove to be the best material for sustainable concrete construction and development. The present research will be of great importance for the concrete industry dealing with concrete manufacturing and to tackle the challenges like increased manufacturing cost, higher concrete performance requirement, risk free environment and society etc..

References

- [1] Zavadskas, E. K., Kaklauskas, A., and Saparauskas, J. Sustainable urban development and web based Multiple Criteria Analysis. *Foundations of Civil and Environmental Engineering*, 6, (2005), 217-226.
- [2] Yurdakul, E., Optimizing Concrete Mixtures with Minimum Cement Content for Performance and Sustainability, Master of Science, Civil Engineering (Civil Engineering Materials), Iowa State University, Ames, Iowa. (2010).
- [3] Vinodh, S., Mulanjur, G. and Thiagarajan, A., 'Sustainable Concept Selection Using Modified Fuzzy TOPSIS: A Case Study', *International Journal of Sustainable Engineering*, 6(2), (2013) 109 -116.
- [4] Abeysundara, U.G.Y., Babel, and S., Gheewala, S., A matrix in life cycle perspective for selecting sustainable materials for buildings in Sri Lanka, *Building and Environment*, 44/5, (2009) 997-1004.
- [5] Akadiri, P. O., Understanding barriers affecting the selection of sustainable materials in building projects, *Journal of Building Engineering*, 4, (2015) 86–93.
- [6] Akadiri, P. O., Olomolaiye, P. O. and Chinyio, E. A., Multi-Criteria Evaluation Model for the Selection of Sustainable Materials for Building Projects. *Automation in Construction*, 30, (2013) 113–125,
- [7] Bakhoun E. and Brown D., A hybrid approach using for sustainable ranking of structural materials, *International Journal of Sustainable Engineering*. 6 (3): (2013) 212-224.
- [8] Govindan, K., Shankar, K. M., Kannan, D., Sustainable material selection for construction industry – A hybrid multi criteria decision making approach, *Renewable and Sustainable Energy Reviews*, 55, (2016) 1274-1288.
- [9] Abdul-Rahman, H., Wang, C., Wood, L. C., Ebrahimi, M., Integrating and Ranking Sustainability Criteria for Housing, *Proceedings of the Institution of Civil Engineers -Engineering Sustainability*, Vol. 169 Issue 1, (2016) 3-30.
- [10] Arroyo, P., Tommelein, I. D., Ballard, G. Selecting Globally Sustainable Materials: A Case Study Using Choosing by Advantages, *Journal of Construction Engineering and Management*, (2015) 10.1061/(ASCE)CO.1943-7862.0001041.
- [11] Zadeh, L. A. Fuzzy sets, *Information Control*, 8(3) (1965)338–353.
- [12] Hwang, C. L.; Yoon, K. Multiple attributes decision making methods and

13th Annual Research Day

Organised by the Deanship of Scientific Research in Collaboration with the College of Engineering
Research Centre
2nd April 2018

- applications, a state-of-the-art survey, New York: Springer-Verlag (1981).
- [13] Wang, M. J., Chang, T. C., Tool steel materials selection under fuzzy environment, *Fuzzy Sets and Systems*, 72(3): (1995) 263–270
- [14] Chen, C. T., Extensions of the TOPSIS for group decision-making under fuzzy environment, *Fuzzy Sets and Systems*, 114(1), (2000) 1–9,
- [15] Zeleny, M. A., Concept of Compromise Solutions and the Method of the Displaced Ideal, *Computers and Operations Research*, 1(3): (1974) 479-496.
- [16] Zhao, R. and Govind, R., Algebraic characteristics of extended fuzzy numbers, *Information Science*, 54(1-2), (1991) 103–130.

Appendix-I

QUESTIONNAIRE 1 FOR FUZZY TOPSIS

With respect to the overall goal of “Selection of the Sustainable Siliceous Materials”, Sample questions included in questionnaire

- Q1. What degree of importance do you assign to Sustainable Indicator *Support to Concrete Curing System* (C_1)?
- Q2. What degree of importance do you assign to Sustainable Indicator *Support to Concrete Compaction System* (C_2)?
- Q3. What degree of importance do you assign to Sustainable Indicator *Support to Cohesiveness of Concrete Mix* (C_3)?
- Q4. What degree of importance do you assign to Sustainable Indicator *Support to Consistency of Concrete Mix* (C_4)?
- Q5. What degree of importance do you assign to Sustainable Indicator *Comply Strength Requirement of Concrete Mix* (C_5)?

With respect to Sustainable siliceous Materials	Importance (or preference) of each criterion
---	--

Questions	Indicator	(0,0.1,0.3) Very Low	(0.1,0.3,0.5) Low	(0.3,0.5,0.7) Medium	(0.5,0.7,0.9) High	(0.7,0.9,1) Very High
Q1	C_1			√		
Q2	C_2				√	
Q3	C_3	√				
Q4	C_4			√		
Q5	C_5			√		

Appendix-II

QUESTIONNAIRE 2 FOR FUZZY TOPSIS

Scoring of alternatives with respect to Sustainable Indicator for overall goal of "Sustainable Siliceous Materials"

- Q21. What scores do you assign to A_1 with reference to Sustainable Indicator *Support to Concrete Curing System* (C_1)?
- Q22. What scores do you assign to A_1 with reference to Sustainable Indicator *Support to Concrete Compaction System* (C_2)?
- Q23. What scores do you assign to A_1 with reference to Sustainable Indicator *Support to Cohesiveness of Concrete Mix* (C_3)?
- Q24. What scores do you assign to A_1 with reference to Sustainable Indicator *Support to Consistency of Concrete Mix* (C_4)?
- Q25. What scores do you assign to A_1 with reference to Sustainable Indicator *Comply Strength Requirement of Concrete Mix* (C_5)?

With respect to the Sustainable siliceous Materials	Performance of each Sustainable siliceous Materials alternative with respect to each Sustainable Indicator
---	--

13th Annual Research Day

Organised by the Deanship of Scientific Research in Collaboration with the College of Engineering
Research Centre
2nd April 2018

Questions	siliceous	(0,1,3) Very Poor	(1,3,5) Poor	(3,5,7) Fair	(5,7,9) Good	(7,9,10) Very Good
Q21	A ₁			√		
Q22	A ₂				√	
Q23	A ₃	√				

Q24	A ₄			√		
Q25	A ₅			√		

The Separation Of A Binary Water/Ethanol Solution Via A Continuous Feed Distillation Column As A Function Of Feed Stage Location And Reflux Ratio

Moutaz M.A.Eldirderi

¹Department of Chemical Engineering, College of Engineering, King Khalid University,
PO Box 394, Abha 61411 KSA.
E-mail address: maldrdery@kku.edu.sa

Abstract: The purpose of this study was to investigate the separation of a binary water/ethanol solution via a continuous feed distillation column as a function of feed stage location and reflux ratio. The column was initially run with the feed entering at the first stage under reflux ratios of 7.3 and 2.36. The composition of the distillate and liquid product were recorded and compared with theoretical results predicted by the McCabe-Thiele graphical method. In addition, the effect of feed stage location was examined by feeding into the fifth stage while at a reflux ratio of 7.3.

It was found that the distillate composition was approximately 20% (by weight) at a reflux ratio of 7.3, whereas this value dropped to 15% when running at a reflux ratio of 2.36. Although a higher reflux ratio is desired to produce a higher concentration of ethanol in the distillate, it must be considered that a higher reboiler duty, and in turn a higher operating cost, is required to accomplish this. It was also observed that changing the feed location to the fifth stage resulted in a decreased ethanol concentration in the distillate. Finally, it was found that for the distillate compositions attained in this experiment, the McCabe-Thiele graphical method predicted significantly fewer stages than found in the laboratory column. This indicates that a high inefficiency exists in the stages of the column and these factors should be further investigated.

Keywords: *Feed stage; Distillation; reflux ratio; binary; Software; experiment.*

1. Introduction:

This experiment was designed to determine the impact of certain variables on the performance of a continuous distillation column in which an ethanol/water mixture is separated. The particular variables examined were the location of the feed stage in the column and the reflux ratio. Through determination of the optimum process parameters, the column can be run in a way that will produce the desired product in the most efficient and economical way, thus decreasing operating costs and therefore maximizing profitability.

In order to determine the optimum combination of these variables, the column was run with two different feed entrance locations, as well as two different reflux ratios. The outlet stream data for

each scenario was recorded and compared to results obtained from the McCabe-Thiele graphical method, which provides the theoretical number of stages necessary to achieve a particular product composition. By doing this comparison, it can be seen how many additional stages were necessary to achieve that composition in the actual process, and the efficiency of the process can be determined.

2. Materials and Methods:

2.1 Materials

ChemCad software and excel software were used in this work.

2.2 Experimental Procedure

Distillation is a method used to separate components based on their presence in both the

liquid and vapor phases, where all components exist in both phases. Separation of the components is achieved through differences in boiling points between the species, however since concentration will affect the boiling point of the liquid phase, the process is also dependent on the vapor pressure of the components.

Distillation columns are therefore designed based on vapor-liquid equilibrium data, and one of the most common methods used for design purposes is the McCabe-Thiele graphical method. This method is based on the assumption of equimolar overflow, meaning that for every mole of liquid that is vaporized, a mole of vapor condenses. This assumption also implies that the components have similar molar heats of vaporization.

By graphing the equilibrium curve for the mixture in question, the McCabe-Thiele method can be applied to determine the theoretical plates needed for the column. Once the equilibrium curve is obtained, operating lines that identify the mass balance relationship between the liquid and vapor phases must be plotted. There are two operating lines, one representing the section of the column above the feed, or the enriching section, and one representing the section of the column below the feed, or the stripping section. In order to obtain these operating lines, the reflux ratio, or amount of top product returned to the column, must be known. This value can be obtained using the following equation

$$R = \frac{L}{D} \quad (1)$$

where L is the reflux flow rate and D is the distillate flow rate.

Using the calculated reflux ratio, the enriching operating line was plotted using the following equation

$$y_{n+1} = \frac{R}{R+1} x_n + \frac{x_D}{R+1} \quad (2)$$

where y_{n+1} is the composition of the vapor entering stage n, x_n is the composition of the liquid leaving stage n and x_D is the composition of the distillate. Refer to the Appendix for calculations.

A diagram of the enriching operating line can be seen in Figure 1. As can be seen in the equation, the line will intersect the y-axis at $\frac{x_D}{R+1}$ and will

have a slope of $\frac{R}{R+1}$.

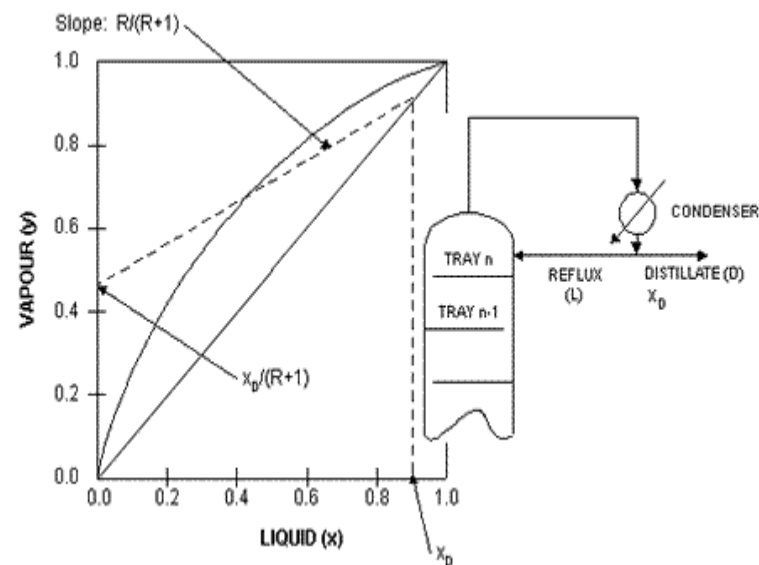


Figure 1: Enriching Section Operating Line Diagram

Before plotting the stripping section operating line, the q-line, or line describing the feed conditions, can be plotted. The q-line is determined by first calculating the value of q through use of the equation below

$$q = \frac{H_v - H_F}{H_v - H_L} \quad (3)$$

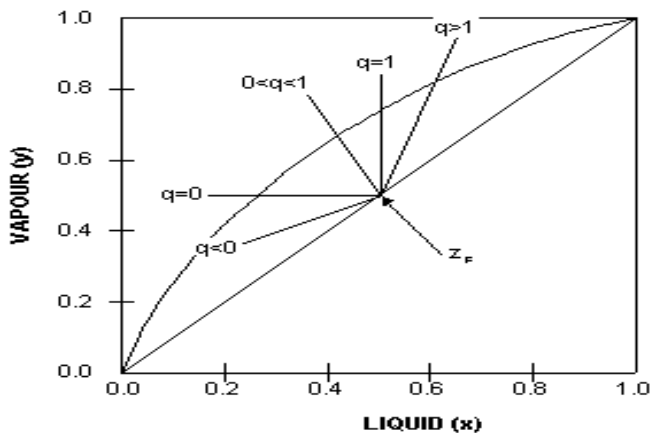
where H_v is the enthalpy of the feed at the dew point, H_F is the enthalpy of the feed at the boiling point, and H_L is the enthalpy of the feed at its entrance condition. This quantity can be found

via hand calculation or through the use of ChemCad software. Using the software, data can be obtained for the amount of heat necessary to vaporize an ethanol/water mixture at the feed conditions used in the experiment. The value for q can then be found by dividing the total heat needed to vaporize the feed from its entrance conditions by the amount of heat needed to vaporize the feed from its boiling point. This graph can be seen in the Appendix.

Once the value of q is determined, the slope of the q -line can be determined using the following equation:

$$\text{slope} = \frac{q}{q-1} \quad (4)$$

It can be seen that Eq. 3 will go to zero if the feed is at its boiling point, and the slope of the line will therefore go to infinity and be a vertical line. The slope of the q -line can be predicted in a similar manner for other feed conditions. For liquids below the boiling point, as in this experiment, it is expected that q will be greater than one and therefore the slope of the line will be greater than one. Figure 2 shows various q -



lines and their corresponding feed conditions.

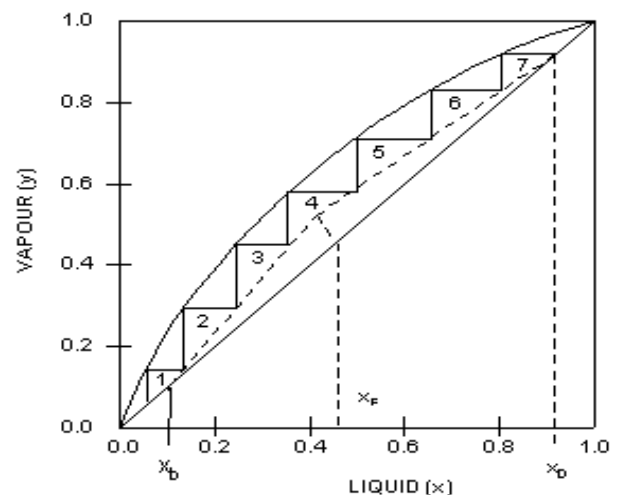
Figure 2: Diagram of q -lines for various feed conditions

Since the enriching section operating line and the q -line are known, the stripping section operating

line can be plotted by simply drawing a line between the point where the q -line and equilibrium line intersect and the point x_b , which is the desired composition of the bottoms.

Once all of the necessary lines are obtained, the number of theoretical stages can be found by “stepping-off” the graph. Beginning on the enriching section operating line at the point x_D , a line is drawn horizontally until the equilibrium curve is reached. At this point, a vertical line is drawn downward until arriving at the enriching section operating line again. This process is continued until the point where the enriching section and stripping section operating lines join. At this point, the vertical lines switch from the enriching line to the stripping line. In addition, the stage where this transition takes place is the optimum feed stage according to this method. An example of this “stepping-off” process can be seen in Figure 3.

Figure 3: Example of stepping off stages using the McCabe-Thiele method



- $q = 0$ (saturated vapour)
- $q = 1$ (saturated liquid)
- $0 < q < 1$ (mix of liquid and vapour)
- $q > 1$ (subcooled liquid)
- $q < 0$ (superheated vapour)

Since ethanol is a appreciably more volatile than water, it is expected that a small number of stages

13th Annual Research Day

Organised by the Deanship of Scientific Research in Collaboration with the College of Engineering
Research Centre
2nd April 2018

will be necessary to separate these components. In addition, it is known that under maximum reflux, where the entire top product is continuously returned to the column as reflux, the number of stages required to reach a desired purity is at a minimum. Therefore, it is expected that when using a fixed number of stages, as with the laboratory column, a higher reflux ratio will result in a higher distillate purity.

3. Results and Discussion

The data obtained in the experiment can be

Experimental Results						
	Distillate Flow Rate (ml/min)	Reflux Flow Rate (ml/min)	Bottoms Flow Rate (ml/min)	Weight % Ethanol in Distillate	Mole % Ethanol in Distillate	Weight % Ethanol in Bottoms
1 st Stage Feed 7.3 Reflux Ratio	18.6	35.7	110	20	10	0
1 st Stage Feed 2.36 Reflux Ratio	44	104	103.3	15	7.24	0.5
5 th Stage Feed 7.3 Reflux Ratio	46.8	104.3	136.4	13	6.11	1.5

seen in following table.

Using the excel software, equilibrium data was acquired for the ethanol/water mixture and distillate flow rate (ml/min) via bottoms flow rate (ml/min) was plotted. This graph is shown below

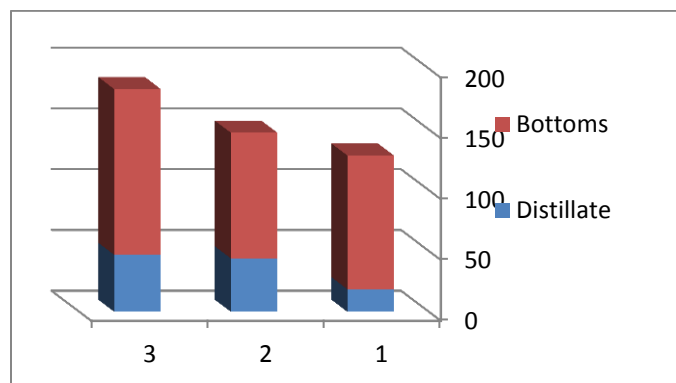


Figure (4) distillate flow rate (ml/min) via bottoms flow rate(ml/min) diagram

Using the ChemCad software, equilibrium data was acquired for the ethanol/water mixture and a x-y diagram was plotted. This graph is shown below in Figure 4

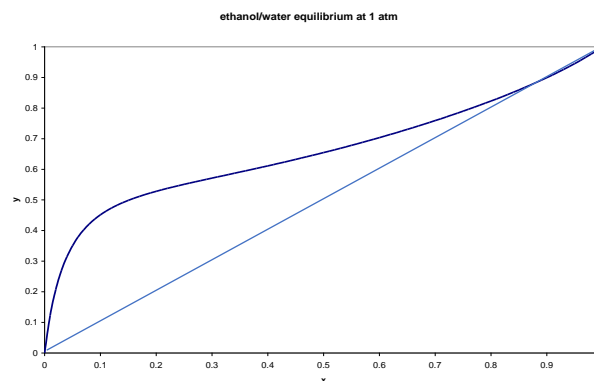


Figure 4: x-y diagram for Ethanol/Water Mixture

It can be seen in above Table that the experimental results were generally consistent with expected trends. As the reflux ratio was increased from 2.36 to 7.3, the concentration of ethanol in the distillate increased from 15% to 20%. It was also found that for the same reflux ratio, as the feed stage was moved from the first to the fifth stage the concentration of ethanol in the distillate decreased.

As expected, the McCabe-Thiele graphical method predicted a far fewer number of stages for the distillate compositions in question than the number of trays found in the laboratory column. While it is expected that there will be some discrepancy between the theoretical and

13th Annual Research Day

Organised by the Deanship of Scientific Research in Collaboration with the College of Engineering
Research Centre
2nd April 2018

actual number of stages, this is a significant difference. Since the graphical method includes the reboiler in the number of stages, the theoretical number of stages is actually one less than the value obtained from the graph. Therefore, the McCabe-Thiele method predicts only one stage necessary for the compositions reached in this experiment. The McCabe-Thiele diagrams for each case can be seen in Figures 6,7 and 8 respectively. The high level of inefficiency present in the laboratory column can be attributed to several different factors. First, the theoretical method assumes no heat loss from the column. Although the column is insulated, it is probable that there is still some degree of heat lost to the atmosphere. In addition, it is assumed that there is adequate contact time at each tray for the liquid and vapor phases to leave in equilibrium. This is an ideal case assumption and it is likely that this is not achieved in the laboratory column. It is possible that running a lower feed rate would allow more contact time at each stage and therefore create better exchange between the two phases. Finally, it is certain that there is a degree of experimental error in the results, which may also account for some of the inefficiency of the column.

It can be seen in Figure 6 that the experimental results show that the bottom flow rate high than distillate flow rate.

4. Conclusions:

The investigation of variables affecting the continuous distillation column showed two clearly evident trends. First, when feeding to a particular stage, increasing the reflux ratio results in an increased ethanol concentration in the distillate. (Refer to above Table)

The second trend noted was that changing the feed from the first to the fifth stage decreased the ethanol concentration in the distillate. This trend, however, should be further investigated since only one sample was taken for this scenario. (Refer to Figure 4)

It was also found that the number of stages predicted by the McCabe-Thiele graphical method was significantly lower than the number found in the laboratory column for the compositions obtained in this experiment. This indicates a large inefficiency in the performance of the laboratory column. This inefficiency may be due to several factors, including heat loss from the column and

Based on the observed trends, it is recommended that the trade-off between increased product purity from the use of a higher reflux ratio and the resulting increase in reboiler duty be further investigated. By doing so, it may be determined the optimum reflux ratio at which to run the column. It is also recommended that the location of the feed stage be further investigated since it is typically expected that a feed near the middle of the column is best. Since only one sample was taken for the fifth stage feed, it is difficult to determine whether the resulting data was accurate. By running another sample at the same conditions, it can be determined whether the lower product purity is a consistent result and should be considered when designing the column operating parameters. Finally, it is suggested that a lower feed flow rate be investigated since only one feed rate was used in this experiment. This may allow longer contact time at each tray and therefore a better equilibrium between the phases leaving the tray.

Acknowledgement

This study was sponsored by Khartoum refinery company, Sudan

References

- [1] Geankoplis, Christie J., "Transport Processes and Unit Operations," 3rd ed., Prentice Hall (1993).
- [2] Perry, Robert H., and Don W. Green. "Perry's Chemical Engineers' Handbook" 7th ed. New York: McGraw-Hill Inc., (1997)

13th Annual Research Day

Organised by the Deanship of Scientific Research in Collaboration with the College of Engineering
Research Centre
2nd April 2018

[3] Introduction to Distillation.
<http://lorien.ncl.ac.uk/ming/distil/distildes.h>

[4] Kister, Henry Z. Distillation Design (1st Edition ed.). McGraw-hill. (1992).

[5] M.T.Tham, Distillation an introduction
"Distillation column design"(1998)

[6] R.K.Sinnolt1993;Chemical Engineering
Volume 6 Pergaman press –Oxford.

Effect of Liquid Forging Process Parameters on Properties of Cast Metals And Alloys

Vineet Tirth¹

¹Department of Mechanical Engineering, College of Engineering, King Khalid University,
PO Box 394, Abha 61411 KSA.
E-mail address: vtirth@kku.edu.sa

Abstract: Liquid Forging is a promising technique for primary and secondary processing of metals, alloys, and composites. It originated in Russia, in 1878. The commercial applications of liquid forging started in Russia in 1930 and later, in Europe, USA, and Japan during 1960-1970. Liquid forging is also known as squeeze casting, squeeze forming, liquid pressing, extrusion casting, pressure crystallization, and liquid metal stamping. It is an innovative technique to reduce manufacturing costs and improved product design. In a single operation, liquid forging combines the advantages of both forging and casting, yielding dense pore-free components in both ferrous and non-ferrous alloys. Permanent molds are required in liquid forging. Process parameters of liquid forging such as temperature of melt, temperature of die, the volume of melt, coating provided on die surface, time delay, time of pressure application, level of forging pressure, speed of press, die material and the effect of forging pressure on solidification and equilibrium diagram are discussed in this study with respect to Aluminium and Al-Alloys. The major attraction of liquid forging is the cost advantage compared with other manufacturing processes. High casting yield greater than 90% was achieved due to the absence of gates and risers and reduced scrap. Equipment is simple and cost-efficient allowing a good rate of production, good surface finish, dimensional reproducibility, reducing finishing operation to a minimum.

Keywords: *Liquid Forging; Forging Pressure; Casting, Squeeze Casting, Process Parameters.*

1. Introduction:

The advantage of forging can be united with the intricacy of form and decent surface finish in liquid forging. An increased casting yield (>90%) may be attained as effectively all the liquid metal may be poured into the molds and wastage is avoided in riser and gating [1]. In addition, the casting can be imperiled by heat treatment, joining, cutting, finishing, coating, electroplating, and other general as well as special secondary processes. Liquid forging (LF) offers superior cost advantage compared with other processes. The foundation of liquid forging initiated in 1878 by Russian researchers who used steam pressure on molten metal while it solidified in mold [2]. Conventionally, forging and casting have advanced distinctly but Plyastka in 1930 in Russia explored the opportunity to combine the

two methods. The parameters related to the combined processes controlling the technique were efficaciously determined in the 1960s and thereafter-liquid forging was ready for commercial applications. At first, about one hundred and fifty large batch industries started using liquid forging in Russia producing more than 200 engineering components [3-16].

Due to the cold war era, initially European countries, Japan and the United States were reluctant to adopt liquid forging but later following the dominance of Russia in the steel industry and robust military machinery, they introduced liquid forging in their industries. Playfully the name of the technique was changed from liquid forging to squeeze casting and its commercial application started on a large scale in US, Europe, and Japan in the late 1960s [3]. The

method can be mechanized with reasonably modest equipment giving decent manufacture rate, decent dimensional replication, and finish, minimizing machining. The liquid forging process is different from pressure die casting however, it fills the gap amid pressure die casting, gravity casting and forging. Figure 1 shows liquid forging technique.

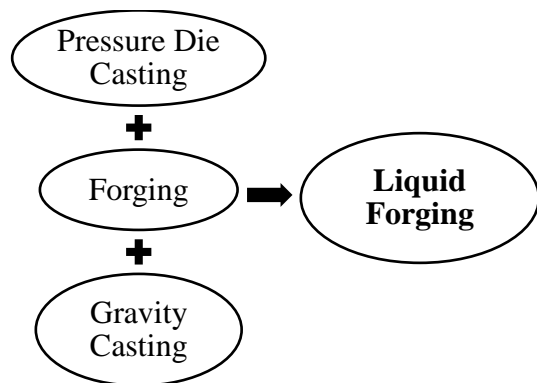


Figure (1) Schematic representation of Liquid Forging and other similar techniques.

Figure 2 shows a comparative study of liquid forging and other similar methods based on productivity.

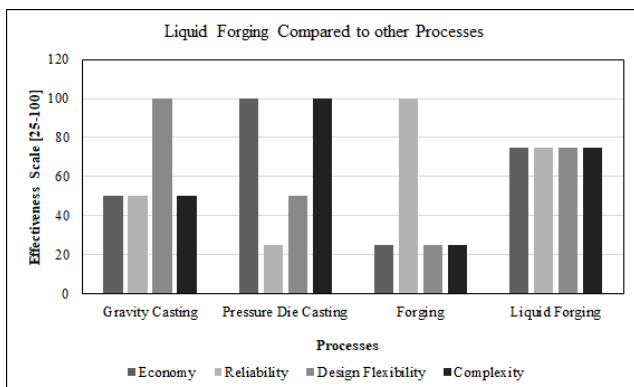


Figure (2) Comparative study of liquid forging and other similar methods based on productivity.

Liquid forging hence syndicates benefits of all the three processes yet, it yields properties not obtainable in any of these processes separately.

2. Materials and Methods:

2.1 Materials

Two materials have been selected for the present study. Firstly, commercially pure (CP) Aluminium (Al) which has been processed through gravity casting (GC) and liquid forging (at pressure 200 MPa) to determine the effect of liquid forging on properties. Secondly, 2124 Aluminium alloy (Al-alloy) has been developed and the effect of liquid forging process parameters on the properties of the alloy has been discussed. CP Aluminium and 2124 Al-alloy were selected because these are most abundantly used materials in industrial applications. The author fabricated the die from chromium-molybdenum die steel and heat-treated it for forging. The vertical hydraulic press was used for forging. The press had capacity 100 tons. Resistance furnace was used for melting the Al and 2124 Al-alloy in graphite crucibles of capacity 3 kg. Strength and ductility were tested on Hounsfield tensometer with load capacity 20 kN as per ASTM E8 M 89b standard. Hardness was estimated by Vicker's hardness tester machine at 5 kg load.

2.2 Experimental Procedure

Two different types of liquid forging techniques are used viz. direct and indirect [14].

In direct liquid forging, the molten metal is frozen under the direct pressure. The pressure is maintained at the level so that gas porosity or shrinkage porosity is prevented. In this process, isotropic properties are obtained and quality and finish of the product are good.

This process is completed in four steps shown in Figure 3 [4] and summarized from (I) to (IV) below.

- (I). Molten metal is poured into the female die cavity.
- (II). The upper punch (male) is lowered, coming in contact with the liquid metal until the forging pressure reaches desired level. The time delay between pressure application and solidification of the melt is to be controlled to prevent premature freezing.

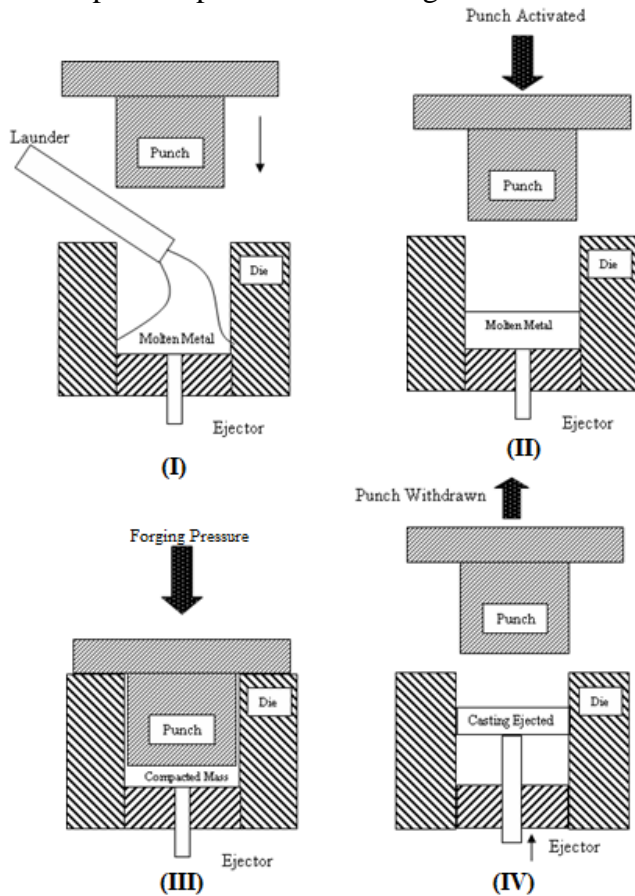


Figure (3) Steps in the Liquid Forging process.

- (III). Pressure is maintained until molten metal freezes.
- (IV). The upper punch is withdrawn to its original position and the frozen casting is ejected.

Another process is In-direct liquid forging, in which, metal is injected into the die cavity by a small diameter plunger and the pressure is also applied during freezing [14]. This technique is a hybrid process between low pressure die casting

and the high pressure die casting. The indirect process has two disadvantages. Firstly, the riser and runner is required and secondly, it is difficult to obtain a defect-free casting. Hence, direct process is preferred over the indirect process of processing of materials to be used for high-end applications.

There is one sole advantage of the indirect process i.e. the dimensional control is good due to the closed die approach.

Overall evaluation indicates that the direct method is better than the later to obtain high strength, defect-free casting and so; the direct method has been employed in this study.

3. Results and Discussion

The composition of 2124 Al-alloy tested by ICP is (Cu-4.26%, Si-0.95%, Mg 0.49%, Fe 0.25%, Mn 0.98%, Ni 0.34%).

Figure 4 to 6 shows mechanical properties of gravity cast and squeeze cast (200 MPa) commercially pure (CP) Al. It can be seen that liquid forging improves hardness by 25.8%.

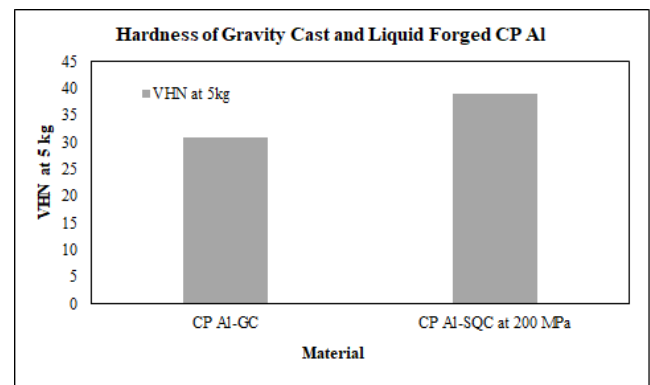


Figure (4) Hardness of Gravity Cast and Liquid Forged (200 MPa) CP Aluminium.

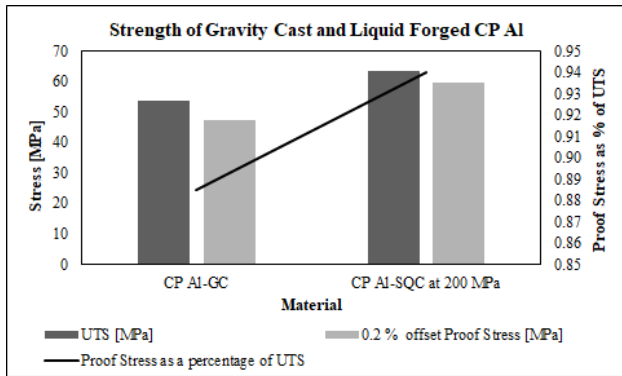


Figure (5) Strength (UTS and Proof Stress) of GC and LF (200 MPa) CP Al.

The UTS and 0.2% offset proof stress is shown in Figure 5 for CP Al and the one, Liquid Forged at 200 MPa.

Also plotted is the percentage retention of proof stress compared with UTS. The UTS of Liquid Forged CP Al is 18% higher than the Gravity Cast CP Al whereas the 0.2% offset proof stress is 25.5% higher. This means that the LF Al has 25% more design stress, which is remarkable. The % retention of UTS is displayed on the secondary vertical axis in Figure 5. In CP Al, the % retention of proof stress is 88.46 % which has increased to 95% in LF Al.

To get a better indication, ductility has been measure by two methods. Firstly, by estimating % elongation and secondly, by calculating the % reduction is area. We can see from Figure 6 that the % elongation decreases in LF Al compared with CP Al but the % reduction in area is almost the same. This indicates that there is little or no compromise on ductility due to LF but on the other hand, the hardness and strength has increased significantly.

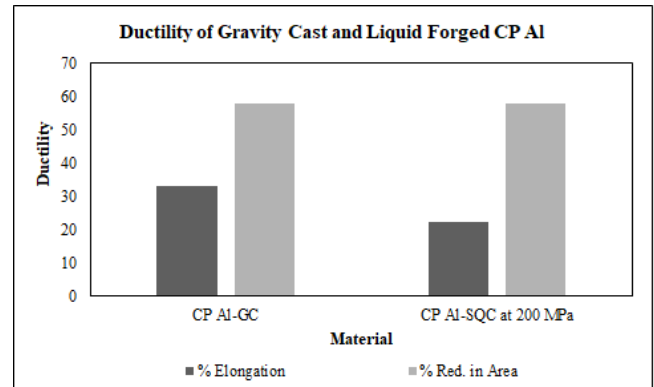


Figure (6) Ductility (%Elongation and % Reduction in Area) of Gravity Cast and Liquid Forged (200 MPa) CP Aluminium.

The results presented in Figures 4 to 6 are based on studies on CP Al. To study the effect of Liquid forging parameters, studies have also been done on 2124 Al-alloy. The author has prepared the alloy and LF has been done at fixed moderate pressure of 200 MPa on which CP Al was prepared.

In Figure 7, it is observed that the density of 2124 Al-alloy decreases with the pouring temperature due to higher degree of superheat enabling expansion of melt and resistance to compression. The lower the pouring temperature, the higher is the density because LF gives better effect in semi-solid state compared to liquid state [3].

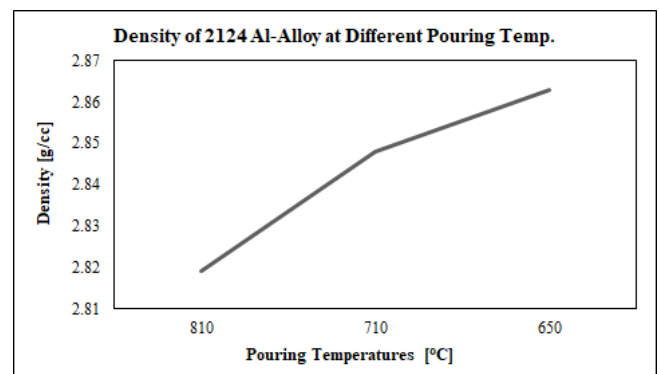


Figure (7) Density of 2124 Al-alloy prepared by LF (200 MPa) as a function of pouring temperature in the die.

13th Annual Research Day

Organised by the Deanship of Scientific Research in Collaboration with the College of Engineering
Research Centre
2nd April 2018

Figure 8 represents UTS and proof stress of the 2124 Al-alloy as a function of different pouring temperatures. The UTS and proof stress decreases with the pouring temperature but the decrease in UTS is insignificant.

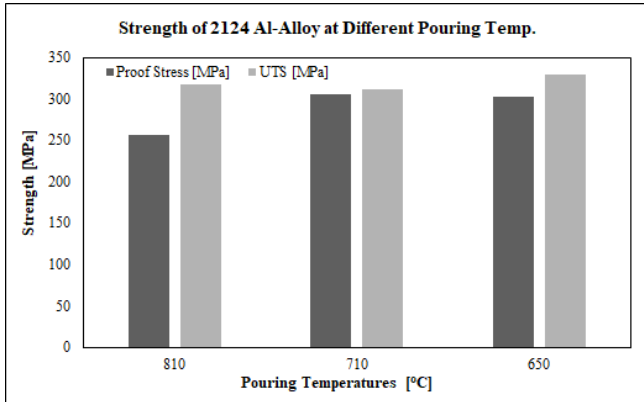


Figure (8) Strength of 2124 Al-alloy prepared by LF (200 MPa) as a function of pouring temperature in the die.

Based on the results, it appears that since the minimum pouring temperature is suitable to achieve high tensile strength.

The ductility of 2124 Al-alloy is plotted as a function of pouring temperature in Figure 9. It is observed that ductility increases with pouring temperature, which is because when the density has decreased and strength has decreased, the material becomes soft and elongates a long way before fracture. Increase in ductility at the expense of density and strength is undesirable.

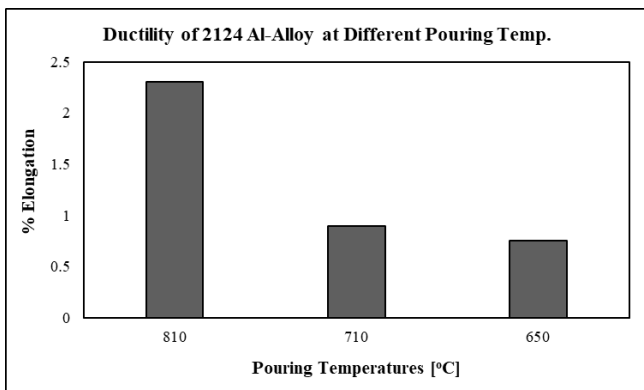


Figure (9) Ductility of 2124 Al-alloy prepared by LF (200 MPa) as a function of pouring temperature in the die.

Effect of time delay between pouring and pressure application (Dwell Time) on density and tensile properties of 2124 Al-alloy are plotted in Figures 10 to 12.

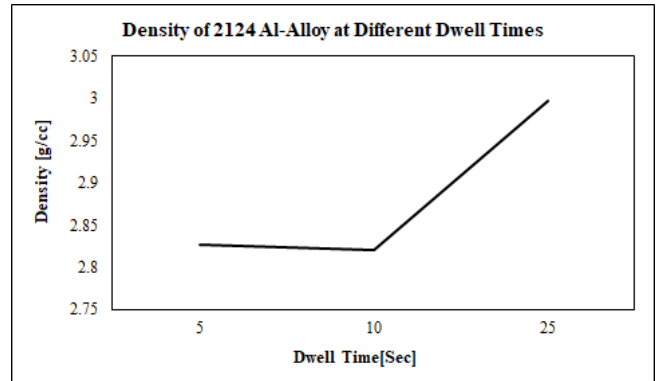


Figure (10) Density of 2124 Al-alloy prepared by LF (200 MPa) as a function of dwell time.

It is observed in Figure 10 that as the Dwell time is increased from 5 s to 10 s there is minor drop in density which may be due to poor averaging of the experimental results. However, as the Dwell time increased from 10 s to 25 s, the density improves. Longer Dwell time resulted in start of solidification and when pressure was applied, the material was almost in semi-solid state, creating conducive conditions of compression and density increase. These results are in accordance with the results observed in Figure 7.

The strength of 2124 Al-alloy is plotted as a function of Dwell time in Figure 11. The strength increases with the Dwell time due to increase in grain refinement and density.

13th Annual Research Day

Organised by the Deanship of Scientific Research in Collaboration with the College of Engineering
Research Centre
2nd April 2018

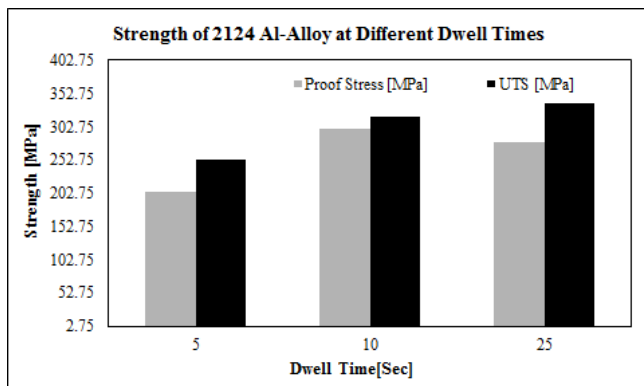


Figure (11) Strength of 2124 Al-alloy prepared by LF (200 MPa) as a function of dwell time.

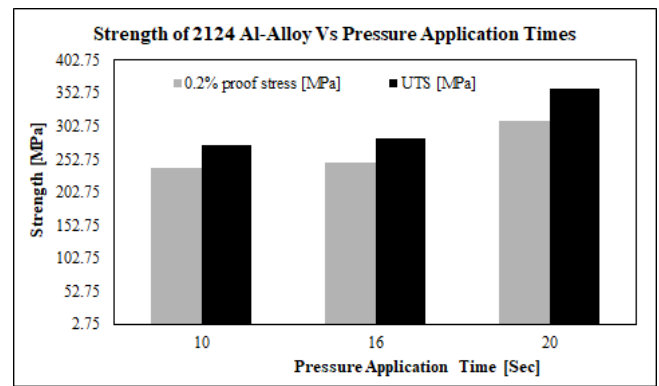


Figure (13) Strength of 2124 Al-alloy prepared by LF (200 MPa) as a function of Pressure Application time.

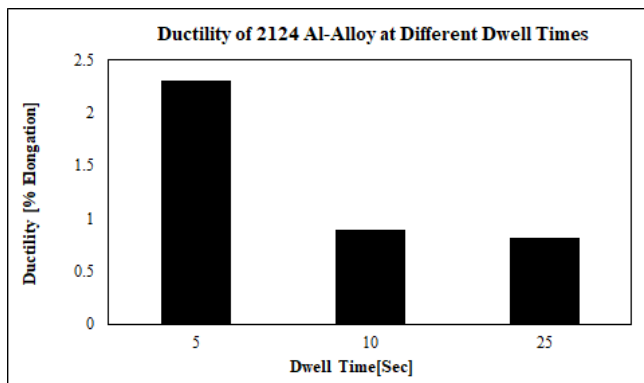


Figure (12) Ductility of 2124 Al-alloy prepared by LF (200 MPa) as a function of dwell time.

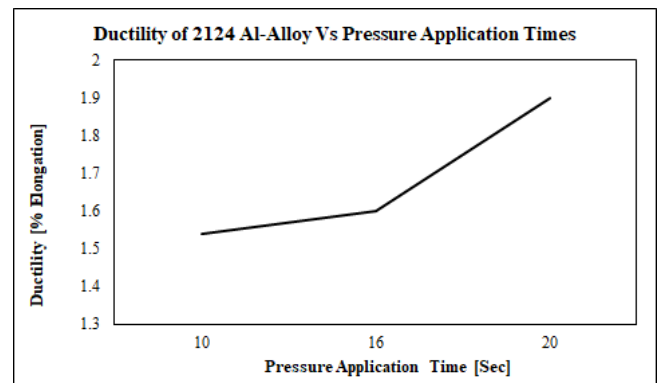


Figure (14) Ductility of 2124 Al-alloy prepared by LF (200 MPa) as a function of Pressure Application time.

The Ductility of 2124 Al-alloy is plotted Vs Dwell time in Figure 12. It may be observed that the ductility is more at lesser dwell time due to softer material and incomplete compression.

The pressure applied by the die is very important. If the pressure is applied for a larger period than required, it wastes energy and increases the cost. The productivity is also adversely affected. On the other hand, if the pressure is applied for a short period and the compression is not complete, the optimal use of Liquid Forging is deferred. An optimal pressure application is therefore required to produce a sound casting. Figure 13 represents pressure application time in sec as a function of strength of 2124 Al-alloy.

As the pressure application time is increased, the strength, both UTS and proof stress is increased. This may be because, if the material is super cooled, the chances of elastic deformation are reduced and so the compression is permanent.

Figure 14 gives an interesting indication. It may be observed that with the increase in the pressure application time, the ductility of the material has increased along with the tensile strength. Thus, increase in pressure application time improves both, the ductility and strength of the material.

4. Conclusions:

1. The hardness as well as the strength of CP Al increases significantly with LF. The %

13th Annual Research Day

Organised by the Deanship of Scientific Research in Collaboration with the College of Engineering
Research Centre
2nd April 2018

retention of proof stress compared with UTS also improves in LF CP Al.

2. The ductility of CP Al remains unaffected with LF. Therefore, a higher strength is achieved without compromising the ductility.
3. In 2124 Al-alloy, density reduces with pouring temperature. Strength also reduces with the increase in pouring temperature but ductility increases with increase in pouring temperature.
4. In 2124 Al-alloy, the density and strength increases as the Dwell time is increased from 5 s to 25 s. However, the ductility decreases.
5. With increase in the pressure application time, the strength as well as the ductility both increases.

Acknowledgement

Authors thankfully acknowledge the funding and support provided by Deanship of Scientific Research, King Khalid University, Abha-Asir, Kingdom of Saudi Arabia, with grant number R.G.P.2/6/38 under research group- Materials & Production to complete the research work.

References

- [1] S.N. Chou, J.L. Huang, D.F. Lii, H.H. Lu, The mechanical properties of Al₂O₃/aluminum alloy A356 composite manufactured by squeeze casting, *J. Alloys Compd.* 419 (2006) 98–102.
- [2] M.T. Abou El-Khair, Microstructure characterization and tensile properties of squeeze-cast AlSiMg alloys, *Materials Letters.* 59 (2005) 894–900.
- [3] X. Fang, S. Lü, L. Zhao, J. Wang, L. Liu, S. Wu, Microstructure and mechanical properties of a novel Mg – RE – Zn – Y alloy fabricated by rheo-squeeze casting, *Jmade.* 94 (2016) 353–359.
- [4] C.G. Kang, K.S. Yun, Fabrication of metal-matrix composite by the die-casting technique and the evaluation of their mechanical properties, *J. Mat. Processing Tech.* 62 (1996) 116–123.
- [5] Y. Liu, Z. Zheng, C. Yang, D. Zhu, W. Chen, Effects of Unreacted Ti Particles on the Dry Sliding Tribological Behavior of Squeeze-Cast (SiCp + Ti)/7075Al Hybrid Composites Under Different Applied Loads, *Tribol. Lett.* 65 (2017) 39.
- [6] H.N. Min, M. Shao, W. Zhang, Composite Squeeze Casting of Large Parts, *Appl. Mech. Mater.* 319 (2013) 369–372.
- [7] R.F. Lynch, R.P. Olley, J.P.C. Gallagher, Squeeze Casting of Brass and Bronze, *Trans. American Foundrymen Society*, 83 (1975) 561–568.
- [8] G.S. Reddy and K.G.R. Murthy, Liquid forging of an Aluminium alloy. *Trans. of The Ind. Inst. of Met.* 31-6 (1978) 484–487.
- [9] A. Onat, H. Akbulut, F. Yilmaz, Production and characterisation of silicon carbide particulate reinforced aluminium-copper alloy matrix composites by direct squeeze casting method, *J. Alloys Compd.* 436 (2007) 375–382.
- [10] K. Sekar, K. Allesu, M.A. Joseph, Mechanical and Wear Properties of Al–Al₂O₃ Metal Matrix Composites Fabricated by the Combined Effect of Stir and Squeeze Casting Method, *Trans. Indian Inst. Met.* 68 (2015) 115–121.
- [11] K. Sukumaran, K.K. Ravikumar, S.G.K. Pillai, T.P.D. Rajan, M. Ravi, R.M. Pillai, B.C. Pai, Studies on squeeze casting of Al 2124 alloy and 2124-10% SiCp metal matrix composite, *Mater. Sci. Eng. A.* 490 (2008) 235–241.
- [12] M.S. Skolianos, G. Kiourtsidis, T. Xatzifotiou, Effect of applied pressure on the microstructure and mechanical properties of squeeze-cast aluminium AA6061 alloy, *Mat. Sc. and Engg. A.* 231 (1997) 17–24.

13th Annual Research Day

Organised by the Deanship of Scientific Research in Collaboration with the College of Engineering
Research Centre
2nd April 2018

- [13] H. Xu, X. Zhang, H. Li, S. Li, C. Wang, Y. Wang, B. Zhang, Hot deformation behavior of squeeze casting SiCp/2A50 matrix composites, J. Wuhan Univ. Technol. Sci. Ed. 27 (2012) 443–449.
- [14] T.M. Yue, G.A. Chadwick, Squeeze Casting of light alloys and their composites, Jr. of Mat. Proc. Tech. 58 (1996) 302-307.
- [15] M. Zhao, G. Wu, L. Jiang, Z. Dou, Friction and wear properties of TiB₂P/Al composite, Compos. Part A Appl. Sci. Manuf. 37 (2006) 1916–1921.
- [16] B. Zantout, A.A. Das, J.R. Franklin, Squeeze-cast Aluminium-matrix composite: Strength at higher temperature, Proc. of Conf.-The Metallurgy of Light Alloys, Loughborough Univ. U.K. (1983) 215-220.

13th Annual Research Day

Organised by the Deanship of Scientific Research in Collaboration with the College of Engineering
Research Centre
2nd April 2018

Impact of Hazardous Wastes on Human Health & Preventive Measures for a Sustainable Environment

Dr. Mohd Abul Hasan, Dr Mohd Ahmed, Dr Javed Mallick & Dr Ram Karan Singh.

Department of Civil Engineering, College of Engineering, King Khalid University,
PO Box 394, Abha 61411 KSA.
E-mail address: mohad@kku.edu.sa

Abstract: Population growth, rising standards of living, increasing urbanization and industrialization have all resulted into the generation of greater amounts of solid wastes in industrializing countries. Most of the sources of solid wastes contribute hazardous waste posing a number of pollution problems. A hazardous material is any material that, because of its quantity, concentration, or physical or chemical characteristics, poses a significant present or potential hazard to human health and safety or to the environment if released into the home, workplace, or the environment. An effective hazardous waste management system should consist of the activities like; Waste minimization at sources, Identification of and Classification of wastes, Treatment of wastes, Regular monitoring of the groundwater quality and Evaluation of the health risk. While substantial progress has been made with regard to the above, hazardous waste management system is still under developing stage. The present study is aimed to understand hazardous wastes and their impact on Human health for solving the hazardous waste related problems. Hazardous wastes have serious impacts on public health and the environment if they are poorly stored, collected and disposed off. The most serious effects of poor waste management include air pollution, contamination of drinking water supplies and spread of human diseases. It causes cities to become untidy and dirty, affects the health and moral of people, harms animals and plants, and hurts the economy and national pride. Some of the preventive measures such as inventorization of hazardous wastes, dilution, tube well design using well logging methods and other types of geophysical logging, specially made for contaminated zone, along with the various treatment systems are also suggested.

Keywords: *Hazardous waste; Solid Waste; Industrial Waste, Inventorization; Ground Water Contamination.*

1. Introduction:

Hazardous wastes are wastes that, in sufficient quantities and concentrations, pose a threat to human life, human health, or the environment when improperly stored, transported, treated or disposed. The impact of hazardous wastes depends on their quantity, concentration, physical, chemical or biological properties. For example, a waste may be hazardous because it is combustible or inflammable (such as many solvents used in the chemical industry), corrosive (such as battery acid), explosive or reactive (such as phosphorus) or infectious (such as hospital wastes, used needles and bandages). Hazardous

wastes are usually a by-product of industrial operations which involve heavy metals such as arsenic, cadmium, chromium, lead, mercury, etc; processes which utilize different categories of oil and petrochemicals; products such as PVC and plastics, waste products from photocopiers, chemicals such as PCBs and DDT, and finally, by-products such as dioxins and furans which are now recognized as extremely toxic substances, affecting all forms of life. Hospitals are also found to be one of the potential sources of hazardous wastes.

Classification of Hazardous Wastes

13th Annual Research Day

Organised by the Deanship of Scientific Research in Collaboration with the College of Engineering
Research Centre
2nd April 2018

Hazardous wastes are classified into following categories as characteristics hazardous wastes and listed hazardous wastes.

Characteristic of Hazardous Wastes

A waste is classified as characteristic hazardous waste if laboratory tests indicate that it exhibits one or more of the following four characteristics (LaGrega et al, 2001):

Ignitability (capability of easily igniting and thus posing a fire hazard)

Corrossivity (capability of deteriorating due to highly acidic or alkaline nature)

Reactivity (capability of potentially harmful, sudden reactions such as explosions)

Toxicity (capability of releasing, i.e. leaching, certain constituents to water in significant concentrations under specified conditions) The classification of hazardous wastes based on their characteristics determined through laboratory testing, as given by the U.S. EPA.

Listed Hazardous Wastes

A listed hazardous waste is that which appears in the list of specific hazardous wastes compiled by the government authorities because it is known or suspected for its potential to exhibit hazardous characteristics. A total of 18 categories of hazardous wastes, as listed by the Ministry of Environment and Forest (MoEF), Government of India, are presented in Table 1. A total of 11 types of hazardous wastes, prohibited for import by the Ministry of Environment and Forest (MoEF), Government of India.

Sources of Generation of Hazardous Wastes

Hazardous wastes are generated from a wide range of industrial, agricultural, commercial, and household activities. Manufacturers of many everyday products, by manufacturers of specialty articles, generate them by both service and

wholesale trade companies, by laboratories in the universities, hospitals, car repair shops, government facilities, and households. After a waste is generated, the generator can either manage the waste on-site or transport it off-site for treatment, disposal, or recycling, typically to a commercial hazardous waste facility. The generation of waste usually correlates with production and technology. Following observations were typically made through a comprehensive study on the hazardous waste generation (U.S. Code of Federal Regulations, 1985): The manufacture of paint generates 4 to 6% of total production by weight as hazardous waste, the manufacture of steel generates 15 to 25 pounds of electric furnace dust per ton of steel produced and the manufacture of printing ink generates 1% of total production by weight as hazardous waste.

Table 1: Categories of hazardous wastes, listed by MoEF, GoI

<i>Waste category</i>	<i>Types of wastes</i>	<i>Regulatory quantities</i>
No. 1	Cyanide wastes	1 kg per year calculated as cyanide.
No. 2	Metal finishing wastes	10 kg per year the sum of the specified substance calculated as pure metal.
No. 3	Waste containing water soluble chemical compounds of lead, copper, Zinc, Chromium, nickel, selenium, Barium and antimony	10 kg per year the sum of the specified substance calculated as pure metal.
No. 4	Mercury, arsenic, thallium and cadmium bearing wastes	5 kg per year the sum of the specified substance calculated as pure metal.
No. 5	Non-halogenated hydrocarbons including solvents	200 kg per year calculated as non-halogenated hydrocarbons.

13th Annual Research Day

Organised by the Deanship of Scientific Research in Collaboration with the College of Engineering
Research Centre
2nd April 2018

<i>Waste category</i>	<i>Types of wastes</i>	<i>Regulatory quantities</i>
No. 6	Halogenated hydrocarbons including solvents	50 kg per year calculated as halogenated hydrocarbons.
No. 7	Wastes from paints, pigments, glue, varnish and printing ink	250 kg per year calculated as oil or oil emulsions.
No. 8	Wastes from dyes and dye intermediates containing inorganic chemical compounds	200 kg per year calculated as inorganic chemicals.
No. 9	Wastes from dyes and dye intermediates containing organic chemical compounds	50 kg per year calculated as organic chemicals.
No. 10	Waste oil and oil emulsions	1000 kg per year calculated as oil and oil emulsions.
No. 11	Tarry wastes from refining and tar residues from distillation or pyrolytic treatment	200 kg per year calculated as tar.
No. 12	Sludges arising from treatment of waste waters containing heavy metals, toxic organics, oils, emulsions and spent chemicals and incineration ash	Irrespective of any quantity.
No. 13	Phenols	5 kg per year calculated as phenols.
No. 14	Asbestos	200 kg per year calculated as asbestos.
No.15	Wastes from manufacturing of pesticides and herbicides and residues from pesticides and herbicides formulation units	5 kg per year calculated as pesticides and their intermediate products
No. 16	Acid/ alkaline/ slurry wastes	700 kg per year calculated as acids/ alkalis.
No. 17	Off-specification and discarded products	Irrespective of any quantity.

<i>Waste category</i>	<i>Types of wastes</i>	<i>Regulatory quantities</i>
No. 18	Discarded container and container liners of hazardous and toxic chemicals and wastes	Irrespective of any quantity.

Groundwater Contamination by Hazardous Wastes

Groundwater contamination may occur as a result of spillages of hazardous chemicals, leakage from underground tanks containing hazardous substances, dumping of toxic wastes, domestic and industrial wastewater discharges, and landfill leachate. The one or more than one of the following contaminants transported from their sources to the aquifers usually contaminates groundwater:

Wastewater: Untreated or inadequately treated domestic or industrial wastewater is a major source of groundwater and surface water pollution in the developing countries.

Pesticides: Run-off from farms, backyards, and golf courses contain pesticides such as DDT that in turn contaminate the water. Groundwater is susceptible to contamination, as pesticides are mobile in the soil.

Petrochemicals: Petrochemicals contaminate the groundwater from underground petroleum storage tanks.

Chlorinated solvents: Metal and plastic effluents, fabric cleaning, electronic and aircraft manufacturing are often discharged and contaminate groundwater.

Heavy metals: These contaminants (lead, mercury, iron, copper, manganese, cadmium, arsenic, nickel, aluminum, silver, and beryllium) come from mining waste and tailings, landfills, or hazardous waste dumps.

13th Annual Research Day

Organised by the Deanship of Scientific Research in Collaboration with the College of Engineering
Research Centre
2nd April 2018

Synthetic organics: Many of the 100 000 synthetic compounds in use today are found in the aquatic environment and accumulate in the food chain. POPs (Persistent Organic Pollutants) represent the most harmful element for the ecosystem and for human health, for example, industrial chemicals and agricultural pesticides. These chemicals can accumulate in fish and cause serious damage to human health. Where pesticides are used on a large-scale, groundwater gets contaminated and this leads to the chemical contamination of drinking water. Among the most common groundwater organic contaminants are carbon tetra chloride (CTC), trichloroethane (TCA), and trichloroethylene (TCE).

Landfill leachate: Leachate is generated within the landfills by the interaction of garbage, water and gravity. When the water (coming in landfill from rain or groundwater inflow or both) content of garbage exceeds its field capacity (i.e. garbage's maximum ability to absorb water), water moves slowly downward through the garbage under gravity until it reaches the bottom. The water, migrating through the garbage under gravity is called leachate.

A contaminant released at the ground surface, e.g. leachate, migrates first in vertically downward direction (i.e. z-direction) and reaches to the groundwater table. After reaching to the groundwater, contaminant is mixed with the groundwater forming a "groundwater plume", which starts migrating in the aquifer (i.e. groundwater body) in the horizontal plane (i.e. x and y directions), as typically shown in Fig. 1 (Connor et al. 1997).

Modeling the transport of a contaminant from ground surface sources, as shown in Fig. 1, consists of developing following two sets of models:

First model for vertically downward transport of contaminant through soil from a ground surface source to the groundwater table (Connor et al. 1997; Ganguly et al. March 1998 and December 1998; Li and Wu 1999; Guyonnet et al. 1999; Mieszkowski 2003). This model is used to estimate the steady-state contaminant concentration reaching to the aquifer (i.e. groundwater exposure concentration).

Second model for transport of contaminant through aquifer in horizontal plane (De Josselin de Jong 1958; Ogata and Banks 1961; Sayre 1968; Baetsle 1969; Bear 1972; Domenico 1987; Runkel 1996; Hossain and Yonge 1997). This model is used to predict the contaminant concentration at any point in the horizontal plane of aquifer using the groundwater exposure concentration (calculated with the help of the first model) as a source term.

2. Materials and Methods:

Impact of Hazardous Wastes on Human Health

Improper storage, handling, transportation, treatment and disposal of hazardous wastes can affect human health and the environment through leakage of toxins into groundwater, soil, and the atmosphere. Population may be adversely affected when toxic wastes are ingested through contaminated water sources and polluted air and Contamination present within the ground has the potential to migrate or be transported by natural groundwater flow processes, and may ultimately enter the human food chain, either directly, or indirectly through agriculture. Exposure to hazardous wastes can cause a number of health problems including: skin irritation, disability and disordering, respiratory problems, cancer, hormonal disruption, nervous system disruption, liver damage, mental retardation, weight loss,

13th Annual Research Day

Organised by the Deanship of Scientific Research in Collaboration with the College of Engineering
Research Centre
2nd April 2018

etc., depending on the type of waste to which exposed.

Lead: It affects human *central nervous system*. It is a poison by ingestion and moderately irritating. A common air contaminant due to use of bad fuel in the auto industry, now being phased out through the introduction of lead-free petrol; also in air in the vicinity of industrial plants using lead where precautions are not taken. It is a carcinogen of the lungs and kidneys. It is flammable in the form of dust when exposed to heat or flame. Lead can cause irreversible behavioral disturbances, neurological damage and other developmental problems in young children, babies and pregnant women. Exposure to high concentrations can lead to mental retardation, coma, convulsions and death.

Cadmium: It is toxic to humans by inhalation and other routes. It can enter through ingestion, intraperitoneal, subcutaneous, intramuscularly and intravenous routes. It is bio-accumulative through the food chain. Increased exposure can increase risk of lung cancer.

Chromium: This exists in two forms, i.e. trivalent and hexavalent chromium. Hexavalent chromium in high dosages has been implicated as the cause of digestive tract cancers, cutaneous and nasal mucous membrane ulcers and dermatitis. Certain chromate salts, e.g. calcium chromate are carcinogenic, at least when inhaled. Lung cancer has been reported in workers employed in chromate industries.

Zinc: It is skin irritant and affects pulmonary system. The difficulty arises from oxidation of zinc fumes prior to inhalation or presence of impurities such as cadmium, antimony, arsenic and lead. Zinc however is a needed micronutrient for humans.

Arsenic: It is toxic by subcutaneous, intramuscularly and intraperitoneal routes and reported to produce systemic, skin and gastrointestinal effects. It is a carcinogen. Arsenic poisoning through water can cause liver and nervous system damage, vascular diseases and also skin cancer.

Mercury: The silvery-white liquid mercury used in common thermometers, is a potent neurotoxin, capable of causing severe brain damage in developing fetuses and mild tremors and emotional disturbances in exposed adults. Mercury and tin can get converted into organic forms like methyl mercury and methyl tin, which become more injurious to health and environment than the parent compounds.

Polychlorinated biphenyls (PCBs): It consists of a series of technical mixtures consisting of many isomers and compounds that vary from mobile oily liquids to white crystalline solids and hard non-crystalline resins. It is toxic by ingestion, inhalation and skin contact. A suspected human carcinogen, affects skin and liver. Usual signs of systemic intoxication include nausea, vomiting, weight loss, jaundice, edema and abdominal pain. Severe liver damage may cause coma and death.

Pesticides: The organophosphates and the carbonates present in pesticides affect and damage the nervous system and can cause cancer. Some of the pesticides contain carcinogens that exceed recommended levels. They contain chlorides that cause reproductive and endocrinal damage.

Petrochemicals: Benzene and other petrochemicals can cause cancer even at low exposure levels.

Hormone disrupting chemicals (HDCs): HDCs include bisphenol, dioxins, PCBs, some polybrominated flame-retardants and some

13th Annual Research Day

Organised by the Deanship of Scientific Research in Collaboration with the College of Engineering
Research Centre
2nd April 2018

phthalates. Hormones influence many aspects of the body, including regulation of its metabolism, and affecting sexual characteristics. Hormone Disrupting Chemicals (HDCs, also known as "gender benders", xenoestrogens, or endocrine disrupting chemicals) are able to imitate, or disrupt the action of natural hormones such as the female hormone oestrogen, the male hormone testosterone or the thyroid hormones. Oestrogens are the hormones that influence the development and maintenance of female sex characteristics, and the maturation and function of the sex organs, and testosterone serves a similar function for males. Thyroid hormones are involved in the growth, development and functioning of the body, including the brain. Hormones are particularly crucial during development in the womb and early childhood, as their signals control developing reproductive organs, growth and the development of the brain. It knows something, though not much, about the potential impact of HDCs on development of the reproductive organs. It is known very little about potential impacts on intelligence and behavior.

Waste oil: When oil is dumped in the open environment, into sewers or in landfills, it is capable of migrating into the soil and underground aquifers. It is found that one gallon of used oil can contaminate one million gallons of water, rendering it non-potable. Marine species can be adversely affected even if exposed to oil concentrations as low as 1 part per million. Since waste oil contains various hazardous contaminants, the burning of such oil increases air pollution as toxic gases are vented to the

atmosphere, affecting not just human beings but plants and birds as well.

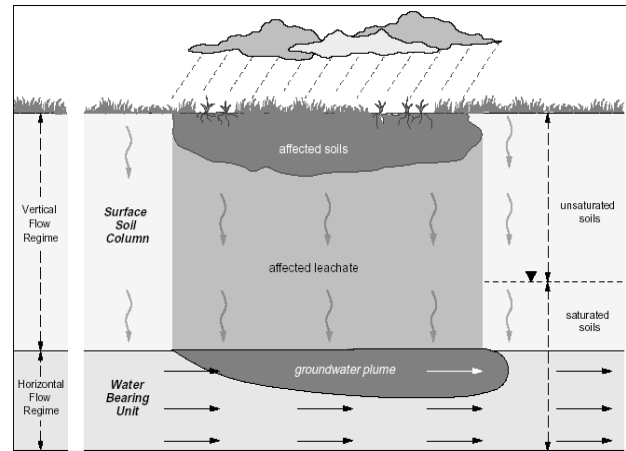


Fig 1: Idealized schematic of soil leachate migration

Model for Contaminant Concentration in the Aquifer the Domenico (1987) three-dimensional analytical contaminant transport model has been considered for estimation of contaminant concentration in aquifer (i.e. groundwater) at a desirable location and time. The Domenico (1987) three-dimensional model for a plume in an aquifer system, as shown in Fig. 2, with first-order decay is given as:

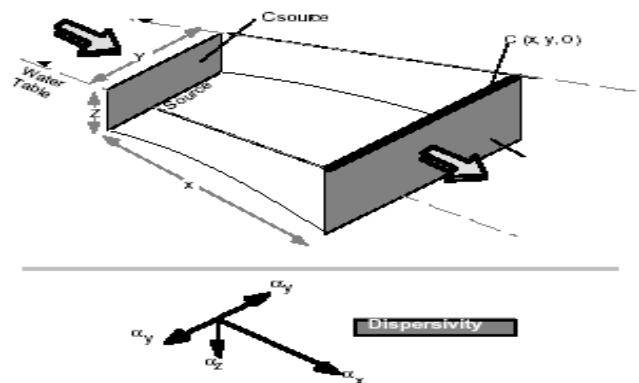


Fig. 2: A plume in an aquifer system

13th Annual Research Day

Organised by the Deanship of Scientific Research in Collaboration with the College of Engineering
Research Centre
2nd April 2018

$$C(x, y, 0, t) = \frac{C_0}{8} \exp \left[\frac{x}{2\alpha_x} \left(1 - (1 + 4\lambda\alpha_x/q)^{1/2} \right) \right] \times \operatorname{erfc} \left[\frac{(x - qt(1 + 4\lambda\alpha_x/q)^{1/2})}{2(\alpha_x qt)^{1/2}} \right] \times \left\{ \operatorname{erf} \left[\frac{(y + Y/2)}{2(\alpha_y x)^{1/2}} \right] - \operatorname{erf} \left[\frac{(y - Y/2)}{2(\alpha_y x)^{1/2}} \right] \right\} \times \left\{ \operatorname{erf} \left[\frac{Z}{2(\alpha_z x)^{1/2}} \right] - \operatorname{erf} \left[\frac{-Z}{2(\alpha_z x)^{1/2}} \right] \right\} \quad (1)$$

where

$C(x, y, 0, t)$ = concentration of contaminant at distance x downstream of source and distance y off centerline of plume at time, t at the top of water table (i.e. $z = 0$)

x = distance down gradient of source, as shown

y = distance from centerline of source

z = vertical distance from groundwater table to measurement point (assumed to be 0; concentration of contaminant is always assumed to be at top of water table)

t = time

C_0 = concentration of contaminant in source zone at $t = 0$, as given

α_x = longitudinal groundwater dispersivity, as shown in Fig. 2

α_y = transverse groundwater dispersivity, as shown in Fig. 2

α_z = vertical groundwater dispersivity, as shown in Fig. 2

λ = first-order decay coefficient for dissolved contaminants

Y = source width, as shown in Fig. 2

Z = source depth, as shown in Fig. 2

H = thickness of mixing layer (H)

q = Darcy flux or Darcy velocity of the contaminant in the aquifer

The initial conditions of the Domenico (1987) model are as follows:

- $C(x, y, 0, 0) = 0$ (Initial concentration = 0 for $x, y > 0$).

- $C(0, Y, Z, 0) = C_0$ (Source concentration for each vertical plane source = C_0 at time 0)

Following are the key assumptions in the Domenico (1987) model:

- The aquifer and flow field are homogeneous and isotropic.
- The groundwater velocity is fast enough that molecular diffusion can be ignored (may not be appropriate for simulation of transport through clays).
- Adsorption is a reversible process represented by a linear isotherm.

Health Risk Assessment Model

The general equation developed by U.S. EPA (1989 and 1991) to estimate the *chronic daily intake* (CDI) for a contaminant under ingestion pathway has been considered. The equation for CDI is as follows:

$$CDI = \frac{CW \times IR \times EF \times ED}{AT \times BW} \quad (2)$$

where

CDI = chronic daily intake (mg/kg-day)

CW = concentration of contaminant in groundwater (mg/L)

IR = ingestion rate (average = 2 L/day for adult)

EF = exposure frequency (350 days/year)

ED = exposure duration (average = 70 years)

BW = body weight (average 70 kg for adult)

AT = averaging time ($ED \times 365$ days/year)

The *excess lifetime cancer risk* (ELCR) can be calculated by multiplying the CDI with a *slope factor* (SF), as follows:

$$ELCR = CDI \times SF \quad (3)$$

Where,

13th Annual Research Day

Organised by the Deanship of Scientific Research in Collaboration with the College of Engineering
Research Centre
2nd April 2018

$ELCR$ = excess lifetime cancer risk

SF = slope factor, which value depends on the type of carcinogenic contaminant
(1/ mg/kg-day)

Using the value of $ELCR$, number of persons expected to develop a cancer over their lifetime as a result of exposure to the contaminant can be calculated as:

$$P_c = ELCR \times P \quad (4)$$

Where,

P_c = number of persons expected to develop a cancer over their lifetime as a result of exposure to the contaminant of concern

P = total number of persons exposed to the contaminant of concern

The program developed on the Excel-sheet for prediction of groundwater quality and health risk assessment consists of interlinking the models, as described in previous section (2). The program carries out calculations in the following steps:

- Calculation of D substituting the values of ℓ (for estimating α value as: $0.1e$), I , n , D_0 , and τ
- Calculation of q by substituting the values of K , i , n , and R .
- Calculation of C_0 by substituting the values of C_s , q , H , I , L , ℓ , n , and D .
- Calculation of $C(x, y, 0, t)$ by substituting the values of x , y , t , C_0 , α_x , α_y , α_z , λ , Y , Z , and q in Eq. 1.
- Calculation of CDI by substituting the values of CW , IR , EF , ED , BW , and AT in Eq. 2.
- Calculation of $ELCR$ by substituting the values of CDI and SF in Eq. 3.

- Calculation of P_c by substituting the values of $ELCR$ and P in Eq. 4

Utility of the Developed Integrated System

In order to illustrate utility of the integrated computerized system developed under the present work for groundwater quality prediction and health risk assessment, a typical example has been considered. In this example, contamination of groundwater and health risk, associated with this contamination, has been considered. The cause of contamination has been taken as the transportation of a carcinogenic contaminant to the groundwater from the base of a hazardous waste landfill. The input parameters, integrated computer program developed on Excel-sheet, and output results are presented, as follows:

Input Parameters

The input parameters typically considered, for running the developed program, are presented in Table 2. (*Integrated Computer Program Developed on Excel-Sheet*)

Output Results

The values of the concentration of contaminant in groundwater and corresponding health risk, predicted using the developed program considering different sets of x , y , and t values, have been presented

Table 2: Input parameters typically selected.

INPUT PARAMETER	Description/ notation	Typical value
Contaminant of concern	Trichloroethylene (a carcinogen)	---
Thickness of single soil layer overlying the aquifer	ℓ	0.5 m
Soil's longitudinal dispersivity coefficient	α	$0.1 \times e$
Infiltration rate through the soil layers overlying the aquifer (infiltration rate is taken as	I	10^{-10} m/s

13th Annual Research Day

Organised by the Deanship of Scientific Research in Collaboration with the College of Engineering
Research Centre
2nd April 2018

INPUT PARAMETER	Description/ notation	Typical value
permeability of soil)		
Porosity of the soil overlying the aquifer	n	0.50
Contaminant free-solution diffusion coefficient	D_0	$10^{-9} \text{ m}^2/\text{s}$
Tortuosity of the soil overlying the aquifer	τ	0.3
Concentration of contaminant at the source (i.e. at the base of the landfill)	C_s	1100 mg/L
Permeability of the aquifer	K	10^{-3} m/s
Hydraulic gradient	i	0.01
Retardation factor	R (as given by Equation	2
First-order decay coefficient for the contaminant	λ	0
Thickness of mixing layer, measured below water table	H	30 m
Length of the site (e.g. a landfill) in the direction of groundwater flow	L	50 m
Distance down gradient of source	x	10-1000 m
Distance from centerline of source	y	0-10 m
Time	t	1-10 year
Longitudinal groundwater dispersivity	α_x (Eq. 2.6)	$0.1 \times x$
Transverse groundwater dispersivity	α_y (Eq. 2.7)	$0.33 \times \alpha_x$
Vertical groundwater dispersivity	α_z (Eq. 2.8)	$0.06 \times \alpha_x$
Source width	Y	25 m
Source depth (= thickness of mixing layer, H)	Z	30 m
Ingestion rate	IR	2 L/day
Exposure frequency	EF	350 d/y
Exposure duration	ED	70 years
Body weight	BW	70 kg

INPUT PARAMETER	Description/ notation	Typical value
Averaging time	AT	$ED \times 365$ d/y
Slope factor for the contaminant	SF	0.011 1/mg/(kg-d)
Total number of persons exposed to the contaminant	P	10^6

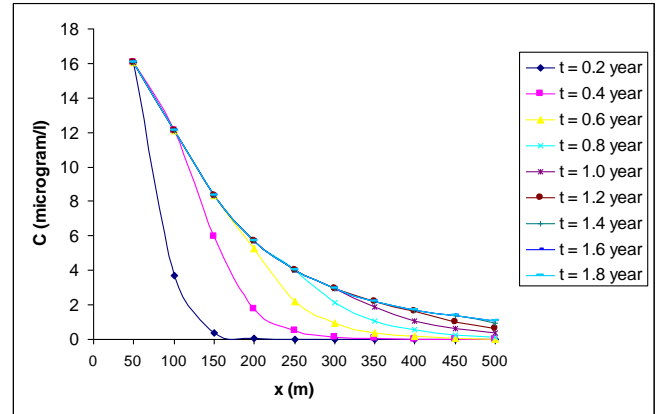


Fig.3: Variation of C with x and t at a constant y (typically equal to 5 m).

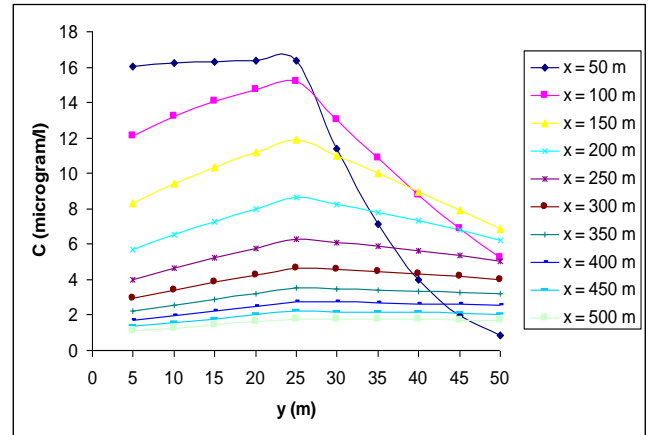


Fig.4: Variation of C with y and t at a constant x (typically equal to 5 m).

3. Results and Discussion

Following observations have been made:

- At a constant transverse distance, y , values of C and P_c are decreasing with increase in longitudinal distance, x , from the source, as shown in Fig.3.

13th Annual Research Day

Organised by the Deanship of Scientific Research in Collaboration with the College of Engineering
Research Centre
2nd April 2018

- C and P_c are found to be approaching towards a steady-state (i.e. invariant with time) with increase in t value. The steady-state condition has been found to be typically reached at $t = 1.6$ years, as shown in Fig. 3.
- The plot of x and y versus C , as shown in Fig. 4, indicates that the contaminant concentration is increasing with increase in y and after reaching to a peak value the concentration is decreasing with increase in y . It is also evident from Fig. 4 that the contaminant concentration is approaching to be invariant with transverse distance y as longitudinal distance x increases.
- The health risk is found to be increasing with time

4. Conclusions:

The ministry of environment and forest has identified various treatment and disposal options of different hazardous wastes that include physical / chemical treatment, landfill, biological treatment, incineration, recycle and recovery and solidification etc. A comprehensive literature review and survey on the hazardous waste generation of different states of India and its effects on human health has been made. After analyzing the quantity and its effects on human health, the trends and prediction of ground water contamination has been shown. Hence it is recommended that the concerned authority should focus more on developing effective means of waste minimization, recycling, its treatment and safe disposal. As the present findings are based on previous observations and assumptions, it is recommended that the local environmental researchers shall help to extend this study by incorporating the economic and environmental aspects. Some of the preventive measures such as inventorization of hazardous wastes, dilution, tube well design using well logging methods and other types of geophysical logging, specially made for contaminated zone, along with the

various treatment systems are also suggested for future scope of the work.

Acknowledgement

The authors acknowledge King Khalid University for proving academic and administrative supports,

References

1. Hazardous Wastes (Management and Handling) Rules, 1989, as amended in January 6, 2000 and May 21, 2003. (2) Published Official Gazette.
2. LaGrega, M.D., Buckingham, P.L., and Evans, J.C., "Hazardous waste management", McGraw-Hill Companies, Inc. 2001.
3. U.S. Code of Federal Regulations, 40 CFR261.1, 1985.
4. Bear, J., "Dynamics of fluids in porous media", Elsevier, New York, 1972.
5. Ministry of Environment & Forests (Department of Environment, Forests and Wildlife) notification, New Delhi, The 28th July, 1989
6. Connor, J.A., Bowers, R.L., Paquette, S.M., and Newell, C.J., "Soil attenuation model for derivation of risk-based soil remediation standards", Groundwater Services, Inc, Houston, Texas, July 1997, pp. 1-34.
7. Ganguly, C., Matsumoto, M.R., Rabideau, A.J., and Benschoten, J.E.V., "Metal ion leaching from contaminated soils: model development", ASCE Journal of Environmental Engineering, March 1998, pp. 278-287.
8. Ganguly, C., Matsumoto, M.R., Rabideau, A.J., and Benschoten, J.E.V., "Metal ion leaching from contaminated soils: model calibration and application", ASCE Journal of Environmental Engineering, December 1998, pp. 1150-1158.
9. U.S. EPA (U.S. Environmental Protection Agency), "Risk assessment guidance for superfund: volume 1 – human health evaluation manual (part A)", Report No. EPA/540/1-89/002, Office of Emergency and Remedial Response, Washington, 1989.
10. U.S. EPA (U.S. Environmental Protection Agency), "Standard default factors", OSWER Directive Report No. 9285.6-03, Office of Emergency and Remedial Response, Washington, 1991.
11. Hossain, M.A. and Yonge, D.R., "Linear finite-element modeling of contaminant transport in

13th Annual Research Day

Organised by the Deanship of Scientific Research in Collaboration with the College of Engineering
Research Centre
2nd April 2018

- groundwater", ASCE Journal of Environmental Engineering, November 1997, pp. 1126-1135.
12. Domenico, P.A., "An analytical model for multidimensional transport of a decaying contaminant species", Journal of Hydrology, 91, 1987, pp. 49-58.
 13. Baetsle, L.H., "Migration of radionuclides in porous media", Progress in Nuclear Energy, Series XII, Health Physics, ed. A.M.F. Duhamel, Elmsford, N.Y.: Pergamon Press, 1969, pp. 707-730.
 14. Sayre, W.W., "Dispersion of mass in open channel flow", Hydraulics Paper, No.3, 73, Colorado State University, 1968.
 15. Runkel, R.L., "Solution of the advection-dispersion equation: continuous load of finite duration", ASCE Journal of Environmental Engineering, September 1996, pp. 830-832.
 16. Mieszkowski, R., "Diffusion of lead ions through the Poznan Clay (Neogene) and through glacial clay", Geological Quarterly, 2003, 47(1), pp. 111-118.
 17. De Josselin de Jong, G., "Longitudinal and transverse diffusion in granular deposits", Am. Geophys. Union Trans. 39, 1958, pp. 67-74.
 18. Ogata, A. and Banks, R.B., "A solution of the differential equation of longitudinal dispersion in porous media", Professional Paper No. 411-A, U.S. Geological Survey, Washington, 1961, D.C., pp.1-7.
 19. Headquarters Department of Army, "Hazardous waste land disposal/land treatment facilities", Technical Manual, No. 5-814-7, Headquarters Department of Army, Washington, November 1984.

Out of Band Radiation Reduction in Multicarrier Cognitive Radio Systems Muneer Parayangat¹

¹Department of Electrical Engineering, College of Engineering, King Khalid University,
PO Box 394, Abha 61411 KSA.

E-mail address: mparayangat@kku.edu.sa

Abstract: In this paper, we discuss the OOB suppression techniques for multiple input multiple output orthogonal frequency division multiplexing (MIMO-OFDM) based CR systems. When an OFDM-based cognitive (CR) switches off its subcarriers to avoid causing interference to the primary user (PU) and in addition employs the interference reduction techniques, the number of subcarriers available for data transmission reduces thus leading to reduction in throughput of the SU. Combining MIMO with OFDM is regarded as a very attractive solution for CR systems to effectively enhance channel capacity over multipath fading channels as compared to SISO-OFDM. In this paper we use the combination of two techniques to minimize the out of band radiation reduction. First one is by projecting the signal onto a new subspace using a precoder designed by selecting the notched frequency. Another way of suppressing the OOB is by mapping the information symbols to a new set of symbols such that overall power spectral density (PSD) is decreased. We combined these techniques effectively to reduce the OBR. The results of the simulation studies illustrate that the proposed technique is very effective in reducing the OBR.

Keywords: *OFDM, Out of band radiation, Cognitive radio, Multicarrier systems, Precoding.*

1. Introduction:

Orthogonal frequency division multiplexing (OFDM) is an attractive modulation technique that allows for high data rates over multipath channels. OFDM mitigates the effect of multipath channel by essentially dividing the source spectrum into many narrow sub-bands that are transmitted simultaneously [1]. The bandwidth of the sub-bands is designed to be narrow enough so that the channel exhibits a flat fading over each sub-band.

Multiple input and multiple output (MIMO) technology is a wireless technology that uses multiple transmitters and receivers to transfer more data at the same time and increase the overall throughput. MIMO techniques have been introduced to increase the capacity without requiring additional bandwidth and power compared to the SISO technique. MIMO can also provide more degrees of freedom to the secondary users (SU) in a cognitive radio (CR) environment. The concept of CR was first

introduced in, where the focus was on the radio knowledge representation language (RKRL) and how the cognitive radio can enhance the flexibility of personal wireless services. CR has evolved to include a wide range of technologies for making wireless systems more flexible via more flexible transceiver [8].

OFDM is one of the most widely used technologies in current wireless communication systems and it has the potential of fulfilling all the requirements of CR systems. The interference caused by the CR users to the primary users is one of the prominent issue in CR systems. Several techniques have been proposed for reducing out of band radiation (OBR) [8]. The OBR of CR users can be reduced by inserting the guard band [9]. However, it will lead to decrease in the spectrum efficiency significantly. Several techniques have been proposed in both time domain and frequency domain for improving the performance of primary users by minimizing OBR. In [9], the time domain signal is multiplied

with a raised cosine windowing function to lower the sidelobes, but at a cost of expanding the symbol duration which results in lower throughput. Adaptive symbol transition technique is proposed in [10] extended the OFDM symbols adaptively at the cost of decrease in the useful symbol energy. Techniques in frequency domain based on the spectrum shaping techniques are also proposed. It can be classified as cancellation and precoding techniques. Active interference cancellation [11] and the introduction of cancellation carrier [12], are two schemes which result in enough suppression of OBR, but it will result in the drastic degradation of the bit error rate (BER).

In this paper we propose a OBR reduction technique for multiple input and multiple output MIMO multiuser OFDM based cognitive radio systems. We propose a new signal transformation technique which can effectively nullify the OBR. The results of the simulation studies illustrate that the proposed technique offers a significant reduction in out of band radiation in MIMO cognitive radio systems.

2. System Model and Proposed OBR Reduction Technique for MIMO-OFDM:

2.1 Transmit Signal and Receive Signal Models of the Precoded MIMO-OFDM System

We consider a MIMO-OFDM system with N secondary (CR) users utilizing the unoccupied spectrum, of licensed users (primary users), identified through suitable spectrum sensing techniques. The system has N_t transmit and N_r receive antennas. The encoder takes a single stream of binary input data and transforms it into N parallel streams of encoded bits followed by interleavers and symbol mappers. After the symbol mappers, the m -th inverse fast Fourier transform (IFFT) input at transmit antenna i is denoted by X_m^i where $m = 0, \dots, (N - 1)$. After performing the IFFT, the n -th OFDM symbol at i -th transmit antenna is denoted by x_n^i is given by

$$x_n^i = \frac{1}{\sqrt{K}} \sum_{m=0}^{K-1} X_m^i e^{\frac{j2\pi nm}{K}} \quad (1)$$

Where $n=0, 1, \dots, K-1$ and $i=0, 1, \dots, N_t$. Here, the CP is omitted for simplicity. Let $h_{n,l}$ be the impulse response of the l -th multipath component at time n from transmit antenna i to receive antenna j . Then n -th received symbol at receive antenna j is

$$y_n^j = \sum_{i=1}^{N_t} \sum_{m=0}^{L-1} h_{n,l}^{j,i} x_{n-l}^i + w_n^j \quad (2)$$

where w_n^j represents AWGN of j -th receive antenna at time n . Note that y_n^j is the sum of transmitted symbols from all transmit antennas. From (1) and (2), y_n^j can be written as

$$y_n^j = \frac{1}{\sqrt{K}} \sum_{i=1}^{N_t} \sum_{m=0}^{K-1} X_m^i e^{\frac{j2\pi nm}{K}} \sum_{l=0}^{L-1} h_{n,l}^{j,i} e^{\frac{-j2\pi lm}{K}} + w_n^j \quad (3)$$

By defining

$$H_{n,(m)}^{j,i} = \frac{1}{\sqrt{K}} \sum_{l=0}^{K-1} h_{n,l}^{j,i} e^{\frac{-j2\pi lm}{K}} \quad (4)$$

The m -th FFT output at receive antenna j is given by

$$Y_m^j = \sum_{i=1}^{N_t} y_n^j e^{\frac{-j2\pi nm}{K}} \quad (5)$$

Thus, we have

$$\begin{aligned} Y_m^j &= \sum_{i=1}^{N_t} \left[\frac{1}{K} \sum_{n=0}^{K-1} H_{n,(m)}^{j,i} \right] X_m^i \\ &+ \frac{1}{K} \sum_{i=1}^{K-1} \sum_{k=0, k \neq m}^{K-1} x_k^i \sum_{m=0}^{K-1} H_{n,l}^{j,i} e^{\frac{-j2\pi n(m-k)}{K}} \\ &+ W_m^j \end{aligned} \quad (6)$$

Note that W_m^j is the frequency domain sample value of the AWGN channel. There are total K_k number of subcarrier used to transmit M_k number of information symbols through single antenna. The OFDM symbol is generated using the method explained in Section (2.1). Thus, we obtain

$$\mathbf{y}_k = \mathbf{H}_k \mathbf{x}_k + \mathbf{w}_k \quad (7)$$

The above equation can be rewritten by incorporating all active users as

$$\begin{bmatrix} \mathbf{y}_1 \\ \vdots \\ \mathbf{y}_{N_r} \end{bmatrix} = \begin{bmatrix} \mathbf{H}_{1,1} & \dots & \mathbf{H}_{1,N_t} \\ \vdots & \ddots & \vdots \\ \mathbf{H}_{1,N_r} & \dots & \mathbf{H}_{N_r,N_t} \end{bmatrix} \begin{bmatrix} \mathbf{d}_1 \\ \vdots \\ \mathbf{d}_{N_r} \end{bmatrix} + \begin{bmatrix} \mathbf{w}_1 \\ \vdots \\ \mathbf{w}_{N_r} \end{bmatrix} \quad (8)$$

Here $\mathbf{H}_{i,j}$ represent a block diagonal matrix of dimension $K_k \times K_k$, \mathbf{d}_i represent the precoded OFDM symbols. The more details regarding the precoding is provided in the next section. By incorporating the idea of precoding, we have

$$\mathbf{d}_i = \mathbf{P} \mathbf{b}_i \quad (9)$$

More details regarding the formulation of the precoding matrix \mathbf{P} is provided in the next section. By taking the precoding into account, we obtain

$$\begin{bmatrix} \mathbf{y}_1 \\ \vdots \\ \mathbf{y}_{N_r} \end{bmatrix} = \begin{bmatrix} \mathbf{H}_{1,1} & \dots & \mathbf{H}_{1,N_t} \\ \vdots & \ddots & \vdots \\ \mathbf{H}_{1,N_r} & \dots & \mathbf{H}_{N_r,N_t} \end{bmatrix} \begin{bmatrix} \mathbf{P} \mathbf{b}_1 \\ \vdots \\ \mathbf{P} \mathbf{b}_{N_r} \end{bmatrix} + \begin{bmatrix} \mathbf{w}_1 \\ \vdots \\ \mathbf{w}_{N_r} \end{bmatrix} \quad (10)$$

The above equation can be rewritten as

$$\begin{bmatrix} \mathbf{y}_1 \\ \vdots \\ \mathbf{y}_{N_r} \end{bmatrix} = \begin{bmatrix} \mathbf{P} \mathbf{H}_{1,1} & \dots & \mathbf{P} \mathbf{H}_{1,N_t} \\ \vdots & \ddots & \vdots \\ \mathbf{P} \mathbf{H}_{1,N_r} & \dots & \mathbf{P} \mathbf{H}_{N_r,N_t} \end{bmatrix} \begin{bmatrix} \mathbf{b}_1 \\ \vdots \\ \mathbf{b}_{N_r} \end{bmatrix} + \begin{bmatrix} \mathbf{w}_1 \\ \vdots \\ \mathbf{w}_{N_r} \end{bmatrix} \quad (11)$$

Where we define

$$\bar{\mathbf{H}} = \begin{bmatrix} \mathbf{P} \mathbf{H}_{1,1} & \dots & \mathbf{P} \mathbf{H}_{1,N_t} \\ \vdots & \ddots & \vdots \\ \mathbf{P} \mathbf{H}_{1,N_r} & \dots & \mathbf{P} \mathbf{H}_{N_r,N_t} \end{bmatrix} \quad (12)$$

The $\bar{\mathbf{H}}$ represents the combined precoder and channel matrix. The precoder is deterministic and we assume that we have channel state information (CSI) at both transmitter and receiver. To recover the information symbols at the receiver, a decoder is needed to revert the spectral precoding operation. In this paper we made use of zero forcing (ZF) and minimum mean squared error (MMSE) equalizer for equalizing the data.

2.2 Precoding Technique for Reducing the OBR reduction in MIMO-OFDM.

Let $\mathbf{b}_n = [b_n(0), b_n(1), \dots, b_n(M_n - 1)]^T$ be a vector containing M_n information symbols without any precoding for the n th user. Here, $b_n(j)$ is the j -th symbol of n -th CR user and takes the value from the constellation used for symbol mapping. Assuming, that the data symbols are independently and identically distributed, we obtain [8]

$$E\{\mathbf{b}_n \mathbf{b}_n^H\} = \mathbf{I}_{M_n} \quad (13)$$

where \mathbf{I}_{M_n} is an $(M_n \times M_n)$ identity matrix. Defining a spectral precoding matrix \mathbf{Q}_n of dimension $(K_n \times M_n)$, we can shape the spectrum of n -th CR user's signal. The first level spectral precoding process for the n -th user is given as

13th Annual Research Day

Organised by the Deanship of Scientific Research in Collaboration with the College of Engineering
Research Centre
2nd April 2018

$$\bar{\mathbf{b}}_n = \mathbf{Q}_n \mathbf{b}_n \quad (14)$$

where $\bar{\mathbf{b}}_n = [\bar{b}_n(0), \bar{b}_n(1), \dots, \bar{b}_n(K_n - 1)]$ is the precoded data vector for n th CR user after first level precoding. Here, $\bar{b}_n(k)$, denotes the precoded symbol on k -th sub-carrier of n -th CR user. With the aid of (14), we get

$$P(f) = \frac{1}{T} \|S_n^T(f) \mathbf{Q}_n\|^2 \quad (15)$$

Where $S_n(f)$ is spectral density at frequency f . Thus, it is clear from (15) that we can shape or modify the PSD, $P(f)$ by choosing a proper precoding matrix \mathbf{Q}_n [30]. To compute the precoding matrix, we first calculate the SVD of S_n as [8,13]

$$\mathbf{S}_n = \mathbf{U}_n \Sigma_n \mathbf{V}_n^H \quad (16)$$

Where \mathbf{U}_n and \mathbf{V}_n are the unitary matrices of dimension $(L_n \times L_n)$ and $(K_n \times K_n)$ respectively. Here Σ_n is the rectangular diagonal matrix of dimension $(L_n \times K_n)$. Then, the spectral precoding matrix for n th user is defined as the last M_n column of \mathbf{V}_n matrix and is given as [8,13]

$$\mathbf{Q}_n = [\mathbf{V}_n^{(K_n - M_n)} \mathbf{V}_n^{(K_n - M_n + 1)} \dots \dots \mathbf{V}_n^{(K_n - 1)}] \quad (17)$$

where $\mathbf{V}_n^{(i)}$ represents the i^{th} column of \mathbf{V}_n . The columns of \mathbf{Q}_n constitute an orthonormal basis for the null space of \mathbf{S}_n . The orthonormality of columns will lead to

$$\mathbf{Q}_n^H \mathbf{Q}_n = \mathbf{I}_{M_n} \quad (18)$$

Apart from the precoding discussed in the last paragraph, we also design another precoding technique and use the combination of both these techniques. Defining the notched matrix $\bar{\mathbf{S}}_n = [S_n(f'_0) S_n(f'_1) \dots S_n(f'_{\bar{L}_n - 1})]^T$, where \bar{L}_n are the notched frequencies that are spaced far from band edges of the n -th CR user. We can do further refinement

on the precoded bits of first level to achieve more OBR suppression without losing the subcarrier utilization efficiency of the system. The refinement scheme can be found by solving the following optimization problem

$$\min_{\bar{\mathbf{b}}_n} \|\bar{\mathbf{b}}_n - \mathbf{d}_n\|_2 \quad \text{subjected to} \quad \bar{\mathbf{S}}_n \mathbf{d}_n = \mathbf{0}_{K_n} \quad (19)$$

The closed form solution for (19) can be obtained as [12-14]

$$\bar{\mathbf{Q}}_n = \mathbf{I} - \bar{\mathbf{S}}_n^H (\bar{\mathbf{S}}_n \bar{\mathbf{S}}_n^H)^{-1} \bar{\mathbf{S}}_n \quad (20)$$

Since, the optimization in the second level is having a closed form solution, we can calculate the combined precoding matrix for the overall precoding scheme as

$$\mathbf{P}_n = \bar{\mathbf{Q}}_n \mathbf{Q}_n \quad (21)$$

Using (21), the precoded and optimized symbol \mathbf{d}_n is given as [2]

$$\mathbf{d}_n = \mathbf{P}_n \mathbf{b}_n \quad (22)$$

2.3 Zero Forcing Equalizer of Received Signal

The ZF equalizer is the simplest equalization technique used to retrieve the information symbol which is corrupted by noise present in the channel. Consider the MIMO-OFDM system model given by (11). Here we want to find the $K_k N_t \times K_k N_r$ equalizer matrix \mathbf{W} which minimizes the cost function

$$E \{ \|\mathbf{b} - \tilde{\mathbf{b}}\|^2 \} \quad (23)$$

where $\tilde{\mathbf{b}} = \mathbf{W} \mathbf{y}$ is the equalizer output vector. If the $K_k N_r \times K_k N_t$ combined channel precoder matrix $\bar{\mathbf{H}}$ is given, the solution of ZF equalizer \mathbf{W} can be obtained by the following equation:

$$\mathbf{W} = (\bar{\mathbf{H}} \bar{\mathbf{H}}^H)^{-1} \bar{\mathbf{H}}^H \quad (24)$$

This matrix is also known as pseudo inverse.

2.4 MMSE Equalizer of Received Signal

The MMSE equalizer is one of the solutions for reducing ICI as well as equalizing mixed signals transmitted from more than one transmit-antenna for MIMO-OFDM systems. Consider the MIMO-OFDM system model as given in (11). The MMSE approach tries to find a coefficient \mathbf{G} which minimizes the criterion

$$E\{\|\mathbf{W}\mathbf{y} - \mathbf{b}\|^2\} \quad (25)$$

The solution of MMSE equalizer \mathbf{W} can be obtained by the following expression:

$$\mathbf{W} = (\bar{\mathbf{H}} \bar{\mathbf{H}}^H + N_0 \mathbf{I})^{-1} \bar{\mathbf{H}}^H \quad (26)$$

We notice that both the coding and decoding operations above are on a user basis so that the data of different users can be processed independently at both the transmitter and receiver. Especially, the individual receivers can avoid any joint processing of data for other users after the FFT block. It is also possible to divide the subcarriers utilized by a user into groups and create several virtual users to further reduce the complexity with a smaller number of subcarriers for each virtual user. If the individual transmitter and receiver know where the utilized subcarriers and notched frequencies are, they will be able to compute the precoder and decoder independently. Whenever the spectrum utilization pattern is changed, they may convey such information via a common control channel. It is unnecessary for them to exchange the precoding matrix, which involves a lot of overhead. With such flexibility, our scheme is suitable for dynamic spectrum sharing between CR and LU where the spectrum environment keeps varying.

3. Results and Discussion

We present the results of simulation studies to illustrate the performance of our proposed spectral precoding scheme in multiple antenna system. A MIMO-OFDM based CR system is considered. We assume $T_s = 1/15$ ms, and $T_g = 3/640$ ms. A total of 480 subcarriers with a single CR user having $K_k = 120$ subcarriers is chosen which is having $N_t = 2$ and $N_r = 2$ antenna. The total sub-carrier index set including all users is numbered as $\{-240, \dots, -1, 1, \dots, 240\}$. BER performance of CR users with the proposed technique under Rayleigh fading channel is considered with Binary phase shift keying (BPSK) as modulation schemes. Without loss of generality, we mainly consider the performance of a single CR user with multiple antennas for evaluating the proposed technique. A perfect channel estimation is also assumed at the receiver.

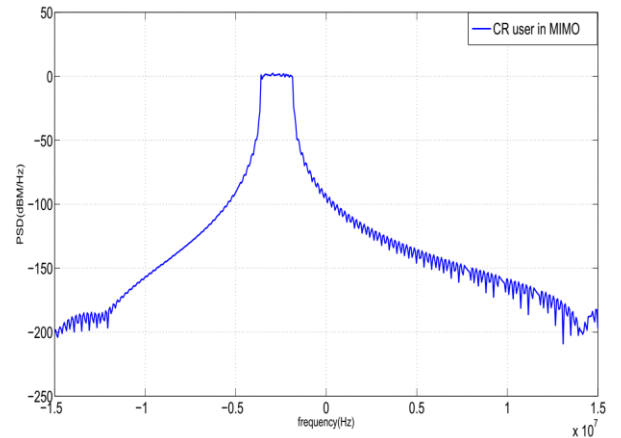


Figure (1) PSD of single CR user with the proposed precoding scheme

In Figure 1, the PSD curves of the precoded OFDM signal of single CR user with multiple antenna is shown. For the first level precoding of user 1, $L_k = 8$ notched frequencies are selected is given as $\{-5040, -5041, -4580, -4581, -720, -721, 600, 601\}$ kHz [2]. Therefore, each user has $M_k = 112$ information symbols. The CR user is allocated the band of -3.6 MHz to -1.86 MHz. For first level precoding scheme, the notched frequency set are selected on two sides of PSD of a CR user 1, which are nearer to the band edges of the spectrum of user 1

spectrum. For second level of optimization $L_k=10$ notched frequencies are selected which are far from the edges of CR user spectrum as {1500, 1499, 1350, 1351, 1100, 1101, 1100, 1101, 1499, 1500} kHz [2]. The resulted PSD curves of CR user is well below the spectral mask. Therefore, sufficient suppression of OOB is achieved with the proposed precoding scheme.

Figure 2 illustrates the BER performance of CR user with 2×2 MIMO system using BPSK under Rayleigh fading channel. Both ZF and MMSE equalization is applied for recovering information symbols. The BER of CR user in MIMO scenario is improved because of the frequency diversity provided by the precoder. The BER of CR user is compared with the BER performance of CR user in SISO under Rayleigh fading-channel.

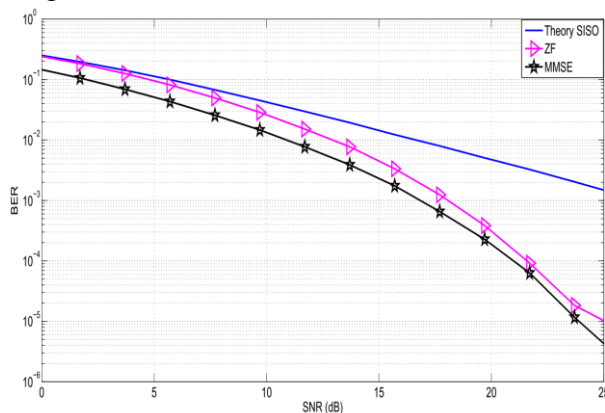


Figure (2) BER of single CR user employed with 2×2 MIMO system

4. Conclusions:

In this paper, a precoding scheme for MIMO-CR is proposed. The results illustrate that the scheme offered sufficient OOB suppression to the PSD of CR user which is employed with multiple antenna system. Also, the proposed precoder provides frequency diversity to the system and improved the BER performance as compare to the uncoded system. Hence, our proposed method serves as a good candidate for 5th generation (5G) MIMO CR system where OFDM will play a leading role as the preferred transmission technique.

Acknowledgement

I would like to thank the King Khalid University for providing the platform to share the research work.

References

- [1] H. A. Mahmoud, H. Arslan, "Sidelobe suppression in OFDM based spectrum sharing systems using adaptive symbol transition," *IEEE Commun. Lett.*, 12(2008)2,
- [2] T. Weiss, F. K. Jondral, "Spectrum Pooling: An Innovative Strategy for the Enhancement of Spectrum Efficiency," *IEEE Communications Magazine.*, 42(2004)3.
- [3] J. Mitola and G. Q. Maguire, "Cognitive radios: making software radios more personal," *IEEE Pers. Commun.*, 6(1999)4.
- [4] J. Mitola III, "Cognitive radio for flexible mobile multimedia communication," *Proc. IEEE International Work-shop on Mobile Multimedia Communications (MoMuC)*, 10(1999).
- [5] T. S. Haykin, "Cognitive radio: brain-empowered wireless communications," *IEEE Journal on Selected Areas in Communications*, 23(2005)2.
- [6] S. Weinstein and P. Ebert, "Data transmission by frequency-division multiplexing using the discrete Fourier transform," *IEEE Trans. Commun. Technol.*, 19(1971)5.
- [7] J. Bingham, "Multicarrier modulation for data transmission: An idea for whose time has come," *IEEE Commun. Mag.*, 28(1990)5.
- [8] Anuradha Pandey, Muneer P. and Sameer SM, "Two level precoding scheme for out of band radiation reduction in multiuser OFDM based cognitive radio," *IEEE Communications Magazine.*, 42(2004)3.

13th Annual Research Day

Organised by the Deanship of Scientific Research in Collaboration with the College of Engineering
Research Centre
2nd April 2018

- [9] I. Weiss, J. Hillenbrand, A. Krohn, and F. K. Jondral, "Mutual interference in OFDM-based spectrum pooling systems," Proc. IEEE Veh. Tech.Conf., 4(2004).
- [10] H. A. Mahmoud and H. Arslan, "Sidelobe suppression in OFDM based spectrum sharing systems using adaptive symbol transition," IEEE Commun. Lett., 12(2008)2.
- [11] H. Yamaguchi, "Active interference cancellation technique for MB-OFDM cognitive radio," Proc. IEEE Eur. Microw. Conj., 2(2004).
- [12] A. Tom, A. Sahin and H. Arslan, "Mask compliant precoder for OFDM spectrum shaping," IEEE Commun. Lett., 17(2013) 3.
- [13] S. Brandes, I. Cosovic, and M. Schnell, "Reduction of out-of-band radiation in OFDM systems by insertion of cancellation carriers," IEEE Commun. Lett. 10(2006)6.
- [14] X. Zhou, G. Ye Li and G. Sun, "Multiuser spectral precoding for OFDM based cognitive radios systems," IEEE Journ. Sel. Areas Commun., 31(2013)3.

Integration Of The Active-Passive Architecture Techniques For Attaining Optimum Building Sustainability In The Hot-Dry Climate Regions Of Saudi Arabia

Farhat Ali¹ and Ahmed Al-Zo'abi¹

¹Department of Architecture & Planning, College of Engineering, King Khalid University,
PO Box 394, Abha 61411 KSA.
E-mail address: faalali@kku.edu.sa

Abstract: The building industry is supposed to be the highest consumers of energy in the present scenario. Even building contribution in energy use with more than 50% of total energy consumed in Saudi Arabia according to Saudi Energy Efficiency Center (SEEC, 2013). So, it's a great demand for energy that the construction & Architectural design of building in Saudi Arabia should be responded to the environment. Due to the rapid development & population growth, Saudi Arabia needs huge construction requirements. Which overrule the adoption of sustainable building standards in hot and arid climates.

Passive Architecture strategies help to reduce the dependency on energy demand as it involves the features of local climate and aspects of traditional passive design.. Also, this paper will help to know the implication of sustainable renewable energy that might be used to reduce the environmental impact on modern building in Saudi Arabia. The study in this paper will suggest the adoption of the integrated approach for the Active- passive building techniques in hot and arid climatic regions of Saudi Arabia.

In buildings, Passive solar design techniques will permit the basic comfort conditions related to heating, cooling for thermal and natural lighting for human comfort and minimize the energy uses through the conventional mechanical system. The research of the hybrid passive design for hot dry climates regions will show significantly minimize the high energy consumption in Saudi Arabia. Also, The implementation of the hybrid method can develop the energy efficiency and carbon footprint of buildings decline. This can be achieved by integrating passive design and vernacular architecture and also implementing innovative sustainable technologies in the accordance with the climatic conditions of Saudi Arabia.

Keywords: *Sustainability, passive architecture, active-passive design techniques, energy consumption, hot & arid climate regions, vernacular architecture.*

1. Introduction:

As we know, Most of building in developing countries are not designed with the parameters of climate like urban surrounding, building materials & orientation which affect the indoor climate hence affect the inhabitant's comfort and health conditions. This problem can be seen in many academic, residential and commercial buildings.

Passive design plays a very important role in to maintain an indoor environment. Passive design

minimizes or eliminates the need for auxiliary heating or cooling. The aim of this paper is to present information about the climatic design of building nowadays, using passive techniques. This paper describes the core ideas in climatic design and gives a recommendation on how to carry out the construction and architecture design in various climates. The focus is majorly on building design and urban climate oriented. Mainly the analysis of the passive design features used to controlling indoor environment aspects.

13th Annual Research Day

Organised by the Deanship of Scientific Research in Collaboration with the College of Engineering
Research Centre
2nd April 2018

Passive architecture involves hybrid conventional architecture principles with solar and wind energy and the inherent properties of building materials to ensure the interior warm in winter and cools in summer, just to create a comfortable environment. Building using passive techniques having the relation between building elements and materials. As we should clearly know that passive architecture design does not mean the elimination of standard mechanical systems. In a recent design, passive system integrated with the active system with high efficiency that reduces the application of traditional methods of heating and cooling system and this integration maintain comfortable indoor temperatures. Apart from this the main criteria of passive design are to describes a building design approach that focuses on the provision of maximum indoor comfort with minimum dependence on energy and building services for the biggest group of society. The objectives of this paper are to explore the progress of sustainability and use of passive design and vernacular architecture in present building in Saudi Arabia in context of following the most of the climate.

2. Materials and Methods:

2.1 Vernacular designs methods in Saudi Arabia

It comprises the implication of local resources to meet the local need and preserving the historical, cultural and climatic conditions. Vernacular designs are free to adopt new technology and materials. It can be implemented in different bioclimatic features as per the climatic zone. Theses designs provide more thermal comfort, suitable lighting and air ventilation in the building. This type of design is more beneficial for the group of building with narrow roads between structure for getting more shade and safe ventilation from the outside climate. Internal courtyard is another important feature which can be used for activities and privacy for the inhabitants and also improve the ventilation system of the building. It also helps the warm air to become cold before the entrance

to the building by flowing air over the wet surface.

In the contemporary building, the research states that the amount of energy used for modern building is six times higher than the traditional building. It's due to our dependency over the artificial cooling system. It involves high energy consumption, environmental impact and operation cost. This practice will end the traditional culture and social aspects. So, we need to adopt the hybrid approach for reducing mechanical operation cost for cooling and heating by introducing a source of renewable energy and climatic features while the designing of the building.

2.2 The application of renewable energy methods at KAUST, KSA through case study

In the present scenario, Saudi Arabia is taking initiative on developing green building design. This will help to reduce the carbon emissions and increase the energy efficiency by considering latest technologies. King Abdullah University for science and technology (KAUST) campus have implemented the buildings by adopting sustainable approaches. They install high-performance roofs using hybrid technologies, such as photovoltaic and solar thermal equipment to generate heat and electricity in 900,000 sqmt of roofs, and it cost to meet 8% of the whole campus demand for energy.



Figure (1) The solar tower & top roof at KAUST

This project also includes a construction of the high solar tower for passive cooling. The tower is well equipped with fans to create different

13th Annual Research Day

Organised by the Deanship of Scientific Research in Collaboration with the College of Engineering
Research Centre
2nd April 2018

pressure as shown in the figure. It is To create a passive pressure difference and continuous breeze along the shaded courtyards, DSE installed two fans, each extracting 95 cum/sec through 3.0m diameter axial blades power fueled of solar power and prevailing winds.



Figure (2) The overview of the ventilation system
Source:- <http://www.aiatopten.org/node/113>

It also includes high-performance glazing that filters daylight and reduces the use of artificial lighting. This project is the first building that has got a platinum LEED certificate in Saudi Arabia. This is one of the largest PV installations in Saudi Arabia till date. The other benefits are as follows:-

- It reduces 1,700 tons of carbon emissions annually.
- Support KAUST's goals to become a leading institute in renewable energy science and engineering.
- Raises consciousness of the benefits of alternative energy

2.3 The application of renewable energy methods at The Princess Noura Bint Abdul Rahman University, Riyadh, KSA

LEED Platinum, awarded in 2012 by the KNX Association Category. The KNX technology ensures efficient lighting and air conditioning control and provides protection against sun and heat by shading technology in large glass fronts of all buildings of the complex. Including BMS control and integration of other multimedia systems.

3. Results and Discussion -

3.1 Hot and Dry/Arid climatic region in KSA

A hot and dry climate is identified by a mean monthly maximum temperature more than 30°C. The regions in this climate mostly find flat and sandy or rocky ground can be seen. In this type of climate, it is essential to control solar radiation, and flowing of hot winds. Thus, building design criteria should consist of suitable shading, minimum exposed area, and enhance thermal capacity. For example, we will discuss the Riyadh city in Saudi Arabia

- Riyadh, Saudi Arabia is at 24°42'N, 46°44'E, 620 m (2034 ft).
- Riyadh has a subtropical desert / low-latitude arid hot climate.
- According to the Holdridge- life zones system of bioclimatic classification Riyadh is situated in or near the subtropical desert biome.

Table 1: Characteristics of Tap water

Climatic Variable	Average					
	Max Temp °C	Temp °C	Min Temp °C	Pre mm	Nos Wet Days	Daylight Hrs/Day
Jan	28	14	3	11	3	10h 46'
Feb	30	16	4	10	1	11h 17'
Mar	35	21	8	24	2	11h 58'
Apr	38	26	12	29	1	12h 42'
May	42	32	18	8	2	13h 19'
Jun	44	34	21	0	0	13h 37'
Jul	45	35	23	0	0.5	13h 29'
Aug	45	35	24	1	0	12h 58'
Sep	43	32	19	0	0	12h 15'
Oct	38	27	14	1	0	11h 31'
Nov	33	21	9	6	5	10h 54'
Dec	28	15	3	11	3	10h 37'
ANNUAL	37	26	13	101	17.5	12h 00'

3.2 Main Characteristics:-

13th Annual Research Day

Organised by the Deanship of Scientific Research in Collaboration with the College of Engineering
Research Centre
2nd April 2018

Air Temperature

- During the day between 43° and 49°c.
- At night - Dry season between 27° and 32°c

Humidity

- Relative Humidity (RH) is low from 10% to almost 55%

Vapor Pressure

- Between 750 to 1500 N/m2

Precipitation

- Slight and variable throughout the year
- Limited rainfall – 50mm rain in a few hours
- Flash rain may occurred but some region may not have any rain for several years

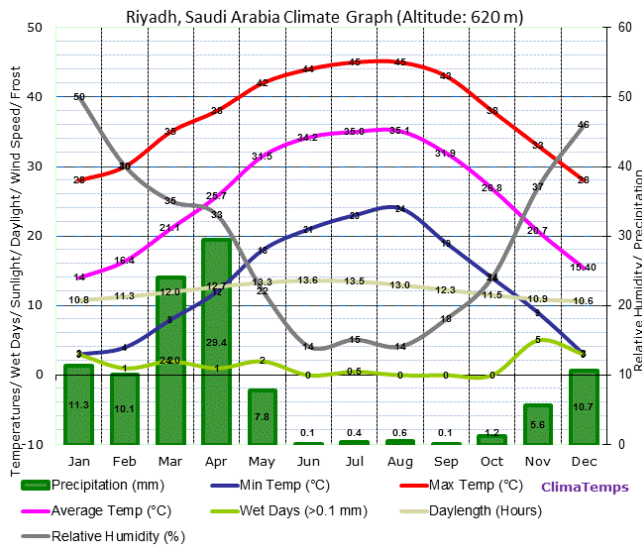


Chart (1) Riyadh, Saudi Arabia Climate Graph for
Table 1

Sky Condition

- Are normally clear clouds are few due to low humidity of the air
- During storms, skies are dark and dull

Solar Radiation

- Strong and mainly direct during the day
- Absence of cloud permits easy release of the heat stored during the day.

Wind

- Hot and together with dust and sand
- Occurrence of sandstorm

Vegetation

- Sparse and difficult to maintain due to lack of rain and low humidity (i.e.: palms, cactus)
- Soil is usually dusty and very dry

3.3 Passive Design Considerations for the hot and dry/arid climate of Saudi Arabia

1. Flat type roof is constructed due to sandstorms but it should not obstruct the flow of wind.
2. Small windows are designed to stop sand and dust from entering the home.
3. Built a thick wall to slow the heat entering the home during daytime and cold air drive the warm air to flow outside during night thus maintaining building comfort
4. A Pitched roof should be built with double skin.
5. Most houses should be constructed in concrete.
6. Building colors should be light and bright
7. Materials used not to crack because of high daytime temperature and rapid cooling at night.
8. Built the high level of well-insulated wall for thermal.
9. Maximum built upside should face north with passive solar access.
10. Design to driven cool air with proper cross ventilation.
11. External wall area should be limited.
12. Select compact planning of floors with central nearest stack ventilation shaft.
13. Adopt the designing of central courtyards with evaporating cooling water features to permit night cooling with windshield.
14. Application of mechanical ventilation in ceiling spaces to ensure the sufficient height to flows cooler air.
15. Designed with screened, shaded outdoor living areas that restrict the direct sun.
16. Built garden ponds and water features outdoor windows to generate evaporate cooling.
17. Minimum use of glazing

13th Annual Research Day

Organised by the Deanship of Scientific Research in Collaboration with the College of Engineering
Research Centre
2nd April 2018

18. Use a different type of glazing for various façade according to their U value.
19. Aluminum frame double glazing window with solar radiation effect
20. Living areas should be covered by double glazed glass
21. For windows in north facing should be high SHGC glazing and passive shading
22. When one window is located higher than another, the thermal force will direct the airflow from the high window to the lower window creating good ventilation.

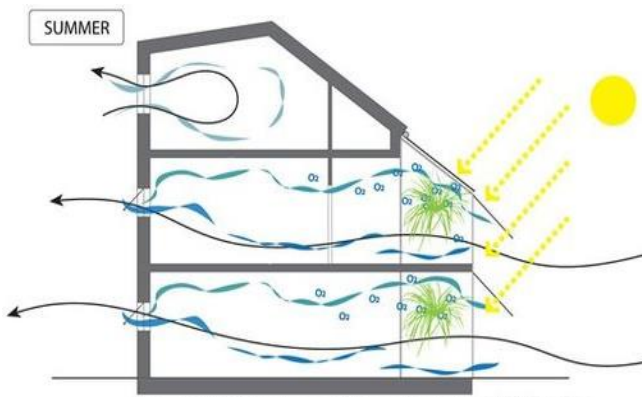


Figure (3) Summer ventilation strategy is focused on crossed ventilation. Pressure differences encourages cross ventilation which also cools the building down (source-google)

23. Shade east and west side glass or the small window in summer
24. Provision of ceiling fans in all sleeping and living spaces
25. Light color for building (external and internal wall surfaces) and roof should be selected.
26. Provide shading and insulate devices for the residence for day heat and move out stored heat in cooler nights.
27. Design the home with the minimum length of east and west wall.
28. Enclose the surrounding adjacent to building space with sufficient depth.
29. Use covered or shaded court or garden spaces, with ponds and water availability, to

cool the lower level air that is entering to the house.

30. Internal courtyards provisions for cross ventilation & natural cooling. Courtyards, patios, and verandas are other common features of buildings in hot climates.



Figure (4 & 5) Internal Courtyard & cut solar heat gain (source:- google)

31. Greenery in courtyard should be given for aesthetic look and trees, shrubs and bushes also provide natural shade with the sun.
32. Majorly opening should be provided in internal courtyard side.

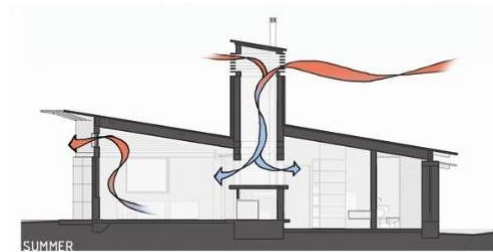


Figure (6) Solar chimney showing ventilation process (source:- google)

33. Solar chimneys can be provided as stack-effect ventilators. The concept, warmer air is lighter and thus more buoyant than cooler air & the temperature differential (stacking) induces a forced upward flow.

4. Conclusions:

The main aim of adopting passive architecture strategies is to reduce energy consumption because 70% of the total building consumption goes to cooling loads. The proposed designed consideration should take into account energy reduction before looking to alternative

13th Annual Research Day

Organised by the Deanship of Scientific Research in Collaboration with the College of Engineering
Research Centre
2nd April 2018

sustainable energy resources; otherwise, we might have faced the serious problem in future due to increasing consumption. We have a renewable source of energy in plenty, we need to consider the climatic factor to design any building in proper balance with the mechanized source of energy. Passive architecture designing of building reduce the energy even we can save the energy by 71% in a Saudi house with the use of photovoltaic. Applying passive cooling strategies, we can enhance our building performance.

Sustainable development can be attained by integrating various architectural principles. The implementation of passive design and vernacular approaches can recover the energy efficiency with the better internal environment. Additionally, the energy balance solution in building describes the importance away from passive solar design and places it on purchasing excessively huge photovoltaic arrays. Building norms are required to reduce the energy consumption and its possible through the hybrid approach of vernacular design with sustainable advanced technologies. This will minimize the problems of buildings in Saudi Arabia with the Integration of the Active-Passive Architecture sustainable techniques in the hot-dry climate regions.

Acknowledgement

This research is conducted by FARHAT ALI, based on my previous papers, contents based on sustainability, renewable energy, climate etc. The authors thank KKU, which created interest to conduct research on Saudi Arabia hot climate & finding out a hybrid approach in the field of passive architecture & energy efficient buildings.

References

[1] Abu-Ghazze, T. M., 'Vernacular architecture education in the Islamic society of Saudi Arabia: Towards the development of an authentic

contemporary built environment'. Habitat International, 21, 229-253, 1997.

[2] Taleb, H. M. and Sharples, S., 'Developing sustainable residential buildings in Saudi Arabia: A case study'. Applied Energy, 88, 383-391, 2011.

[3] Singh, M. K., Mahapatra, S. and Atreya, S. K., 'Solar passive features in vernacular architecture of North-East India'. Solar Energy, 85, 2011-2022, 2011.

[4].<https://global.sunpower.com/sites/international/files/media-library/case-studies/cs-sp-saudi-arabia-kaust-cs-1q15-d.pdf>

[5] Aboul Naga, M. M. and Elsheshtawy, Y. H., 'Environmental sustainability assessment of buildings in hot climates: the case of the UAE'. Renewable Energy, 24, 553-563, 2001.

[6] Mohammed A. E. S., 'The Integration of Tradition and Modernity: A Search for an Urban and Architectural Identity in Arriyadh, The Capital of Saudi Arabia'. Habitat International, 22, 571-589, 1998.

[7] International energy agency (IEA). Key world energy statistics, [Online].

[8].<https://www.witpress.com/Secure/elibrary/papers/ARC12/ARC12015FU1.pdf>

[9] Alawaji, S. H., 'Evaluation of solar energy research and its applications in Saudi Arabia: 20 years of experience'. Renewable and Sustainable Energy Reviews, 5, 59-77, 2001.

[10] Huraib, F. S., Hasnain, S. M. and Alawaji, S. H., 'Lessons learned from solar energy projects in Saudi Arabia'. Renewable Energy, 9, 1144-1147, 1996.

[11] Almatawa, M. S., Elmualim, A. A. and Essah, E. E., 'Passive and active hybrid approach to building design in Saudi Arabia'. Eco Architecture IV, 163-173, 2012.

[12] Hyde, R. 2000 Climate responsive design: a study of buildings in moderate and hot dry climates, London: E and FN Spon.

High voltage driver electronics design for DIODE based field emission display based on silicon nano electron emitters.

Dr. M. Z. Shamim¹

¹Department of Electrical Engineering, College of Engineering, King Khalid University,
PO Box 394, Abha, 61411, KSA.
E-mail address: mzmohammad@kku.edu.sa

Abstract: To demonstrate field emission from silicon based cold cathode nano electron emitters, it was essential to develop simple driver electronics to exemplify their potential as a future flat panel display technology. Here we have demonstrated the design and development of 32×32 lines demountable silicon devices, which would be housed within a vacuum system and driven using custom driver electronics solutions. We also demonstrate the driver electronics development for DIODE (non-gated) field emission devices.

Keywords: *field emission, driver electronics, cold cathode, electron emitter.*

1. Introduction:

Flat-panel display technology (FPD) is a broad and rapidly evolving area. Conventional cathode-ray tube (CRT) displays had a dominant position in products such as television and PC monitors for many decades. But in recent years, flat panel display technologies have overtaken the CRT market share. The size of the FPD market is huge and rapidly expanding. Diverse display technologies are involved e.g. liquid crystal display (LCD), plasma display, field emission display (FED), etc. and major technological and product breakthroughs are occurring on a regular basis.

Field emission displays is one such technology that is being extensively researched into finding the optimum electron emitter source which bombard a phosphor coating which acts as a light emission medium. Unlike, CRT's field emission displays use a large array of fine metal tips or carbon nanotubes positioned behind a phosphor coated anode plate to emit electrons through a process called electron emission. FEDs are considered to provide the closest matching picture quality to CRTs [1]. They are also energy

efficient by consuming less power than existing LCDs and plasma displays. The major drawback that is preventing commercialization of this technology is the extensive photolithography required for micro-tip fabrication or development of new manufacturing facilities for large scale CNT deposition which increases the production cost. Here, planar field emitters pave the way for moving this technology forward by using non-photolithography based fabrication of field emitters [2 – 4]. Silicon being the backbone of the semiconductor industry, silicon production is an established manufacturing process. Hence the use of silicon as cold cathode emitters leads towards the possibility of making commercially viable field emission displays [5, 6].

Preliminary research in using laser annealed planar silicon cold cathode emitters has shown that silicon has the potential to become the desired material for field emission displays. Laser annealing is also well known in the manufacturing world to produce crystalline silicon. Hence the combination of two well established manufacturing and processing

technique pave the way towards the holy-grail of cheap field emission displays.

2. Experimental Procedure:

2.1 Fabrication of 32×32 lines demountable silicon FED devices.

Simple non-patterned silicon devices have been used for field emission measurements in the past. However, for commercial prototypes, we need to be able to pattern these devices if we are to matrix address them using bespoke high voltage driver electronics. Here, we discuss only the development of demountable 32 × 32 diode silicon FED devices.

The photomasks were designed using “ELPHY QUANTUM” software (developed by RAITH GmbH, Germany) The design was to fit a 5 inch square piece of “glass/quartz” with the design substrate area restricted to 8 x 5 cm.

The active area of the device would be used for depositing commercial grade amorphous silicon in the case of the cathode plate and low voltage phosphor in the case of anode plate. The only difference between the cathode and anode photomasks was the fan-out being available on both the sides for the cathode enabling us to more easily make pin connections with the 32 cathode lines individually if necessary. The photomasks were patterned on 5 inch glass plates by Compugraphics (Compugraphics photomask solutions, UK), who specialize in developing photomasks for customers worldwide.

These photomasks were then used to fabricate several devices using conventional photolithography to be used in the vacuum test chamber to test their operation using driver electronics designed ‘in-house’. In the case of the cathode, different metals were used to form the 32 lines of back metal (e.g. Mo, Cr, Al). This was

then followed by the plasma deposition of commercial grade amorphous silicon. The excess silicon between the metal lines was etched off to completely isolate the 32 emitter lines from each other. This allowed for individually addressing the 32 silicon cathode emitters. Several devices were made with different silicon deposition conditions and thickness. These devices were then excimer laser irradiated with varying annealing conditions and beam profiles to assess their performance (Fig. 1, top). As for the Anode (Fig. 1, bottom), the anode photomask was used to fabricate 32 lines of ITO (Indium Tin Oxide) to form a transparent high voltage contact. This was then deposited on with different thickness of low voltage field emission phosphors, developed by Phosphor Technology (Phosphor Technology, UK).

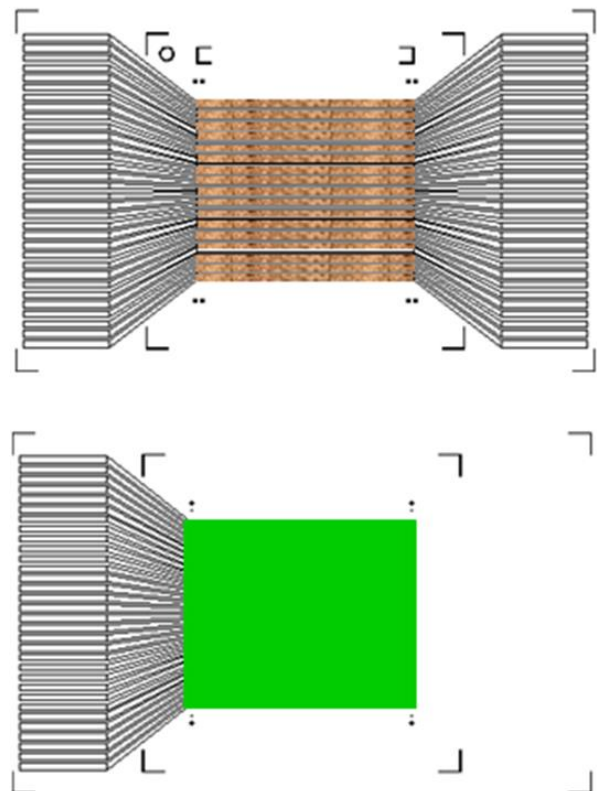


Figure (1) Schematic representation of (top) amorphous silicon deposited cathode photomask, (bottom) phosphor deposited anode photomask.

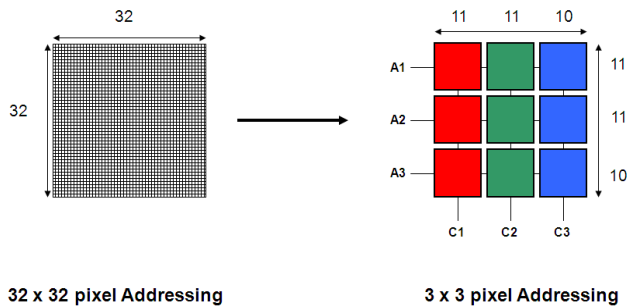


Figure (2) Schematic representation of the 3 × 3 DIODE device configuration.

2.2 Circuit Design & Testing

For test purposes, the 32 × 32 silicon diode device was rewired to a 3 × 3 silicon diode device. This was achieved by grouping the rows and columns in groups of 11, 11 and 10 lines. This was done for practical reasons, as the field emission chamber high voltage feed through could only take 7 inputs and for a 3 × 3 device we needed 3 high voltage anode and 3 cathode lines (Fig. 2).

To drive diode based field emission devices involved switching high anode voltages in order to matrix address the prototype display. Hence for a screen size of $m \times n$ pixels, the high voltage driver would need to address $m+n$ number of lines directly. Hence when a row and column are activated, only the pixel at the intersection of the row and column is addressed. In this way, only a single pixel can have its state set or maintained at any one time. This can be achieved using a passive matrix addressing (diode structure) scheme in the case of DIODE based devices. The requirements for the diode driver system would be, a) To be able to switch 3 high voltage anodes and 3 cathodes and b) Develop a computer user interface, for operating the field emission driver

test system. The proposed design strategy is presented in Fig. 3, which highlights the primary components of the diode device driver test system. A 30KV@100W power supply HW030P, (Applied Kilovolts Ltd, UK) was used to power the field emission prototypes. Six high voltage relays (developed by Crydom, USA) were used to switch the nine pixels of the 3 × 3 matrix array. The controller unit was designed to act as an interface between the low voltage DAQ control signals and the high voltage signals being applied on the field emission test device. Data acquisition was performed using a Keithley, 96-channel USB board KUSB-3160 (Keithley Instruments, UK), this allowed us to setup a computer interface to switch the relays using low voltage digital signals. Figure 4, shows the completed driver prototype.

Pure silicon based field emitters generally having higher emission threshold (20 to 30 V/μm) compared to carbon nanotube emitters (2 to 3 V/μm), need a significantly higher voltage on the anode to be able to extract electrons from the cathode.

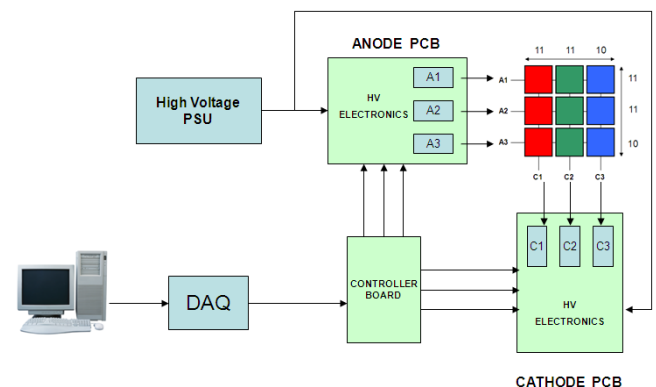


Figure (3) Schematic representation of the 3 × 3 DIODE driver system. Here, A1 to A3 and C1 to C3 are the HV switching relays which allowed selecting the relevant pixel to the tested.

3. Software Design & Implementation:

13th Annual Research Day

Organised by the Deanship of Scientific Research in Collaboration with the College of Engineering
Research Centre
2nd April 2018

TestPoint developed by CEC (Capital Equipment Corporation), is a tool for creating custom test, measurement, and data acquisition applications.

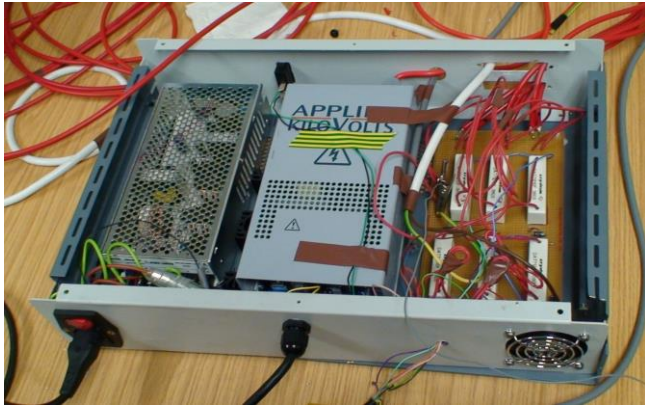


Figure (4) Image of bespoke DIODE driver system designed to switch a 3×3 pixel FED.

It includes features for controlling external hardware, creating user interfaces, processing and displaying data, creating report files, and exchanging information with other Windows programs. The graphical user interface was designed using TestPoint software (Fig. 5). This enabled us to create a simple graphical front panel to control the switching of the high voltage relays which allowed us to select a particular pixel to address.

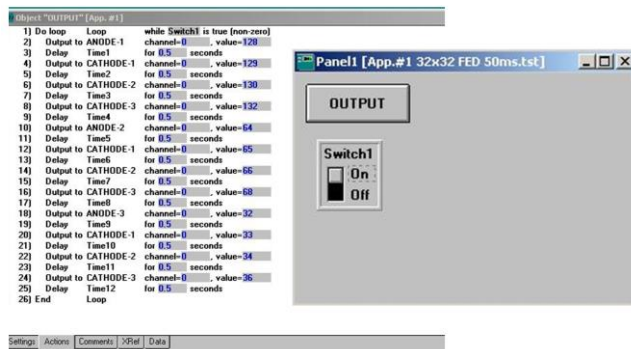


Figure (5) Schematic representation of the 3 × 3 DIODE driver system. Here, A1 to A3 and C1 to

C3 are the HV switching relays which allowed selecting the relevant pixel to be tested.

The software was designed to address each pixel by selecting a single anode i.e. for example A1 and then scan through three cathodes C1, C2 and C3 sequentially. This would then be repeated for A2 and A3, thereby addressing the entire display. The time delay between each programmed sequence would allow us flexibility to be able to increase or decrease the response rate. It can be seen from the above instruction set, that the program will scan through sequentially through all the pixels having a response/refresh rate of 0.5 sec. The entire program is in a loop; hence the instructions would cycle until interrupted. The program is controlled via a GUI (Graphical User Interface) which represents a virtual switch for the device. Below you can see a timing diagram for 1 cycle of the switching process.

4. Conclusions:

We have successfully designed and tested driver electronics to drive DIODE configuration field emission prototype displays based on silicon nano electron emitters. Design of a high voltage switching system required taking many safety precautions. It was decided to have two separate pcb's for anode and cathode. Also the track spacing on the pcb's were spaced out in order to prevent corona or arcing at high voltages. Also, the entire system was housed in an grounded electrical enclosure. The enclosure was partitioned; the bottom half being used for housing the High Power Supplies and the top partition to house the ANODE and CATHODE printed circuit boards.

References

- [1] A. Buldum, J.P. Lu, "Electron field emission properties of closed carbon nanotubes,"

13th Annual Research Day

Organised by the Deanship of Scientific Research in Collaboration with the College of Engineering
Research Centre
2nd April 2018

- Phys. Rev. Lett., vol. 91 (23), pp. 236801, 2003
- [2] Y. B. Li, Y. Bando and D. Goldberg, "MoS₂ nanoflowers and their field-emission properties," Appl. Phys. Lett., vol. 82, No. 12, pp. 1962, 2003.
- [3] S.R.P. Silva, R.D. Forrest, J.M. Shannon, "Electron field emission from amorphous silicon," J. Vac. Sci. Technol., vol. B17, No. 2, pp. 596, 1999.
- [4] Y. F. Tang, S. R. P. Silva, M. J. Rose, "Electron field emission from excimer laser crystallized amorphous silicon," Appl. Phys. Lett., vol. 80, No. 22, pp. 4154, 2002.
- [5] M. Z. Shaikh, K. A. O'Neill, S. K. Persheyev, "Excimer laser crystallized HWCVD thin silicon films: electron field emission," Proc. of the MRS Spring, vol. 862, No. A6.8, 2005
- [6] K. O. Neil, M. Z. Shaikh, S. K. Persheyev, "Laser annealed HWCVD and PECVD thin silicon films. Electron field emission," Thin Solid Films, vol. 501, pp. 310, 2006

Computationally Efficient Equalization Technique for High Mobility OFDMA Uplink Systems

Thafasal Ijyas V. P and Muneer Parayangat¹

¹Department of Electrical Engineering, College of Engineering, King Khalid University,
PO Box 394, Abha 61411 KSA.
E-mail address: ithafasal@kku.edu.sa

Abstract: Equalization of data symbols in the OFDMA uplink characterized by a high mobility, high data rate doubly selective channel condition is not an adequately addressed problem in the contemporary wireless communication field. The proliferation of hand-held, mobile devices used by commuters in high speed vehicles and requiring high data rates demands the development of efficient methods to deal with the impairments in such channel conditions. In this work, we propose a computationally efficient signal model and a zero-forcing equalizer based on that to address this problem. Simulation results validate the efficacy of the proposed method.

Keywords: *OFDMA, Equalization, Uplink, Doubly-Selective Channel (DSC), ZFE.*

1. Introduction:

Orthogonal Frequency Division Multiple Access (OFDMA) and Single Carrier Frequency Division Multiple Access (SCFDMA) reign supreme as the most prominent multiple access technologies for contemporary and emerging wireless communication systems [1]. A challenging issue in OFDMA systems is the impairment caused to the received signal due to carrier frequency offsets (CFO), timing offsets and the wireless fading channel. Joint estimation of CFOs and channel coefficients as well as equalization issues in OFDMA uplink have been intensely-explored during the recent years. The computational complexity of the problem is very high and many low-complexity suboptimal solutions have been proposed [2,3]. Many of these works presume a time-invariant or quasi-invariant scenario. The problem becomes extremely challenging when the channel condition becomes doubly-selective, that is, the channel exhibits both time-selectivity as well as frequency selectivity. The simultaneous demands for high mobility and high data rates make such channels inevitable. Estimation and equalization in OFDMA uplink is more complex than in the downlink.

An efficient equalization technique is essential for the proper detection of data symbols. Only a few works are available in the literature which addresses low complexity equalization in high mobility OFDMA uplinks. Also, CFO compensation and timing error correction in such systems are critical issues. Techniques such as zero-forcing (ZF), matched filter (MF) and minimum means square error (MMSE) filtering are discussed in [4] and [5] based on the assumption that both time and frequency synchronization have already been done at the receiver and residual CFOs are incorporated in the channel estimation step. Also, these schemes require matrix inversion, where the computational complexity increases exponentially with the number of sub-carriers. Equalization of data symbols in OFDMA uplink with high mobility users is rarely discussed in the literature. As hand-held wireless devices are extremely mobile, there is great demand for computationally lighter equalization schemes for OFDMA uplink systems.

In this paper, we propose a low complexity signal model for the uplink received signal, which significantly reduces the computational

complexity of ZF equalization. Based on that, ZF equalization is implemented. The proposed scheme is suitable for a generalized carrier assignment scheme (CAS). Extensive simulation studies are conducted to verify the efficacy of this scheme in a high mobility scenario.

2. System Model:

A baseband model of OFDMA uplink with K active users is shown in Figure 1. It is assumed that each user communicates with the base station (BS) through the subcarriers allotted to them using specific CAS. Users in OFDMA uplink acquire their coarse frequency and timing information through the downlink synchronization channel before the uplink transmission begins. In general, users are spatially distributed in a cell. The BS receives a superposition of signals from all the active users in the uplink. Hence the BS receiver has to perform the estimation of synchronization and channel parameters from the received composite signal. The estimated parameters are then used to equalize the effects of synchronization and channel impairments.

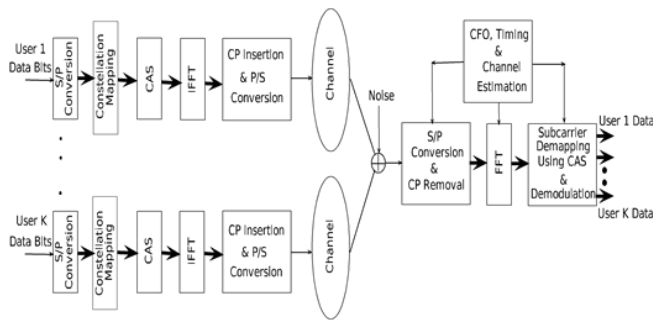


Figure (1) Base band model of a generic OFDMA uplink system

2.1 Transmitted Signal Model

The signal frame transmitted by a user comprises of one OFDM preamble (training) symbol for synchronization and channel estimation followed by many data symbols in general. In the case of static or quasi-static channel environments, one

preamble is sufficient for obtaining synchronization parameters and channel estimates for the complete signal frame. However, in DSC environments, the time variations of channel will be very rapid. The power profile of a DSC channel is shown in Figure 2. Hence by dividing a long frame into shorter burst (frame) structures and performing the estimation task for each burst structure is also discussed in the literature [4,6].

A burst structure of an OFDMA transmission having M symbols with P out of them as pilot symbols is shown in Figure 3. Here, m denotes the symbol index in a burst and N is the total number of sub-carriers available. N_k subcarriers are randomly allocated to each user exclusively such that $\sum_{k=1}^K N_k = N$.

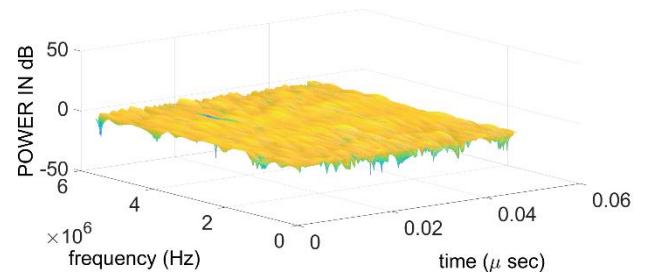


Figure (2) Power profile of a typical DSC channel

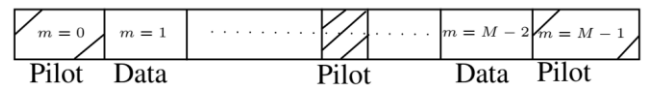


Figure (3) Burst structure of OFDMA symbols with each frame having M symbols

Since they are distributed in space, it is reasonable to assume that the users communicate with the BS through independent channels. The allocated subcarriers to each user are modulated using the data/pilot symbols, as the case may be, which takes the value from the constellations like BPSK, QPSK, QAM etc. After performing the IFFT operation at the transmitter, the n^{th} sample in the m^{th} OFDMA symbol of k^{th} user is written as

13th Annual Research Day

Organised by the Deanship of Scientific Research in Collaboration with the College of Engineering

Research Centre

2nd April 2018

$$x_m^k(n) = \frac{1}{\sqrt{N}} \sum_{i=0}^{N-1} X_m^k(i) e^{j2\pi ni/N} \quad (1)$$

where $m \in \{0, 1, \dots, M-1\}$ and $X_m^k(i)$ is the data/pilot on i^{th} sub-carrier in the m^{th} OFDMA symbol of the k^{th} user. Note that $X_m^k(i)$ takes its value from a constellation only if i^{th} sub-carrier is assigned to k^{th} user and is zero otherwise. The discrete time symbol vector is written as $\mathbf{x}_{k,m} = [x_m^k(0), x_m^k(1), \dots, x_m^k(N-1)]^T$. The signal $\mathbf{x}_{k,m}$ is appended with a cyclic prefix (CP) so that each symbol will have $N_s = N + N_{cp}$ samples.

2.2 Received Signal Model

Consider the transmit signal model given in (1). The data bits are encoded using a convolutional encoder with a code rate R_c and are partitioned into blocks of size J . After the bitwise interleaving, they are mapped into QPSK symbols. The mapped symbols are then symbol-wise interleaved and modulated on to the subcarriers according to generalized CAS. The time domain samples can be written in vector form as $\mathbf{x}_{k,m}$ and appended with CP of length N_{cp} as mentioned above. If the m^{th} time domain symbol is a pilot symbol, then it will have a length N_p and is given as $\mathbf{x}_{k,m} = [x_m^k(0), x_m^k(1), \dots, x_m^k(N_p-1)]^T$. The received signal including the effect of timing offset is given as

$$y_m(n) = \sum_{k=1}^K \sum_{l=0}^{L-1} e^{\frac{j2\pi\epsilon_k}{N}(n+\tilde{m}(m))} h_m^k(n,l) x_m^k(n-l-\rho_k) + v_m(n) \quad (2)$$

where $\tilde{m}(m) = n_d^m N_s + (n_p^m + 1) N_{cp} + n_p^m N_p$ with n_p^m and n_d^m being the number of pilot symbols and data symbols, respectively, preceding the m^{th} symbol in a frame. Here ρ_k represents the integer part of the timing offset. The fractional part of the timing offset can be absorbed to the channel impulse response because it appears as linear phase across the FFT output at the receiver. In order to avoid the inter-symbol interference (ISI), the CP length is taken

as $N_{cp} > L + \rho$, where L is the maximum number of channel taps and $\rho = \max\{\rho_1, \dots, \rho_K\}$ is the maximum expected integer timing offset [2]. Hence CP will take care of channel delay spread and residual timing offset so as to avoid ISI. Collecting all the received signal samples of the m^{th} symbol, we obtain

$$y(m) = \sum_{k=1}^K y_{k,m} + v_m = \Psi_m(\epsilon_k) \mathbf{H}_{k,m} \mathbf{x}_{k,m}(\rho_k) \quad (3)$$

Note that the length of pilot vector is N_p instead of N , where $N_p \leq N$. Here $\Psi_m(\epsilon_k) = \text{diag}\left([e^{\frac{j2\pi\epsilon_k}{N}(0+\tilde{m}(m))}, \dots, e^{\frac{j2\pi\epsilon_k}{N}(N-1+\tilde{m}(m))}]^T\right)$ denotes the phase shift introduced due to CFO on m^{th} symbol of the k^{th} user and $\mathbf{x}_{k,m}(\rho_k)$ is the circularly shifted version of $\mathbf{x}_{k,m}$ by ρ_k units. For pilot symbols, the CFO matrix is expressed as $\Psi_m(\epsilon_k) = \text{diag}\left([e^{\frac{j2\pi\epsilon_k}{N}(0+\tilde{m}(m))}, \dots, e^{\frac{j2\pi\epsilon_k}{N}(N_p-1+\tilde{m}(m))}]^T\right)$.

The proposed equalizer operates in frequency domain. By taking the FFT of (3), the m^{th} received OFDMA symbol in frequency domain is obtained as

$$\mathbf{Y}_m = \mathbf{F} \mathbf{y}_m \quad (4)$$

where $\mathbf{F} = [\mathbf{f}_0, \mathbf{f}_1, \dots, \mathbf{f}_{N-1}]^H$ is the FFT matrix of size $(N \times N)$ with \mathbf{f}_i as the i^{th} column. The received signal in (4) can be written as

$$\mathbf{Y}_m = [\mathbf{F} \psi_m(\hat{\epsilon}_1) \hat{\mathbf{H}}_{1,m} \mathbf{F}^H, \dots, \mathbf{F} \psi_m(\hat{\epsilon}_1) \hat{\mathbf{H}}_{1,m} \mathbf{F}^H] \mathbf{X} \begin{bmatrix} \mathbf{X}_m^1 \\ \vdots \\ \mathbf{X}_m^K \end{bmatrix} \quad (5)$$

Where,

$$\mathbf{X}_m^k = [X_m^k(0), \dots, X_m^k(N-1)]^T \quad (6)$$

The first term in (5) is a matrix of dimension $(N \times NK)$ and the second term has a dimension $(NK \times I)$. Hence, \mathbf{Y}_m has a dimension $(N \times I)$. Even though the solution to (5) seems to be impossible, it can be solved by reformulating the received signal equation by considering only the column space spanned by the channel of each user. By making use of CFOs and channel estimates, the combined frequency domain channel matrix after incorporating the effect of CFO is expressed as

$$\mathbf{G}_m^{full} = \mathbf{F} \sum_{k=1}^K \psi_m(\hat{\epsilon}_k) \hat{\mathbf{H}}_{k,m} \mathbf{F}^H \tilde{\mathbf{\Omega}}_k \quad (7)$$

where

- $\hat{\epsilon}_k$ is the estimated CFO
- $\hat{\mathbf{H}}_{k,m}$ is the channel matrix constructed from channel estimates.
- $\tilde{\mathbf{\Omega}}_k = \Upsilon(\rho_k) \mathbf{\Omega}_k$ is the timing correction matrix for the k^{th} user.
- $\Upsilon(\rho_k) = \text{diag}\left(1, e^{\frac{-j2\pi\rho_k}{N}}, \dots, e^{\frac{-j2\pi\rho_k(N-1)}{N}}\right)$ is the timing correction factor
- $\mathbf{\Omega}_k$ represents the diagonal matrix with i^{th} diagonal entry as one, if and only if the i^{th} subcarrier is allocated to the k^{th} user and is zero otherwise.

It has been observed that \mathbf{G}_m^{full} is a banded matrix with significant coefficients concentrated in a banded structure along the main diagonal. The m^{th} received symbol in frequency domain in (4) can be rewritten as

$$\mathbf{Y}_m = \mathbf{G}_m^{full} \mathbf{X}_m + \tilde{\mathbf{v}}_m \quad (8)$$

Where, $\tilde{\mathbf{v}}_m$ is the noise vector in frequency domain. A zero-forcing formulation can be obtained from this as

$$\hat{\mathbf{X}}_m = (\mathbf{G}_m^{full})^{-1} \mathbf{Y}_m \quad (9)$$

3. Results and Discussion

In this section, we discuss the bit-error rate performance of the low-complexity ZF equalizer. The simulation parameters are given in Table 1.

Table 1: Simulation Parameters

Simulation parameter	Value
Carrier frequency	2 GHz
Number of subcarriers (N)	512
Subcarriers for each user (N_k)	N/K
Useful symbol duration	91.4 μ s
Subcarrier spacing	10.941kHz
OFDMA signal bandwidth	5.6018 MHz
Frame size (M) and pilot symbols (P)	M = 6, P = 2
CAS	Generalized CAS

In Figure (4), we have plotted the bit error rate performance of the proposed method.

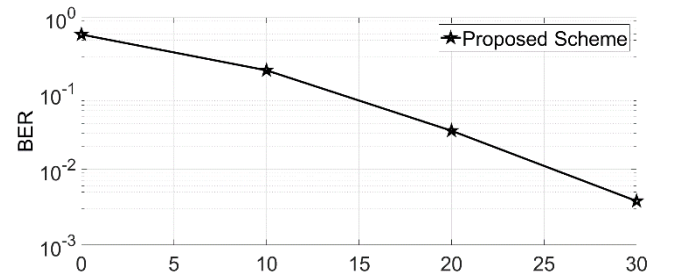


Figure (4) BER performance of the proposed method

The number of active users in the uplink is chosen to be $K = 4$. A mobile speed of 295 km/hr (i.e. $fdT = 0.05$) is considered in all the simulation studies. This corresponds to a normalized Doppler spread $fdT = 0.05$. Given, the high

13th Annual Research Day

Organised by the Deanship of Scientific Research in Collaboration with the College of Engineering
Research Centre
2nd April 2018

mobility condition, it can be seen that the proposed method gives an impressive performance.

4. Conclusions:

In this work, we have proposed a computationally efficient signal model and a ZF equalizer based on that for OFDMA uplink systems in a high mobility scenario characterized by a DSC channel. The equalizer gives an impressive performance even in a challenging channel condition. This signal model can also be further used for developing estimators using MMSE and subspace projection methods. Simulation results demonstrate the efficacy of this method.

References

- [1] H. Yin, S. Alamouti, OFDMA: A broadband wireless access technology, Proc. IEEE Sarnoff Symposium, New Jersey, USA, (2006).
- [2] X. N. Zeng, A. Ghayeb, Joint CFO and channel estimation for OFDMA uplink: an application of the variable projection method, IEEE Trans. Wireless Commun., vol. 8, no. 5, pp. 2306–2311, May 2009.
- [3] M.-O. Pun, M. Morelli and C.-C. Kuo, “Maximum-likelihood synchronization and channel estimation for OFDMA uplink transmissions,” IEEE Trans. Commun., vol. 54, no. 4, pp. 726–736, Apr. 2006
- [4] M. F Rabbi, S. W. Hou, and C.C. Ko, “High mobility orthogonal frequency division multiple access channel estimation using basis expansion model,” IET. Commun., vol. 4, no. 3, pp. 353-367, Feb. 2010.
- [5] S.-W. Hou and C. C. Ko, “Inter-carrier interference suppression for OFDMA up-link in time-and frequency-selective fading channels,” IEEE Trans. Veh. Tech., vol. 58, no. 6, pp. 2741–2754, Jul. 2009.
- [6] H. Nguyen-Le and T. Le-Ngoc, “Pilot-aided joint CFO and doubly-selective channel estimation for OFDM transmissions,” IEEE Trans. Broadcast., vol. 56, no. 4, pp. 514–522, Dec. 2010.
- [7] X. N. Zeng and A. Ghayeb, “Joint CFO and channel estimation for OFDMA uplink: an application of the variable projection method,” IEEE Trans. Wireless Commun., vol. 8, no. 5, pp. 2306–2311, May 2009

Investigation On The Influence Of Errors On The Chatter Vibrations During Drilling Operation

Amir Kessentini^{1,2}, Sofien Toumi³, Jamel Madiouli^{1,4}

¹Department of Mechanical Engineering, College of Engineering, King Khalid University,
PO Box 394, Abha 61411 KSA.

E-mail address: akessentini@kku.edu.sa

²Department of Engineering science and technology, IPEIN, Carthage University

³Department of Electro-Mechanical Engineering, U2MP – ENIS, Sfax University

⁴National Engineering School of Monastir, E.N.I.M, University of Monastir, Tunisia.

Abstract: The operation of Drilling and High Speed Drilling (HSM) is a fundamental operation of machining in industry for the production of the aeronautical and automobile parts, molds, and dies. The productivity of the parts manufactured is highly affected by holes' quality, and decrease by the vibrations due to the discontinuity of the contact tool part and the variations of the feed-rate caused by the Chatter vibration phenomenon.

In the present work, an investigation of the influence of errors on the chatter vibrations during Drilling operation based on simulation is presented. The dynamic model incorporates two types of errors which are the geometrical errors and alignment errors. The developed dynamic model demonstrates the ability to predict chatter vibrations during the drilling operation such as radial vibrations, axial vibrations and torsional vibrations.

Keywords: *Machining, Drilling, chatter vibrations, Errors.*

1. Introduction:

The drilling operation is by far the most used as finishing operation of structures made of metallic materials. It allows above all to make orifices necessary for the assembly of the elements of a given mechanical system. To succeed in a drilling operation is therefore to eliminate all types of mounting errors or geometrical defects for the drill. These errors constitute a set of additional factors that affect the cutting dynamics and the overall dynamic and vibration behavior of the machine - tool - part system.

Several research works give a particular interest in the modeling of the dynamics of the cutting in drilling. Given the three traditional manufacturing processes, turning, milling and drilling, the latter remains poorly understood and unstated because of the complexity of the geometry of the drill [1-4-12-13-14] and the hidden aspect of this operation. Bayly et al [5] developed the theory of

torsional-axial chatter vibrations. He showed that coupling between torsional and axial vibrations is the main cause of chatter. Ulsoy et al. [6] has studied in this work the influence of lateral vibrations on the drilling torque and the pushing force.

Jochem Roukema [7] presented in his works a general modeling of the drilling operation and he studied the different types of vibrations such as; lateral and torsional vibrations as well as axial vibrations and are influencing the quality of the drilled holes.

The study of the drilling operation in the with defects and errors discussed by researchers. Gupta [8] developed a cutting model that involved tool misalignment and showed that the vibration increases when the angular error increases, then he studied the influence of the errors on the profile of holes produced [9], but he did not study the presence of mounting errors. In

this paper we will present a numerical solution of the motion equation in the presence of defects.

2. Dynamical Model:

2.1 dynamical motion equation

The dynamical motion equation is presented as following:

$$[M] \begin{Bmatrix} \ddot{x}_c(t) \\ \ddot{y}_c(t) \\ \ddot{z}_c(t) \\ \ddot{\theta}_c(t) \end{Bmatrix} + [C] \begin{Bmatrix} \dot{x}_c(t) \\ \dot{y}_c(t) \\ \dot{z}_c(t) \\ \dot{\theta}_c(t) \end{Bmatrix} + [K] \begin{Bmatrix} x_c(t) \\ y_c(t) \\ z_c(t) \\ \theta_c(t) \end{Bmatrix} = \begin{Bmatrix} F_x(t) \\ F_y(t) \\ F_z(t) \\ T_c(t) \end{Bmatrix}$$

Where x_c and y_c , are the lateral deflections, z_c is the axial deflection and θ_c is the angular deflection. The following figure illustrates this dynamic pattern of drilling.

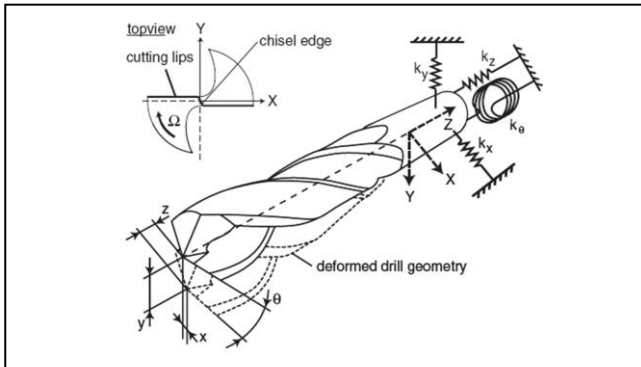


Figure 1. Dynamical model with 4DOF [7]

F_x , F_y , F_z and T_c represent the residual forces generated by the cutting phenomenon.

They can be written as following:

$$F_x = F_y = k_r(r, h) \cdot \Delta b \cdot \Delta h$$

$$F_z = K_z(r, h) \cdot \Delta b \cdot \Delta h$$

$$T_c = K_c(r, h) \cdot \Delta b \cdot \Delta h \cdot r$$

The instantaneous variation of the chip thickness is a function of the vibrations of the tool in the x and y directions at the instant 't' and at the delayed instant 't- t/2' can be in the form [10]:

$$\Delta h = [(X(t) - X(t - \tau/2)) \cos \alpha + (Y(t) - Y(t - \tau/2)) \sin \alpha] d\alpha$$

3. Errors definition:

3.1 The drill fixture errors definition

The drill fixture errors that are always present during a drilling operation are:

- The radial error of axis offset
- Angular errors between the drill bit axis and the spindle axis

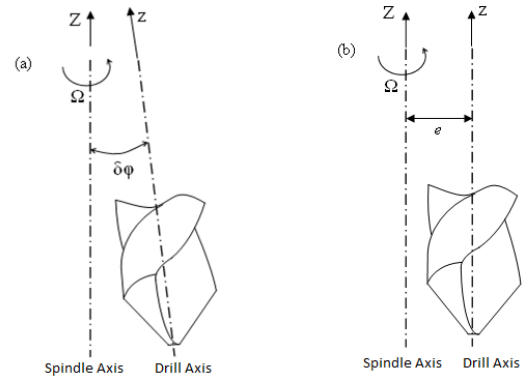
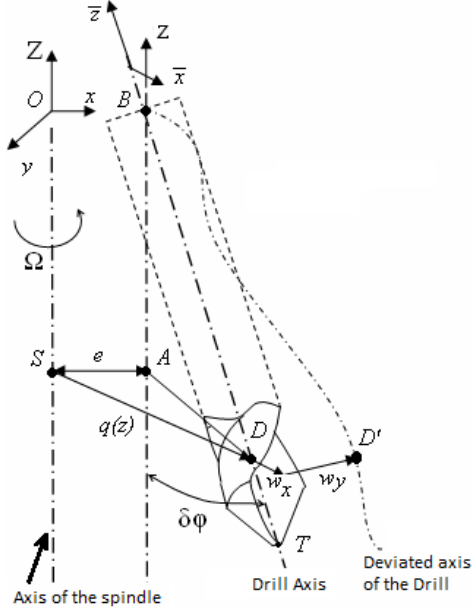


Figure 2. Drill Positioning Errors
(a) angular error; (b) radial error

3.2 Mathematical model of misalignment

Figure 3 shows the alignment errors associated with the location of the drill in the spindle. $(O; x, y, z)$ is the frame axis related to the spindle, the z axis coincides with the axis of the spindle



and the x axis belongs to the base of the drill (point B). (D) is a point on the axis of the drill, (T) is the peak of the drill. The plane of the drill is the plane that contains the main axis of the drill and perpendicular to the plane (x, y) .

Figure 3. Alignment errors associated with drill positioning in the spindle

Alignment errors are defined in Figure 3 as follows:

- Linear offset " e "
- Angular error " $\delta\phi$ "
- Angle of orientation of the drill " ϕ "

The overall misalignment of the drill bit at each point (D) is determined by the following formula that was developed by [8]:

$$q(z) = \sqrt{(|BD|\sin\delta\phi)^2 + e^2 + 2e|BD|\sin\delta\phi\cos\phi}$$

3.3 Definition of geometrical defects of the drill

The geometrical shape defects of the drill that can affect the dynamic behavior of the machine - tool - part system are:

- The relative height between the two lips
- The relative inclination of the lips

The value of this defect is added to the chip thickness in the numerical calculation model of the cutting forces and the drilling torque.

$$\Delta h_r(t) = h_r(t)$$

The main causes of these defects are problems of sharpening the drills as well as manufacturing defects.

Since the chip thickness on the two lips is not the same under due to this defect, the cutting forces also will not be the same and the cutting movement of the drill will not be balanced. This defect influences and excites the surface regeneration mechanism. Figure 4 illustrates this error.

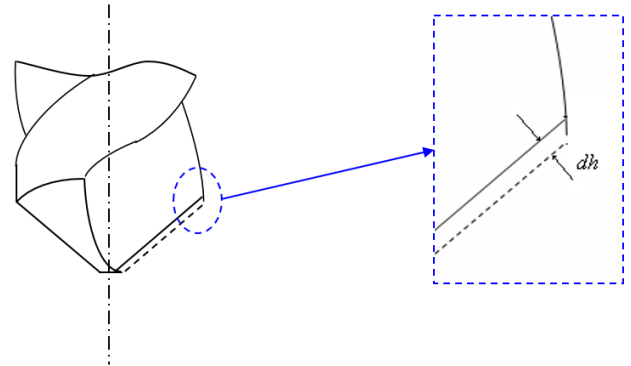


Figure 4. Geometrical defects: relative height of the lips

The relative inclination angle of the cutting lips is another type of geometrical errors which appear following the sharpening of the drills. The effect

of this angular error on the chip thickness depends on the coordinate ξ of a given point on the cutting edge of the lip. The effect of this angular defect decreases from the drill diameter to the center. The thickness of the chip influences the fluctuations of the cutting forces. The chip thickness due to this error is given by the following formula [11]:

$$\Delta h_\theta(t) = z(\tan(p + \delta p) - \tan p) \cos(p + \delta p)$$

The following figure illustrates the relative tilt error between the lips.

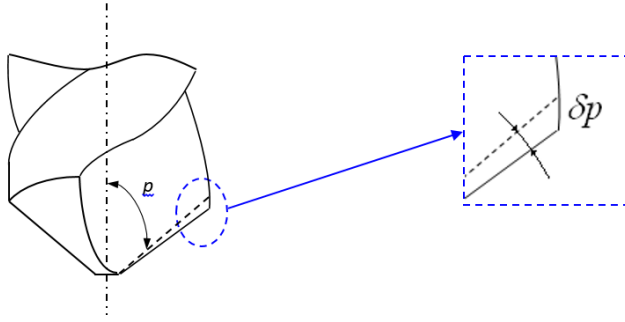


Figure 5. Geometrical defects: Angle of inclination relative to the cutting lips

3.4 Modeling of the cutting forces in the presence of defects

The instantaneous variation of the chip thickness is a function of the vibrations of the drill tip. The following formula gives the expression of chip thickness as a function of radial displacements [10]:

$$\Delta h = [(X(t) - X(t - \tau/2)) \cos \alpha + (Y(t) - Y(t - \tau/2)) \sin \alpha] d\alpha$$

$\theta = \Omega t$ and " τ " represents the time corresponding to one revolution of the tool.

This expression does not take into account the different defects. Indeed, the additional chip thickness that appears as a result of these defects is added to this expression which defines the surface regeneration mechanism.

The total chip thickness caused by the surface regeneration mechanism, fixture errors, and sharpening errors is given by the following formula:

$$\Delta h_T(t) = \Delta h(t) + \Delta h_\theta(t) + \Delta h_r(t) + z(t)$$

By adding the total chip thickness the cutting forces become:

$$F_x = F_y = k_r(r, h) \cdot \Delta b \cdot \Delta h_T$$

$$F_z = K_z(r, h) \cdot \Delta b \cdot \Delta h_T$$

$$T_c = K_c(r, h) \cdot \Delta b \cdot \Delta h_T \cdot r$$

Hence the equation of motion is of the form:

$$[M] \begin{Bmatrix} \ddot{x}_c(t) \\ \ddot{y}_c(t) \\ \ddot{z}_c(t) \\ \ddot{\theta}_c(t) \end{Bmatrix} + [C] \begin{Bmatrix} \dot{x}_c(t) \\ \dot{y}_c(t) \\ \dot{z}_c(t) \\ \dot{\theta}_c(t) \end{Bmatrix} + [K] \begin{Bmatrix} x_c(t) \\ y_c(t) \\ z_c(t) \\ \theta_c(t) \end{Bmatrix} = \begin{Bmatrix} K_r(r, h) \cdot \Delta b \cdot h_T \\ K_r(r, h) \cdot \Delta b \cdot h_T \\ K_z(r, h) \cdot \Delta b \cdot h_T \\ K_c(r, h) \cdot \Delta b \cdot h_T \cdot r \end{Bmatrix}$$

3. Results and Discussion

The study of vibratory behavior of the tool consists of solving the equation of motion relative to this model, which is nonlinear:

$$\{\ddot{U}(t)\} + [M]^{-1}[C]\{\dot{U}(t)\} + [M]^{-1}[K]\{U(t)\} = [M]^{-1}\{F(U, t)\}$$

In this present work we will work with an equivalent damping which favors the stability of our system.

Moreover, we consider that the tool is symmetrical in both directions x and y.

We choose the initial conditions as follows:

$$x(0) = y(0) = 7.10^{-6} m, z(0) = 0 m, \theta(0) = 6.10^{-5}$$

$$\dot{x} = \dot{y}(0) = 2.10^{-5} m/s, \dot{z}(0) = 3.10^{-5} m/s, \dot{\theta}(0) = 2.10^{-5} m/s$$

13th Annual Research Day

Organised by the Deanship of Scientific Research in Collaboration with the College of Engineering
Research Centre
2nd April 2018

In this resolution we will use the values of the following defects:

Defect	Value
Relative inclination error δp	0.01rd
$\delta \varphi$	0.01rd
w_y	0.01mm
Relative height error Δh_r	0.4mm
Axis offset "e"	0.02mm

The simulation results show that dynamic responses increase in the presence of defects. Figure 7 shows the influence of the defects on the dynamic response of the tool according to the lateral cutting direction. We can see the increase of the amplitude of the vibrations in the presence of the defects.

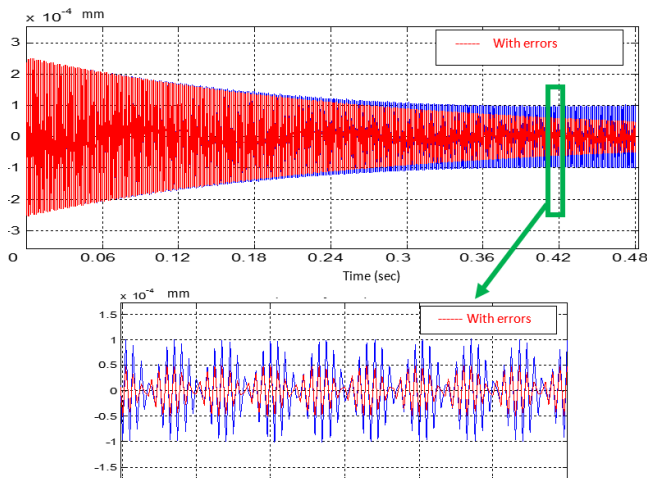


Figure 7. Influence of defects on lateral dynamic response

Figure 8 shows the influence of the defects on the dynamic response of the cutting tool in the axial direction.

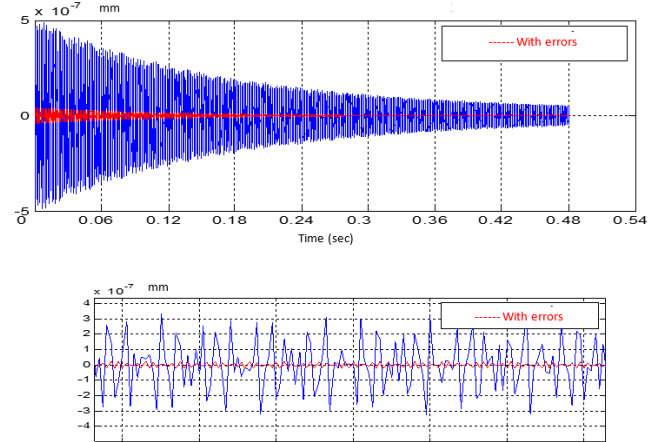


Figure8. Influence of defects on axial dynamic response

Figure 9 shows the influence of defects on the dynamic response of the tool according to torsional direction.

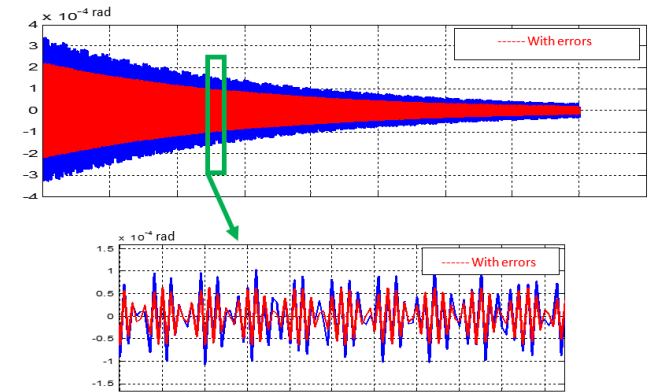


Figure 9. Influence of defects on torsional dynamic response

4. Conclusions:

This paper was devoted for the study of the drilling operation in the presence of defects that we studied their influence on the vibrations of our system.

The equation of these defects allowed to incorporate them into the global equation of motion to solve the model again in the presence of defects.

The numerical resolution of this equation has shown that vibrations increase in the presence of

13th Annual Research Day

Organised by the Deanship of Scientific Research in Collaboration with the College of Engineering
Research Centre
2nd April 2018

defects. Furthermore, the amplitudes of the lateral, axial and torsional dynamic responses are significantly increased under the effect of errors. These results prove that the quality of drilling does not only depend on the behavior of the elementary machining cell (tool-piece system) but also on some additional factors related to fixture errors setting. According to the required quality of drilled holes in high serial production, traditional setting for drill fixture and sharpening methods are not efficient to avoid chatter vibration consequences.

References

- [1] Mustapha Elhachimi*, Serge Torbaty, Pierre Joyot. (1999) Mechanical modelling of high speed drilling. 1: predicting torque and thrust. *International Journal of Machine Tools & Manufacture* 39 (1999) 553–568.
- [2] Yang, J.A.; Jaganathan, V. (2002). A new dynamic model for drilling and reaming processes. *International Journal of Machine Tools & Manufacture* Vol.42, 299–311
- [3] Xia, R.S; Mahdavian, S. M. (2004). Experimental studies of step drills and establishment of empirical equation for the drilling process. *International Journal of Machine Tools & Manufacture* Vol.44, 1–6
- [4] J.S. Strenkowski, C.C. Hsieh, A.J. Shih, An analytical finite element technique for predicting thrust force and torque in drilling. *International Journal of Machine Tools & Manufacture* Vol.44, 1413–1421
- [5] Bayly et al, Philip V. Bayly, Michael T. Lamar, Sean G. Calvert. « Low- Frequency Regenerative Vibration and the Formation of Lobed Holes in Drilling ». *Journal of Manufacturing Science and Engineering* MAY 2002, Vol. 124.
- [6] R.M. Rincon, A.G. Ulsoy, Complex geometry rotary inertia and gyroscopic moment effects on drill vibrations, *Journal of Sound and Vibration* 188 (5) (1995) 701–715.
- [7] Jochem C. Roukema, Yusuf Altintas”Time domain simulation of torsional– axial vibrations in drilling” Department of Mechanical Engineering, The University of British Columbia. These de doctorat de l’université de British Columbia 2006
- [8] Khagendra Gupta O. Burak Ozdoganlar Shiv G. Kapoor Richard E. DeVor: Modeling and Prediction of Hole Profile in Drilling, Part 1: Modeling Drill Dynamics in the Presence of Drill Alignment Errors. Department of Mechanical and Industrial Engineering, University of Illinois at Urbana-Champaign, Urbana, IL 61801-2906
- [9] Khagendra Gupta O. Burak Ozdoganlar Shiv G. Kapoor Richard E. DeVor: Modeling and Prediction of Hole Profile in Drilling, Part 2: Modeling Hole Profile. Department of Mechanical and Industrial Engineering, University of Illinois at Urbana-Champaign, Urbana, IL 61801-2906
- [10] Juhchin A. Yang a, Venkatraman Jaganathan b,1, Ruxu Du c, « A new dynamic model for drilling and reaming processes », *International Journal of Machine Tools & Manufacture* 42 (2002) 299–311.
- [11]Yongping Gong Cheng Lin Kornel F. Ehmann. « Dynamics of Initial Penetration in Drilling: Part 1— Motion Mechanistic Model for Dynamic Forces ». *Journal of Manufacturing Science and Engineering*. MAY 2005, Vol. 127.

13th Annual Research Day

Organised by the Deanship of Scientific Research in Collaboration with the College of Engineering
Research Centre
2nd April 2018

- [12] L.B.Rau, V.S.Jakukore. « Cylinder Block Fixture for Mistake Proofing». American Journal of Engineering Research (AJER). e-ISSN : 2320-0847 p-ISSN : 2320-0936 Volume-03, Issue-10, pp-145-150.
- [13] K. Siva Kumar & G. Paulraj. « Geometric error control of workpiece during drilling through optimisation of fixture parameter using a genetic algorithm». International Journal of Production Research, Vol. 50, No. 12, 15 June 2012, 3450–3469.
- [14] Amir Parsian, Martin Magnevall, Tomas Beno, Mahdi Eynian. « Sound Analysis in Drilling, Frequency and Time Domains». Procedia CIRP Volume 58, 2017, Pages 411-415.